Master Thesis

Modelling of semi-floating XXL monopiles

by Gerardus Cornelis van Egmond

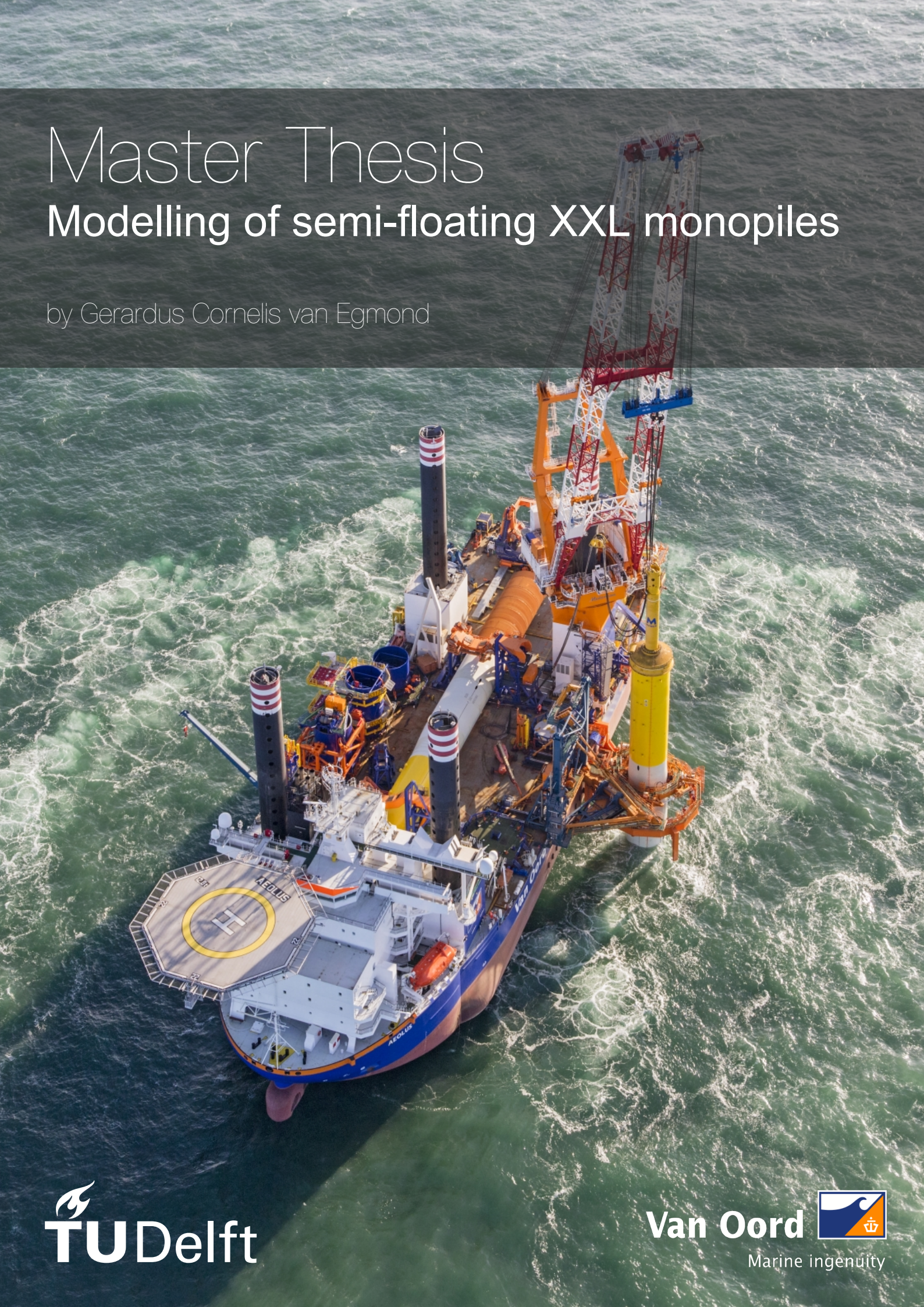

TU Delft

Van Oord
Marine ingenuity

Modelling of semi-floating XXL monopiles

Modelling the behavior of an upright semi-floating XXL monopile using the concept of trapped air.

by

Gerardus Cornelis van Egmond

to obtain the degree of

Master of Science
in Offshore and Dredging Engineering
at the Delft University of Technology,

to be defended publicly on Thursday July 13, 2023 at 15:00

Thesis committee:	Dr. ir. P.R. Wellens,	TU Delft,	Chair and Supervisor
	Dr. ir. G.H. Keetels,	TU Delft	
	ir. D. Fidalgo Domingos,	TU Delft	
	ir. K. van de Leur,	Van Oord,	Supervisor

Student number:	4495578
Project duration:	March 1, 2022 – July 13 2023

This thesis is confidential and cannot be made public until July 13, 2025.

An electronic version of this thesis is available at `http://repository.tudelft.nl/`.
Cover Image: Aeolus installing a monopile foundation, retrieved from Van Oord

TU Delft

Van Oord
Marine ingenuity

Preface

Upon completing a Bachelor's degree in Mechanical Engineering, this thesis represents the end of my Master's degree in Offshore and Dredging Engineering at the Technical University of Delft. I would like to express my gratitude to all who have supported me throughout my academic journey.

This research was carried out in collaboration with Van Oord, driven by my keen interest in the offshore wind industry and the company's outstanding professional and personal reputation. I am thankful for the opportunity to have worked alongside Van Oord that provided me the chance to conduct model experiments, which was the most exciting component of my thesis. I gained valuable knowledge and experience from working with a diverse team of experienced professionals during my time at Van Oord.

First and foremost, I would like to express my gratitude to K. van de Leur from Van Oord for his valuable guidance and support throughout the process of my thesis. His expertise, daily assistance and his constructive feedback have played a crucial role in shaping my research. I would also like to thank the rest of the Van Oord staff, particularly the members of the Hydrodynamics department, who have provided valuable insights during my research. Their contributions have been highly appreciated.

Secondly, I want to thank P.R. Wellens for his advice, interesting discussions and daily guidance throughout this project. Our meetings have been incredibly valuable, as they provided me with a fresh perspective and served as a constant source of motivation and improvement. In addition, I would like to thank the other committee members, D. Fidalgo Domingos for his useful feedback and G.H. Keetels for joining the committee as an external member at my graduation. Furthermore, I would like to express my gratitude to J. G. den Ouden, C. P. Poot and S. Schreier for their contributions in designing and assisting with the execution of the experiments.

A special thanks goes to my roommates, Bart, Koen and Leon for supporting and motivating me during my studies and throughout my thesis project. I would also like to thank my friend Tjeerd for the countless hours we spent studying together during our Master's program in Offshore and Dredging Engineering.

Finally, my deepest gratitude goes to my parents and my sisters, who have always been there for me. Your support has been a source of strength and motivation throughout my entire studies. We have faced difficult and challenging times during the completion of my thesis, but I am immensely grateful for your unwavering support. Without the five of you, I would not have been able to accomplish this significant milestone. Thank you for always being there for me and supporting me, no matter the circumstances.

Gerardus Cornelis van Egmond
Delft, July 2023

Abstract

Over the past few decades, there has been a significant increase in global energy consumption. To address the risks associated with climate change, there is an increasing urgency to transition towards renewable energy sources. With this growing demand, the interest in offshore wind energy has increased significantly, leading to the construction of larger bottom-founded offshore wind farms. In order to fulfill this rising demand, The International Renewable Energy Agency has estimated that a total of 2000 GW of installed offshore wind power is required to achieve net-zero emissions by 2050. However, the current installed capacity stands at approximately 35 GW, indicating a substantial gap that needs to be addressed. The offshore industry faces a major challenge in meeting this demand and making a substantial contribution to the supply of renewable energy sources.

As the size of wind turbines continues to increase, their monopile foundations also grow in weight and dimensions. Conventionally, monopiles are installed by upending them on the vessel, lifting them into the air and lowering them onto the seabed. However, this installation procedure is not feasible for extra-large (XXL) monopiles. This is because these XXL monopiles exceed the crane capacity of the, relatively new, installation vessels. To prevent the vessels from becoming outdated, an alternative approach to upending has been devised. This method involves utilizing the buoyancy of the monopile itself to compensate for the insufficient crane capacity on board of the vessel. This innovative upending technique is referred to as the trapped air method. This research explores this method as the influence of imposed buoyancy on the system's behavior in such operations has not been addressed in earlier research.

The main objective of this thesis is to examine the dynamic behavior and determine the natural frequencies of a monopile experiencing an upward facing buoyancy force. Moreover, it is desired to quantify the workable limits of the concept. First, a literature study is conducted, followed by a study that investigates the mechanics of the system. The monopile suspended from a crane, can be simplified using double pendulum models. Through the analytical approach, the influence of each force, mass and inertia component in the complex system can be examined individually. This assessment results in the equations of motion that serve as the foundation for the numerical model.

To gain initial insights into the behavior of the monopile, exploratory tests are conducted in a purpose-built experimental setup. It is observed that as the buoyant force increased, the monopile searches for an equilibrium to stabilize the system. Hydrodynamic effects induce a noticeable shift of the center of gravity of the monopile towards the waterline. Additionally, when a current is applied to the partially submerged monopile, motions in the sway direction are observed and suggests the presence of vortex induced motions.

Building upon the exploratory tests, decay tests are conducted at TU Delft to investigate the behavior and loads experienced at the cranetip. The results revealed that the presence of buoyancy significantly reduces the side-lead load to approximately X%-Y% of the maximum allowable load in the horizontal direction, which nearly half of the load observed without induced buoyancy. Additionally, the vertical loads reached approximately X%-Y% of the maximum allowed vertical loads. The buoyancy in the system effectively reduces both the vertical and horizontal loads in the cranetip. Furthermore, the presence of buoyancy leads to a significant decrease in the natural frequency of the system.

The numerical model is based on the equations of motion derived through the analytical approach. Initially, validation of the model is performed by using the scaled model dimensions. The frequency alignment indicates that the numerical model accurately models the natural frequencies on model scale. The model is then used to simulate a full-scale scenario. It can be concluded that numerical approximations of the frequencies closely align with those derived through the analytical approach and those observed during the model experiments. The close agreement among three different approaches provides strong validation of the accuracy and reliability of the numerical model in predicting the natural frequencies in full-scale scenarios.

Contents

Preface **i**

Abstract **ii**

List of Figures **v**

List of Tables **xi**

List of Symbols **xiii**

1 Introduction **1**
1.1 Conventional installation procedure . . . 2
1.2 Research motivation . . . 2
1.2.1 Literature review . . . 4
1.2.2 Knowledge gap . . . 6
1.2.3 Relevance . . . 6
1.2.4 Problem description . . . 6
1.2.5 Objective . . . 8
1.2.6 Hypothesis . . . 9

2 Physical phenomena **11**
2.1 Floating body . . . 12
2.1.1 Hydrostatic stability . . . 12
2.2 Waves . . . 13
2.3 Current . . . 14
2.3.1 Current loading . . . 16
2.3.2 Vortex-induced motions . . . 17
2.4 Sloshing . . . 17
2.5 Wind . . . 19

3 Analytical model **20**
3.1 Natural frequency . . . 20
3.2 System simplification . . . 21
3.3 Methods . . . 24
3.3.1 Principle of virtual work . . . 24
3.3.2 Newton's method . . . 25
3.3.3 Lagrange's method . . . 26
3.4 Single pendulum . . . 27
3.5 Double pendulum . . . 27
3.6 Double pendulum - Inertia . . . 28
3.6.1 Results . . . 30
3.7 Conclusions . . . 31

4 Exploratory tests **32**
4.1 Experimental set-up . . . 32
4.2 Prototype I . . . 32
4.2.1 Results . . . 33
4.2.2 Conclusions . . . 35
4.3 Prototype II . . . 36
4.3.1 Results . . . 36
4.3.2 Conclusions . . . 36

5 Model test set-up **37**
5.1 Purpose of physical modelling . . . 37
5.2 Tank set-up . . . 37
5.3 Scaling . . . 38
5.3.1 Scaling methods . . . 38
5.3.2 Model scale . . . 39
5.3.3 Monopile . . . 39
5.3.4 H-frame . . . 40
5.3.5 Support structure . . . 41
5.3.6 Measurement instruments . . . 41
5.4 Runs . . . 42

6 Model test results **44**
6.1 Single pendulum . . . 44
6.2 Buoyancy . . . 46
6.3 Double pendulum - In-line mode . . . 49
6.4 Double pendulum - Out of line mode . . . 50
6.4.1 Frequency analysis . . . 53
6.4.2 Vortex induced motions . . . 62
6.5 Reliability . . . 62
6.5.1 Uncertainties . . . 63
6.6 Conclusions . . . 63

7 Numerical model **64**
7.1 Method . . . 64
7.2 System characterization . . . 65
7.3 Inertia . . . 67
7.4 Damping . . . 68
7.4.1 Viscous damping . . . 68
7.4.2 Linear damping . . . 69
7.4.3 Damping coefficients . . . 70
7.5 Model . . . 71
7.5.1 Scaled model characteristics . . . 72

8 Numerical results **73**
8.1 Numerical model - Scaled . . . 73
8.1.1 Excluding hydrodynamic effects . . . 73
8.1.2 Including hydrodynamic effects . . . 75
8.2 Numerical model - Full scale . . . 76
8.2.1 Excluding hydrodynamic effects . . . 77
8.2.2 Including hydrodynamic effects . . . 77
8.3 Conclusion . . . 78

9 Conclusions **81**

10 Recommendations **83**

A Kinematics and derivations **84**
A.1 Single pendulum - Vertical . . . 84
A.2 Single pendulum - Inline . . . 87
A.3 Double pendulum . . . 90
A.4 Double pendulum - Inertia . . . 94
A.4.1 Lagrangian method . . . 94
A.4.2 Verification using small approximation method . . . 97
A.4.3 Equations of motion . . . 98
A.5 Compound double pendulum . . . 98

B Newton's second law of motion **101**
B.1 Constraints . . . 102
B.2 Single Pendulum . . . 103

B.3 Double Pendulum . . . 104

C Exploratory test set-up **107**

D Experimental set-up **109**
D.1 Scaling of Inertia . . . 109
D.2 Support structure . . . 110
D.3 H-frame . . . 111
D.4 Monopile . . . 112
D.5 Measurement equipment . . . 113
D.6 Technical drawings . . . 114

E Model test results **116**
E.1 Single pendulum . . . 116
E.2 Double pendulum - In-line mode . . . 118
E.2.1 Pitch angle . . . 118
E.3 Double pendulum - Out of line mode . . . 121
E.3.1 Pitch angle . . . 121
E.3.2 Forces in the crane tip . . . 125
E.3.3 Displacements . . . 127
E.3.4 Vortex shedding frequency . . . 132
E.4 Small initial angles . . . 134
E.5 Reliability . . . 134

F Damping **136**
F.1 Single Pendulum . . . 138
F.2 Double Pendulum Out-line mode . . . 138

G Numerical model results **140**
G.1 User interface . . . 140
G.2 Inertia contribution . . . 141
G.3 Numerical simulations - Model scale . . . 142
G.3.1 Double pendulum - Out-line . . . 142
G.4 Numerical simulations - Full scale . . . 157
G.5 Uncertainties: Frequency range . . . 161

Bibliography **162**

List of Figures

1.1 Future outlook on installed power [GW] by IRENA [16] . . . 1
1.2 Van Oord's installation vessel: the Aeolus, retrieved from Van Oord . . . 2
1.3 The existing method for upending an MP on deck of the Aeolus, retrieved from Van Oord . . . 2
1.4 The trapped air method for upending an MP . . . 3
1.5 Spar-buoy concept supporting a floating wind turbine . . . 4
1.6 A truss spar supporting an oil and gas facility . . . 4
1.7 Top, side and front view of a sketch of the Aeolus, presenting the side- and off-lead angles . . . 7
1.8 Closer look to the side-lead angle of a more detailed sketch of the crane wires . . . 7
1.9 A damaged sheave, retrieved from site visit . . . 7

2.1 Definition of ship motions in six degrees of freedom, retrieved from [18] . . . 11
2.2 Schematic view of a floating body with center of gravity (G), center of buoyancy (B), keel (K) and metacenter (M) in neutral and slightly heeled position. Originally after [30] . . . 12
2.3 Schematic view of a floating cylinder with center of gravity (G), center of buoyancy (B), keel (K) and metacenter (M) in neutral and slightly heeled position. . . . 13
2.4 Harmonic wave definitions, retrieved from [18] . . . 13
2.5 Flow regimes at a circular cylinder for incompressible flow, retrieved from [10] . . . 15
2.6 Inertia and drag coefficient vs Keuligan Carpenter number for constant values of the frequency parameter and the Reynolds number. Originally after Sarpkaya (1976) [24]. . . . 16
2.7 Strouhal number for a smooth circular cylinder as a function of the Reynolds number, retrieved from [28] . . . 17
2.8 The highest natural period $T_{1,1}$ as a function of radius R0 for an upright circular cylindrical tank. The framed values of $T_{1,1}$ are relevant for the ballast tanks of a column-stabilized offshore platform (from [8], p. 135) . . . 18

3.1 Sketch of the MP suspended from a crane of the Aeolus . . . 20
3.2 1: The system converted to a simplification 2: The system represented as point masses 3: The system including all components 4: Only two masses and buoyancy force are considered . . . 21
3.3 The input parameters h_{sub}, h_{int}, l_a and l_{int} . . . 22
3.4 Small angle approximation near $\phi = 0$ for *left:* $\sin\phi$ and *right:* $\cos\phi$ . . . 25
3.5 a) Single pendulum system b) Forces and its force components acting on the mass m . . . 25
3.6 Mass spring system . . . 26
3.7 Visualization of the in-phase mode (left) and the out of phase mode (right) . . . 28
3.8 Double pendulum (for all components) . . . 28
3.9 Parameters: l_{mp}, h_{sub}, h_{int} and l_{int} . . . 29
3.10 Natural frequency vs submerged length for different h_{int}, considering all components and inertia of m_2, m_{int} and m_a . . . 30
3.11 Filling up the MP during lowering as a potential solution . . . 31

4.1 Sketch of first experimental set-up . . . 32
4.2 First experimental set-up (vertical MP) . . . 33
4.3 Vortices due to applied current . . . 34
4.4 Initiated in-line double pendulum system of exploratory tests. (left) No submergence (right) Partially submerged . . . 34
4.5 Initiated out-line double pendulum system of exploratory tests. (left) No submergence (right) Partially submerged . . . 35
4.6 'Searching' phenomenon of the MP while lowered (forces are not a representation of reality) 35
4.7 Flexible tube to facilitate water inlet at the bottom . . . 36

5.1 Schematic top-view of the towing tank . . . 37
5.2 Model scale MP . . . 40
5.3 H-frame . . . 41
5.4 The force transducers in the cranetip . . . 41
5.5 Sketch of the decay tests 1. S.P. In-line mode 2. D.P. Out of phase mode 3. D.P. In-phase mode . . . 43

6.1 Test matrix of single pendulum system . . . 44
6.2 SP Decay with damping curve fit for h(0, 0) Run 17 . . . 45
6.3 Damping ratio ν for each test run for a single pendulum system . . . 46
6.4 x- and z-displacement vs. time when lowering the MP for $h_{\text{int}} = 0$ (Run 137) . . . 47
6.5 x- and z-displacement vs. time when lowering the MP for $h_{\text{int}} = 0$ (Run 138) . . . 47
6.6 Visualization of generated moment around the pivot point . . . 48
6.7 In-line mode . . . 49
6.8 Test matrix of double pendulum system initial In-line mode . . . 49
6.9 Test run - Pitch angle for $h(0,0)$ (Run 329) . . . 49
6.10 Test run - Pitch angle for $h(10,20)$ (Run 155) . . . 49
6.11 Test run - FFT for pitch motion for $h(0,0)$ (Run 329) . . . 50
6.12 Out of line mode . . . 50
6.13 Pitch angle of DP decay test for $h(0,10)$ . . . 50
6.14 Pitch angle of DP decay test for $h(10,10)$ . . . 50
6.15 Pitch angle of DP decay test in air for $h(0,0)$ (Run 317) . . . 51
6.16 Pitch angle of H-frame in air, peak detection and damping . . . 51
6.17 Damping ratio ν_{Hframe} and ν_{mp} for each test run for a double pendulum system out-line . . 52
6.18 Natural period T_{Hframe} and T_{mp} for each test run for a double pendulum system out-line . . 52
6.19 Natural frequency ω_{Hframe} and ω_{mp} for each test run for a double pendulum system out-line 53
6.20 FFT for pitch motion for $h(0,0)$, extreme angles (Run 317) . . . 54
6.21 Definition of F_x and F_z . . . 55
6.22 Forces in x- and z-direction for $h(0,10)$ . . . 55
6.23 Two maximum forces in x-direction including the pitch angle for $h(0,10)$ . . . 56
6.24 Two minimal forces in z-direction including the pitch angle for $h(0,10)$ . . . 56
6.25 Displacements in x- and z-direction for $h(10,10)$ (Run 207) . . . 58
6.26 Roll angle when given a certain initial angle $\theta = 0.2°$ for $h(10,10)$ (Run 207) . . . 59
6.27 FFT for roll motion for $h(10,10)$, extreme angles (Run 207) . . . 59
6.28 Yaw angle when given a certain initial angle $\psi = -4°$ for $h(10,10)$ . . . 59
6.29 FFT for yaw motion for $h(10,10)$, extreme angles (Run 207) . . . 60
6.30 FFT for yaw motion for $h(10,10)$, small angles (Run 272) . . . 61
6.31 x-, y-displacement and yaw angle of top MP vs. time for $h(10,10)$ (Run 207) . . . 61
6.32 x- vs. y-displacement including yaw angle of bottom MP for $h(10,10)$, extreme angles (Run 207) . . . 62

7.1 1: The system converted to a simplification 2: The system represented as point masses 3,4: The system including two particles m_1 and m_2 and angles ϕ_1 and ϕ_2 . . . 64
7.2 1: The system converted to a simplification 2: The system represented as point masses 3: The system including all components with degrees of freedom, ϕ_1 and ϕ_2 . . . 66
7.3 Simplification of the contribution of the inertia of the H-frame . . . 67
7.4 System including drag force F_d . . . 68
7.5 Damping in the degrees of freedom ϕ_1 and ϕ_2 . . . 70
7.6 Flowchart of the numerical model written in Python . . . 71
7.7 Model test run - x-displacement vs. time for $h(10,10)$ (Run 207) . . . 72

8.1 Test run pitch angles (Run 317) and Numerical pitch angles on model scale for $h(0,0)$ . . . 73
8.2 Test run (Run 317) vs. Numerical pitch angles for $h(0,0)$ on model scale, for large initial angles 74
8.3 Test run (Run 317) - FFT for pitch motion for $h(0,0)$, for large initial angles . . . 74
8.4 Numerical model - FFT for pitch motion for $h(0,0)$, for large initial angles . . . 74
8.5 Test run pitch angles (Run 278) and Numerical pitch angles for $h(10,20)$, for small initial angles 75

8.6 Test run (Run 278) vs. Numerical pitch angles for $h(10,20)$ on model scale, for small initial angles . . . 75
8.7 Test run (Run 278) - FFT for pitch motion for $h(10,20)$, for small initial angles . . . 76
8.8 Numerical model - FFT for pitch motion for $h(10,20)$, for small initial angles . . . 76
8.9 Simplification of the mass and inertia contribution of the cable . . . 76
8.10 Numerical pitch angle for $h(0,0)$ on full scale, for small initial angles . . . 77
8.11 Numerical model - FFT for pitch motion for $h(0,0)$ on full scale, for small initial angles . . . 77
8.12 Numerical pitch angle for $h(10,20)$ on full scale, for small initial angles . . . 78
8.13 Numerical model - FFT for pitch motion for $h(10,20)$ on full scale, for small initial angles . . . 78
8.14 Comparison of **model scale** frequencies of the Model tests vs. Numerical model . . . 79
8.15 Comparison of **full scale** frequencies of the Analytical model vs. Model tests vs. Numerical model . . . 80

A.1 Single pendulum - Vertical (for m_2 and m_{int}) . . . 84
A.2 Natural frequency vs submerged length for different h_{int}, considering m_2 and m_{int} . . . 86
A.3 Natural frequency vs submerged length for different h_{int}, considering $m_{1,2,3}$, m_{int} and m_a . . . 87
A.4 Single pendulum - Inline (for m_2 and m_{int}) . . . 87
A.5 Natural frequency vs submerged length for different h_{int}, considering m_2 and m_{int} . . . 89
A.6 Natural frequency vs submerged length for different h_{int}, considering $m_{1,2,3}$, m_{int} and m_a . . . 89
A.7 Comparison of the natural frequency behavior with $h_{\text{int}} = 20$ m . . . 90
A.8 Comparison of the natural frequency behavior of the Single Pendulum (Vertical vs Inline) with $h_{\text{int}} = 20$ m . . . 90
A.9 Double pendulum (for $m_{1,2,3}$ and m_{int}) . . . 90
A.10 Natural frequency vs submerged length for different h_{int}, considering m_2 and m_{int} . . . 93
A.11 Natural frequency vs submerged length for different h_{int}, considering $m_{1,2,3}$, m_{int} and m_a . . . 94
A.12 Closer look to the crane wire that is reeved twice . . . 100

B.1 1: The system converted to a simplification 2: The system represented as point masses 3,4: The system including two particles m_1 and m_2 and angles ϕ_1 and ϕ_2 . . . 101
B.2 A single pendulum (left) with its free body diagram (right) . . . 103
B.3 A double pendulum (left) with its free body diagram (right) . . . 104

C.1 Camera views of the exploratory experimental set-up . . . 107
C.2 Static offset in sway direction increases because of the manually generated wave forces acting on the MP . . . 108
C.3 Motions of the MP in surge and sway direction as a result of vortices around the MP caused by the applied current . . . 108

D.1 Model test set-up . . . 110
D.2 *Top*) H-frame *Bottom)* Top and bottom hinges . . . 111
D.3 Monopile *Top left)* Shortened MP *Top right)* Aluminium MP with Bottom Cap *Bottom)* MP suspended from cranetip . . . 112
D.4 Measurement equipment: *Top left)* Target plate *Top right)* Surface elevation measurement device *Bottom left)* Electromagnet *Bottom rigt)* Force transducers . . . 113
D.5 Technical drawing U-frame including MP in Rhino . . . 114
D.6 Overview of the experimental set-up in Rhino . . . 115

E.1 SP Decay test pitch angle vs. time for $h(0,10)$ . . . 116
E.2 SP Decay test pitch angle vs. time for $h(0,20)$ . . . 116
E.3 SP Decay test pitch angle vs. time for $h(10,10)$ . . . 116
E.4 SP Decay test pitch angle vs. time for $h(10,20)$ . . . 117
E.5 SP Decay test pitch angle vs. time for $h(10,30)$ . . . 117
E.6 SP Decay test pitch angle vs. time for $h(20,20)$ . . . 117
E.7 SP Decay test pitch angle vs. time for $h(20,30)$ . . . 117
E.8 SP Decay test pitch angle vs. time for $h(30,30)$ . . . 117
E.9 Test run - Pitch angle for $h(0,0)$ (Run 329) . . . 118
E.10 Test run - FFT for pitch motion for $h(0,0)$ (Run 329) . . . 118

E.11 Test run - Pitch angle for $h(0,10)$ (Run 131) . . . 118
E.12 Test run - FFT for pitch motion for $h(0,10)$ (Run 131) . . . 118
E.13 Test run - Pitch angle for $h(10,10)$ (Run 146) . . . 119
E.14 Test run - FFT for pitch motion for $h(10,10)$ (Run 146) . . . 119
E.15 Test run - Pitch angle for $h(10,20)$ (Run 155) . . . 119
E.16 Test run - FFT for pitch motion for $h(10,20)$ (Run 155) . . . 119
E.17 Test run - Pitch angle for $h(20,20)$ (Run 168) . . . 120
E.18 Test run - FFT for pitch motion for $h(20,20)$ (Run 168) . . . 120
E.19 Test run - Pitch angle for $h(20,30)$ (Run 177) . . . 120
E.20 Test run - FFT for pitch motion for $h(20,30)$ (Run 177) . . . 120
E.21 Test run - Pitch angle for $h(30,30)$ (Run 191) . . . 121
E.22 Test run - FFT for pitch motion for $h(30,30)$ (Run 191) . . . 121
E.23 Test run - Pitch angle for $h(0,0)$ (Run 317) . . . 121
E.24 Test run - FFT for pitch motion for $h(0,0)$ (Run 317) . . . 121
E.25 Test run - Pitch angle for $h(0,10)$ (Run 201) . . . 122
E.26 Test run - FFT for pitch motion for $h(0,10)$ (Run 201) . . . 122
E.27 Test run - Pitch angle for $h(10,10)$ (Run 207) . . . 122
E.28 Test run - FFT for pitch motion for $h(10,10)$ (Run 207) . . . 122
E.29 Test run - Pitch angle for $h(10,20)$ (Run 223) . . . 123
E.30 Test run - FFT for pitch motion for $h(10,20)$ (Run 223) . . . 123
E.31 Test run - Pitch angle for $h(20,20)$ (Run 232) . . . 123
E.32 Test run - FFT for pitch motion for $h(20,20)$ (Run 232) . . . 123
E.33 Test run - Pitch angle for $h(20,30)$ (Run 241) . . . 124
E.34 Test run - FFT for pitch motion for $h(20,30)$ (Run 241) . . . 124
E.35 Test run - Pitch angle for $h(30,30)$ (Run 254) . . . 124
E.36 Test run - FFT for pitch motion for $h(30,30)$ (Run 254) . . . 124
E.37 Forces in x- and z-direction including the pitch angle for $h(0,10)$ . . . 125
E.38 Comparison of F_x and F_z for $h(0,10)$ vs. $h(10,10)$ . . . 126
E.39 Displacements in y- and z-direction vs. x-direction for $h(0,10)$ . . . 127
E.40 Displacements in y- and z-direction vs. x-direction for $h(0,10)$ and $h(10,10)$ . . . 127
E.41 x- vs. y-displacement including yaw angle of bottom MP for $h(10,10)$, small angles (Run 272) 128
E.42 x- vs. y-displacement including yaw angle of bottom MP for $h(20,20)$, small angles (Run 282) 128
E.43 x- vs. y-displacement including yaw angles of top MP for $h(0,10)$ (Run 201) . . . 129
E.44 x- vs. y-displacement including yaw angles of bottom MP for $h(0,10)$ (Run 201) . . . 129
E.45 x- vs. y-displacement including yaw angles of top MP for $h(10,10)$ (Run 207) . . . 129
E.46 x- vs. y-displacement including yaw angles of bottom MP for $h(10,10)$ (Run 207) . . . 129
E.47 x- vs. y-displacement including yaw angles of top MP for $h(10,20)$ (Run 223) . . . 130
E.48 x- vs. y-displacement including yaw angles of bottom MP for $h(10,20)$ (Run 223) . . . 130
E.49 x- vs. y-displacement including yaw angles of top MP for $h(20,20)$ (Run 232) . . . 130
E.50 x- vs. y-displacement including yaw angles of bottom MP for $h(20,20)$ (Run 232) . . . 130
E.51 x- vs. y-displacement including yaw angles of top MP for $h(20,30)$ (Run 241) . . . 131
E.52 x- vs. y-displacement including yaw angles of bottom MP for $h(20,30)$ (Run 241) . . . 131
E.53 x- vs. y-displacement including yaw angles of top MP for $h(30,30)$ (Run 254) . . . 131
E.54 x- vs. y-displacement including yaw angles of bottom MP for $h(30,30)$ (Run 254) . . . 131
E.55 Test run - FFT for y-displacement for $h(0,10)$ (Run 201) . . . 132
E.56 Test run - FFT for y-displacement for $h(10,10)$ (Run 207) . . . 132
E.57 Test run - FFT for y-displacement for $h(10,20)$ (Run 223) . . . 133
E.58 Test run - FFT for y-displacement for $h(20,20)$ (Run 232) . . . 133
E.59 Test run - FFT for y-displacement for $h(20,30)$ (Run 241) . . . 133
E.60 Test run - FFT for y-displacement for $h(30,30)$ (Run 254) . . . 133
E.61 Comparison of F_x and F_z (small vs. extreme initial angles) for $h(0,10)$ . . . 134
E.62 Comparison of roll, pitch and yaw angles (small vs. extreme initial angles) for $h(0,10)$ . . . 134
E.63 Reliability check of forces vs. time for three iterations (Run 220, 223, 226) . . . 135
E.64 Reliability check of angles vs. time for three iterations (Run 220, 223, 226) . . . 135

F.1 Single pendulum decay test in air . . . 136

F.2 Logarithmic decrement [18] . . . 137
F.3 SP Decay with damping curve fit for h(0, 10) Run 43 . . . 138
F.4 SP Decay with damping curve fit for h(10, 10) Run 73 . . . 138
F.5 SP Decay with damping curve fit for h(10, 20) Run 64 . . . 138
F.6 DP Out-line Decay H-frame with damping curve fit for h(10, 10) (Run 207) . . . 138
F.7 DP Out-line Decay MP with damping curve fit for h(10, 10) (Run 207) . . . 138
F.8 DP Out-line Decay H-frame with damping curve fit for h(20, 30) (Run 241) . . . 139
F.9 DP Out-line Decay MP with damping curve fit for h(20, 30) (Run 241) . . . 139
F.10 DP Out-line Decay H-frame with damping curve fit for h(30, 30) (Run 254) . . . 139
F.11 DP Out-line Decay MP with damping curve fit for h(30, 30) (Run 254) . . . 139

G.1 Snapshot of the double pendulum animated over time . . . 140
G.2 Simplification of the inertia of the monopile as m_2 . . . 141
G.3 Simplification of the inertia of the internal water column as m_{int} . . . 141
G.4 Simplification of the inertia of the added mass as m_a, and resultant forces of the buoyancy F_b and drag F_d . . . 141
G.5 Simplification of the inertia of the bottom cap as m_3 . . . 141
G.6 Damping coefficient b_{Hframe} and b_{mp} for each test run for a double pendulum system out-line 142
G.7 Test run pitch angles (Run 317) and Numerical pitch angles on model scale for $h(0,0)$ . . . 143
G.8 Test run (Run 317) vs. Numerical pitch angles for $h(0,0)$ on model scale . . . 143
G.9 Test run (Run 317) - FFT for pitch motion for $h(0,0)$, large initial angles . . . 143
G.10 Numerical model - FFT for pitch motion for $h(0,0)$ . . . 143
G.11 Test run pitch angles (Run 201) and Numerical pitch angles on model scale for $h(0,10)$ . . . 144
G.12 Test run (Run 201) vs. Numerical pitch angles for $h(0,10)$ on model scale . . . 144
G.13 Test run (Run 201) - FFT for pitch motion for $h(0,10)$, large initial angles . . . 144
G.14 Numerical model - FFT for pitch motion for $h(0,10)$ . . . 144
G.15 Test run pitch angles (Run 207) and Numerical pitch angles on model scale for $h(10,10)$ . . . 145
G.16 Test run (Run 207) vs. Numerical pitch angles for $h(10,10)$ on model scale . . . 145
G.17 Test run (Run 207) - FFT for pitch motion for $h(10,10)$, large initial angles . . . 145
G.18 Numerical model - FFT for pitch motion for $h(10,10)$ . . . 145
G.19 Test run pitch angles (Run 223) and Numerical pitch angles on model scale for $h(10,20)$ . . . 146
G.20 Test run (Run 223) vs. Numerical pitch angles for $h(10,20)$ on model scale . . . 146
G.21 Test run (Run 223) - FFT for pitch motion for $h(10,20)$, large initial angles . . . 146
G.22 Numerical model - FFT for pitch motion for $h(10,20)$ . . . 146
G.23 Test run pitch angles (Run 232) and Numerical pitch angles on model scale for $h(20,20)$ . . . 147
G.24 Test run (Run 232) vs. Numerical pitch angles for $h(20,20)$ on model scale . . . 147
G.25 Test run (Run 232) - FFT for pitch motion for $h(20,20)$ . . . 147
G.26 Numerical model - FFT for pitch motion for $h(20,20)$, large initial angles . . . 147
G.27 Test run pitch angles (Run 241) and Numerical pitch angles on model scale for $h(20,30)$ . . . 148
G.28 Test run (Run 241) vs. Numerical pitch angles for $h(32,30)$ on model scale . . . 148
G.29 Test run (Run 241) - FFT for pitch motion for $h(20,30)$, large initial angles . . . 148
G.30 Numerical model - FFT for pitch motion for $h(20,30)$ . . . 148
G.31 Test run pitch angles (Run 254) and Numerical pitch angles on model scale for $h(30,30)$ . . . 149
G.32 Test run (254) vs. Numerical pitch angles for $h(30,30)$ on model scale . . . 149
G.33 Test run (Run 254) - FFT for pitch motion for $h(30,30)$, large initial angles . . . 149
G.34 Numerical model - FFT for pitch motion for $h(30,30)$ . . . 149
G.35 Test run pitch angles (Run 300) and Numerical pitch angles on model scale for $h(0,0)$ . . . 150
G.36 Test run (Run 300) vs. Numerical pitch angles for $h(0,0)$ on model scale . . . 150
G.37 Test run (Run 300) - FFT for pitch motion for $h(0,0)$, small initial angles . . . 150
G.38 Numerical model - FFT for pitch motion for $h(0,0)$, small initial angles . . . 150
G.39 Test run pitch angles (Run 263) and Numerical pitch angles on model scale for $h(0,10)$ . . . 151
G.40 Test run (Run 263) vs. Numerical pitch angles for $h(0,10)$ on model scale . . . 151
G.41 Test run (Run 263) - FFT for pitch motion for $h(0,10)$, small initial angles . . . 151
G.42 Numerical model - FFT for pitch motion for $h(0,10)$, small initial angles . . . 151
G.43 Test run pitch angles (Run 272) and Numerical pitch angles on model scale for $h(10,10)$ . . . 152
G.44 Test run (Run 272) vs. Numerical pitch angles for $h(10,10)$ on model scale . . . 152

G.45 Test run (Run 272) - FFT for pitch motion for $h(10,10)$, small initial angles 152
G.46 Numerical model - FFT for pitch motion for $h(10,10)$, small initial angles 152
G.47 Test run pitch angles (Run 278) and Numerical pitch angles on model scale for $h(10,20)$ . . 153
G.48 Test run (Run 278) vs. Numerical pitch angles for $h(10,20)$ on model scale 153
G.49 Test run (Run 278) - FFT for pitch motion for $h(10,20)$, small initial angles 153
G.50 Numerical model - FFT for pitch motion for $h(10,20)$, small initial angles 153
G.51 Test run pitch angles (Run 281) and Numerical pitch angles on model scale for $h(20,20)$ . . 154
G.52 Test run (Run 281) vs. Numerical pitch angles for $h(20,20)$ on model scale 154
G.53 Test run (Run 281) - FFT for pitch motion for $h(20,20)$, small initial angles 154
G.54 Numerical model - FFT for pitch motion for $h(20,20)$, small initial angles 154
G.55 Test run pitch angles (Run 290) and Numerical pitch angles on model scale for $h(20,30)$ . . 155
G.56 Test run (Run 290) vs. Numerical pitch angles for $h(32,30)$ on model scale 155
G.57 Test run (Run 290) - FFT for pitch motion for $h(20,30)$, small initial angles 155
G.58 Numerical model - FFT for pitch motion for $h(20,30)$, small initial angles 155
G.59 Test run pitch angles (Run 293) and Numerical pitch angles on model scale for $h(30,30)$ . . 156
G.60 Test run (293) vs. Numerical pitch angles for $h(30,30)$ on model scale 156
G.61 Test run (Run 293) - FFT for pitch motion for $h(30,30)$, small initial angles 156
G.62 Numerical model - FFT for pitch motion for $h(30,30)$, small initial angles 156
G.63 Damping coefficient b_{cable} and b_{mp} for each test run scaled to full-scale 157
G.64 Numerical pitch angle for $h(0,0)$ on full scale 157
G.65 Numerical FFT of pitch angle for $h(0,0)$ on full scale 157
G.66 Numerical pitch angle for $h(0,10)$ on full scale 158
G.67 Numerical FFT of pitch angle for $h(0,10)$ on full scale 158
G.68 Numerical pitch angle for $h(10,10)$ on full scale 158
G.69 Numerical FFT of pitch angle for $h(10,10)$ on full scale 158
G.70 Numerical pitch angle for $h(10,20)$ on full scale 159
G.71 Numerical FFT of pitch angle for $h(10,20)$ on full scale 159
G.72 Numerical pitch angle for $h(20,20)$ on full scale 159
G.73 Numerical FFT of pitch angle for $h(20,20)$ on full scale 159
G.74 Numerical pitch angle for $h(20,30)$ on full scale 160
G.75 Numerical FFT of pitch angle for $h(20,30)$ on full scale 160
G.76 Numerical pitch angle for $h(30,30)$ on full scale 160
G.77 Numerical FFT of pitch angle for $h(30,30)$ on full scale 160

List of Tables

1.1 Maximum allowable loads in the cranetip 7

2.1 Kinematic viscosity for different fluids and temperatures, retrieved from DNV-RP-C205 [27] 16
2.2 The first few roots $j'_{m,n}$ of the derivative of the Bessel function $J'_m(x)$ (from [9], orignally after Bauer [2])) 18
2.3 The natural frequencies for the 1st asymmetric sloshing mode ω_{11} [rad s^{-1}] for a cylinder with D = 9.5m 19
2.4 The natural frequencies for the 2nd asymmetric sloshing mode ω_{12} [rad s^{-1}] for a cylinder with D = 9.5m 19

3.1 Assigned values for input parameters 23
3.2 Natural frequencies and periods of the analytical approach for double pendulum incl. inertia 30

4.1 Rough scaling parameters (scaling 200:1) 32

5.1 Towing tank No.1 dimensions 37
5.2 Scaling conversion factors for different scaling methods 38
5.3 Required parameters of full- and model scale 39
5.4 Desired vs. real parameters MP model scale 40

6.1 Buoyancy requirements for the maximum submergence 48
6.2 Analytical model results vs. Model test results - Frequencies **Mode 1** 54
6.3 Analytical model results vs. Model test results - Frequencies **Mode 2** 54
6.4 Weights of different parameters suspended from the cranetip 55
6.5 Maximum forces in the cranetip corresponding to the 2nd peak ● for large initial angles . . 56
6.6 Maximum forces in the cranetip corresponding to the 2nd peak ● for small initial angles . . 57
6.7 Forces experienced in the cranetip as percentage of maximum allowed forces 57
6.8 Predicted sloshing frequencies ω_{11} and ω_{12} on full scale and model scale with $\lambda = 56.5$, $h_{\text{int}} =$ 10m 60
6.9 Max. velocity of object w.r.t. fluid, Reynolds nr. and vortex shedding frequency for each configuration 62

8.1 Comparison frequencies of Analytical model vs. Model test result vs. Numerical model - **Mode 1** 78
8.2 Comparison frequencies of Analytical model vs. Model test result vs. Numerical model - **Mode 2** 79

A.1 Desired and actual weight of the cable on full- and model scale 100

D.1 Height and mass of internal water column for full- and model scale 110

E.1 Maximum forces in the cranetip corresponding to the 1st peak ● for extreme initial angles . 125
E.2 Maximum forces in the cranetip corresponding to the 1st peak ● for small initial angles . . 125
E.3 Max. velocity of object w.r.t. fluid, Reynolds nr. and vortex shedding frequency for each configuration 132

G.1 Uncertainty analysis: Frequency range of Model test results and Numerical model results on model-scale for mode 1 and mode 2 161
G.2 Uncertainty analysis: Frequency range of Model test results and Numerical model results on full-scale for mode 1 and mode 2 161

List of Symbols

Abbreviations

Abbreviation	Description
CoG	Center of Gravity
CoM	Center of Mass
DoF	Degree of Freedom
EoM	Equation of Motion
FFT	Fast Fourier Transform
MP	Monopile
MSL	Mean sea level
ODE	Ordinary Differential Equation
OWT	Offshore Wind Turbine
p.o.a.	Point of application
RAO	Response Amplitude Operator
RNA	Rotor Nacelle Assembly
SWL	Safe Working Load
VIM	Vortex-induced Motions

Symbols

Symbol	Description	Unit
δT	Kinetic energy	J
δV	Potential energy	J
δx	Virtual displacement in x-direction	m
δz	Virtual displacement in z-direction	m
$\delta\phi_1$	Virtual angle cable	°
$\delta\phi_2$	Virtual angle MP	°
λ	Scaling factor	-
λ_{wave}	Wave length	m
μ	Dynamic viscosity	$\text{kg m}^{-1}\,\text{s}^{-1}$
∇	Submerged volume	m^3
ν	Damping ratio	-
ν_f	Kinematic viscosity of a fluid	$\text{m}^2\,\text{s}^{-1}$
ω_d	Damped natural frequency	rad s^{-1}
ω_n	Natural frequency	rad s^{-1}
ω_{mn}	Sloshing frequency	rad s^{-1}
ϕ_1	Pitch angle cable	°
$\dot{\phi}_1$	Angular velocity cable	$°\,\text{s}^{-1}$
$\ddot{\phi}_1$	Angular acceleration cable	$°\,\text{s}^{-2}$
ϕ_2	Pitch angle MP	°
$\dot{\phi}_2$	Angular velocity MP	$°\,\text{s}^{-1}$
$\ddot{\phi}_2$	Angular acceleration MP	$°\,\text{s}^{-2}$
ψ	Yaw angle	°
ρ_{fw}	Density fresh water	kg m^{-3}
ρ_{sw}	Density sea water	kg m^{-3}
θ	Roll angle	°
ζ_a	Wave amplitude	m

A_p	Projected area	m^2
b	Linear damping coefficient	$kg\,m^{-2}\,s^{-1}$
b_1 / b_{cable}	Linear damping coefficient cable	$kg\,m^{-2}\,s^{-1}$
b_2 / b_{mp}	Linear damping coefficient MP	$kg\,m^{-2}\,s^{-1}$
c	Restoring coefficient	$kg\,m^{-2}\,s^{-2}$
C_D	Drag coefficient	-
C_m	Inertia coefficient	-
D_i	Inner diameter MP	m
D_o	Outer diameter MP	m
E	Total energy in a system	J
f_n	Natural frequency	$m\,s^{-1}$
f_s	Vortex shedding frequency	$m\,s^{-1}$
F_b	Buoyancy force	N
F_T	Tension force in the cable	N
F_x	Force cranetip in x-direction	N
F_z	Force cranetip in z-direction	N
F_d	Drag force	N
F_g	Gravitational force	N
g	Gravitational acceleration	ms^{-2}
h	Water depth	m
h_{airgap}	Height of airgap	m
$h_{cranetip}$	Height of cranetip	m
h_{deck}	Deck height	m
h_{int}	Internal water level	m
h_{lift}	Lifting height	m
h_{sub}	Submergence of the MP	m
H_s	Significant wave height	m
j'_{mn}	n^{th} zero derivative of Bessel function	-
J'_m	Bessel function of order m	-
J_2	Inertia MP	$kg\,m^{-2}$
J_a	Inertia added mass	$kg\,m^{-2}$
J_{cable}	Inertia cable	$kg\,m^{-2}$
J_{Hframe}	Inertia H-frame	$kg\,m^{-2}$
J_{int}	Inertia inernal water column	$kg\,m^{-2}$
k	Spring constant	$N\,m^{-1}$
k_{mn}	Wave number	m^{-1}
K	Stiffness	$N\,m^{-1}$
KC	Keuligan Carpenter number	-
l_1	Length cable	m
l_2	Length top MP to CoG MP	m
l_3	Length top MP to bottom cap	m
l_a	Length top MP to p.o.a. added mass	m
l_d	Length CoG MP to p.o.a. drag force	m
l_{mp}	Length of MP	m
l_{int}	Length top MP to p.o.a. internal water column	m
L	Lagrangian	J
m_1	Mass of the top cap	kg / t
m_2	Mass of the monopile	kg / t
m_3	Mass of the bottom cap	kg / t
m_a	Added mass	kg / t
m_{int}	Mass of the internal water column	kg / t
m_{cable}	Mass of the cable	kg / t
m_{Hframe}	Mass of the H-frame	kg
M	Mass	kg / t
Re	Reynolds number	-
R_o	Outer radius MP	m

St	Strouhal number	-
t	Time	s
t_{mp}	Wall thickness MP	m
T	Oscillation period	s
T_p	Wave peak period	s
T_n	Natural period	s
u_m	Max. fluid velocity	$\mathrm{m\,s^{-2}}$
V_{ext}	Volume submerged MP	$\mathrm{m^3}$
V_{int}	Volume internal water column	$\mathrm{m^3}$
x	Displacement in x-direction	m
$\dot{x}$	Velocity in x-direction	$\mathrm{m\,s^{-1}}$
$\ddot{x}$	Acceleration in x-direction	$\mathrm{m\,s^{-2}}$
z	Displacement in z-direction	m
$\dot{z}$	Velocity in z-direction	$\mathrm{m\,s^{-1}}$
$\ddot{z}$	Acceleration in z-direction	$\mathrm{m\,s^{-2}}$

1 Introduction

Over the last century, the global energy demand has grown rapidly due to an immense growth in the world population, economical and technological developments. It took humanity 200.000 years to reach one billion and only 200 years to reach seven billion. Today, the earth's population is reaching eight billion and this growth is expected to continue over the coming decades. These rapidly increasing numbers in population correlate to a significant increase in the global energy consumption, in which fossil fuels had and still have a remarkable contribution. The consumption of these fossil fuels has lead to a dramatic change in the atmospheric composition. Since the beginning of the Industrial Revolution around the year 1750, human activities have increased the amount of carbon dioxide in the atmosphere by about 50% [21]. Carbon emissions and several other greenhouse gases can be seen as the primary driver of the global climate change humanity is facing today.

To avoid dangerous climate change in a greater extent, 196 countries throughout the world have signed the Paris Agreement in 2015, agreeing on terms to limit the global warming to well below 2 °C and preferably below 1.5 °C [3]. All countries involved need to reach their peak of greenhouse gases as soon as possible in order to achieve this ultimatum.

With the global energy demand increasing over the coming decades and the larger need for renewable energy, the interest in offshore wind energy has increased significantly. With bottom founded offshore wind turbines growing larger and more efficient, the Levelized Cost of Energy (LCOE)[1] of newly commissioned projects has declined by almost 48% and the global offshore market grew on average by 22% each year, both over the past decade [15]. This brings the total installed power to 35.3 GW, of which Europe remains the largest offshore market with 70% of the total global offshore installations [6]. As of 2020, China takes a strong lead in the developments of the Asian offshore market and deployment of installations in the U.S. are expected to accelerate from 2023. The International Renewable Energy Agency IRENA believes that a total of 2000 GW installed power is needed to reach net zero emissions by 2050, of which 270 GW will be expected by the year 2030. This future outlook can be found in figure 1.1 [16]. The global offshore wind industry awaits a major challenge to make a significant contribution to achieve carbon neutrality and help sustain the Paris Agreement in 2050.

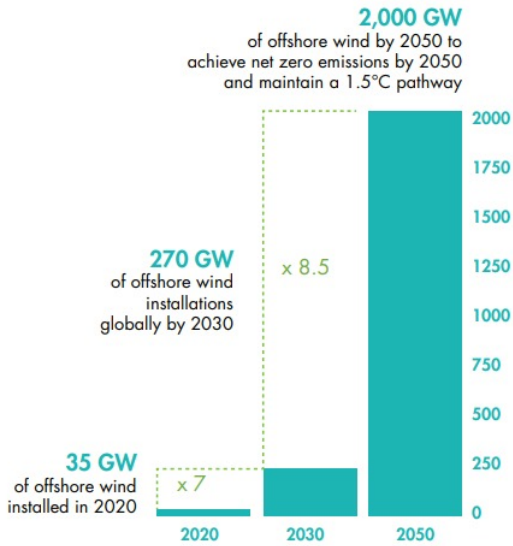

Figure 1.1: Future outlook on installed power [GW] by IRENA [16]

[1] "The LCOE of a given technology is the ratio of lifetime costs to lifetime electricity generation, both of which are discounted back to a common year using a discount rate that reflects the average cost of capital." [15]

1.1. Conventional installation procedure

Van Oord is one of the global leaders in the construction of offshore wind farms and installs offshore wind turbines (OWT) throughout the world. Since 2014, Van Oord has been equipped with the Aeolus, responsible for a large contribution of the OWT installed by Van Oord. The Aeolus is a jack-up vessel that is able to elevate itself out of the water in order to install foundations and wind turbines without experiencing excessive motions due to current or incoming waves. Figure 1.2 illustrates the Aeolus in two primary modes: sailing mode (1.2a) and jack-up mode (1.2b). In sailing mode, the vessel sails to the designated offshore wind farm site. Once on location, the Aeolus transitions into jack-up mode using its jacking system to raise itself above the water surface. This transformation provides a stable platform for the installation of foundations and monopiles for the wind turbines. In this section, a brief description of the installation of foundations and monopiles is presented.

(a) In sailing mode **(b)** In jack-up mode

Figure 1.2: Van Oord's installation vessel: the Aeolus, retrieved from Van Oord

A lifting capacity of 1600 tonnes makes the Aeolus suitable for transport and lifting operations of foundations and wind turbines. With four jack-up legs, each measuring 85m, the Aeolus is capable of working in water depths up to 45 metres and able to safely install wind turbines. An OWT can be divided into two parts; the substructure, the monopile (MP) in this case, which is the foundation of the wind turbine and the superstructure, which includes the tower and the Rotor Nacelle Assembly (RNA). Monopiles are the most commonly used support structures for offshore wind turbines in water depths up to 40 metres.

If the vessel is jacked-up, the crane lifts the MP and brings it in a vertical position together with an upending frame that provides support at the point of rotation. Once the MP is upright, the crane hoists it high into the air, positioning it within the gripper mechanism. The gripper prevents excessive lateral motions and guides the MP during the lowering phase. Additionally, it provides support to the MP during the initial stage of driving the pile into the seabed, using a hydraulic hammering tool. Once the MP is in positioned and secured in the seabed, the superstructure can be installed.

(a) Upending the MP using the vessel's crane **(b)** The upending frame supporting the MP

Figure 1.3: The existing method for upending an MP on deck of the Aeolus, retrieved from Van Oord

1.2. Research motivation

With the increasing demand for renewable energy, the offshore wind industry is still growing rapidly. To meet the challenges of the future and make a substantial contribution to the renewable energy sector, con-

tinuous innovation is essential. The industry is engaged in a constant race to develop larger and more efficient wind turbines capable of providing the increasing global demand for renewable energy sources.

Due to the ever-increasing size of the turbines, the monopiles also increase in weight and size, which is a trend expected to continue. These XXL monopiles cannot be installed by the existing, yet relatively new, installation vessels. During the conventional upending process, as described in section 1.1, the weight of XXL monopiles exceed the existing crane capacity of the vessel. To overcome this limitation, a novel approach called the trapped air concept or trapped air method has been devised. This alternative method utilizes the principle of buoyancy to facilitate the upending of monopiles, effectively compensating for the insufficient crane capacity on board of the vessel. By using significant buoyancy, the trapped air method offers a solution to overcome the challenge posed by the excessive size and weight of XXL monopiles during the installation procedure.

Trapped air method

The trapped air method makes use of closed end caps at the bottom and top of the MP to create an air bubble inside, thereby generating an imposed buoyancy force. These water-tight end caps enable the MP to float by its own buoyancy. Once the floating MP is transported and connected to the crane hook of the Aeolus, the lifting operation can start. The main tug boat ensures that the semi floating MP stays in its most favourable heading w.r.t. to the vessel and the environmental conditions acting on the MP (see fig. 1.4a). It is important to note that this method is still undergoing development, the exact execution of the process has not been finalized yet.

Once the bottom of the MP is sufficiently submerged, water inlet valves on the plug are opened to allow water to flow into the structure. The introduction of ballast water increases the stability of the semi-floating MP. By allowing water to enter the closed MP without releasing the air inside, it becomes compressed and pressurized. This internal overpressure enables a water level difference to exist between the inside and outside of the MP (refer to fig. 1.4b), creating buoyancy that compensates for the limited crane capacity on the vessel. The water level difference can be regulated by controlling the water inlet through the bottom plug, while the amount of trapped air can be adjusted by changing the internal air pressure via the top plug.

The water intake is gradually increased until the pressure difference across the bottom plug is equalized. At this point, the bottom cap can be removed, and the MP will retain its floating capacity due to the trapped air. In the existing plan, the recovery of the bottom plug is carried out by the main tug (refer to fig. 1.4c).By carefully lowering the crane hook while controlling the internal water level and, consequently, creating the buoyancy, the MP can be gradually lowered to the seabed. By consistently maintaining a sufficient water level difference, enough buoyancy will be generated to compensate for insufficient crane capacity. This method was selected during an extensive study by A. Vellekoop [26], which identified this concept as the most feasible approach for upending monopiles that exceed the crane capacity.

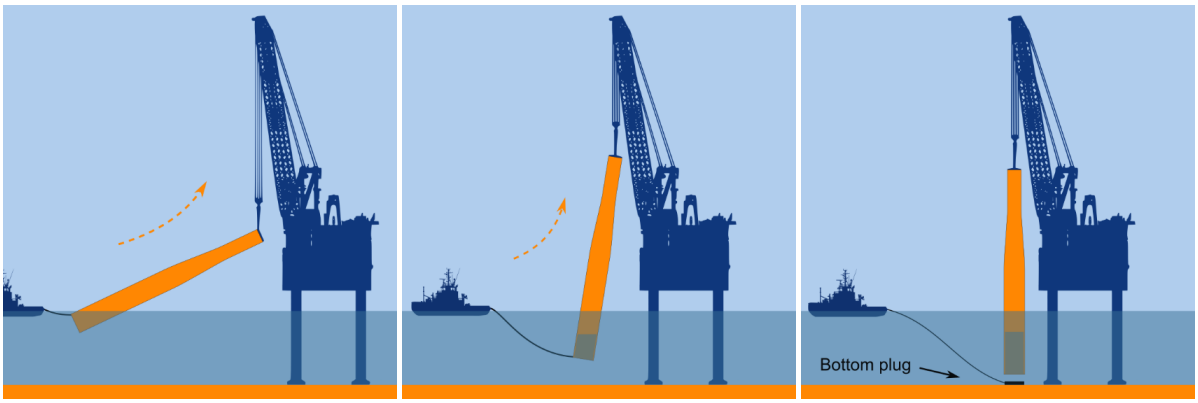

(a) Upending of an MP while a tugboat keeps control of the bottom of the MP

(b) Water inflow through the bottom plug allows for a controlled amount of floatation

(c) Decrease waterlevel difference until bottom plug can be released

Figure 1.4: The trapped air method for upending an MP

1.2.1. Literature review

To summarize section 1.1, the installation of a monopile after transport generally includes the following three steps:

1. Upending the MP from a horizontal position to a vertical position
2. Lowering the MP through the splash zone down to the seabed, guided by a gripper
3. Driving the MP into the seabed using a hydraulic hammer or other pile driving force

Previous research is done regarding the second step of the installation procedure, the lowering of the MP through the wave or splash zone down to the seabed. Dam [7] investigated the cause of unexpected excessive motions during the lowering of the MP guided by a gripper during his thesis research. He found that these motions were governed by wave components with frequencies close to the natural frequency of the system. He also found that the lifting operation (with a gripper) can be simplified to a system with a single degree of freedom (DoF). Even though his research does not include the modelling of extra buoyancy, lessons can be learned from his model tests, conclusions and even further recommendations can be taken into account during this research.

However, the present research focuses on the first step of the installation phase, the upending of an MP. Previous research has been performed, analyzing the installation of floating spar type foundations. For now, two different spar types can be distinguished; the spar-buoy concept for floating wind turbines and a truss spar commonly used for floating oil and gas facilities. Both concepts can be found in figure 1.5 and 1.6 respectively. They both make use of buoyancy and need upending during installation. Research can be of interest because of similarities in geometry between a spar and an MP, although the upending of a jacket structure is also considered.

Figure 1.5: Spar-buoy concept supporting a floating wind turbine

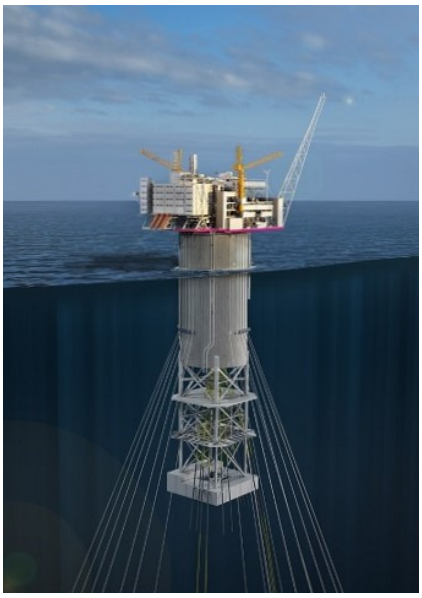

Figure 1.6: A truss spar supporting an oil and gas facility

Different studies have been performed examining motions of spar platforms over the last years, but only a few of them consider the upending phase of the installation.

Prislin et al. [12] presents a numerical method to predict motions and structural loads on a spar platform during upending. The upending of a spar-type foundation is usually achieved by flooding its ballast tanks, which makes the mass properties of the spar time-dependent and increases the complexity of the equations of motion. They eventually simulate this process by coupling the equations of motion of the spar with the hydraulic equations of the ballast tanks. Interesting to see is that in this simulation, the rate of mass change shows an oscillatory behavior of the spar during the first stages of flooding. This is due to partially opened air valves whereby the air does not escape quickly enough to make room for the incoming water. This results in oscillatory spar motions in heave and pitch direction, a phenomenon which can also be expected during the flooding stage of a floating MP.

Liu et al. [20] has conducted an experimental study on the process of towing a spar structure in irregular waves and upending it in calm water conditions. They investigated the pitch angle and bending moment of the spar by slowly flooding the compartments with water during experiments in a wave tank. Both the bending moment and the pitch angle of the truss spar were increasing significantly during the first stage of the process. This is because the ballast water of the first stage of the flooding imposes a large bending moment that initiates the upending. The bending moment of the monopile is not expected to be significant because of the small moment arm and because it is supported by the vessel's crane.

Aliyar et al. [1] investigated the response of a jacket substructure during the upending process, in the presence of waves. Two cases have been analyzed in this experimental study, one free-floating jacket and another suspended from a crane. They concluded that the initial horizontal position for the jacket is the most critical for installation, as the natural periods for heave, roll and pitch motions are in the range of possible wave periods. Furthermore, it is observed that the connection of crane cables reduces the response amplitude in all aforementioned directions by a factor 2-3, due to the restricted motion in heave direction. This observation could result in high load variations once the crane is hooked up and the cables are under tension.

Liu et al., Aliyar et al. and Prislin et al. all performed model tests to verify their numerical model. From the first two studies, it can be understood that heave, roll and pitch motions will peak at their respective natural period, for any floating structure under different wave heading angles. Aliyar et al. found that the natural period in heave direction increases from 9.8 tot 13.4 seconds, which is still in the range of possible wave periods at sea.

Another study that did investigate the use of buoyancy is a feasibility study by Voges et al. [29] concerning a Floater for Upending Piles (FlUP). The key component of this concept is that the unmanned structure uses ballast water pumps and water tanks in order for the MP to upend by itself. In this study, the heave motion of a vertically upended MP was investigated. They state that the vertical floating position is the most critical, which is in contrast to what Aliyar et al. found in their study. This contrast could be explained by different limiting criteria and the difference in buoyancy requirements.

The water intake at the bottom of the MP may be seen as a controlled way of flooding compartments of damaged ships. A few studies have been performed that relate to the flooding process.

Zhang et al. [32] studied the effect of air compression on the flooding process and the stability of a damaged ship. The interesting part is in the transient stage of the flooding with closed compartments. Here, the free surface of the flooded compartment is fluctuating significantly because of sloshing. After this phase, the water level seem to rise smoothly until it reaches equilibrium. Sloshing could have an impact on the motions of the MP and should be considered in this research.

Ruponen et al. [23] presented time-domain flooding simulations of a tank with controlled ventilation levels and conducted full-scale experiments. Both studies considered air as an ideal gas and applied Boyle's law, assuming the air temperature is constant. Ruponen et. al, however, concluded that the assumption of an ideal gas and the application of Boyle's law in their simulation may be not fully valid when considering totally trapped air. In reality, it was found that the compartment was not fully airtight and the internal overpressure slowly decreases over time. This leakage of air influences the internal air pressure and therefore the buoyancy of a semi-floating MP. Maintaining the air pressure by means of air compressors should be considered.

Little research has been performed by Van Oord itself regarding the workability of this concept. It mostly covers the entire process, from launching the MP in port all the way through to the final driving of the pile. The scope of this research will be just the upending phase of this operation.

Nevertheless, D. Scheltens of Van Oord performed a short assessment on the dynamic behavior of an MP exceeding crane capacity to make a rough estimate on the workable limits of this concept, the side- and off-lead angles in this case. These side- and off-lead angles are the rotation angles in the lateral and longitudinal direction respectively and are clarified using a schematic overview in figure 1.7. Scheltens used a quasi-static python model to assess the natural modes of the model to determine a realistic inflow of water during this process. The water content calculated with this quasi-static model is imposed on a transient model. Here, the crane lifts the MP while it fills up with water from the bottom.

This model resulted in the Response Amplitude Operators of the system. A Response Amplitude Operator (RAO) describes the response of an object to wave-frequency excitation. He then found that high side- and off-lead angles do not specifically result in high forces in the crane tip but these angles however, exceed

the geometrical allowable limits, stated in crane manual of the vessel. Based on these geometrical limits he estimated a maximum workable significant wave height for different wave periods. Interesting to see is that a constant tow force has been applied at the bottom of the MP, in line with the waves. Without this force, the MP slowly starts to drift rotationally around the crane wire.

His simulations only cover the upending and filling of the MP. No data has been assessed about the actual displacement of the MP and to what extent the MP would interfere with the vessel or crane boom. Furthermore, water dynamics inside the MP have not been considered and the water inside the MP is assumed to be fixed. The bobbing and stabilization of the floating MP have also not been considered. At last, he mentioned that proper attention is required for the simulation of the vertical stage of upending and he expects that the use of properly designed tuggers can reduce the motions of the MP substantially.

1.2.2. Knowledge gap

The literature mentioned earlier provide some insights into several aspects associated with the proposed concept. However, it does not specifically address the natural frequencies of a double pendulum system that takes into account several important parameters, such as inertia and hydrodynamic effects. Additionally, the studies did not have explored the use of buoyancy or its influence on this system. Therefore, this research aims to bridge this gap by investigating the dynamics of a partially submerged cylinder with two degrees of freedom, taking into account the effects of buoyancy.

1.2.3. Relevance

The findings of this research have the potential to contribute to the understanding of the principles, challenges, and key considerations associated with this concept. By gaining a deeper understanding of these aspects, Van Oord will be able to optimize the use of existing installation vessels and maximize their operational capacity and efficiency.

Secondly, by making use of the trapped air method, Van Oord can potentially reduce the need for additional investments in new equipment or vessels with higher crane capacity. Instead of acquiring new assets, the company can use the trapped air method to handle the installation of larger monopiles that exceed the current crane capacity. This can result in significant cost savings for Van Oord, as it reduces the need for expensive equipment upgrades or replacements.

Moreover, the trapped air method has the potential to contribute to the company's efforts in minimizing its environmental footprint. By utilizing the existing installation vessels more efficiently and avoiding unnecessary equipment upgrades, Van Oord supports the transition to a more sustainable offshore wind industry. By proving the merits of the concept, Van Oord can optimize the use of its existing installation vessels, reduce investment costs, and minimize its environmental footprint.

1.2.4. Problem description

Van Oord is confident in the potential of using the trapped air method to upend monopiles that exceed the crane capacity. However, in order to validate and demonstrate the feasibility of this concept, it is crucial to have the necessary data and model requirements to examine and quantify its behavior. This research aims to address the lack of substantiation that currently exists regarding the feasibility of the trapped air method and its applicability in full-scale scenarios.

At present, the trapped air method is still in the conceptual stage, with the hypothesis that it should be working at full-scale. However, there is limited existing literature that provides a comprehensive model describing the motions and behavior associated with this method, accurately. As a result, many aspects of the trapped air method remain unknown and require further investigation. Exploring this alternative upending technique presents various potential challenges that can be addressed.

- How will the system react to different buoyancy conditions and is it possible to define the limiting conditions?
- Is it possible to define the correlation between the buoyancy requirements and the side-lead angles?
- Will sloshing of the water column have an impact on the motions or can it be assumed to be fixed?
- Does vortex shedding have a significant influence on the motions of the vertical MP or during the upending process?

Because there is little to no data to answer these and other questions, model experiments and numerical computations could provide the required data and observations to try to understand the actual behavior of the MP. It is therefore a challenge to examine the system through analytical analysis, validate its outcome through model experiments and extend the understanding of its behavior through the development of a numerical model, capable of accurately predicting its behavior at full scale.

Workable limits

Two angles are defined when lifting an MP; the off-lead angle and the side-lead angle. The definition of these angles is shown in figure 1.7 and are important angles that define the workable limits of offshore lifting operations. The crane manual of the Aeolus allows for a maximum side-lead angle of X° and a maximum off-lead angle of X°. It is however expected that the side-lead angle and will be governing w.r.t. the workable limits this process.

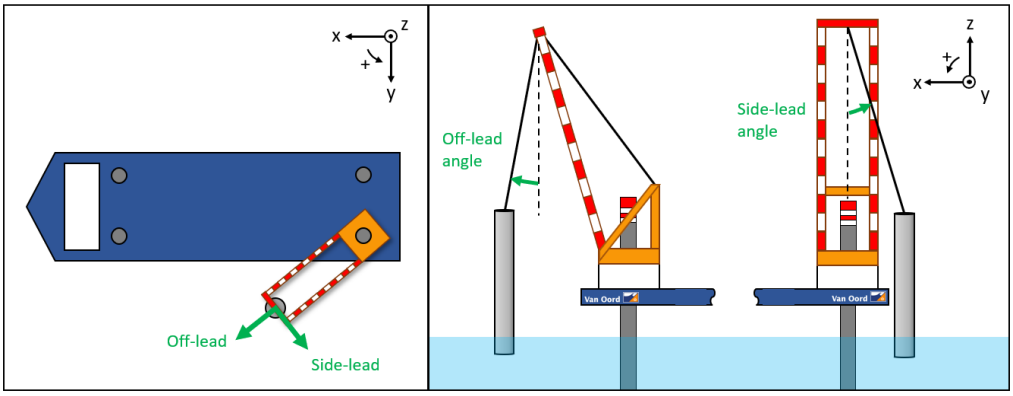

Figure 1.7: Top, side and front view of a sketch of the Aeolus, presenting the side- and off-lead angles

The forces experienced at the cranetip have predefined limits that must not be exceeded. Therefore, when considering the maximum allowable forces, it is crucial to also take into account the safe operating radius of the crane. Table 1.1 provides the maximum allowable Safe Working Load (SWL) for a radius of X m and X m, retrieved from the crane manual. The maximum allowable load in the cranetip reduces significantly with a decreasing radius. It is therefore important to find the forces experienced in the cranetip.

Table 1.1: Maximum allowable loads in the cranetip

Max. Side lead load	-	X	t	X	kN
Max. Vertical load	X m	X	t	X	kN
	X m	X	t	X	kN

A detailed sketch of the crane wire is presented in figure 1.8. The sheaves that support the crane wires allow for a maximum geometrical side-lead angle and a maximum side lead force. If the maximum allowable angle of X° or side lead force of X t is exceeded, the sheaves will fail. An example of a damaged sheave can be found in figure 1.9 and is a result of exceeding those limits. This phenomenon should be avoided at all times.

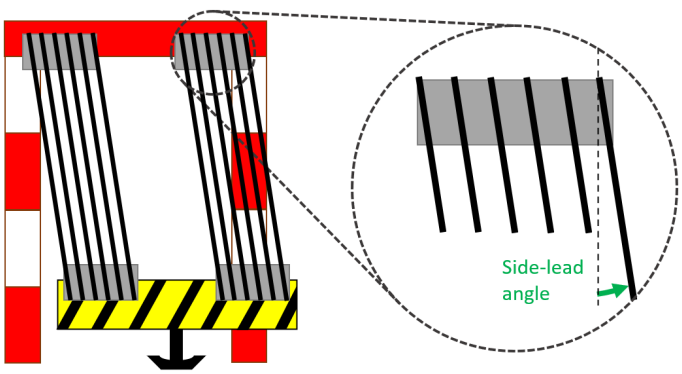

Figure 1.8: Closer look to the side-lead angle of a more detailed sketch of the crane wires

Figure 1.9: A damaged sheave, retrieved from site visit

1.2.5. Objective

The main objective of this research is to create an understanding of the natural frequency response of the MP during its most critical stage in the upending process. By gaining insights into this behavior, it will be possible to identify the specific frequencies of exciting waves that can cause resonance in the MP, resulting in significant motions and resulting forces in the crane tip. These aspects include the angles in three degrees of freedom, as well as the displacements and forces experienced by the MP in both the x-, y- and z-directions.

As D. Scheltens mentioned, proper attention is required for the vertical stage of upending. Therefore, the situation in which an MP is suspended from a crane, will be converted to a couple of systems representing the vertical stage and a simplification of reality. These systems enable to specify the motions of the MP in the frequency domain. By analysing the system gradually, the influence of each component on the response of the system can be examined. The most important influence to be investigated is the buoyancy acting on the system.

The result of these governing equations of motion can then be used to set-up a computational model considering different initial conditions. The primary focus of the model will be to assess the impact of buoyancy on the side-lead angles of the crane wire and the forces experienced at the cranetip during the vertical stage. Model experiments are essential for validating both the analytical and numerical model. To validate the computational models with experiments, it is necessary to translate the numerical model to a model scale. This process involves applying the principle of a 'model the model' translation.

In order to fulfill the main objective, it shall be divided in to the following sub-objectives:

- Create an understanding of physical phenomena that can have significant influence on the motions of the monopile.
- Develop an analytical model to investigate the influence of the buoyancy and different other components of the system by gradually identifying the governing equations that describe this system. This can be done by indicating allowable/tolerable initial and boundary conditions and assumptions that satisfy a simplification of reality.
- Construct an experimental set-up and perform model tests to examine the natural frequencies of a scaled MP for different conditions.
- Develop a numerical model able to predict the movements of a semi-floating MP.
- Validate the numerical model and the analytical approach using the results of the model tests.

The problem assessed in this research can be outlined in to the following research question and additional sub questions:

Research question

What is the behavior of a semi-floating monopile during the most critical stage of upending, using the concept of trapped air?

Sub questions

1. **Physical phenomena** - A study into the potential impact of various physical phenomena on the behavior of the MP.
   (a) Which physical phenomena can be of influence during the most critical stage of upending?
   (b) Which of these phenomena are expected to be the main contributor(s) to excessive motions during the process?

2. **System** - A study into the kinematics of the system.
   (a) How can the system be converted to a simplification of reality?
      i. Which characteristics need to be taken into account?

ii. Which initial/boundary conditions can be applied without deviating too much from the real situation?

(b) Which equations of motion represent the simplified system?

(c) What are the natural frequencies of the system and how do the various components of the system, such as buoyancy and added mass, influence this behavior?

3. **Model tests** - A study into the behavior of a monopile with scaled model tests to create an understanding of its behavior. In the end the results can be usede to validate the computational model.

   (a) Which scaling is preferred and what are the consequences?

   (b) How will the scaled monopile behave during the following decay tests?

      i. Single pendulum

      ii. Double pendulum with initial out of line-mode

      iii. Double pendulum with initial in-line-mode

   (c) Can the natural frequency of the system be determined (during decay tests)?

   (d) Can the limiting factors for the workability be determined and quantified?

   (e) Can the drag and mass coefficients be determined as well as the damping to refine the numerical model?

4. **Numerical model** - A computational model is required to describe the motions of the monopile.

   (a) Which equations of motion represent the complex system?

   (b) Can the system be converted to a numerical model?

      i. Starting with the double pendulum without viscous damping. Extend by implementing damping and refine with knowledge gained during model tests.

   (c) Can numerical simulations accurately reproduce the behavior of the semi-floating model scaled monopile observed in the experiments?

   (d) Can numerical simulations provide accurate predictions for its behavior in a full-scale scenario?

1.2.6. Hypothesis

Before any research is done, it is important to formulate the expectations. This is done for every phase of this research.

1. **Physical phenomena**

   When considering a floating MP suspended from a crane, it is expected that the MP will move in different directions such as the surge, heave and pitch direction. Forces that will probably cause these motions are: wind, waves and current. All of these forces will generate motions of the MP, although it is expected that waves will be the main contributor to these motions.

   In certain current conditions, vortex-induced motions can cause different lift forces on each side of the MP, leading to motions transverse to the current. This can result in a swinging motion causing the MP to move in sway or surge direction. Vortex-induced shedding can become dangerous when it takes place at the natural frequency of the system. Furthermore it is expected that the static current force acting on the MP results in a static offset in surge direction.

   Sloshing is a common phenomenon observed in hydrodynamic environments, characterized by its sloshing frequency. In the case of an MP, it is expected that sloshing will occur. However, it is unlikely that it will be governing the motion of the MP.

The wind forces are expected to be negligible compared to the loads that waves and current will exert on the MP. It is, however, important to investigate the contribution of all environmental forces before one of these can be neglected.

2. **System**

   The real situation should be converted to a simplification, which can be created by using existing methods for defining kinematics. An important step is to define initial and boundary conditions which create a relatively simple system that can be examined in the frequency domain. It is expected that the system can be converted to a simplified 2D pendulum model with presumably two degrees of freedom. That means that the system could be described using two independent variables, indicated by two angles of rotation. The equations of motion can then be derived and the natural frequencies of the system can be determined. Furthermore, it is expected that the natural frequency of the system decreases with the increasing internal water volume or decreasing buoyant forces.

   If wave components close to the natural frequency cause large heave motions of the MP, the buoyant force acts like a restoring force and could cause a bobbing or stabbing effect of the MP. This phenomenon could lead to highly alternating cable loads and uncontrolled motions of the MP. Rough sea-states could hypothetically lead to the aforementioned bobbing effect. Because of this, it is expected that an alternating lifting capacity of the crane could be observed during model tests.

   Because a jack-up vessel is hardly subjected to waves or currents compared to a floating heavy lift vessel, it is expected that the crane tip motion will not have a large impact on the response of the system. It should be noted that specific environmental conditions could trigger the vessel's motion when matching its natural frequency.

3. **Model tests**

   Model tests allow for the most realistic simulations of real physical phenomena and provide useful data for understanding the principles behind these phenomena. The use of scaling methods allows for experiments to be carried out on a series of relatively inexpensive physical models. The prototype requires a form of similarity in geometry, kinematics and dynamics. Therefore, scaling is of great importance when performing model experiments. Since waves are expected to be the main contributor to the motions of the MP, Froude scaling will potentially be the most appropriate. This scaling method makes use of the ratio between inertia to gravitational forces. Gravity plays a dominant role in the behavior of the free surface and is also important when considering problems involving buoyancy. Because the Reynolds number is not scaled properly, the viscous forces will be distorted. This phenomenon should be further investigated and other corresponding consequences should be accounted for.

   Furthermore, it is anticipated that the model experiments can be used to find the appropriate coefficients which can be implemented into the numerical model. The model tests should validate the numerical model and modifications can be applied to refine the numerical model, such as the drag and damping coefficients.

4. **Numerical model**

   Based on the kinematics of the system and the equations of motion of the system, a numerical model should be created. By implementing different boundary conditions and starting with a more simple system, a first version of this model can be made. Simplifications and assumptions should be implemented to minimize the complexity of the model. The numerical model should first be validated with data of the model-scale experiments. It is expected that by conducting numerical simulations, a better understanding of the behavior should be achieved and predictions can be made on the behavior of a full-scale MP.

   Since it is expected that little to no information is available in the literature on the drag and mass coefficients, they first have to be assumed according to the offshore classification standards.

To create an insight in this method of upending and test some of the statements of the hypothesis, exploratory tests have been performed and are discussed in Chapter 4. First, the influence of various physical phenomena are discussed in Chapter 2.

2

Physical phenomena

This chapter presents various physical phenomena and their potential influence on the behavior of the MP. In addition to these phenomena, it is important to consider at least three key environmental conditions:

- Waves
- Current
- Wind

The physical meaning of these three environmental conditions and their relevance to this research are discussed in the following sections. First it is important to define the direction of motion of a ship or any other body in a 3D-system. The motion of a ship can be described in terms of six degrees of freedom: surge, sway, heave, roll, pitch and yaw. The first three DoF's are defined as translations in the x-, y- and z-directions and the latter three are defined as rotations about the x-, y- and z-axes. The definitions are summarized below and visualized in figure 2.1.

1. *Surge* is the for- and backward movement of the ship along its longitudinal x-axis.
2. *Sway* is the lateral movement of the ship along its transverse y-axis.
3. *Heave* is the vertical movement of the ship along its vertical z-axis.

4. *Roll* is the rotation of the ship around its longitudinal x-axis.
5. *Pitch* is the rotation of the ship around its transverse y-axis.
6. *Yaw* is the rotation of the ship around its vertical z-axis.

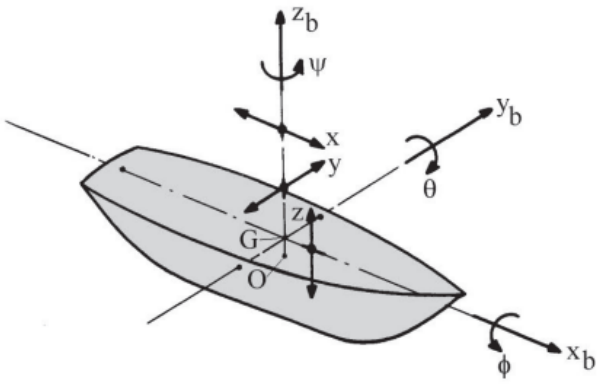

Figure 2.1: Definition of ship motions in six degrees of freedom, retrieved from [18]

2.1. Floating body

Buoyancy is the upward force exerted by a fluid on an object immersed in it. It is determined by the volume of the displaced fluid and the density of the displaced fluid. Understanding the principles of buoyancy is crucial in analyzing the behavior of floating bodies, such as the monopile, as it directly influences their stability and floating characteristics. First, the hydrostatics of a floating body and its buoyancy will be discussed.

2.1.1. Hydrostatic stability

According to the law of Archimedes, a floating body remains buoyant by displacing water equal to its weight. The center of buoyancy, denoted as B in figure 2.2, corresponds to the center of gravity of the displaced water. When a small heel angle θ is applied to the structure, the center of buoyancy (B) shifts, resulting in a restoring moment around the center of gravity (G). These restoring forces are only determined by the structural displacements and are not influenced by time. The metacenter (M) represents the point of intersection between the vertical line passing through the center of buoyancy and the initial vertical line. The following statements are true considering the hydrostatic stability of a floating object:

1. If M lies above the center of gravity, a restoring moment is generated and the body will tend to return to its equilibrium position. GM is regarded as positive and the system is considered stable.
2. If M lies below the center of gravity, an overturning moment is generated and the body will tend to tilt. GM is regarded as negative and the system is considered unstable.
3. If M coincides with the center of gravity, the body is neutral equilibrium.

The first scenario depicted in figure 2.2 presents a stable system due to the presence of a restoring moment.

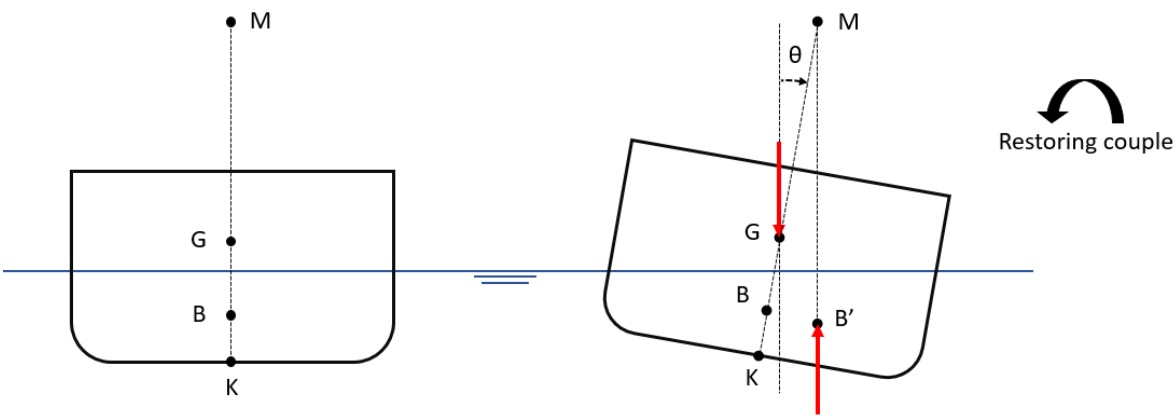

Figure 2.2: Schematic view of a floating body with center of gravity (G), center of buoyancy (B), keel (K) and metacenter (M) in neutral and slightly heeled position. Originally after [30]

In the second scenario illustrated in figure 2.3, a vertical cylinder is depicted. In this configuration, the metacenter is located below the center of gravity, resulting in the generation of an overturning moment and causing instability. This situation occurs when the metacenter lies below the center of gravity of the cylinder. When the cylinder experiences a disturbance or tilting, the buoyancy force acting through the center of buoyancy creates an overturning moment around the center of gravity. Since the metacenter is below the center of gravity, this moment tends to further tilt the cylinder in the same direction as the initial disturbance, leading to instability.

Important to note that a MP suspended from a crane, its movements are constrained by the crane cable. The rotation point is then in the cranetip and thus above the center of gravity. By having the rotation point above the center of gravity, the MP's stability is improved. The crane cable acts as a stabilizing force, limiting excessive tilting of the MP and prevents the system from becoming unstable. Only if the buoyant force is greater than the weight of the object, there is a net upward force exerted on the object, leading to instability.

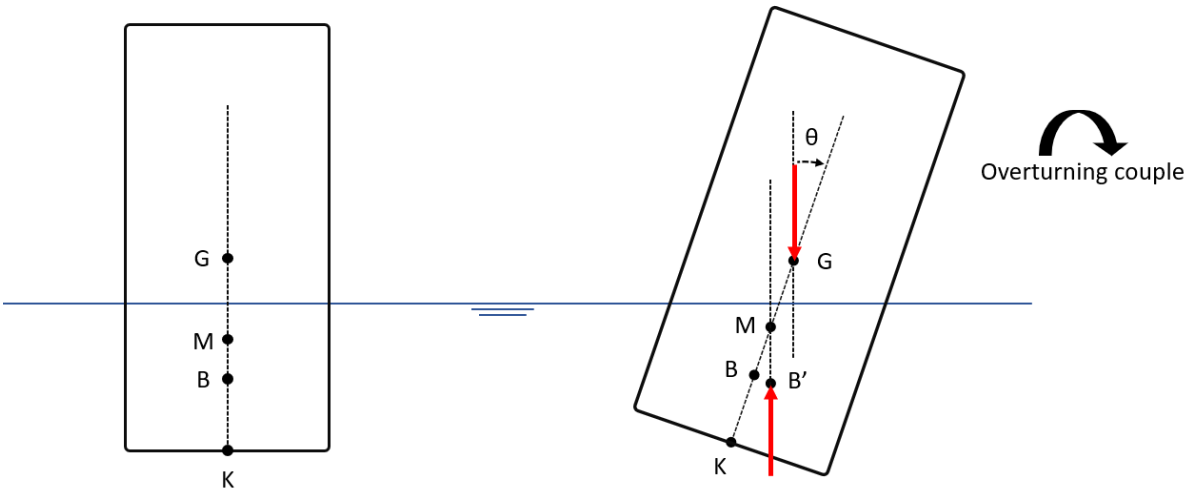

Figure 2.3: Schematic view of a floating cylinder with center of gravity (G), center of buoyancy (B), keel (K) and metacenter (M) in neutral and slightly heeled position.

2.2. Waves

Waves can be generated in many different ways but most of the waves originate from the interaction between the wind and the sea surface. Two basic types of wind generated waves can be distinguished: sea and swell waves. Wind sea waves are generated by local wind while swells are waves that have travelled a long distance from where they were generated. Swells are no longer dependent upon the wind and can propagate for hundreds of kilometers. Some basic definitions for a harmonic wave are introduced.

A general harmonic wave can be described by its main parameters. These general characteristics of waves can be found below and are clarified in figure 2.4.

Wave amplitude	ζ_a or a	The distance between MSL and the wave crest or trough (if the wave is described as a sine wave)	[m]
Wave height	H	The vertical distance from trough to crest $H = 2\zeta_a$	[m]
Wave length	λ_{wave}	The horizontal distance between two successive wave crests	[m]
Wave period	T	The time interval between successive wave crests passing a particular fixed point along the time axis	[s]
Wave frequency	f	The inverse of the wave period $f = \frac{1}{T}$	[Hz]
Water depth	h	The (positive) vertical distance between the seabed and the MSL	[m]

The wave crest and trough are respectively the highest and lowest point of the wave w.r.t. the mean sea level (MSL). The MSL is represented as the x-y plane and as the time-axis in figure 2.4 a and b respectively.

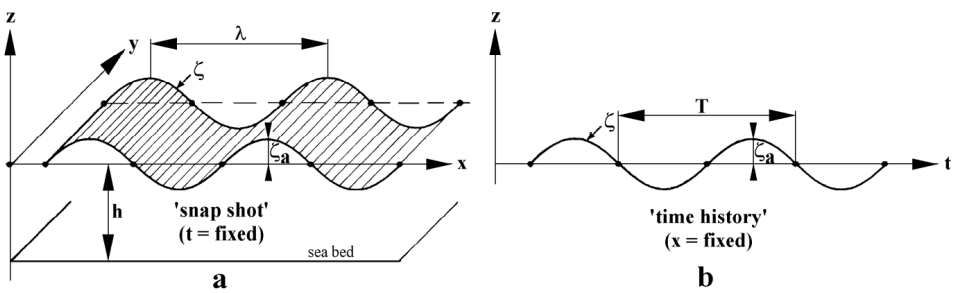

Figure 2.4: Harmonic wave definitions, retrieved from [18]

The offshore workability is mainly determined by the sea-state at the place of operation. This sea-state

consists of two important parameters, the significant wave height (H_s or H_{m0}) and the peak period (T_p). The significant wave height is defined as the mean of the highest one-third of the waves in the record.

$$H_s = \frac{1}{N/3} \sum_{j=1}^{N/3} H_j \tag{2.1}$$

where j resembles the ranking of the waves based on their wave height. Waves are generally described by their characteristic wave height or significant wave height H_s and their characteristic wave period or significant wave period. According to Holthuijssen [11], the significant wave period for swell waves is practically equal the peak period (T_p) of the wave spectrum (see eq. 2.2). This peak period can be seen as the period of the most energetic ocean waves in the spectrum. This parameter is important because the higher the energy in the waves, the larger the wave loads acting on the structure. The peak period can be described as the reciprocal of the frequency corresponding to the largest (peak) value in the wave energy spectrum:

$$T_P = \frac{1}{f_p} \tag{2.2}$$

Dam [7] found that the MP experienced its largest inclinations with a period ranging from 6 to 8 seconds. This corresponds to wave frequencies ranging from 0.125 to 0.167 Hz and are considered typical frequencies observed offshore.

2.3. Current

Currents can have a significant impact on the partly submerged MP but also on the installation vessel itself. Because the Aeolus is in a jacked position when installing these MPs, it is assumed the current has no impact on the vessel. The vessel is considered fixed and the impact of the current on the MP will be governing. The MP is typically modelled as a circular cylinder and is subjected to the flow of the current around the cylinder. The most important fluid-structure interaction is defined by the flow regime. A flow regime refers to the pattern of fluid flow within a system, characterized by specific flow characteristics, such as flow velocity. These characteristics can be influenced by factors such as the geometry of the system, the fluid properties and the boundary conditions. Flow regimes are often classified based on the dimensionless Reynolds number, which is a dimensionless number used in fluid mechanics to characterize the relative importance of fluid inertia w.r.t. the viscous forces. Mathematically, the Reynolds number (Re) is defined as follows:

$$Re = \frac{u_m \cdot D}{\nu_f} \qquad [\,-\,] \tag{2.3}$$

where u_m is the maximum horizontal particle velocity of the current, D the diameter of the cylinder and ν_f the kinematic viscosity of the fluid. For Reynolds numbers close to zero, the flow around a circular cylinder is laminar and steady, there is no separation of the flow. The drag coefficient decreases somewhat linearly as a function of the increasing Reynolds number. The laminar flow is maintained up to $\mathrm{Re}_{\mathrm{crit}} = 4 \cdot 10^5$ and is called the critical Reynolds number. For subcritical Reynolds numbers below this critical value, the flow can be considered laminar. As the Reynolds number increases, the supercritical range is reached and the flow is then strictly turbulent. This behavior holds for Reynolds numbers greater than $3.5 \cdot 10^6$, where the drag coefficient approaches a constant value. An overview of the different flow regimes is shown in figure 2.5.

Reynolds number regime	Flow regime	Flow form	Flow characteristic	Drag coefficient c_D
$\mathrm{Re} \to 0$	Creeping flow		Steady, no wake	see Fig. 1.12
$3-4 < \mathrm{Re} < 30-40$	Vortex pairs in wake		Steady, symmetric separation	$1.59 < c_D < 4.52$ (Re = 30) (Re = 40)
$\substack{30\\40} < \mathrm{Re} < \substack{80\\90}$	Onset of Karman vortex street		Laminar, unstable wake	$1.17 < c_D < 1.59$ (Re = 100) (Re = 30)
$\substack{80\\90} < \mathrm{Re} < \substack{150\\300}$	Pure Karman vortex street		Karman vortex street	
$\substack{150\\300} < \mathrm{Re} < \substack{10^5\\1.3\cdot 10^5}$	Subcritical regime		Laminar, with vortex street instabilities	$c_D \approx 1.2$
$\substack{10^5\\1.3\cdot 10^5} < \mathrm{Re} < 3.5\cdot 10^6$	Critical regime		Laminar separation Turbulent reattachment Turbulent separation Turbulent wake	$0.2 < c_D < 1.2$
$3.5\cdot 10^6 < \mathrm{Re}$	Supercritical regime (transcritical)		Turbulent separation	$c_D \approx 0.6$

Figure 2.5: Flow regimes at a circular cylinder for incompressible flow, retrieved from [10]

Drag and inertia coefficients are terms used in fluid dynamics to describe the resistance encountered by an object moving through a fluid. The drag coefficient (C_D) measures the efficiency of drag forces generated by the object, while the inertia coefficient (C_m) quantifies the resistance caused by the fluid's inertia.
The empirical values for the drag and inertia coefficient are depending on the flow regime around the cylinder. This flow regime is different for an oscillatory flow than for a steady flow. Extensive research has already been done to obtain the values of these coefficients C_D and C_m. One of the pioneering works was done by Keulegan and Carpenter [19]. They determined values for C_D and C_m for various cylinders in an oscillating flow. On top of that, they discovered that their data could be plotted as a function of the dimensionless Keulegan Carpenter number KC:

$$KC = \frac{u_m \cdot T}{D} \qquad [\,-\,] \qquad (2.4)$$

where u_m is the maximum horizontal particle velocity of the current, T is the period of the oscillatory flow and D is the diameter of the cylinder. The Keuligan Carpenter number basically determines the relative contribution of the drag and inertia forces and can be a very important parameter to investigate the importance of C_D and C_m. For this to be the case, the KC-value can be used and according to Journee et. al [18], the following statements do hold:

$KC < 3$	For low KC-values, the inertia force is dominant. Potential flow is still applicable and the drag can simply be neglected.
$3 < KC < 15$	In this range, the drag on the system is often linearized.
$15 < KC < 45$	Here, both the inertia and drag terms need to be considered.
$KC > 45$	For KC-values higher than 45, the drag force becomes dominant. Because the vortex shedding frequency becomes high compared to the wave frequency, the flow tends to behave more like a constant current. The inertia term can be neglected.

Later in 1976, Sarpkaya et al. [24] found, trough extensive experimental research, that the drag and inertia coefficients are not only functions of the KC-number but are also dependent on the Reynolds number. Figure 2.6 shows the results of his experiments and depicts the values for the drag and inertia coefficient for a certain KC-value, accounting for the Reynolds number using the frequency parameter β.

$$\beta = \frac{Re}{KC} = \frac{D^2}{\nu_f T} \qquad [\,-\,] \qquad (2.5)$$

It should be noted that these coefficients are also dependent on the relative roughness k/D of the cylinder. They differ significantly from those corresponding to the smooth cylinder. However, a smooth cylinder is considered in this research.

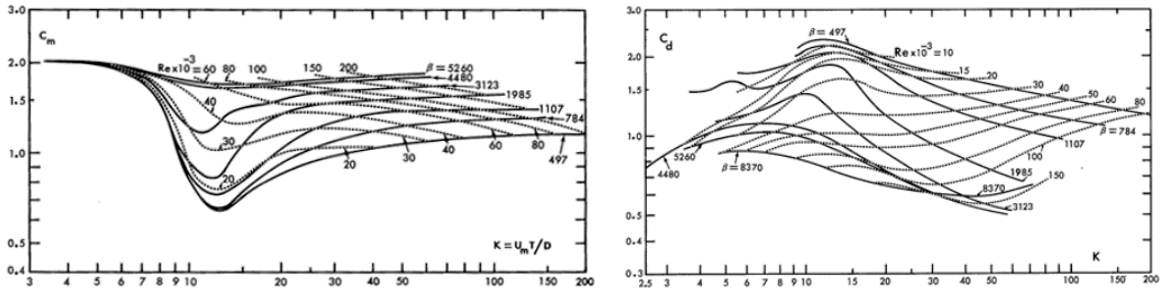

(a) The inertia coefficient vs KC

(b) The drag coefficient vs KC

Figure 2.6: Inertia and drag coefficient vs Keuligan Carpenter number for constant values of the frequency parameter and the Reynolds number. Originally after Sarpkaya (1976) [24].

As said, the drag coefficient C_D is influenced by the Reynolds number and to determine the Reynolds number, the kinematic viscosity (ν_f) of the fluid is required. The kinematic viscosity represents the fluid's resistance to flow and is defined as the ratio of dynamic viscosity (μ) to fluid density (ρ). The kinematic viscosity values provided by DNV [27] for various fluids are presented in table 2.1. These values indicate the fluid's resistance to flow and can be used in calculations to determine the Reynolds number for a specific fluid and object geometry.

Table 2.1: Kinematic viscosity for different fluids and temperatures, retrieved from DNV-RP-C205 [27]

	Density, ρ, [kg m^{-3}]			Kinematic viscosity, ν_f, [m^2 s^{-1}]		
Temperature [°C]	Fresh water	Sea water	Dry air	Fresh water	Sea water	Dry air
0	999.8	1028.0	1.293	1.79×10^{-6}	1.83×10^{-6}	1.32×10^{-5}
5	1000.0	1027.6	1.270	1.52	1.56	1.36
10	999.7	1026.9	1.247	1.31	1.35	1.41
15	999.1	1025.9	1.226	1.14	1.19	1.45
20	998.2	1024.7	1.205	1.00	1.05	1.50
25	997.0	1023.2	1.184	0.89	0.94	1.55
30	995.6	1021.7	1.165	0.80	0.85	1.60

2.3.1. Current loading

The forces exerted on the structure by a current can be divided into two parts; A viscous part and a potential part. Viscous forces arise due to the fluid's viscosity and the relative motion between the fluid and the structure's surface. These forces are proportional to the velocity of the fluid and can result in drag forces on the structure. The viscous forces are primarily responsible for dissipating energy from the fluid flow. Potential forces arise from the pressure distribution induced by the fluid flow around the structure. These forces are related to the potential energy of the fluid and are typically associated with the hydrodynamic lift and added mass effects. Potential forces can cause the structure to experience lift, or rotational moments depending on the flow conditions and the geometry of the structure.

The force experienced by the structure depends on the fluid density, the flow velocity and the frontal area of the structure.

$$F_D = \frac{1}{2}\rho C_D A_p u^2 \qquad (2.6)$$

where ρ is the fluid density, A_p is the projected area of the cylinder normal to the flow with flow velocity u and C_D is known as the dimensionless drag coefficient. This coefficient is dependent on the Reynolds number and can be obtained through literature or by experimental model tests.

2.3.2. Vortex-induced motions

Vortex-induced motions, also known as VIM, refer to the phenomenon where the interaction between a fluid flow and a structure, such as an MP, leads to the generation of vortices that induce unwanted motion or vibrations. These vortices create alternating forces on the structure, resulting in oscillatory motions or vibrations perpendicular to the flow velocity. The frequency and magnitude of VIM depend on factors such as the flow velocity, the shape and geometry of the structure and the properties of the fluid.

In order to identify vortex shedding and its potential interference with the natural frequency of the system, the vortex shedding frequency can be determined. In steady flow conditions, for KC-values larger than 40, the shedding frequency can be determined with equation 2.7 [28].

$$f_s = St\frac{u}{D} \qquad \text{[Hz]} \qquad (2.7)$$

where St is the Strouhal number, u the velocity of fluid normal to the structure's axis and D is the diameter of the structure. For a smooth cylinder, the Strouhal number is a function of the Reynolds number, as presented in figure 2.7.

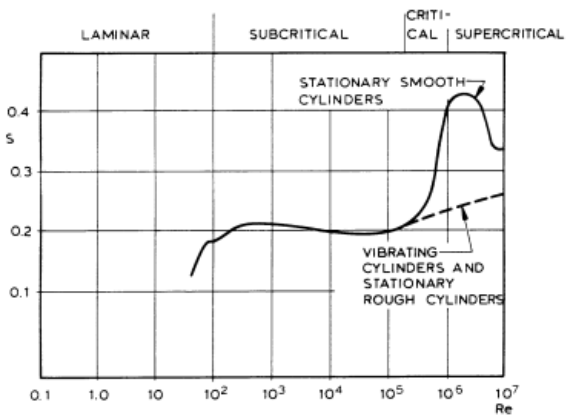

Figure 2.7: Strouhal number for a smooth circular cylinder as a function of the Reynolds number, retrieved from [28]

2.4. Sloshing

Sloshing in cylinders refers to the dynamic fluid motion that occurs when a partially filled cylindrical container is subjected to external forces or motions. It is a phenomenon commonly encountered in systems with an oscillating cylinder. As the cylinder moves or experiences external forces, the fluid inside undergoes complex oscillatory motion, resulting in the sloshing phenomenon.

Sloshing in cylinders can have significant implications for stability and can greatly influence the dynamic behavior of the system. To study the dynamics of sloshing, various analytical, numerical and experimental methods are established. These methods include principles of fluid mechanics, Computational Fluid Dynamics (CFD) simulations and physical model testing. Faltinsen and Timokha [8] conducted experimental tests to explore this phenomenon and found that the natural frequencies and corresponding modes of liquid motion are significantly influenced by both the geometrical characteristics of the tank and the ratio of liquid depth to tank length. Equation 2.8 [8] presents the formula for the highest natural period as a function of radius R_0 of an upright cylindrical tank.

$$T \approx T_{1,1} = \frac{2\pi}{\sqrt{g\, i_{1,1} \tanh\left(i_{1,1} h/R_0\right)/R_0}} \qquad (2.8)$$

Figure 2.8 presents the change of the first natural period as a function of the radius and internal water level h of the cylinder. According to Faltinsen and Timokha [8], there is a minimum value of $T_{1,1}$ for a given R_0, which corresponds to the scenario where the internal water level of the cylinder is infinite. This can be seen in figure 2.8, where values of $h/R_0 > 1.5$ makes the difference with the infinite internal water column less than 1%. Ibrahim [13] states that a constant period is reached when the ratio $h/R_0 > 2$

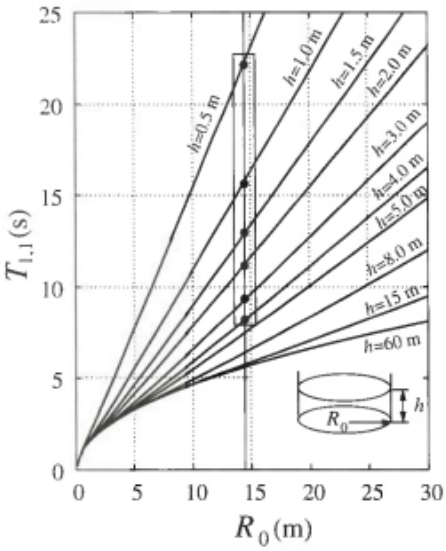

Figure 2.8: The highest natural period $T_{1,1}$ as a function of radius R0 for an upright circular cylindrical tank. The framed values of $T_{1,1}$ are relevant for the ballast tanks of a column-stabilized offshore platform (from [8], p. 135)

Gerritsen [9] conducted his thesis research with the objective of predicting realistic motions and loads induced by waves for a large diameter, thin-walled, open-ended cylinder in water. This was achieved through a linear radiation-diffraction analysis. Experimental tests were conducted to validate these models, with the focus on capturing the internal water motions. With equation 2.8 and with the use of the dispersion relation he found the following relation between the wave frequency ω and wave number k:

$$\omega_{mn} = \sqrt{g\, k_{mn} \tanh(k_{mn} h)} \qquad [\text{rad s}^{-1}] \qquad (2.9)$$

The wave number k_{mn} for a circular tank of radius R is defined as:

$$k_{mn} = \frac{j'_{mn}}{R}, \qquad n = 1, 2, ..., \qquad m = 0, 1, 2, ... \qquad (2.10)$$

where j'_{mn} is the nth zero of the derivative of Bessel function of order J'_m, as stated in table 2.2. Here, the first view roots are of most interest where the symmetric sloshing modes are denoted by $m = 0$ and the asymmetric sloshing modes by $m = 1$. The asymmetric sloshing mode, denoted as $\omega_{1,n}$, refers to the back-and-forth movement of water along the longitudinal direction of the free surface. It is highly probable to observe the occurrence of asymmetric sloshing during model experiments.

Table 2.2: The first few roots $j'_{m,n}$ of the derivative of the Bessel function $J'_m(x)$ (from [9], orignally after Bauer [2]))

n	$J'_0(x)$	$J'_1(x)$	$J'_2(x)$
1	3.8317	1.8412	3.0542
2	7.0156	5.3314	6.7061
3	10.1735	8.5363	9.9695

By considering the MP with a diameter of D = 9.5m as reference, the natural frequencies for the first asymmetric sloshing mode (ω_{11}) can be approximated and are presented in table 2.3. The obtained values for the natural frequencies confirm the lower limit associated with an infinite internal water level h or h_{int}.

Table 2.3: The natural frequencies for the 1st asymmetric sloshing mode ω_{11} [rad s^{-1}] for a cylinder with D = 9.5m

D_{mp} [m]	h_{int} [m]	ω_{11} [rad s^{-1}]	T_{11} [s]	f_{11} [s^{-1}]
9.5	1	1.185	5.302	0.188
	2	1.572	3.997	0.250
	5	1.910	3.290	0.304
	10	1.949	3.224	0.310
	20	1.950	3.222	0.310

The second asymmetric sloshing can also be predicted by using the value of $J'_{12}(x)$.

Table 2.4: The natural frequencies for the 2nd asymmetric sloshing mode ω_{12} [rad s^{-1}] for a cylinder with D = 9.5m

D_{mp} [m]	h_{int} [m]	ω_{12} [rad s^{-1}]	T_{12} [s]	f_{12} [s^{-1}]
9.5	1	2.983	2.106	0.475
	2	3.281	1.915	0.522
	5	3.318	1.894	0.528
	10	3.318	1.894	0.528
	20	3.318	1.894	0.528

2.5. Wind

Another important environmental factor influencing the workability offshore is the wind. Wind is not only generating the incoming waves, but can also have a direct influence on the structure or on the offshore operation. High winds can make it difficult for ships to maintain stability and can also make it dangerous for workers to move around on deck. Additionally, high winds can cause problems with the use of cranes and other heavy equipment, making it difficult to move materials and equipment around the site. Overall, wind conditions can greatly impact the safety and efficiency of offshore operations and must be carefully considered and monitored before and during operation.

Considering that the upending procedure is taking place partly submerged in the water, it is expected that the wave and current loads are significantly larger than the wind loads. Wind is therefore not expected to be the main contributor to high loads or excessive motions of the MP.

3

Analytical model

This chapter presents a detailed evaluation of several simplified systems that aim to capture the dynamic behavior of the MP. These simplified systems allow for the determination of the natural frequencies and provide insights into the dynamic behavior of the system. Figure 3.1 illustrates a schematic view of the vessel, serving as a visual representation of the system discussed in this chapter.

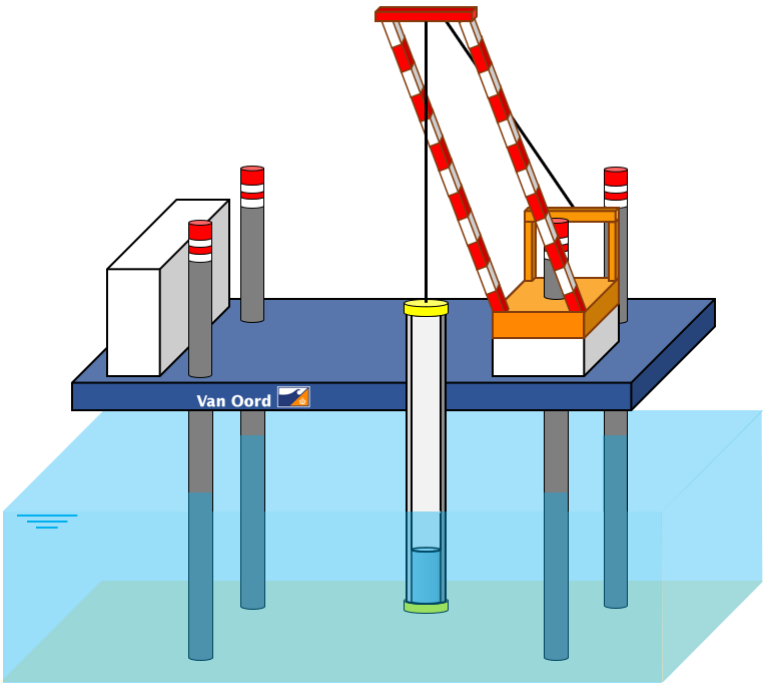

Figure 3.1: Sketch of the MP suspended from a crane of the Aeolus

3.1. Natural frequency

Understanding the natural frequency characteristics of a system is crucial as it offers valuable insights into the system's response to different inputs and disturbances. The natural frequency represents the frequency at which the system will naturally vibrate or oscillate when subjected to a disturbance. It is primarily influenced by the system's physical properties, such as its mass, stiffness and damping. The equation for the natural frequency is stated in equation 3.1.

$$\omega_n = \sqrt{\frac{K}{M}}, \qquad \text{or} \qquad f_n = \frac{1}{2\pi}\sqrt{\frac{K}{M}} \qquad [\text{rad s}^{-1} \ / \ \text{s}^{-1}] \quad (3.1)$$

The natural frequencies of a system are closely associated with its eigenmodes, which describe the pattern of vibration that occurs when the system is excited at a particular frequency. Eigenmodes play a crucial role in understanding the system's response, particularly when it approaches resonance near its natural frequencies. To determine the natural frequencies analytically, the system is analyzed without considering damping and external excitation forces. By examining the system's behavior under these simplified conditions, the natural frequencies and corresponding eigenmodes can be identified, creating a better understanding of its dynamic characteristics.

To prevent resonance and ensure the safety of offshore operations, it is essential to analyze the natural frequencies of the system. Resonance can occur when the natural frequency of the monopile matches the frequency of external excitation forces, resulting in excessive vibrations and potential damage. This chapter focuses on the analytical solution for determining the natural frequencies.

3.2. System simplification

For this analysis, focus will be given to the following four systems. The initial findings and results of these systems will be presented in the next sections.

1. Single Pendulum - Vertical *(see App. A)*
2. Single Pendulum - Inline *(see App. A)*
3. Double Pendulum *(see App. A)*
4. Double Pendulum including Inertia

The monopile (MP) and crane wire shown in figure 3.1 can be simplified into a simple pendulum model as depicted in figure 3.2. The system can be further simplified in the second stage by representing it with point masses. Each component of the system, including their respective lengths, is considered in the third stage. However, adding more components increases the complexity of the system. It is therefore convenient to analyze the influence of every component individually, especially for the buoyancy. In this way, the influence and importance of each component and their contribution to the dynamics of the system can be examined. To accomplish this, the fourth system only consists of two masses and the buoyancy force. The buoyancy force is always considered as this is the component that should prove the concept of trapped air. The mass of the MP itself is the most important mass to take into account and is from now on referred to as m_2. The other mass is the mass of the water column inside the MP (m_{int}). The mass of the internal water column is considered important because it directly influences resulting upward buoyancy force.

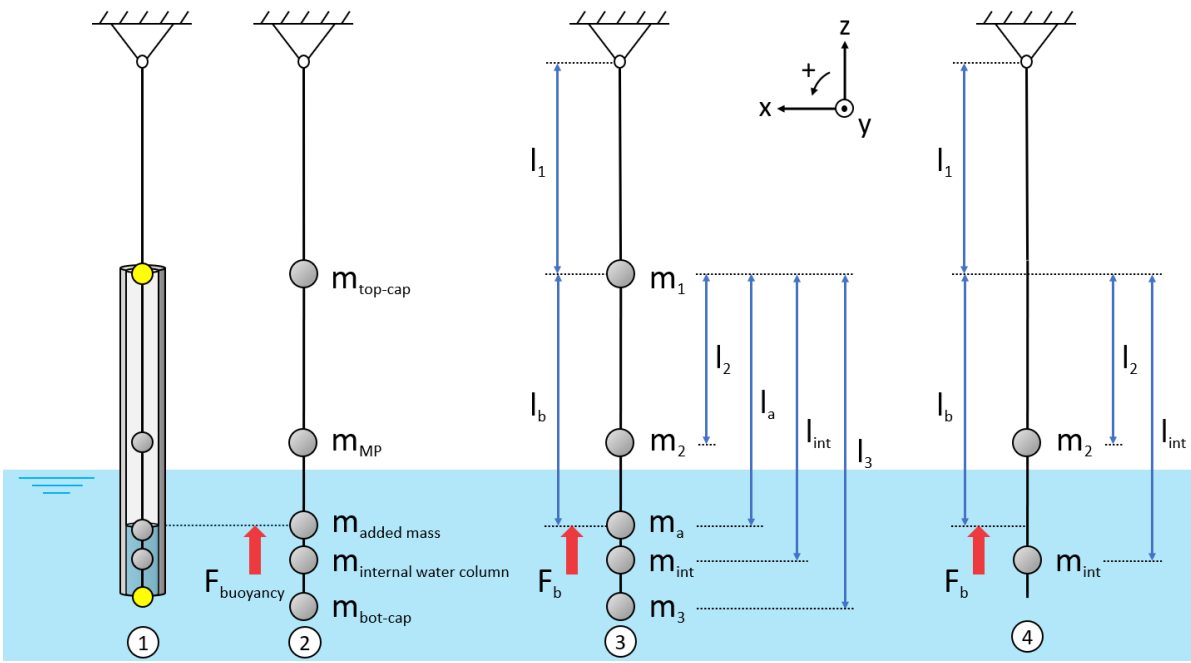

Figure 3.2: 1: The system converted to a simplification 2: The system represented as point masses 3: The system including all components 4: Only two masses and buoyancy force are considered

As said, these four systems are investigated gradually to examine the influence of different components to the behavior of the system. This is done by adding components to the system and creates three different cases:

1. m_2 and m_{int}
2. m_1, m_2, m_3 and m_{int}
3. m_1, m_2, m_3, m_{int} and m_a

The submerged length of the MP is defined as h_{sub} and the internal level of the water column is defined as h_{int}, both depicted in figure 3.3. The buoyant force is determined by multiplying the submerged volume of the MP and the mass of the displaced water. The length l_a represents the point of application (p.o.a.) of the added mass as well as the buoyancy force, which is clarified in the third stage of figure 3.2.

These systems are investigated using four different internal water levels to assess the impact of buoyancy on the system. The following internal water levels are defined as input values for the coming sections.

- $h_{\text{int}} = 0$ m
- $h_{\text{int}} = 10$ m
- $h_{\text{int}} = 20$ m
- $h_{\text{int}} = 30$ m

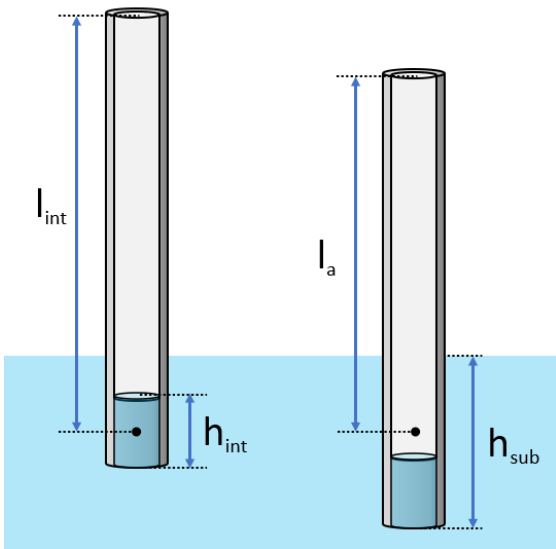

Figure 3.3: The input parameters h_{sub}, h_{int}, l_a and l_{int}

When the internal waterlevel is set to 0, maximum buoyancy is generated. When h_{int} is equal to h_{sub}, there is no water level difference and thus no imposed buoyant force, except for buoyancy created by the submergence of the MP.

Parameters

In order to perform the first calculations for the simplified systems, the parameters stated in table 3.1 have to be determined. To calculate the mass of the internal water column, the inner diameter of the MP is needed and is defined as D_i:

$$D_i = D_{\text{mp}} - 2 \cdot t_{\text{mp}} \qquad [\text{m}] \quad (3.2)$$

Where D_{mp} and t_{mp} are the outer diameter and thickness of the MP respectively. To calculate the buoyant force F_b acting on the system, the displaced volume of the submerged part of the MP (V_{ext}) needs to be determined. To calculate the mass of the internal water column, the internal volume (V_{int}) is needed:

$$V_{\text{int}} = \frac{\pi}{4} D_i^2 h_{\text{int}} \qquad [\text{m}^3] \quad (3.3)$$

$$V_{\text{ext}} = \frac{\pi}{4} D_{\text{mp}}^2 h_{\text{sub}} \qquad [\text{m}^3] \quad (3.4)$$

One component to account for in the systems is the added mass component. Added mass, also known as virtual mass, is a concept in fluid mechanics that refers to the effective mass that a body appears to have when it is accelerated by a fluid flow. In other words, when a body is moving through a fluid, the fluid surrounding the body will also be set in motion and this motion of the fluid will contribute to the inertia of the body. This contribution is known as the added mass of the body.

The added mass of a body is dependent on the shape and size of the body, as well as the properties of the fluid in which it is moving. It is important to take into account the added mass of a body when analyzing the motion of the body in a fluid, as it can have a significant effect on the force required to accelerate the body. The added mass force is defined in the opposite direction of the motion of the accelerating body and can be included in the system equation as follows:

$$m\ddot{x} + b\dot{x} + kx = f(t) - m_a\ddot{x} \qquad \rightarrow \qquad (m + m_a)\ddot{x} + b\dot{x} + kx = f(t) \tag{3.5}$$

where m_a is the added mass term. For a circular two-dimensional cylinder, the added mass is precisely equal to the displaced mass of the fluid. The buoyancy force F_b, the mass of the internal water column m_{int} and the added mass component m_a can be calculated using the parameters mentioned earlier:

$$F_b = \rho_w g V_{\text{ext}} \quad = \rho_w g \frac{\pi}{4} D_{\text{mp}}^2 h_{\text{sub}} \qquad \text{[N]} \tag{3.6}$$

$$m_{\text{int}} = \rho_w V_{\text{int}} \quad = \rho_w \frac{\pi}{4} D_i^2 h_{\text{int}} \qquad \text{[kg]} \tag{3.7}$$

$$m_a = \rho_w V_{\text{ext}} \quad = \rho_w \frac{\pi}{4} D_{\text{mp}}^2 h_{\text{sub}} \qquad \text{[kg]} \tag{3.8}$$

The aforementioned lengths depicted in figure 3.2 are calculated using the equations below. The height of the cranetip is calculated by taking the sum of the lifting height (h_{lift}), the deck height (h_{deck}) and the air gap (h_{airgap}). It is worth mentioning that in specific projects with high earthquake risks, there may be situations where the airgap can become negative in a semi-jacked configuration. This means that the hull of the vessel is partially submerged. The deck height can be less in the semi-jacked situation than during the fully jacked situation. These parameters can therefore be varied according to the desired situation.

$$\begin{aligned} h_{\text{cranetip}} &= h_{\text{lift}} + h_{\text{deck}} + h_{\text{airgap}} & l_3 &= l_{\text{mp}} \\ l_1 &= h_{\text{cranetip}} - l_{\text{mp}} + h_{\text{sub}} & l_{\text{int}} &= l_{\text{mp}} - \frac{h_{\text{int}}}{2} \\ l_2 &= \frac{l_{\text{mp}}}{2} & l_a &= l_b = l_{\text{mp}} - \frac{h_{\text{sub}}}{2} \end{aligned} \qquad \text{[m]} \tag{3.9}$$

The assigned values of the parameters of equations 3.9 are depicted in table 3.1. The abbreviation t.b.c. stands for 'to be calculated' which means that these specific values are dependent on input variables h_{sub} or h_{int} and are calculated in the model. The point of application is denoted as p.o.a.

Table 3.1: Assigned values for input parameters

Parameter	**Symbol**	**Value**	**Unit**
Length MP	l_{mp}	82.7	m
Diameter MP	D_{mp}	9.5	m
Thickness MP	t_{mp}	0.076	m
Mass MP	m_2	1480	t
Mass top-cap (incl. lifting tool)	m_1	90	t
Mass bottom-cap	m_3	40	t
Height of crane tip	$h_{\text{crane tip}}$	153	m
Length crane wire	l_1	t.b.c	m
Length from top-cap till p.o.a. of m_2	l_2	41.35	m
Length from top-cap to bottom cap	l_3	82.7	m
Length from top-cap till p.o.a. of F_b	l_b	t.b.c	m
Length from top-cap till p.o.a. of m_{int}	l_{int}	t.b.c	m
Length from top-cap till p.o.a. of m_a	l_a	t.b.c	m
Gravitational acceleration	g	9.81	m s^{-2}
Density of water	ρ_{water}	1025	kg m^{-3}
Density of air	ρ_{air}	1.225	kg m^{-3}

3.3. Methods

There are different methods available to solve these kind of systems and the most commonly used methods are listed below and briefly discussed in the next sections.

1. Principle of virtual work
2. Newton's method
3. Lagrange's method

3.3.1. Principle of virtual work

The first method used to solve these types of systems is by applying the principle of virtual work [4]. This method allows for the determination of the natural frequency of the systems described in section 3.2. However, it should be noted that the equations of motion cannot be directly derived using the principle of virtual work. This principle is based on evaluating the virtual work done by either:

- A **virtual force** acting trough a **real displacement** or
- A **real force** acting trough a **virtual displacement**

where a virtual displacement is any displacement consistent with the constraints of the system and satisfy the boundary criteria of the system. This virtual displacement is not necessarily experienced in reality but is assumed to exist for the purpose of analyzing the system. Similarly, a virtual force refers to a system of forces in equilibrium.

Work is defined as a force multiplied with the corresponding displacement. It is a form of energy and the energy that goes into the system is stored in the system in the form of strain energy. The law of conservation of energy states that the energy of interacting bodies or particles in a closed system remains constant. So the external work done on the structure is equal to internal strain energy stored in the system or structure. A result of this conservation is the energy balance with an internal energy part (δT) and an external energy part (δV). Because this conservation means that there is no loss of energy in the system, the energy balance is always equal to zero and is stated in equation 3.10.

$$E \quad = \delta T + \delta V \quad = 0 \tag{3.10}$$

This principle becomes straightforward when considering the system simplification shown in figure 3.2. In this system, the internal energy component is associated with the inertia of the bodies, while the external energy component is derived from the gravitational forces (F_g) and buoyancy forces (F_b). The inertia of the bodies in the system consists of two components: mass accelerated in the x- and z-direction. The gravitational and buoyancy forces only act in the vertical z-direction, as indicated in equation 3.11.

$$\begin{aligned} E \quad &= \overbrace{F_x\delta x \quad + \quad F_z\delta z}^{\text{Internal energy}} \quad + \quad \overbrace{F_g\delta z \quad + \quad F_b\delta z}^{\text{External energy}} \quad = 0 \\ &= \underbrace{m\ddot{x}\delta x \quad + \quad m\ddot{z}\delta z}_{\text{Inertia}} \quad + \quad \underbrace{mg\delta z \quad + \quad \nabla\rho_{sw}\delta z}_{\text{Vertical forces}} \quad = 0 \end{aligned} \tag{3.11}$$

where m is the mass of a certain body in the system, ∇ is the displaced volume of the body that creates buoyancy in the system and ρ_{sw} is the density of the seawater. This method is very useful to describe any system with small displacement or small angles. To apply this method to the considered system, the small angle approximation theorem can be used. This theorem is explained in the next section.

Small angle approximation theorem

The small-angle approximation theorem is often used in physics and can be used to simplify some of the mathematics involved. This method is based on the assumption that the angles defining the system are small. The following set of basic trigonometric functions are then valid when $\phi \approx 0$:

$$f(\phi) \qquad \rightarrow \qquad \sin\phi \approx \phi, \qquad \cos\phi \approx 1 - \frac{\phi^2}{2} \approx 1 \qquad \text{and} \qquad \tan\phi \approx \phi \tag{3.12}$$

It is important to note that these equations are approximations and as the angle gets larger, their accuracy decreases. To better understand the small angle approximation and to be able to justify them, a comparison

can be made. The sine and cosine as stated in the set of equations 3.12 are visualized in figure 3.4. It can be seen that the small angle approximations (orange) of the sine and cosine are valid for relatively small angles. The error (green) is relatively small for angles less than or equal to 15 degrees or 0.26 radians. From this point on, the term 'small' angles refers to angles below these values.

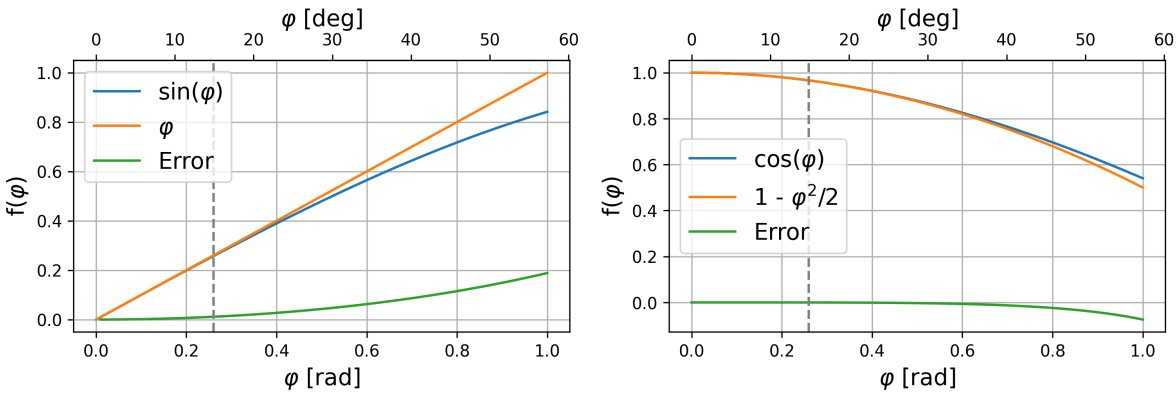

Figure 3.4: Small angle approximation near $\phi = 0$ for *left:* $\sin\phi$ and *right:* $\cos\phi$

The small-angle approximation is used to simplify the kinematics of the systems discussed in this chapter. This method is applicable because it is expected that the governing angles will remain below the given limit for small angles. Small rotations are assumed and the following statements do hold:

$$\begin{aligned} \phi^2 &\approx 0, & \phi\dot{\phi} &\approx 0 \\ \dot{\phi}^2 &\approx 0, & \phi\ddot{\phi} &\approx 0 \end{aligned} \tag{3.13}$$

3.3.2. Newton's method

This method makes use of the balance of forces acting on the system as stated in equation 3.14. The forces acting on a simple pendulum system are depicted in figure 3.5b and includes only two forces. These forces are the inline tension force F_T in the cable and the gravitational force of the mass m. Equation 3.14 is stated in a vector notation, but the only relevant force is the tangential component of the gravity. This is the component of the force and the acceleration that point along the circle where the particle is constrained to move. The tension F_T is not contributing and is pointing towards the center of that circle, perpendicular to the tangential component of the gravitational force. Using geometry as shown in figure 3.5b, the tangential component is defined as $mg\sin\phi$ and is pointing back to the pendulum's equilibrium position.

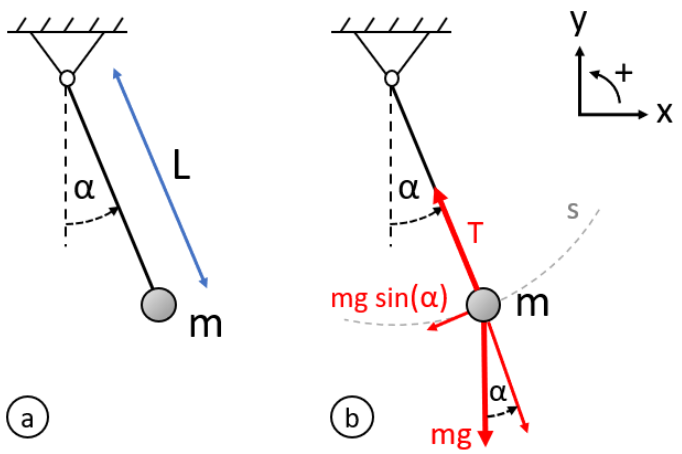

$$\sum \vec{F} = m\vec{a} \tag{3.14}$$

Figure 3.5: a) Single pendulum system b) Forces and its force components acting on the mass m

$F = ma$ for the circular path s and simply reads $m\ddot{s} = -mg\sin\phi$. Because $\ddot{s} = L\ddot{\phi}$, the equation can be rewritten as stated in equation 3.15. This is called the equation of motion for the angle ϕ and it is the differential

equation that describes the motion of this particular single pendulum. If the system contains more degrees of freedom such as in a double pendulum system, this method becomes more complex rather quickly.

$$\ddot{\phi} = -\frac{g}{l}\sin\phi \quad \rightarrow \quad \ddot{\phi} = -\frac{g}{l}\phi \qquad \text{when} \quad \phi \quad \text{is small} \tag{3.15}$$

From this equation, the oscillation frequency ω can be derived by assuming a solution in the form $\phi(t) = A\cos\omega t + B\sin\omega t$:

$$\begin{aligned}\dot{\phi} &= -A\omega\sin\omega t + B\omega\cos\omega t\\ \ddot{\phi} &= -A\omega^2\cos\omega t - B\omega^2\sin\omega t\\ &= -\omega^2\phi\end{aligned}$$

Comparing this with equation 3.15 leads to the following relation for ω and for the oscillation period $T = \frac{2\pi}{\omega}$:

$$\omega^2 = \frac{g}{l} \quad \rightarrow \quad \omega = \sqrt{\frac{g}{l}} \qquad \text{and} \qquad T = 2\pi\sqrt{\frac{l}{g}} \tag{3.16}$$

3.3.3. Lagrange's method

Lagrange's method can be used to find the equations of motion of a system. By assuming small angles, a set of equations can be defined to find the natural frequency of the system. This small approximation method is defined in section 3.3.1.

The Lagrangian for a double pendulum system is given by $L = T - V$, where T and V are the kinetic and potential energy respectively. The Lagrangian is a mathematically useful quantity, because the kinetic energy minus the potential energy does not mean anything physically. In the presence of a plus sign, the equation becomes just the addition of both energies and results in the total energy of the system. The kinetic and potential energy of a simple mass-spring system, as shown in figure 3.6, are stated in equation 3.17 and 3.18 respectively.

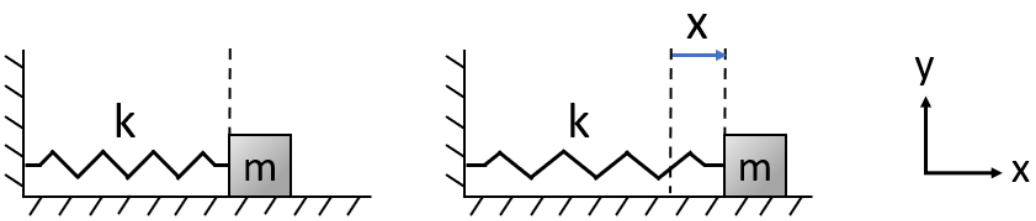

Figure 3.6: Mass spring system

$$T = \frac{1}{2}mv^2 \tag{3.17}$$

$$V = \frac{1}{2}kx^2 \tag{3.18}$$

where v is the velocity of the mass m, i.e. the time derivative of the position x of the mass m and k is defined as the spring constant. For the purpose of this research, it is more convenient to switch to a pendulum model as shown in figure 3.5. The principle is the same as for the mass-spring system but the displacement parameter x is now defined by a rotational displacement ϕ and the potential energy is defined in the vertical direction with displacement parameter y. The kinetic and potential energy no become:

$$T = \frac{1}{2}m\dot{x}^2 \tag{3.19}$$

$$V = mgy \tag{3.20}$$

together with the definition of x and y as depicted in figure 3.5:

$$x = l\cdot\sin\phi \qquad \dot{x} = \dot{\phi}l\cdot\cos\phi \qquad y = -l\cdot\cos\phi \qquad \dot{y} = \dot{\phi}l\cdot\sin\phi$$

For Lagrange's method, the Euler-Lagrange equation 3.21 is used. It should be noted that this equation is valid for a double pendulum system with angles ϕ_1 and ϕ_2, whereas the single pendulum system only depends on the angle ϕ.

$$\frac{\mathrm{d}}{\mathrm{d}t}\left(\frac{\partial L}{\partial \dot{q}_i}\right) - \frac{\partial L}{\partial q_i} = Q_i \qquad \text{for} \qquad q_i = \phi_1, \phi_2 \tag{3.21}$$

The equation of motion can be found by applying equation 3.21 with the definitions of the Lagrangian L and the displacement parameters x and y. This method results in the same equation as equation 3.15, found with Newton's method. However, Newton's method needs a lot more steps than Lagrange's method when the system is getting more complex. So this method becomes more convenient if more complicated systems with multiple forces are considered, such as a double pendulum system that includes multiple variables. Besides that, the latter is the preferred method because it results in the equation of motion without considering forces at all, only energy is considered.

3.4. Single pendulum

To simplify the analysis of the complex system, the vertical single pendulum is initially studied. This first analysis focuses on three components: the buoyancy force F_b, and the masses m_2 and m_{int}. Details of the derivations can be found in Appendix A.1. The derived equation of the natural frequency without considering the related damping, is formulated as follows:

$$f_n = \frac{1}{2\pi}\sqrt{\frac{K}{M}} \qquad = \frac{1}{2\pi}\sqrt{\frac{l_1\left((m_2+m_{\text{int}})g - F_b\right)}{l_1^2(m_2+m_{\text{int}})}} \qquad = \frac{1}{2\pi}\sqrt{\frac{(m_2+m_{\text{int}})g - F_b}{l_1(m_2+m_{\text{int}})}} \quad [\text{s}^{-1}] \tag{3.22}$$

If the equation is simplified regarding its units, the result is in accordance with the unit of the natural frequency [Hz]. This is shown in the formula below, where the red units represent the expected stiffness K and the blue one represents the expected mass M.

$$f_n = \frac{1}{2\pi}\sqrt{\frac{K}{M}} \qquad = \frac{1}{2\pi}\sqrt{\frac{m\cdot(kg\cdot ms^{-2})}{m^2\cdot kg}} \qquad = \frac{1}{2\pi}\sqrt{\frac{kg\cdot m\cdot s^{-2}}{m\cdot kg}} \qquad = \sqrt{s^{-2}} \qquad = s^{-1} \qquad = \text{Hz}$$

The single pendulum inline accounts for the rotation of the MP and shows similar results as the vertical pendulum. The derivations and results can be found in Appendix A.2. The most important observation of examining the single pendulum system is the ease of incorporating additional mass or inertia components into the equations of motion. This is convenient for analyzing more complex systems, such as a double pendulum system. This single pendulum analysis serves as the basis for the analytical model discussed in the next sections.

3.5. Double pendulum

The system becomes more complex with the introduction of a second degree of freedom, represented by the angles ϕ_1 and ϕ_2. These angles are independent and considered as separate degrees of freedom. Consequently, the natural frequency analysis yields to two distinct mode shapes: one where the masses m_1 and $m_{2,3}$ & m_{int} are in phase and another where these components are out of phase. The natural frequency of this system is found by assuming the general solution will be a sine function. This assumption reduces the set of equations to an eigenvalue problem that can be solved:

$$\vec{\Phi} = \begin{bmatrix}\phi_1\\ \phi_2\end{bmatrix} = \begin{bmatrix}\phi_{1i}\\ \phi_{2i}\end{bmatrix}\sin(\omega t) \qquad \rightarrow \qquad \ddot{\vec{\Phi}} = -\omega^2\begin{bmatrix}\phi_{1i}\\ \phi_{2i}\end{bmatrix}\sin(\omega t) \tag{3.23}$$

The natural frequencies of the system can be found with equation 3.25. The full derivation is stated in Appendix A.3.

$$K\vec{\Phi} = \omega^2 M\vec{\Phi} \qquad (3.24) \qquad\qquad f_i = \frac{1}{2\pi}\sqrt{\lambda_i} \qquad \text{with:} \quad i = 1,2 \qquad (3.25)$$

By considering all components, the following set of equations is obtained, where the added mass terms are highlighted in red:

$$M\ddot{\vec{\Phi}} + K\vec{\Phi} = \vec{0} \quad \begin{cases} M = \begin{bmatrix} l_1^2(m_1+m_2+m_3+m_{\text{int}}+m_a) & l_1(m_2l_2+m_3l_3+m_{\text{int}}l_{\text{int}}+m_al_a) \\ l_1(m_2l_2+m_3l_3+m_{\text{int}}l_{\text{int}}+m_al_a) & m_2l_2^2+m_3l_3^2+m_{\text{int}}l_{\text{int}}^2+m_al_a^2 \end{bmatrix} \\ K = \begin{bmatrix} l_1\left(m_2g+m_3g+m_{\text{int}}g-F_b\right) & 0 \\ 0 & (m_2l_2+m_3l_3+m_{\text{int}}l_{\text{int}})g-F_bl_b \end{bmatrix} \\ \vec{\Phi} = \begin{bmatrix} \phi_{1i} \\ \phi_{2i} \end{bmatrix} \sin(\omega t) \end{cases} \tag{3.26}$$

The results of including the added mass terms are shown in figure A.11. It can be concluded that the added mass component influences the natural frequency but a significant shift of this frequency is not observed.

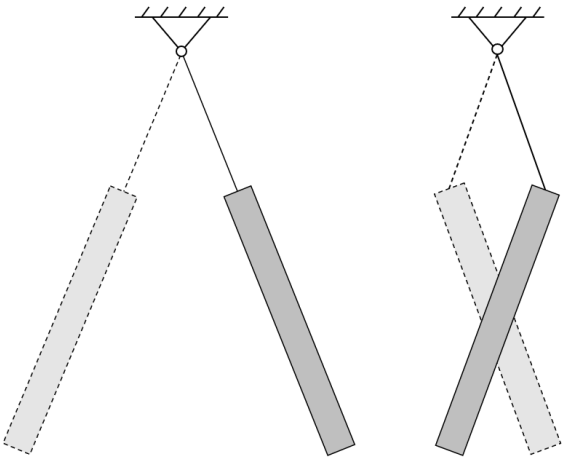

Figure 3.7: Visualization of the in-phase mode (left) and the out of phase mode (right)

As said, this system has two degrees of freedom which means the system contains two modes. One mode in the low-frequency range where the masses are in phase with each other and the high-frequency mode where the masses are out of phase to each other. A sketch can be found in figure 3.7 to visualize both modes. In the low frequency mode, the rotation point is at the cranetip, while in the high frequency mode, the inertia is defined with the rotation point assumed to be located at the top of the MP. The influence of inertia on the system is considered in the next section.

3.6. Double pendulum - Inertia

In the previous systems, each mass component was represented as a point mass for simplicity in the derivations. However, in reality, the masses are distributed over their own length. To account for this distributed mass, two possibilities exist. The first option is to divide the masses into smaller segments equally distributed along their length. However, due to system's two degrees of freedom, this approach is considered complex. Instead, the assumption of using point masses can be compensated by incorporating inertia terms in the equations. In this section, the third case is considered, where the system includes all components, as shown in Figure 3.8, with the added mass term depicted in green.

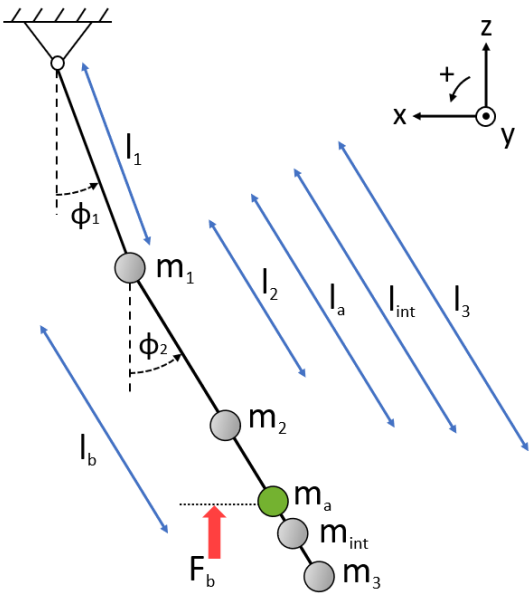

Figure 3.8: Double pendulum (for all components)

The inertia term for the masses of the MP, the internal water column and the added mass are calculated using equations 3.27 - 3.29. An equally divided mass is assumed for all inertia terms. Parameters required to calculate the moments of inertia for the out-of-phase mode are clarified in figure 3.9. It is important to note

that the internal water column is assumed to be a rigid water column. This means that the system does not account for any hydrodynamic effects of the column, f.e. the sloshing phenomenon. This should be considered during the post-processing of the model experiments.

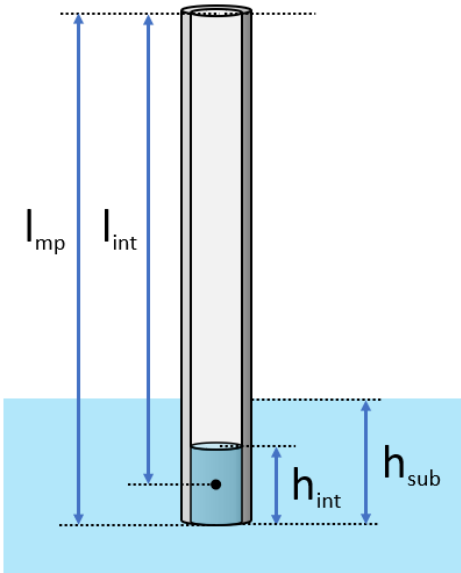

Figure 3.9: Parameters: l_{mp}, h_{sub}, h_{int} and l_{int}

$$J_2 = \frac{1}{12} m_2 l_{\text{mp}}^2 \tag{3.27}$$

$$J_{\text{int}} = \frac{1}{12} m_{\text{int}} h_{\text{int}}^2 \tag{3.28}$$

$$J_a = \frac{1}{12} m_a h_{\text{sub}}^2 \tag{3.29}$$

The inertia of each component is defined around its own center of gravity, so that inertia is defined as $J = \frac{1}{12} m l^2$. This is done as Lagrange's method results in the equations of motion that eventually consider the point of rotation to where the inertia is defined. In this case, the rotation point is at the top of the MP. In other words, the term md^2 according to the parallel axis theorem, is accounted for in the derivations of the kinematics. This principle of considering inertia is discussed in detail in Appendix A.5.

Lagrange's method

As mentioned, this system is identical to the double pendulum examined in the previous section, except that the inertia terms are now accounted for. This means that the kinematics of the system remain nearly identical, as explained in detail in Appendix A. To be able to account for the moment of inertia, Lagrange's method is used. Both the kinematics and the application of this method can be found in Appendix A.4.

By using a second method, the set of equations found by the small angle approximation method can be validated. It was concluded that both methods resulted in the same outcome, except for the additional inertia terms. It was found that the inertia terms for the MP (J_2), the internal water column (J_{int}) and the added mass (J_a) can be added relatively easy to equation 3.26. This is convenient as it simplifies the process of incorporating additional inertia components into the equation if it becomes necessary. The inertia components are added in red and the set of equations becomes:

$$M\ddot{\vec{\Phi}} + K\vec{\Phi} = \vec{0} \quad \begin{cases} M = \begin{bmatrix} l_1^2(m_1+m_2+m_3+m_{\text{int}}+m_a) & l_1(m_2 l_2 + m_3 l_3 + m_{\text{int}} l_{\text{int}} + m_a l_a) \\ l_1(m_2 l_2 + m_3 l_3 + m_{\text{int}} l_{\text{int}} + m_a l_a) & m_2 l_2^2 + m_3 l_3^2 + m_{\text{int}} l_{\text{int}}^2 + m_a l_a^2 + J_2 + J_{\text{int}} + J_a \end{bmatrix} \\ K = \begin{bmatrix} l_1\left(m_2 g + m_3 g + m_{\text{int}} g - F_b\right) & 0 \\ 0 & (m_2 l_2 + m_3 l_3 + m_{\text{int}} l_{\text{int}}) g - F_b l_b \end{bmatrix} \\ \vec{\Phi} = \begin{bmatrix} \phi_{1i} \\ \phi_{2i} \end{bmatrix} \sin(\omega t) \end{cases} \tag{3.30}$$

3.6.1. Results

The frequencies of the different configurations for increasing submergence of the MP are shown in figure 3.10a and b. This comprehensive system considers all components and inertia terms and offers a more realistic representation for this analysis. It is noteworthy that incorporating inertia terms in the system leads to a considerable reduction in the natural frequency of the second mode. This decrease in frequency is significant when compared to the double pendulum without inertia, as shown in figure A.11. The resulting natural frequency aligns more closely with the typical values observed in offshore operations, where periods of 6-8s have been commonly observed [7].

Note that through the relation stated in equation 3.9, the length of the cable l_1 accounts for the change in submergence. This means that the cable length increases if the submerged length increases.

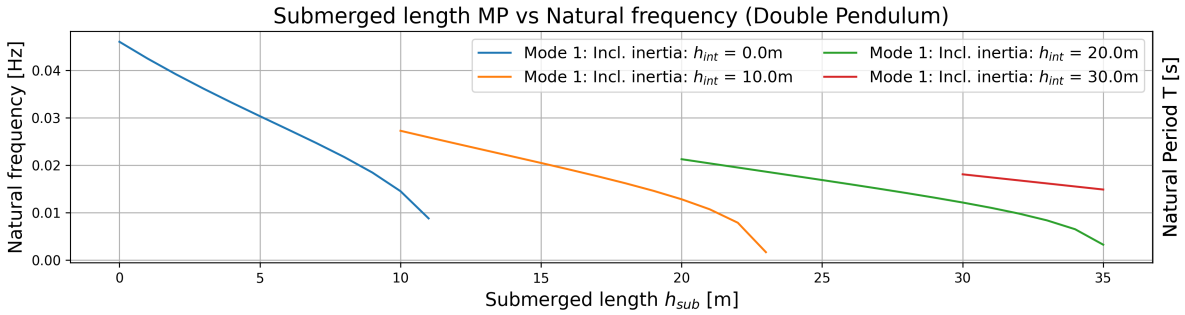

(a) In-phase mode

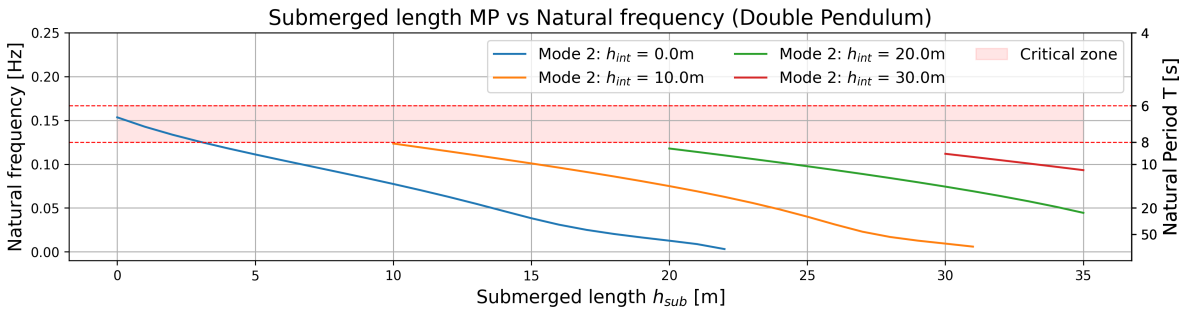

(b) Out-phase mode

Figure 3.10: Natural frequency vs submerged length for different h_{int}, considering all components and inertia of m_2, m_{int} and m_a

The frequencies associated with various configurations of internal water level (h_{int}) and submergence level (h_{sub}) are summarized in table 3.2. The first mode corresponds to the low-frequency mode and exhibits significantly longer natural periods, making it highly unlikely to be excited by waves. On the other hand, the second mode represents the high-frequency mode with relatively shorter natural periods. This mode is expected to be within the range of frequently observed wave periods offshore.

Table 3.2: Natural frequencies and periods of the analytical approach for double pendulum incl. inertia

		Mode 1		Mode2	
h_{int} [m]	h_{sub} [m]	f_1 [Hz]	T_1 [s]	f_2 [Hz]	T_2 [s]
0	0	0.046	21.7	0.153	6.5
0	10	0.015	66.7	0.077	13.0
10	10	0.027	37.0	0.124	8.1
10	20	0.013	76.9	0.075	13.3
20	20	0.021	47.6	0.118	8.5
20	30	0.012	83.3	0.074	13.5
30	30	0.018	55.6	0.112	8.9

3.7. Conclusions

The natural frequency assessment for the four different systems has been conducted and their respective natural frequencies have been determined. The single pendulum models provide a good initial understanding of the natural frequencies for the simplest systems. Introducing a second degree of freedom brings the system closer to the real situation, although the corresponding natural periods are relatively high. However, by incorporating inertia terms for the distributed mass components into the double pendulum system, the overall range of natural frequencies shifts to a lower bound that aligns closely with the expected values offshore (T = 6 - 8s) [7], denoted as the critical zone. The double pendulum model, incorporating all inertia components, provides the most accurate representation of reality. Hence, the set of equations from equation 3.30 will be used in the numerical model and throughout the rest of this research.

If the out of phase mode in figure 3.10b is observed, it can be seen that the blue line, representing an internal water column of 0 meters, only crosses the critical zone within the range of 0 to 3.0 meters. As the monopile is further lowered to the seabed, beyond a submerged length of 3.0 meters, the blue line reaches natural periods of 10-20 seconds. The decrease in natural frequency can be primarily attributed to two factors: the increase in cable length l_1 and the increasing buoyancy force. This relationship can be derived from the definition of the natural frequency, as indicated by equation 3.22.

It is therefore beneficial to fill the monopile and increase the internal water column to 10 meters within the range of submerged lengths of 10-15 meters. This results in a frequency shift towards the yellow line (h_{int} = 10m) and allows for further lowering of the monopile without reaching the submerged range where the buoyancy force becomes too large. This process can be repeated until the submerged length of the monopile is sufficient to reach the seabed. This approach of filling the monopile during the lowering process is illustrated in figure 3.11 using the dashed lines and presents a favourable and practical solution.

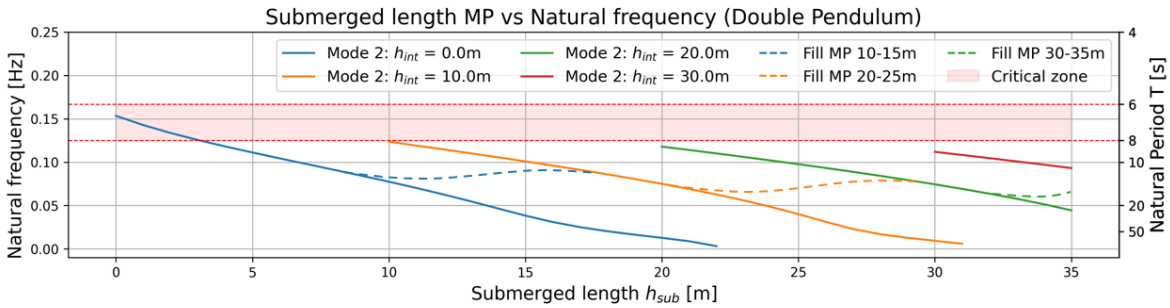

Figure 3.11: Filling up the MP during lowering as a potential solution

Important to consider that the MP will not be lifted completely out of the water because the upward lifting force, i.e. the buoyancy force, should be present at all times. This observation is very convenient when looking at figure 3.11. Since the submerged length of the MP will never be zero with this method, h_{sub} potentially starts between 5-10 meters, depending on the buoyancy requirements. If this is the case, the natural frequency will never reach the critical zone, which makes the aforementioned solution only more interesting.

4

Exploratory tests

To create an initial understanding of the upending principle of using trapped air, a series of exploratory tests were conducted. This chapter elaborates on the set-up, design steps and the observations made during the tests. These exploratory tests aim to provide an initial understanding of the behavior of a scaled version of the real scenario. They serve as a foundation for conducting more detailed model experiments in the following stage of this research. Appendix C provides a more detailed overview of the experiments.

4.1. Experimental set-up

Initial sketches of the experimental set-up can be found in Figure 4.1. In order to create a practical and simplified testing environment, rough scaling factors are used. These scaling factors are based on the scaling of a large monopile and set at a ratio of 200 : 1. Other relevant parameters were adjusted accordingly whenever possible, as outlined in table 4.1. The exploratory tests are conducted in a bathtub, that serves as a still water environment. Generating controlled waves proved challenging due to wave reflections against the walls, resulting in interference and the inability to simulate regular waves. As a result, only random sea states with standing waves could be generated. Consequently, drawing conclusions about the influence of regular waves was difficult under these conditions.

Table 4.1: Rough scaling parameters (scaling 200:1)

	Full scale	Model scale	Unit
L_{mp}	92	0.46	[m]
D_{mp}	10	0.05	[m]
$h_{\text{crane tip}}$	120	0.60	[m]

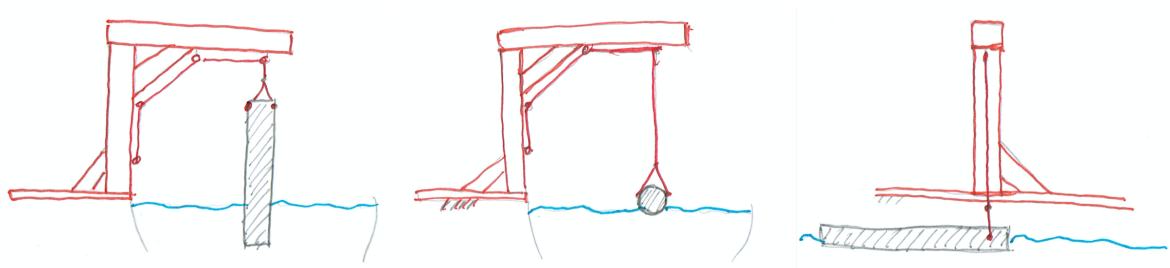

(a) Front view of vertical MP **(b)** Front view of horizontal MP **(c)** Side view of horizontal MP

Figure 4.1: Sketch of first experimental set-up

4.2. Prototype I

In the first version of the experimental set-up (see figure 4.2), the crane structure was constructed using wooden materials in an L-shaped configuration. A rigid rope served as the crane cable, which was manually hoisted. To ensure a vertical motion unaffected by external factors, screw-eyes were used to guide the crane cable. The crane hook was simulated by the connection between the rope and a PVC pipe with corre-

sponding PVC end-caps, representing the MP. PVC was chosen for its ease of handling and sealing properties, crucial for achieving the required buoyancy. However, it should be noted that the material properties of PVC do not accurately match the scaling requirements. This could result in a difference in buoyancy and easier initiation of MP movements due to its lower weight and inertia compared to a similarly sized steel pipe. Additionally, no water inlet was incorporated in this initial stage of the experiments. At this scale, the pressure was insufficient to compress the air inside the MP and allow water to enter. The tests were recorded using two cameras: one capturing the front view and the other recording movements from above the crane tip as depicted in figure C.1.

4.2.1. Results

The initial tests were conducted in a still water environment using the first version of the set-up. The upending process was simulated by manually hoisting the crane cable while imposing an internal water level that created a water level difference between the inside and outside of the MP. Since measuring the water level inside the MP was challenging, three different internal water levels were used: no internal water column, a small and a large column. These varying water level differences allowed for the execution of the upending procedure. Additionally, the influence of an applied current on a partly submerged vertical MP was investigated and at last, decay tests were performed to gain an insight into the behavior of the MP. The following tests were conducted:

1. Upending with three different internal water levels
2. Apply current on a vertical, partly submerged MP
3. Decay test with different initial angles

Figure 4.2: First experimental set-up (vertical MP)

Internal water column

In the case of no internal water level, maximum buoyancy is created. One observation is a static offset angle in the sway direction, which may be attributed to an asymmetrical connection between the cable and the MP. During the upending process, the MP appears to be stable but it becomes highly unstable in the vertical stage. In this stage, where there is little to no submerged part of the MP, even a small push results in a significant swinging motion of the MP. When the MP is slightly lowered in the vertical direction, the bottom of the MP shows deviates from its vertical position. Currently, the direction of this deviation seems random, but it could also be influenced by the aforementioned asymmetrical connection between the cable and the MP.

When a small internal water level is applied, the same offset angle of the MP in the sway direction is observed, in its horizontal position. When waves are manually generated, the offset angle becomes larger. This can be explained by the wave force acting on the side of the MP, causing it to move further in the sway direction. This phenomenon is depicted in figure C.2. During the upending process in still water, no unexpected movements are observed.

In the third case, where the internal water level is increased, the same offset angle as before is observed in the MP's sway direction. The upending process in still water does not show significant differences compared to the case with the small internal water column. Additionally, when the MP is lowered, it continues to search for the direction with the least resistance. Due to the larger internal column, the submerged part of the MP naturally increases, causing this phenomenon to occur slightly later in time.

Current

The presence of an applied current induces oscillatory motion in the y-direction, which is perpendicular to the current. The observed phenomenon of the vertical MP remaining stationary while exhibiting motion in the sway direction suggests the potential influence of vortices around the partly submerged MP. This behavior is commonly encountered in offshore operations and indicates the presence of vortex-induced motions.

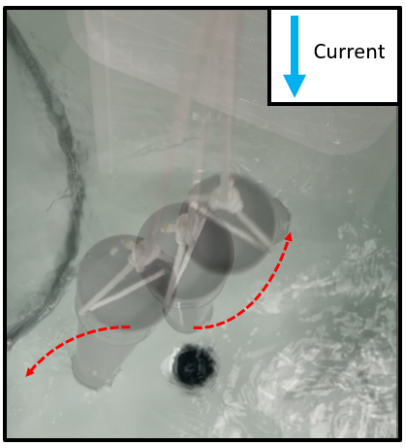

Figure 4.3: Vortices due to applied current

Decay tests

Decay tests were conducted to examine the behavior of the MP in a double pendulum system. These tests were initially conducted without considering hydrodynamic effects, in order to identify the natural modes of such a system. The MP was set with initial angles in the in-line mode, where the angles are in-line with each other. The tests were performed without a bottom cap to examine the effects of the internal water column. This means that there is no water level difference and thus no buoyancy in the system.

Snapshots of the recordings from the exploratory tests are presented in figure 4.4. The left side shows the scenario with no submergence, while the right side presents the MP partially submerged. The first low-frequency mode in air is clearly visible and the damping is minimal, allowing the MP to swing for a long period of time. The rotation point can be easily identified at the cranetip. When the MP is partially submerged, the damping is increased significantly and the MP reaches is equilibrium position much faster.

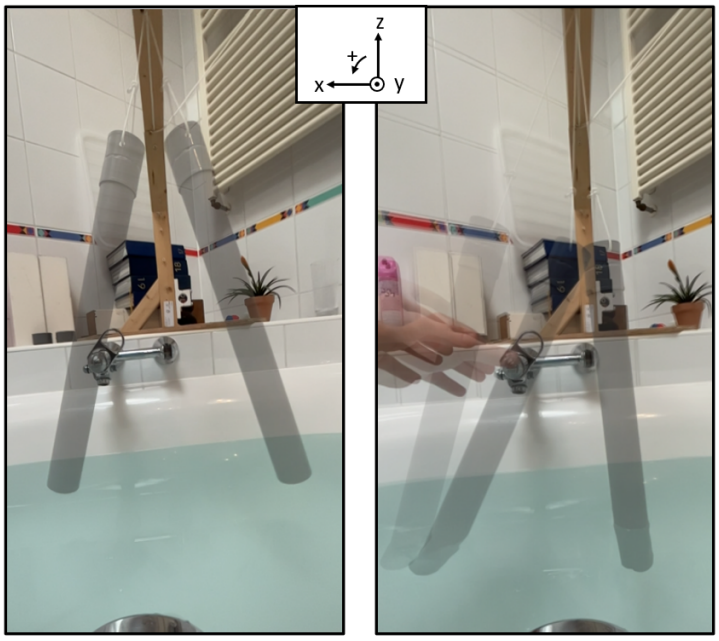

Figure 4.4: Initiated in-line double pendulum system of exploratory tests.
(left) No submergence (right) Partially submerged

The second mode of the double pendulum system is the high-frequency mode, referred to as the out-line mode. During the decay tests, the MP is allowed to swing freely with opposite initial angles. Figure 4.5 illustrates the out-line double pendulum mode, with the decay test in air shown on the left and the partially submerged MP, on the right. When the MP is allowed to swing freely without any hydrodynamic interactions, it experiences low damping. The center of gravity (CoG) of the MP is clearly located in the middle of the MP, as shown in figure 4.5. However, when the MP is partially submerged, the center of gravity shifts towards the waterline or even slightly below it.

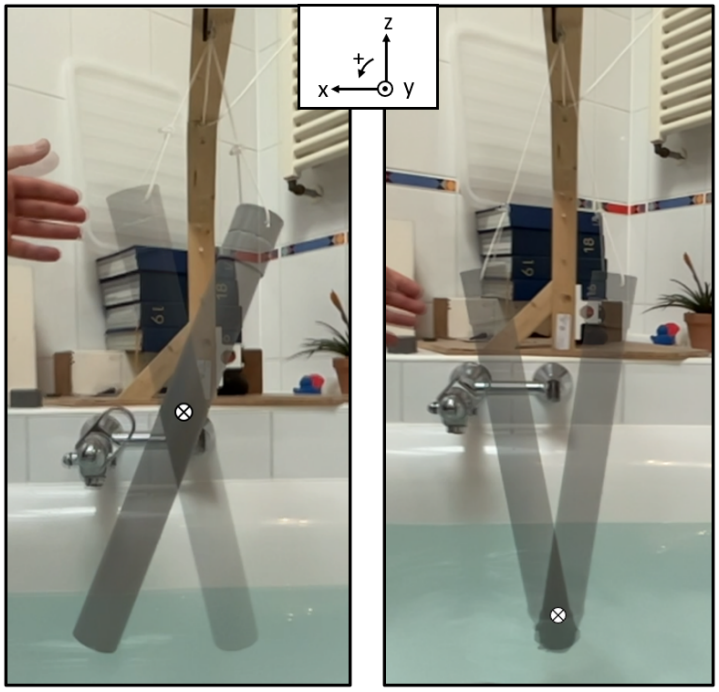

Figure 4.5: Initiated out-line double pendulum system of exploratory tests.
(left) No submergence (right) Partially submerged

4.2.2. Conclusions

The presence of a static offset in the lateral direction observed in all three upending scenarios is likely attributed to the asymmetry in the connection between the crane cable and the MP. It is worth noting that if a static offset exists in the horizontal plane, the forces exerted by waves on the MP can potentially amplify the offset angle over time. However, this study primarily focuses on the vertical stage and does not include the effects of wave-induced forces on the MP.

If vortex-induced motions occur during the upending process, they could potentially pose a significant problem as the MP may collide with the hull of the ship or cause excessive forces on the cranetip. It is important to keep in mind that these vortices could have an impact during the scaled model tests. The influence of vortex-induced motions should be considered in the post processing of the experimental data.

The phenomenon of the MP deviating from its vertical position and 'searching' for the path of least resistance when slightly lowered, is a result of establishing a static equilibrium between the increasing buoyancy force and the weight of the MP minus the lifting force. As the submerged internal air volume increases, the buoyancy force (indicated by the red arrow in figure 4.6) also increases, while the weight of the MP minus the lifting force remains constant. Eventually, the system reaches a static equilibrium where the buoyancy force equals the weight of the MP minus the lifting force. To achieve this equilibrium, the internal air volume needs to decrease back to its original volume from step 1, resulting in the observed searching phenomenon depicted in figure 4.6. It is important to take this observation into consideration during the model tests.

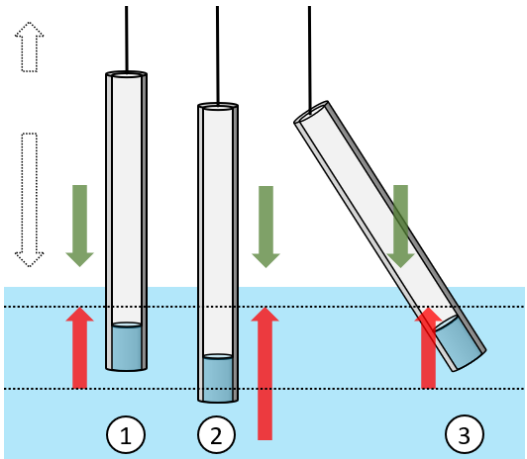

Figure 4.6: 'Searching' phenomenon of the MP while lowered (forces are not a representation of reality)

The rotation point in the first low-frequency mode is clearly observed at the cranetip. The high damping in the in-line mode indicates that for the model tests, the signal includes significant damping, potentially making the high-frequency mode more prominent. In this second mode, when the MP is partially submerged,

the CoG undergoes a significant shift towards the waterline. This shift is due to the substantial mass of water in the bottom of the MP, which becomes a significant portion of the total mass within the system. Consequently, the CoG is located closer to the waterline.

4.3. Prototype II

To ensure a smooth vertical lowering process, the internal water column can be increased by letting water in at the bottom of the MP. However, due to the limitations in scaling, it is not possible to facilitate water injection. As an alternative, air is released from the top of the MP to achieve the desired effect. This is accomplished through the use of a flexible tube, which can be manually closed to stop the water inlet at the bottom. The tube facilitating air release at the top and water inflow at the bottom of the MP is shown in figure 4.7. The second prototype allows for water inlet and thus facilitates both the upending and lowering procedure. Though this process is not particularly investigated, it may result in some insights of the procedure.

Figure 4.7: Flexible tube to facilitate water inlet at the bottom

4.3.1. Results

If the MP is fully emerged from the water, a little push at the bottom of the MP results in a large swinging motion in the natural frequency of the system. When the MP is lowered, the water dampens the motion and it is observed that the oscillations decrease over time when the submerged part of the MP increases. This is in correspondence to the decrease in natural frequency as a result of a larger submergence, found in Chapter 3.

4.3.2. Conclusions

By accurately controlling the water inlet, the MP can be lowered to the bottom in a smooth manner. It is important to manage the hoisting speed, as a high velocity can cause the MP to exhibit the searching behavior, mentioned earlier. This indicates the importance of effectively managing the water level difference between the inside and outside of the MP to ensure a controlled lowering process. Additionally, it is crucial to maintain a hoisting speed that allows for a vertical and stable MP.

5 Model test set-up

Model experiments will be conducted to obtain the natural frequencies of an MP, to validate and improve the numerical model presented, later in Chapter 7. Furthermore, it is convenient to find the forces experienced in the cranetip as well as the damping coefficients, to create a valuable data set that can be used for refining the numerical model. This data will help to gain insight into the relation of the response of the MP, resulting side-lead angles of the crane wire and the influence of buoyancy on the system. The wave tank used for these experiment is located at the faculty of Mechanical Engineering of the TU Delft.

5.1. Purpose of physical modelling

This method of trapped air is a concept of which is thought that it will work offshore but it has never been executed. Relying solely on assumptions and presumptions about the behavior of the MP is not a sufficient basis for executing real offshore operations. By conducting model experiments, valuable data and observations can be obtained that create better insight than every other numerical model could. Model experiments help in understanding the fundamental principles and dynamics of the system, validating theoretical models and gaining insights into its dynamic behavior under different conditions.

Model tests will be done to obtain data of the lead-angles of the crane cable, forces in the cranetip as a result of a swinging MP and buoyancy force. This data will help to gain insight into the relation of the buoyant force, submergence of the MP, frequencies, lead-angles and forces in the cranetip. The overall behavior in roll, pitch an yaw of the MP during this operation will create an understanding of the response of the MP in all degrees of freedom.

5.2. Tank set-up

The towing tank that will be used is towing tank no. 1 and is located at the faculty of 3ME of the TU Delft. The dimensions of the tank is depicted in 5.1. The most important parameters are the waterdepth of the wave tank and the distance between the MSL and the ceiling because they govern the size of the scaled MP. The tank's depth is sufficient for the MP to be unaffected by the influence of the bottom.

Table 5.1: Towing tank No.1 dimensions

Parameter	Value	Unit
Length	142	m
Width	4.22	m
Max. water depth	2.50	m

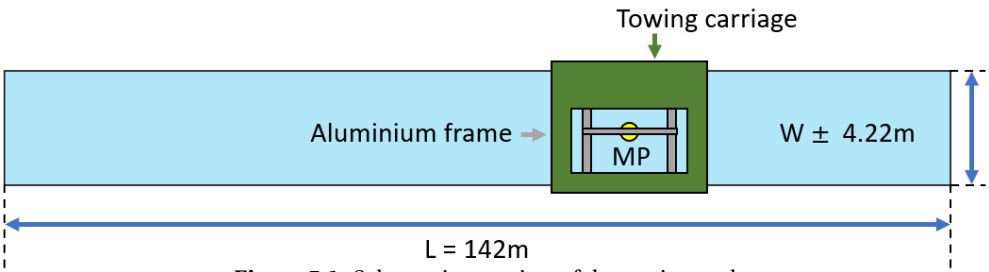

Figure 5.1: Schematic top-view of the towing tank

The wave tank has a width of 4.22m and a length of 142m. It is possible to observe wave reflections resulting from the motions of the MP in the direction of the width of the tank. Nevertheless, due to the significant length of the tank, wave reflections will potentially not affect the behavior of the MP in the first tens of seconds of the runs. This should be taken into consideration when designing the model test set-up.

5.3. Scaling

Before any model scaling can be done, it is important to have a clear understanding of the scaling laws. The real situation should be scaled properly, where three factors are considered most important: geometric, kinematic and dynamic similarity. The typical current/wave-structure interaction situations involve the Reynolds number, Froude number and the Keuligan-Carpenter number, as mentioned in section 2.3. The next section elaborates on the advantages and disadvantages of different scaling methods.

5.3.1. Scaling methods

When conducting model experiments in fluid dynamics, it is important to properly scale the various parameters involved to accurately replicate the behavior and calculate the natural frequencies in full-scale scenario's. Two commonly used scaling methods are Reynolds and Froude scaling, each with its own limitations. Careful consideration of the limitations of each method and appropriate adjustments can help ensure reliable and useful data from model experiments. Scaling factors of important parameters are depicted in table 5.2 and can be used to choose the most convenient method.

Table 5.2: Scaling conversion factors for different scaling methods

Parameter			**Froude scaling**			**Reynolds scaling**		
	Symbol	Unit	Scaling factor	Preferred scale	Scale effect	Scaling factor	Preferred scale	Scale effect
Angles	ϕ	[°]	1	1	1	1	1	1
Length	l_{mp}	[m]	λ^1	λ^1	1	λ^1	λ^1	1
Wave height	H	[m]	λ^1	λ^1	1	λ^1	λ^1	1
Wave period	T	[m s^{-1}]	$\lambda^{0.5}$	$\lambda^{0.5}$	1	λ^2	λ^2	1
Wave length	λ	[m]	λ^1	λ^1	1	λ^1	λ^1	1
Fluid velocity	u_c	[m s^{-1}]	$\lambda^{0.5}$	$\lambda^{0.5}$	1	λ^{-1}	λ^{-1}	1
(Added) Mass	m_i	[kg]	λ^3	λ^3	1	λ^3	λ^3	1
Gravitational forces	F	[N]	λ^3	λ^3	1	1	λ^3	λ^3
Viscous forces	F	[N]	$\lambda^{1.5}$	λ^3	$\lambda^{1.5}$	1	1	1
Pressure forces	F	[N]	λ^3	λ^3	1	λ^3	1	λ^{-3}
Pressure	p	[Pa]	λ^1	λ^1	1	λ^1	λ^1	1
Reynolds nr.	Re	[-]	$\lambda^{1.5}$	1	$\lambda^{-1.5}$	1	1	1
Nat. frequency	ω_n / f_n	[s^{-1}]	$\lambda^{-0.5}$	$\lambda^{-0.5}$	1	$\lambda^{-0.5}$	λ^{-2}	$\lambda^{1.5}$
Nat. Period	T_n	[s]	$\lambda^{0.5}$	$\lambda^{0.5}$	1	$\lambda^{0.5}$	λ^2	$\lambda^{1.5}$

From table 5.2, it can be concluded that Reynolds scaling results in undesired scale effects on the gravitational and pressure forces, which is far from ideal. When dealing with a free water surface or waves, gravitational forces become significant and changing the acceleration of gravity is very difficult, if not impossible. Besides that, this method does not scale the natural frequency properly and can negatively affect the accurate modeling of the behavior of the system. Froude scaling, on the other hand, provides a correct scaling of gravitational forces, inertia and frequencies. However, this scaling method has its limitations when it comes to scaling the Reynolds number and viscous forces. This may not cause major issues since the motion will be primarily driven by inertia and the drag coefficient can be adjusted later on.

In conclusion, the Froude scaling method is chosen as the preferred method. It provides accurate scaling for several important parameters, considered in this research. Despite these limitations, Froude scaling remains a valuable tool in fluid dynamics. Therefore, it is the preferred method for conducting the research and analyzing the system's behavior.

5.3.2. Model scale

The model scale should preferably be as large as possible to minimize the scaling effects. The geometric scaling factor (λ) should be determined. Proper scaling of the MP depends on careful consideration of several important parameters, with the weight being the most critical. In addition to weight, the length and diameter of the MP are also crucial as they impact inertia and viscous forces, respectively. Unfortunately, suitable thin-walled steel pipes of the required size were unavailable. Although PVC could be considered as an alternative, its use would significant justification concerning its inertia and may not guarantee an uniform mass distribution, potentially resulting in inaccurate scaling. Aluminium however, is available in the right diameter and a wall thickness that resulted in (almost) the correct scaled weight and thus a correct scaled inertia of the MP within the limits of ± 5%. A geometric scaling of $\lambda = 56.5$ is chosen to achieve the right diameter of 0.168m for an aluminium pipe with a length of approximately 1.46m. Other parameters are scaled according to this scale factor, as depicted in table 5.3.

It is also important to note the difference in density between seawater and fresh water. Seawater, with a density of approximately 1026 kg m^{-3} at 15°C [5], provides greater buoyancy for floating structures. Fresh water in towing tanks, roughly has a density of around 997 kg m^{-3} at 25°C [5]. Accurately accounting for these density differences is crucial as it directly affects buoyancy, fluid dynamics and the behavior of objects submerged in water.

Table 5.3: Required parameters of full- and model scale

λ = 56.5	Symbol	Scale factor	Full scale	Model scale	Unit
Length MP	l_{mp}	λ^1	82.7	1.464	m
Diameter MP	D_{mp}	λ^1	9.5	0.168	m
Thickness MP	t_{mp}	λ^1	76	1.345	mm
Height of crane tip	$h_{crane\ tip}$	λ^1	153	2.708	m
Mass MP	m_2	λ^3	1480	8.206	t/kg
Mass top-cap (incl. lifting tool)	m_1	λ^3	90	0.499	t/kg
Mass bottom-cap	m_3	λ^3	40	0.222	t/kg
Water depth	h	λ^1	35	0.619	m
Internal water level	h_{int}	λ^1	0 - 30	0 - 0.531	m
Submerged length MP	h_{sub}	λ^1	0 - 30	0 - 0.531	m
Gravitational acceleration	g	1	9.81	9.81	m s^{-2}
Density of sea water	ρ_{sea}/ρ_w	1	1025	1025	kg m^{-3}
Density of fresh water	ρ_{fresh}	1	1000	1000	kg m^{-3}

Scaling of Inertia

Accurately scaling inertia is essential in model experiments as it directly affects the dynamic behavior of the system being modeled. Inertia is a fundamental property of a body and its accurate scaling is crucial for predicting the system's natural frequencies. Section D.1 presents the derivation of the inertia of the scaled model MP. The inertia of the model differs from the desired value by 3.42%. Based on this small difference, it can be concluded that the inertia of the model is accurately scaled.

5.3.3. Monopile

The most important aspect to scale correctly is the MP, for various reasons explained in section 5.3.2. The desired values for important parameters of the scaled model are depicted in table 5.4. The actual values are also presented in the table, indicating the difference with the desired scaled parameters. It should be noted that these values are based on an aluminum pipe with a wall thickness t = 4mm. This results in a difference of almost 67% w.r.t the desired parameter. However, the thickness of the aluminum tube results in a weight of the MP that is significantly close to the desired scaled weight of the MP. Because the weight of the MP has much more influence to the natural frequency than the thickness, it is an accepted difference.

Table 5.4: Desired vs. real parameters MP model scale

Parameter	Symbol	Desired	Scale Model	Unit	Difference
Length MP	l_{mp}	1.4643	1.464	m	-0.02 %
Outer diameter MP	D_o/D_{mp}	0.1681	0.168	m	-0.08 %
Wall thickness MP	t_{mp}	1.345	4.0	mm	197.37 %
Inner diameter MP	D_i	0.165	0.160	m	-3.29 %
Mass aluminum MP	m_2	8.206	8.44	kg	2.85 %
Mass top cap	m_1	0.499	0.166	kg	-201.01 %
Mass bottom cap	m_3	0.222	0.214	kg	-3.63 %
Weight other components*		-	0.22	kg	
Total weight of the MP		8.927	9.04	kg	1.25 %

* Weight of hinges, target plates (holder) and one magnet

It should be noted that that both the analytical and numerical models do not consider an additional length associated with the rotation point between the MP and the H-frame. In practice, the hinges that represent the lifting tool have a length from the bottom to the center of the axis of 15 mm. To accommodate for this discrepancy, the length of the MP is reduced by 15 mm compared to the desired value. Additionally, this reduction in length results in a weight reduction of 0.1 kg, bringing the total weight of the MP closer to the desired value. The mass of the MP is then 8.44 kg, as indicated in table 5.4.

In order to fill of the MP efficiently and ensure control over the internal water level, the top cap was designed as a ring. Additionally, the bottom cap is closed and sealed using adhesive material to ensure a watertight connection. To enable drainage when necessary, a valve is incorporated in the bottom cap. It is important to note that the bottom cap has a thickness of 18 mm and is not accounted for in the computational models. In reality, it scaled to roughly 1 m and is considered a reasonable thickness of the bottom cap. To take thickness into account, the height of the first internal water level is set to 9 meters. This ensures that the water level difference is 0 m with a submergence level of 10 m.

Because of the significant thickness of the bottom cap, the internal diameter of the MP is not accurately scaled, resulting in a smaller volume inside compared to the desired specifications. However, instead of adjusting the mass directly to compensate for this difference, a decision was made to maintain a zero water level difference. Scaling the mass in accordance with the desired parameters would result in an excessively large internal water levels, which could lead to undesired side effects. Instead of scaling the mass directly, the focus is on maintaining a zero water level difference. This approach allows for a simpler adjustment in the numerical model, where the mass can be scaled accordingly. A detailed overview is presented in table D.1. Finally, a yellow protective coating was applied to the model to prevent corrosion caused by its interaction with water, as shown in figure 5.2.

Figure 5.2: Model scale MP

5.3.4. H-frame

The analysis conducted thus far has been limited to a two-dimensional approach. In order to achieve accurate validation of the 2D models, it is crucial to restrict the movement of the MP to the y-direction and impose constraints on its yaw motion. A framework has been constructed to mimic the behavior of the crane cable. This framework is referred to as the H-frame and can be seen in figure 5.3. The main disadvantage is that the frame is relatively heavy (2.84 kg), which introduces an extra mass and inertia term to the system. This needs to be taken into account during the numerical simulation, to accurately model the dynamics of the system.

The connection between the H-frame and the MP is established through the use of two, in-line hinges with a rotating axis. This configuration introduces two degrees of freedom to the system, resulting in a double pendulum effect. In order to simplify the system to a single pendulum, two C-shapes have been designed. These C-shapes are positioned at the bottom of the H-frame to create a rigid connection and eliminate one degree of freedom.

Lastly, the design of the H-frame enables the adjustment of submergence. This is achieved by moving the rotation point between the frame and the MP up and down. The rotation point is depicted as the lowest horizontal brace, along with its hinges, in figure 5.3. By lowering this brace, the submergence increases and the cable length increases, allowing for individual adjustment during each test.

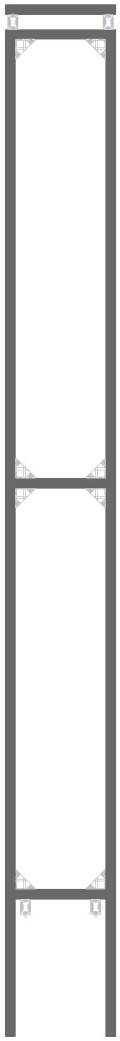

Figure 5.3: H-frame

5.3.5. Support structure

The structure supporting the cranetip is constructed using aluminum profiles. To ensure a rigid construction that minimizes its influence on the test runs, the U-shaped frame is supported with braces positioned at a 45-degree angle. This configuration enhances a high stiffness and structural integrity of the frame during the experiments. Figure D.1 provides a clear illustration of the support structure, cranetip and the MP suspended from its H-frame.

5.3.6. Measurement instruments

The faculty of 3ME had access to a camera tracking system that could directly measure six degrees of freedom, including displacement in the x, y, and z directions, as well as roll, pitch, and yaw angles. The camera tracked black target plates positioned on both the MP and the H-frame to monitor their movements. This system allowed for easy and precise adjustment of the initial angles. The target plates were quite randomly positioned on both the MP and the H-frame, which resulted in a certain offset. Displacements of random points provide limited information about the displacement of the MP itself. Therefore, it is convenient to account for this offset during the post-processing stage.

To facilitate the adjustment of the initial angles for the decay tests, electromagnets were used. These electromagnets were positioned on the U-shaped frame, while their opposing magnets were attached to both the MP and the H-frame. This configuration allowed for precise control and adjustments of the angles between each test run. Additionally, it was controlled via the PC on the towing tank by adjusting the voltage, ensuring that both magnets were released simultaneously.

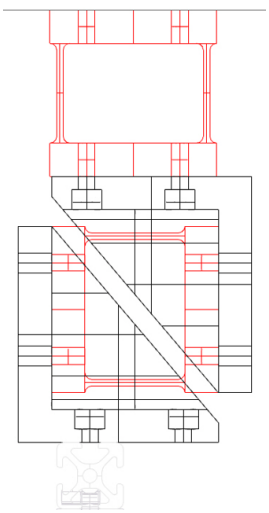

Figure 5.4: The force transducers in the cranetip

To capture and quantify the vertical and horizontal forces exerted at the cranetip, two force transducers were positioned just above this cranetip. These transducers are strategically positioned in a rotated configuration, oriented 90 degrees from each other, as shown in figure 5.4. This configuration allows for compensation of moments and ensures that the transducers exclusively capture forces in the x- and z-direction. The upper force transducer captures the horizontal forces in x-direction and the lower only measures the forces in z direction.

As discussed in section 5.2, the presence of physical boundaries in the towing tank can result in wave reflections, leading to unwanted disturbances in the motion of the MP. In order to capture the fluctuations in the free water surface and accurately measure the wave heights caused by these reflections, a wave height measurement tool has been installed. This tool allows for precise monitoring and analysis of the wave patterns.

Finally, each experiment is recorded using a video camera, capturing the entire test run. These video recordings provide a visual representation of the data obtained during the experiments, allowing for a clearer understanding of the observed phenomena and the behavior of the system. An overview of the measurement tools is depicted in figure D.4 in Appendix D.

5.4. Runs

During the scaled model tests, a series of decay tests were performed to gain insights into the behavior of the MP. These decay tests aimed to examine the dynamic response in six degrees of freedom of the model under different circumstances. In this section, a detailed explanation of these decay tests will be provided.The following parameters will be measured during the model tests:

1. **Side-lead angle** - ϕ_1
   This parameter will be measured to determine the angle at which the cable deviates from the vertical axis in the x-z-plane.
2. **Inclination angle** - ϕ_2
   This parameter will be measured to determine the angle at which the MP deviates from the vertical axis in the x-z-plane.
3. **Displacements of the MP in x-, y- and z-direction**
   The MP's displacements in the horizontal plane (x- and y-direction) as well as in the vertical z-direction will be measured to assess its movements and responses.
4. **Forces F_x and F_z in the cranetip**
   The forces acting at the cranetip in the x- and z-directions will be measured to assess the dynamic loads experienced by the crane cable. Measuring the force in the z-direction will provide valuable insights into the impact of buoyancy on the system. The side-lead force, in the x-direction, will create a better understanding of the lateral forces exerted on the cable as the angle ϕ_1 increases and can be used to quantify the side-lead load in the cranetip. It also provides a quantification to the load limits experienced in the cranetip.

The natural frequencies obtained during the natural frequency assessment in Chapter 3 can be validated by decay tests. These tests can be divided into three categories: a single pendulum in-line, a double pendulum in-line and a double pendulum out-line system. It should be noted that all tests will be performed for different internal water levels (h_{int}) and submerged lengths of the MP (h_{sub}). The following tests will be performed and are visualized in figure 5.5, where ϕ_1 and ϕ_2 are given an initial value.
In order to obtain the desired output data, the following decay tests are executed:

1. **Single pendulum** - In-line mode
   (a) Extreme initial angle ϕ_1
      - $\phi_1 = 15°$
2. **Double Pendulum** - In-line mode (ϕ_1 and ϕ_2 both positively defined)
   (a) Extreme initial angles ϕ_1 and ϕ_2
      - $\phi_1 = 10°$ and $\phi_2 = 15°$
   (b) Small initial angles ϕ_1 and ϕ_2
      - $\phi_1 = 5°$ and $\phi_2 = 5°$
3. **Double Pendulum** - Out of line mode (positive ϕ_1 and negative ϕ_2)
   (a) Extreme initial angles ϕ_1 and ϕ_2
      - $\phi_1 = 10°$ and $\phi_2 = -15°$
   (b) Small initial angles ϕ_1 and ϕ_2
      - $\phi_1 = 5°$ and $\phi_2 = -5°$

To ensure the reliability of the results, three iterations are performed for almost every test. Given that the viscous damping is rather high, the initial tests are conducted with larger angles to capture any significant effects. Subsequently, the tests are repeated with the smaller initial angles to validate the consistency and reliability of the obtained data. This approach ensures a thorough analysis of the system's behavior across

different test scenarios. Before each test run, two zero measurements were performed to establish a baseline for the specific run.

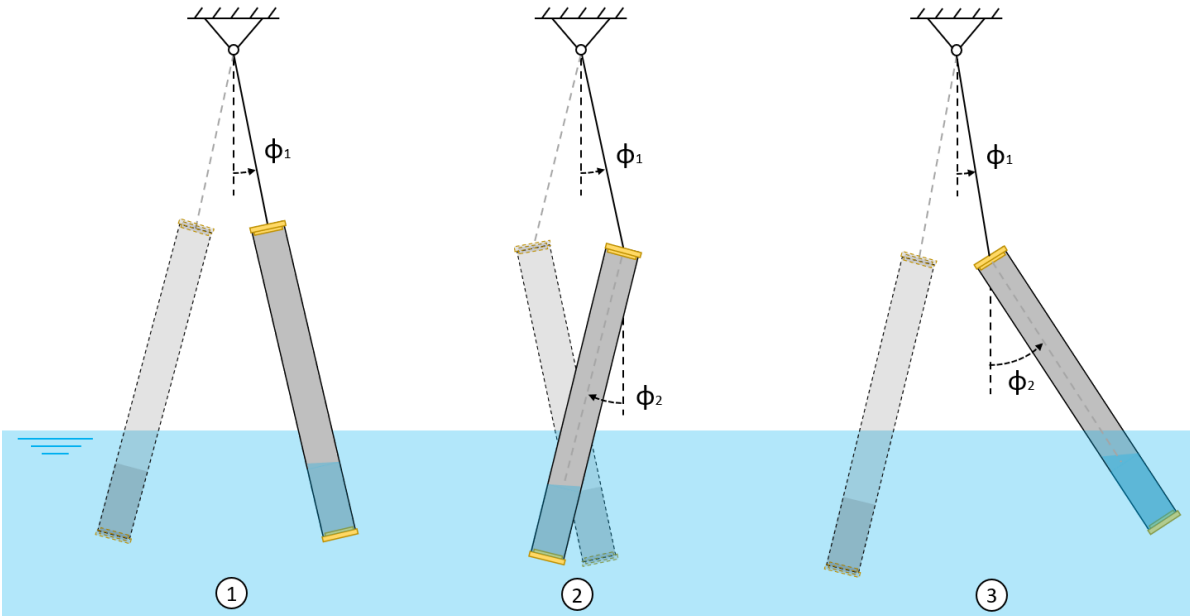

Figure 5.5: Sketch of the decay tests 1. S.P. In-line mode 2. D.P. Out of phase mode 3. D.P. In-phase mode

The single pendulum decay tests are performed to identify the damping coefficient of a system with one single degree of freedom. The double pendulum decay tests will also result in a damping term which is needed to define the linear damping term in the numerical model. For all decay tests, certain initial angles, ϕ_1 and , ϕ_2 are given to the MP w.r.t. to the vertical while being submerged at a certain water depth. The starting inclination angle is kept the same in every step of these decay tests. Because of this starting angle, the MP is left to swing freely in still water.

6

Model test results

To ensure the reliability of the data, three iterations per test are performed. This approach provides a more robust dataset, increasing confidence in the observed trends and patterns and ensuring that the conclusions drawn from the experiments are more reliable and accurate. Moreover, it allows for the detection of any inconsistencies or discrepancies that may arise during the experiments.

The natural frequencies of the analytical model developed in Chapter 3 will be verified using scaled decay tests. During the test, the MP is submerged at specific water depths and starting angles. The starting angle remains consistent across all tests before the MP is released to swing freely. The natural frequency of the system is affected by the still water both inside and around the MP, as it adds mass and inertia to the system.

6.1. Single pendulum

The single pendulum system was subjected to a series of tests to evaluate its behavior under various scenarios. A test matrix, as shown in figure 6.1, outlines the nine different test scenarios that were conducted. Each test run was performed three times, resulting in a total of 27 tests. As mentioned earlier, all the tests within this series focused on a specific set of initial angles, $\phi_{1,2} = 15°$. By keeping the initial angles consistent across the tests, it becomes possible to compare and analyze the system's response and behavior under different conditions. The single pendulum tests are performed to create a first insight in the natural frequency and damping behavior of a simple pendulum system.

S.P. test matrix			Internal water level h_{int} [m]					
	Full scale		0	10	20	30		
		Model scale	0	0.177	0.354	0.531	Iterations	Totals
Submerged length MP h_{sub} [m]	0	0.00	x				3	3
	10	0.177	x	x			3	6
	20	0.354	x	x	x		3	9
	30	0.531		x	x	x	3	9
							Totals:	27

Figure 6.1: Test matrix of single pendulum system

The single pendulum decay response of the pitch angle can be found in the figures E.1 - E.8. The presence of water in the system leads to a significantly more damped signal. Although the initial angle remains the same for each run, it is evident that the decay rate of the amplitude is considerably higher when the MP is influenced by hydrodynamic effects. Furthermore, it can be observed that an increase in buoyancy force, in combination with the added mass, significantly affects the natural period of the system. The pitch angle response in figure E.2 exhibits a longer natural period compared to the signal in figure E.1, indicating a slower oscillation. This behavior is a direct result of the increased buoyancy force, added mass and their influence on the system dynamics.

Damping

The initial decay test was conducted in the absence of water, both inside and outside the MP. This allowed for the observation of the system's behavior under purely dry conditions. By examining the decay response in air, valuable insights can be gained into the inherent damping characteristics of the system. Figure 6.2 illustrates the decay response of the single pendulum system in air. The response is represented by a decaying sinusoidal function, where the peaks of the oscillations can be identified.

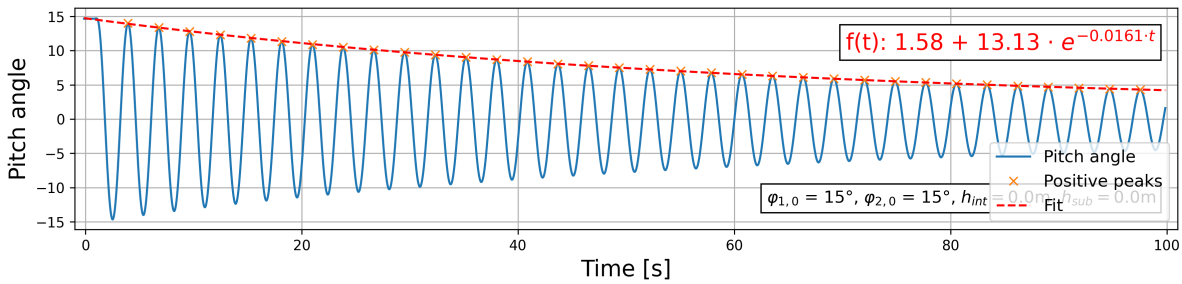

Figure 6.2: SP Decay with damping curve fit for h(0, 0) Run 17

One method to obtain the damping ratio involves curve-fitting the measured peaks of the decaying signal, depicted by the dashed line in the figure. This decay envelope of an underdamped system can be described by $\phi_a e^{-\nu t}$. A detailed derivation can be found in Appendix F. The Ordinary differential equation (ODE) for a decaying angular motion for a cylinder in still water is defined as:

$$(m+a)\ddot{\phi} + b\dot{\phi} + c\phi = 0 \quad \rightarrow \quad \mathrm{kg\,m^2} \cdot \frac{\mathrm{rad}}{s^2} + b \cdot \frac{\mathrm{rad}}{s} + c \cdot \mathrm{rad} = 0 \tag{6.1}$$

The damping coefficient b is characterized by the unit $\mathrm{kg\,m^2\,s^{-1}}$, while the restoring coefficient c is denoted in terms of $\mathrm{kg\,m^2\,s^{-2}}$. It is assumed that the oscillatory motion is an angular harmonic motion with a general solution in a complex notation, $e^{i\omega t}$. Substituting this formulation in equation 6.1 leads to the following expression:

$$\left(-(m+a)\omega^2 + ib\omega + c\right)\phi_a e^{i\omega t} = 0 \quad \rightarrow \quad \omega^2 - \frac{ib\omega}{m+a} - \frac{c}{m+a} = 0$$

where m represents the mass, a denotes the hydrodynamic added mass component, b represents the damping coefficient and c is the restoring spring coefficient of the system. Solving it for ω results in the values for the decay rate, which subsequently leads to the determination of the damping coefficients. The full derivation can be found in Appendix F. The following formulations for the damping ratio ν and the natural frequency ω_0 are found:

$$(1) \quad \nu = \frac{b}{2(m+a)} \qquad \text{and} \qquad (2) \quad \omega_0 \approx \sqrt{\frac{c}{m+a}} \tag{6.2}$$

The damping ratio for each test run is shown in figure 6.3. It is important to note that in each figure illustrating the damping parameters or frequencies, the test run is plotted against the internal water level (h_{int}) and submergence level (h_{sub}) on the horizontal axis. For convenience of writing, the values of these water levels are represented using the full-scale values, where (f.e.) a full scale value of (10, 20) corresponds to an internal water level of 0.177 meters and 0.354 meters of submergence on model scale. From this point onward, these configurations will be referred to as 'h-configurations'. The blue areas in the figures correspond to the configurations where a water level difference is present, indicating the configurations with an imposed buoyancy force. The values shown in this chapter represent the results of the model scale experiments.

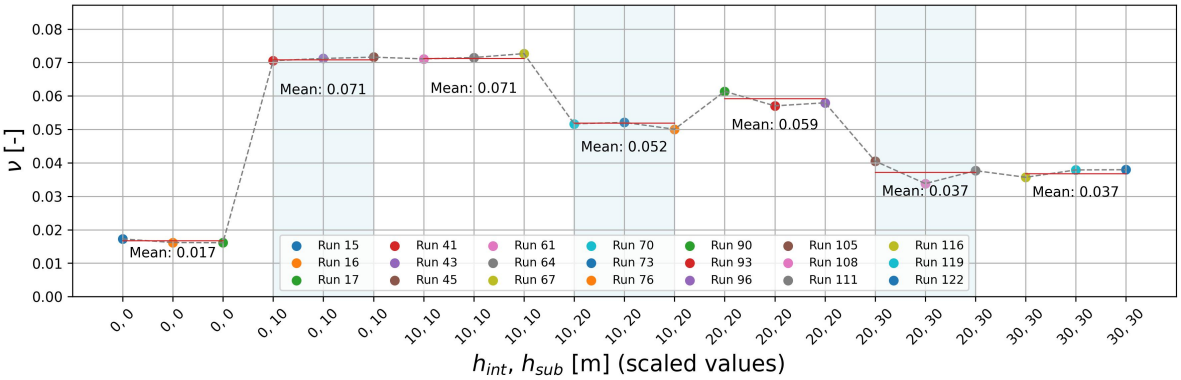

Figure 6.3: Damping ratio ν for each test run for a single pendulum system

It is worth noting that the damping ratios for configurations with equal submergence are nearly identical. This observation becomes evident when examining the figures in Appendix F, as these signals exhibit a similar decaying nature. From equation 6.3 for the damping ratio ν, the damping coefficient b can be derived and will be used in Chapter 7 when defining the damping parameters for the numerical model.

$$b = 2\nu(m + a) \tag{6.3}$$

In the remaining tests, the MP was subjected to an initial inclination angle of 15° while being submerged at various water levels. Additionally, different internal water levels were introduced to the MP. The detailed results of signals with damping can be found in Appendix F.1.

6.2. Buoyancy

After completing the single pendulum tests, the experimental set-up was reconfigured to prepare it for the double pendulum test series. The configuration of the double pendulum system contains two degrees of freedom associated with the angles ϕ_1 and ϕ_2.

As the test matrix for the single pendulum system already states, a total of 27 tests were performed. The initial plan was to test the same configurations of h_{int} and h_{sub} for the double pendulum system. However, during the testing of an h-configuration of (0, 20), it was observed that the MP started to deviate from its equilibrium position much earlier than anticipated. This deviation from equilibrium, which was observed during the exploratory tests, discussed in Chapter 4, was referred to as the 'searching phenomenon.'

In order to investigate this phenomenon, additional tests are conducted by manually lowering the MP. The objective is to determine the point at which the submergence becomes significant enough for the buoyancy force to exceed the downward weight of the MP, causing it to drift away from its original position. This is exactly what can be observed from the figures 6.4 and 6.5. These figures depict the x-displacement and corresponding z-displacement of the bottom of MP over time. In both runs, the same experiment is conducted with the same parameters.

As the MP is gradually lowered, the submergence level h_{sub} increases over time, resulting in a corresponding negative increase in the z-coordinate, shown between the green lines in the figures. The sudden increase in the z-coordinate observed in the graph together with the increase of the x-coordinate, indicates that the MP is deviating from its equilibrium position. This phenomenon is shown between the red lines in both figures. This z-coordinate represents the maximum submergence achievable when there is no water inside the MP. It indicates the depth to which the MP can be lowered into the water while maintaining its equilibrium position and not drifting away. Note that the MP was already at a submergence level of h_{sub} = 0.177m at the start of these tests. The rebound that is observed between the red lines of the signal, is caused by the MP drifting in a positive x-direction and subsequently bouncing back and forth. This motion leads to an increase in the z-coordinate and a decrease in the x-coordinate of the MP.

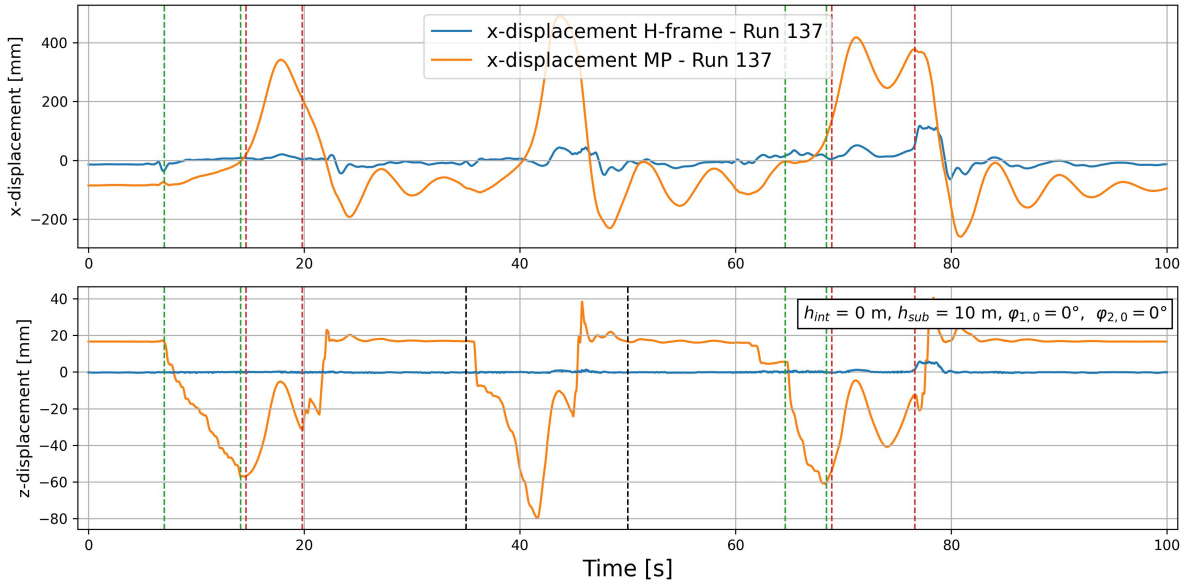

Figure 6.4: x- and z-displacement vs. time when lowering the MP for $h_{\text{int}} = 0$ (Run 137)

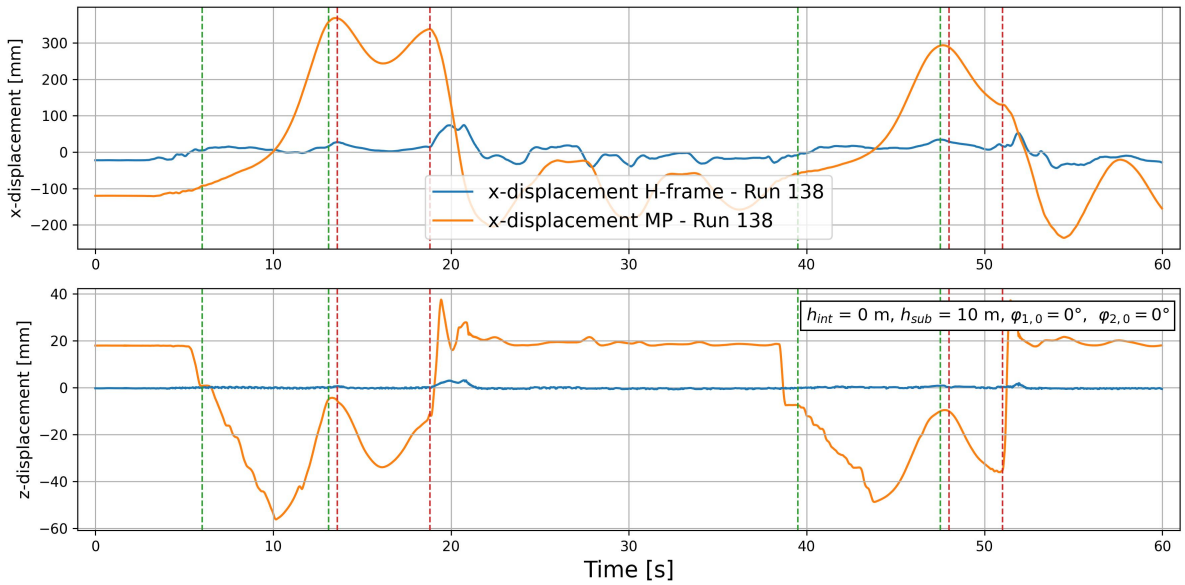

Figure 6.5: x- and z-displacement vs. time when lowering the MP for $h_{\text{int}} = 0$ (Run 138)

It is important to consider that the slope of the z-displacement should ideally be around 45° to ensure the accuracy of determining the maximum submergence. This criterion ensures that the MP is lowered at an appropriate rate, preventing the negative z-coordinate from becoming too large, too quickly. It is therefore wise to exclude the negative peak between the black lines in figure 6.4 when determining the maximum submergence. From the other four peaks in both graphs, the mean z-coordinate for maximum submergence can be determined by taken the average:

$$18 + \frac{57 + 61 + 56 + 44}{4} \approx 73 \qquad \text{[mm]} \qquad (6.4)$$

This average is an absolute value because it represents the displacement of the target plate on the MP. However, it is representative to determine the maximum submergence based on the average displacement of 73 mm. With a scale factor of $\lambda = 56.5$, this value translates to approximately X m. Considering the (scaled) 10 meters of submergence the test started with, the maximum submergence before reaching instability is roughly X meters.

The analytical model presented in Chapter 3 assumed a perfectly vertical alignment, where the MP never deviates from its equilibrium position. However, in reality, even a slight inclination can cause the MP to start drifting away when the forces are in equilibrium and create a moment around the the rotation point. Figure 6.5 illustrates the relationship between the forces and the resulting moment. The following set of equations should give more clarity to which amount.

$$X_{\text{cog}} = L_{\text{cog}} \cdot \sin\phi_2$$
$$X_b = L_b \cdot \sin\phi_2$$

The moment equilibrium visualized in figure 6.6 then becomes:

$$F_g \cdot X_{\text{cog}} = F_b \cdot X_b$$
$$F_g \cdot L_{\text{cog}} \cdot \sin\phi_2 = F_b \cdot L_b \cdot \sin\phi_2$$
$$F_g \cdot L_{\text{cog}} = F_b \cdot L_b$$

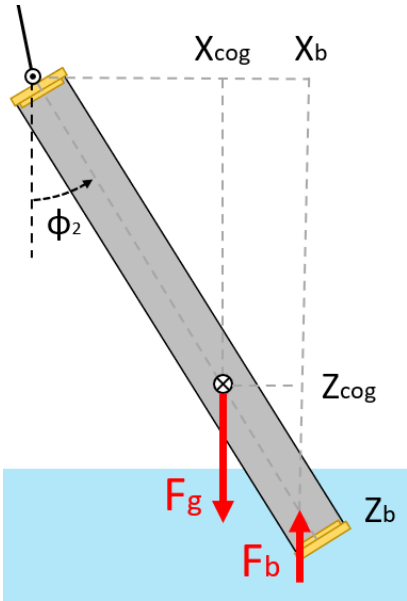

Figure 6.6: Visualization of generated moment around the pivot point

The distance from the pivot point to the center of gravity of the MP (L_{cog}) is approximated and denoted as $5/8 \cdot l_{mp}$. Additionally, for a submergence level of 10 meters, the distance from the pivot point to the point where the buoyancy force is applied (L_b) is taken as $15/16 \cdot l_{mp}$. This approximation is made based on the assumption that l_{mp} is approximately 80 meters, and the point of application is at $h_{\text{sub}}/2$.

$$F_g \cdot \frac{5}{8} l_{mp} \approx F_b \cdot \frac{15}{16} l_{mp}$$
$$F_g \cdot \frac{2}{3} \approx F_b \tag{6.5}$$

When the buoyancy force is larger than the gravitational forces in the system, a moment is generated and causes the MP to rotate or deviate from its equilibrium position. From equation 6.5, it can be concluded that the buoyancy force F_b needs to be roughly 66.7 % of the gravitational forces to induce instability in the double pendulum system. To check this conclusion, table 6.1 provides the real and scaled values for the buoyancy, where the submergence of 10m is provided as reference. Please note that the aforementioned observations are based on a simplified approximation, intended to clarify the underlying principle.

Table 6.1: Buoyancy requirements for the maximum submergence

	ρ_w [kg m^{-3}]	Mass [t/kg]	D_{mp} [m]	h_{sub} [m]	F_b [kN]	F_g [kN]	F_b/F_g
Real	1026	1610	9.5	10*	7134	15794	45.2%
Scaled	997	9.04	0.168	0.177*	38.4	88.7	43.3%
Real	1026	1610	9.5	X**	X	15794	X %
Scaled	997	9.04	0.168	X**	X	88.7	X %

* Stable situation ** Submergence level when deviation from equilibrium is initiated

Based on these calculations, it has been determined that with a maximum submergence of X meters, the buoyancy force corresponds to approximately X % of the gravitational force, instead of the initially estimated 66.7%. This difference is the results of the previous length approximations. However, it can concluded that the buoyancy force F_b needs to be roughly between X - Y% of the gravitational forces to initiate instability in the system. Specifically for this MP, it means that the water level difference between the in- and outside of the MP, should not exceed X meters when the MP is in a vertical position. This limitation is based on the consideration of the tension in the crane cable and its impact on the stability of the system. By ensuring that the water level difference remains below this threshold, the MP can maintain its equilibrium and avoid drifting or instability.

6.3. Double pendulum - In-line mode

The initial runs of the double pendulum system focused on testing configurations that induce the inline mode. Similar to the double pendulum in-line mode, a series of tests is conducted following the same procedure. The test matrix in figure 6.8 presents an overview of which tests are conducted. It is important to mention that the test matrix excludes configurations with a water level difference of 20 meters. This decision was based on the findings discussed in section 6.2, which indicated that the buoyancy forces becomes to large under this condition. Therefore, the h-configurations (0, 20) and (10, 30) are considered infeasible for testing and thus excluded from the test plan.

Each test configuration was executed three times, resulting in a total of 21 tests. All experiments in this series maintained a constant initial angle configuration of $\phi_1 = 10°$ and $\phi_2 = 15°$. This consistent choice of initial angles enables effective comparison and analysis of the system's response and dynamics across different test scenarios.

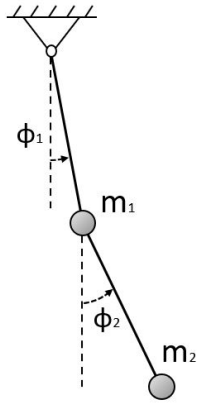

Figure 6.7: In-line mode

D.P. In-line test matrix			Internal water level h_{int} [m]					
	Full scale		0	10	20	30		
		Model scale	0	0.177	0.354	0.531	Iterations	Totals
Submerged length MP h_{sub} [m]	0	0.00	x				3	3
	10	0.177	x	x			3	6
	20	0.354		x	x		3	6
	30	0.531			x	x	3	6
							Totals:	21

Figure 6.8: Test matrix of double pendulum system initial In-line mode

Pitch angle

When the system is examined in dry conditions, figure 6.9 demonstrates that it behaves almost like a single pendulum. The dominant mode is the low-frequency mode and the signal does not exhibit significant damping.

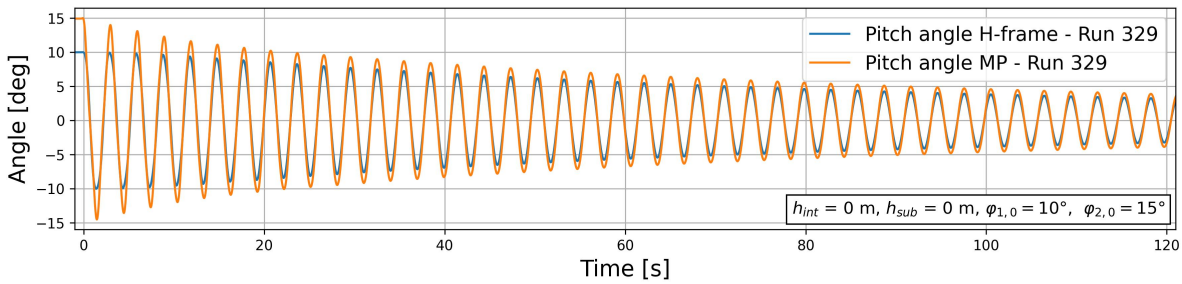

Figure 6.9: Test run - Pitch angle for $h(0,0)$ (Run 329)

Figure 6.10 presents the behavior of the system with an internal water column of 10m and a submerged length of 20m. It is evident that the damping is significant and the hydrodynamic effects cause the system to exhibit more dominant oscillations in both modes. This observation is further supported by the Fast Fourier Transform (FFT) of figure 6.11, which reveals the increased prominence of both frequency components.

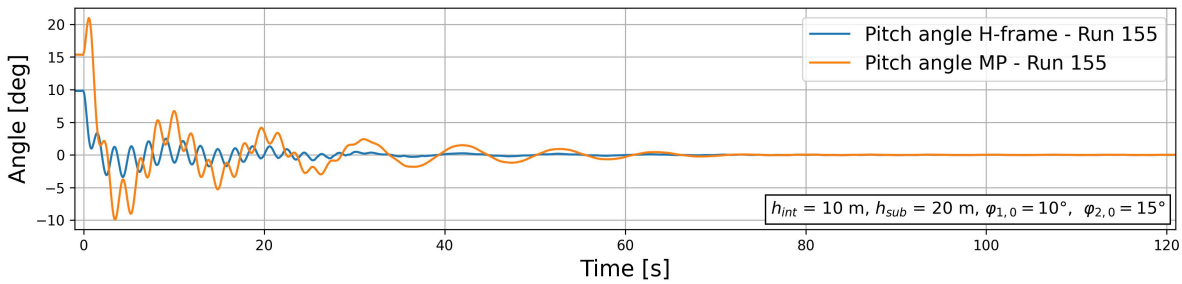

Figure 6.10: Test run - Pitch angle for $h(10,20)$ (Run 155)

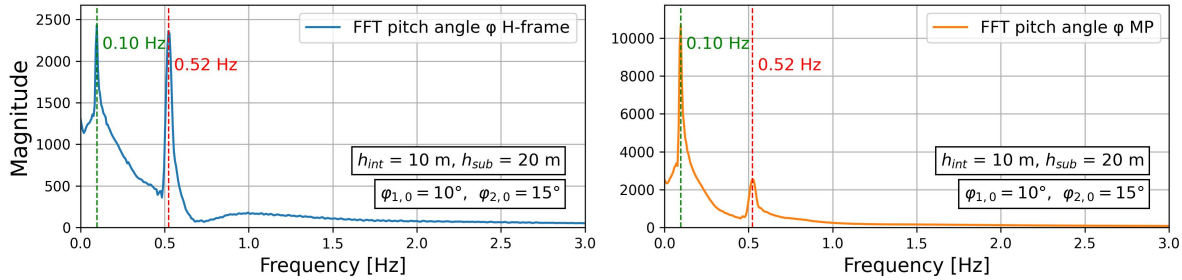

Figure 6.11: Test run - FFT for pitch motion for $h(0,0)$ (Run 329)

The results of the pitch response and frequencies for the other configurations can be found in Section E.2. However, due to the dominant presence of the high-frequency mode in these experiments and the high probability of this mode being excited offshore, further analysis will be conducted on the double pendulum out-line, high-frequency mode.

6.4. Double pendulum - Out of line mode

The out of line mode is illustrated in figure 6.12. Similar to the double pendulum in-line mode, a series of tests is conducted following the same procedure.

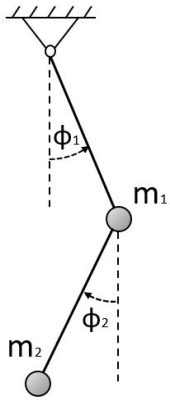

Figure 6.12: Out of line mode

Pitch angle

The most important parameter that has been measured is the pitch angle of the H-frame, together with the pitch angle of the MP. The angle ϕ_1 corresponds to the side-lead angle at the cranetip. To find the influence of the buoyancy on the system, the configuration $h(0,10)$ and $h(10,10)$ are shown in figures 6.13 and 6.14 respectively. The signal demonstrates a well-damped sinusoidal function, in accordance with the expected behavior. The presence of the high frequency mode is clear due to the initial angles being in opposite directions. Subsequently, the system gradually transitions to the first low-frequency mode and then the oscillations quickly dissipate due to the damping in the system.

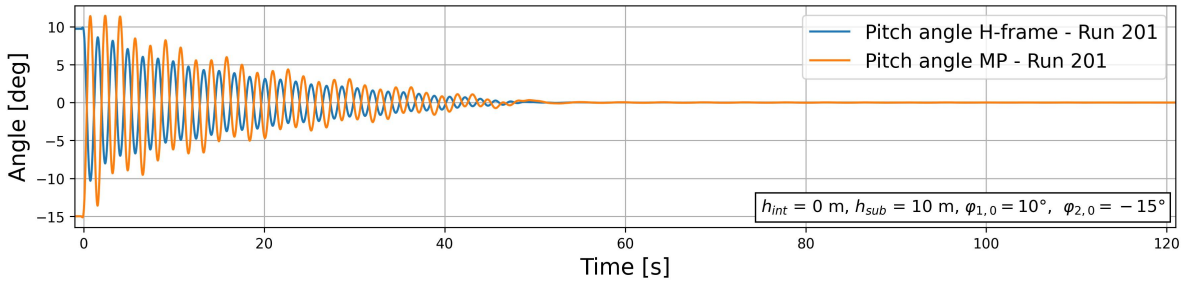

Figure 6.13: Pitch angle of DP decay test for $h(0,10)$

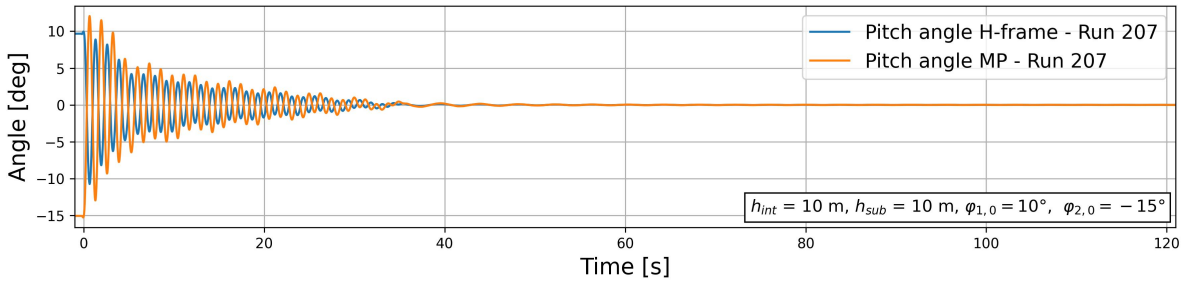

Figure 6.14: Pitch angle of DP decay test for $h(10,10)$

As observed, the configuration h(10, 10) shows a significantly more damped response. The next section will provide further details on the damping characteristics.

Damping

The initial double pendulum decay test was conducted in the absence of water, both inside and outside the MP. Figure 6.15 illustrates the decaying response.

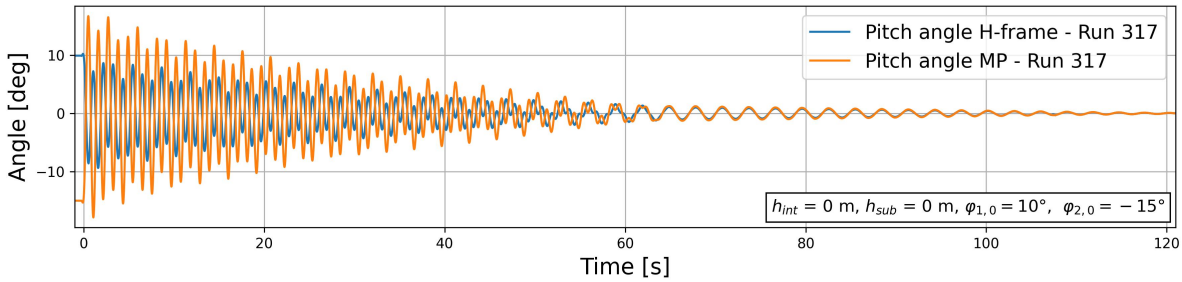

Figure 6.15: Pitch angle of DP decay test in air for $h(0,0)$ (Run 317)

The plot in figure 6.15 displays two degrees of freedom and thus two signals. Before identifying the peaks of those signals, it is necessary to separate the response of the H-frame from that of the MP. Figure 6.16 depicts pitch response of the H-frame, including the decaying fitted line. It is important to mention that the fit being used is intended for linear signals. However, as clearly seen in the figures, the signals exhibit strong non-linear behavior. Consequently, it should be kept in mind that the application of this particular method may not yield accurate results due to the non-linear interaction of the signals. The rest of the linear figures that depict the damping behavior are presented in Appendix F.2

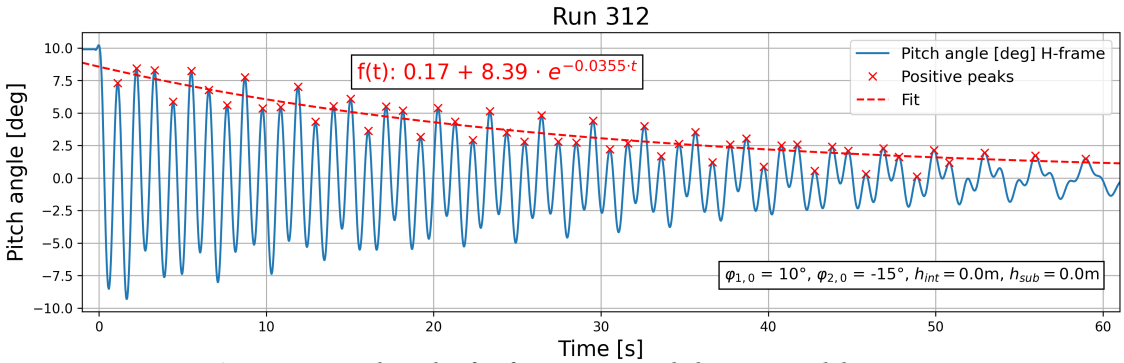

Figure 6.16: Pitch angle of H-frame in air, peak detection and damping

Similar to the determination of damping in the single pendulum system, the damping ratio ν is estimated by fitting a decay envelope to the peaks of the signal. In the case of the double pendulum, separate damping coefficients ν_{Hframe} and ν_{mp} can be identified, corresponding to the decaying signals of the H-frame and MP, respectively. Figure 6.17 displays the damping coefficients for each run. The trend appears to be regular, except for the configurations $h(10,10)$ and $h(20,30)$, where the damping coefficient is significantly higher compared to the other configurations, which is remarkable. The decaying signal for these configurations are presented in figures F.6 - F.11. These test results confirm the the higher damping coefficients because of the high decay rate of the amplitude of the signals. Note that a high decay rate does not necessarily results in a high damping coefficient as that also depends on inertia. Furthermore, the results and thus the variations in the damping coefficients, make it challenging to establish a clear relationship between the decay rate of the signal and the buoyancy force. The presented figures do not provide direct insight into this relationship.

As said earlier, the logarithmic decrement method is typically applied to signals with linear damping, as it assumes an exponential decay of the signal. This assumption may not hold for signals with nonlinear interactions, as they can exhibit complex and irregular behavior. It is therefore important to note that the accuracy and validity of the results obtained from applying the logarithmic decrement method to these signals may be limited but it still can serve as a first approximation for the damping coefficients.

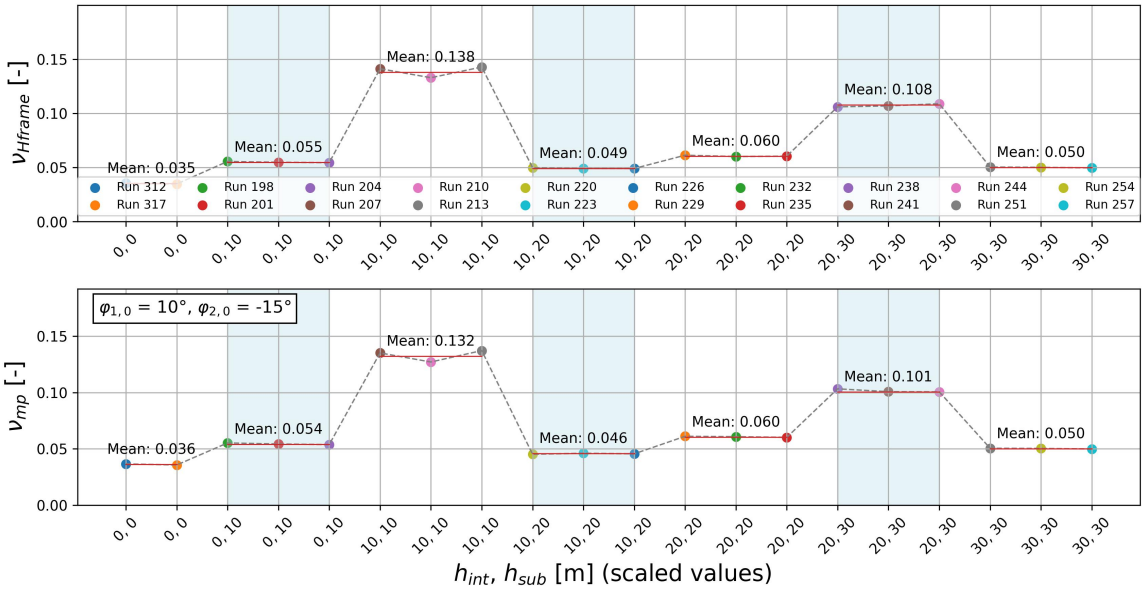

Figure 6.17: Damping ratio ν_{Hframe} and ν_{mp} for each test run for a double pendulum system out-line

The damped period of the signal can be determined by averaging a series of periods corresponding to the number of peaks (n) of the signal, which is set to n = 10 for this double pendulum inline signal.

$$(1) \quad T_d = \frac{T_n - T_0}{n} \quad , \quad (2) \quad \omega_d = \frac{2 \cdot \pi}{T_d} \quad \text{and} \quad (3) \quad \omega_d = \omega_n \sqrt{1 - \nu^2} \tag{6.6}$$

Additionally, both the H-frame and the MP exhibit slightly longer oscillation periods when subjected to buoyancy. The variations in oscillation periods and frequencies across the runs are depicted in figures 6.18 and 6.19, respectively. The presence of damping in the system lowers the natural frequency by a factor of $\sqrt{1-\nu^2}$, as indicated by equation 6.6 (3). The highest damping ratio observed in the system is approximately $\nu \approx 0.138$, which was measured at a submergence depth of 10 meters. The maximum factor that lowers the natural frequency is therefore ($\sqrt{1-(0.138)^2} = 0.99$), close to one. This decrease in natural period due to the damping, can potentially make a difference when comparing the frequency content of the test runs and numerical approximations.

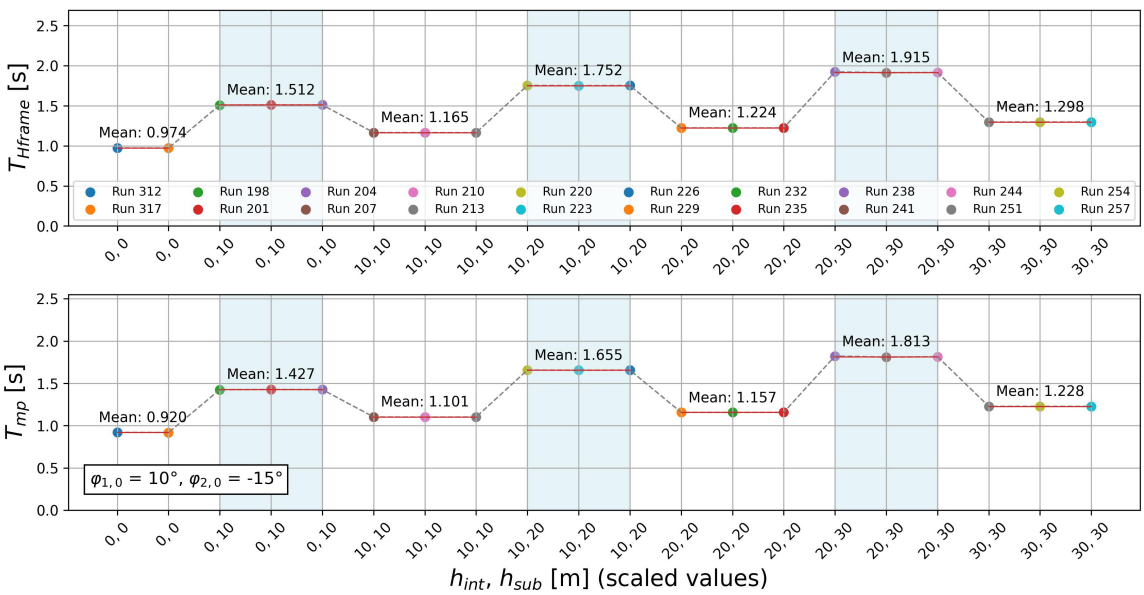

Figure 6.18: Natural period T_{Hframe} and T_{mp} for each test run for a double pendulum system out-line

An increasing oscillation period T with an increased buoyancy in the system, can be explained by considering the underlying mathematics of the system. Revisiting the definition of ω in equation 3.16 and redefining it for a compound pendulum results in equation 6.7, in which the natural period depends on its moment of inertia I_{DP}.

$$T = 2\pi\sqrt{\frac{L}{g}} \qquad = 2\pi\sqrt{\frac{mL^2}{mgd}} \qquad = 2\pi\sqrt{\frac{I_{DP}}{mgd}} \tag{6.7}$$

where m is the mass of the object, g is the gravitational acceleration and d is the distance from the pivot point to the center of mass of the object. When the buoyancy is increased, the added mass increases because of the larger submergence. The inertia of added mass increases as well and from the relation in equation 6.7, the oscillation period increases. The relationship between submergence and oscillation frequency is inverse: an increase in submergence and thus inertia, results in a decrease in the natural frequency.

$$\omega = \sqrt{\frac{g}{L}} \qquad = \sqrt{\frac{mgd}{mL^2}} \qquad = \sqrt{\frac{mgd}{I_{DP}}} \tag{6.8}$$

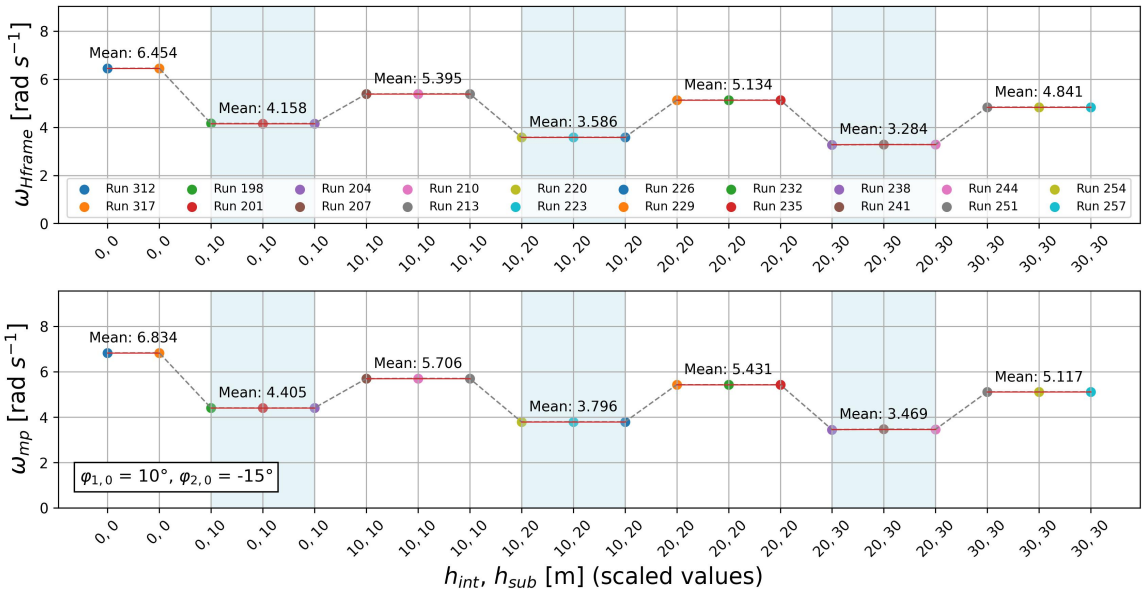

Figure 6.19: Natural frequency ω_{Hframe} and ω_{mp} for each test run for a double pendulum system out-line

Not only does inertia play a role in the variation of oscillation periods, but the buoyancy force also has a significant impact. As previously stated in the analytical analysis, the buoyancy force and the natural period are positively related. The model test results presented in this section further confirm these early findings outlined in Chapter 3.

6.4.1. Frequency analysis

By performing a Fast Fourier Transform (FFT) on the signals, the distribution and characteristics of different frequencies present in the signal can be analyzed. The Fourier analysis on the pitch signal without hydrodynamics effects is considered. Figure 6.20 presents two prominent peaks in both the signal for the H-frame and the signal of the MP. The first peak observed in the frequency spectrum corresponds to a low-frequency mode with a frequency of approximately 0.34 Hz. This mode represents the oscillatory behavior of the system with a longer period. The second peak corresponds to a higher frequency mode at around 0.96 Hz, indicating a faster oscillation within the system. The presence of multiple peaks suggests the existence of multiple modes in the system, each with its own characteristic frequency.

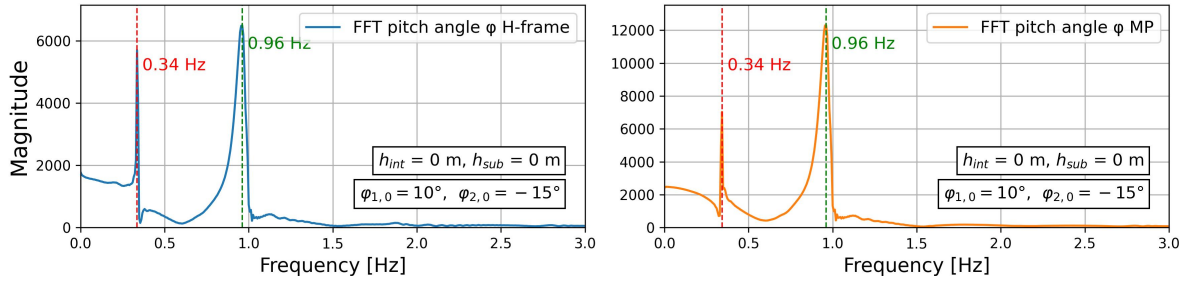

Figure 6.20: FFT for pitch motion for $h(0,0)$, extreme angles (Run 317)

To validate the frequencies obtained through the analytical approach in Chapter 3, they can be compared with the frequencies derived from the model experiments. Prior to comparison, the model frequencies need to be scaled to full scale using the scale factor $\lambda = 56.5$. As indicated in table 5.2, the frequency scaling is carried out according to the following relation:

$$f_{\text{real}} = f_{\text{model}} \cdot \lambda^{-0.5} \tag{6.9}$$

The natural frequencies for each configuration obtained with both approaches are presented in tables 6.2 and 6.3, for mode 1 and 2 respectively. The model frequencies are highlighted in grey in order to clearly indicate the difference between the model-scale and full-scale frequencies.

Table 6.2: Analytical model results vs. Model test results - Frequencies **Mode 1**

Configuration	**Analytical model** f_{real} [Hz]	**Model test results** f_{model} [Hz]	f_{real}* [Hz]	**Difference** [%]
$h(0,0)$	0.046	0.335	0.045	3%
$h(0,10)$	0.015	0.150	0.020	-25%
$h(10,10)$	0.027	0.219	0.029	-7%
$h(10,20)$	0.013	0.103	0.014	-5%
$h(20,20)$	0.021	0.165	0.022	-4%
$h(20,30)$	0.012	0.090	0.012	0%
$h(30,30)$	0.018	0.135	0.018	0%

* Model test frequency scaled using eq. 6.9

Table 6.3: Analytical model results vs. Model test results - Frequencies **Mode 2**

Configuration	**Analytical model** f_{real} [Hz]	**Model test results** f_{model} [Hz]	f_{real}* [Hz]	**Difference** [%]
$h(0,0)$	0.153	0.961	0.128	20%
$h(0,10)$	0.077	0.594	0.079	-3%
$h(10,10)$	0.124	0.781	0.104	19%
$h(10,20)$	0.075	0.516	0.069	9%
$h(20,20)$	0.118	0.742	0.099	20%
$h(20,30)$	0.074	0.477	0.063	17%
$h(30,30)$	0.112	0.716	0.095	18%

* Model test frequency scaled using eq. 6.9

From both tables, it is evident that the presence of buoyancy in the system results in lower natural frequencies. When comparing the analytical model with the model experiments, it can be observed that the calculated frequencies are quite accurate. Based on the results of the model experiments, it can be concluded that the analytical approach for determining the equations of motion was correct.

Forces in the cranetip

The forces acting at the cranetip can be characterized as F_x and F_z, representing the side-lead force and the vertical downward force, respectively. During each test, the forces F_x and F_z at the cranetip are measured and can be plotted over time. Figure 6.22 displays the direction of the forces, F_x and F_z, for the configuration $h(0,10)$. The measured forces in each iteration align perfectly, providing a high level of confidence in the accuracy of the force measurements.

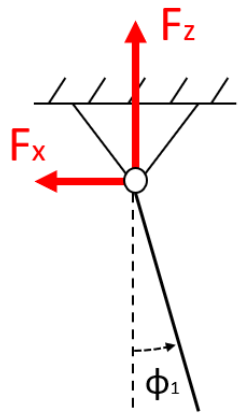

Figure 6.21: Definition of F_x and F_z

For ease of reference, table 6.4 presents the weights of different parameters that are suspended from the cranetip. The table includes the mass and corresponding weight in newtons for each parameter.

Table 6.4: Weights of different parameters suspended from the cranetip

Parameter	Mass [kg]	Weight [N]
Monopile	9.04	88.68
H-frame	2.84	27.86
Total suspended	11.88	116.54

Section E.3.2 provides a verification of the additional mass of the water column. The amount of mass added to the system determines the magnitude of the resulting upward buoyancy force. The conclusion drawn from this verification is that the water column was accurately included in the system.

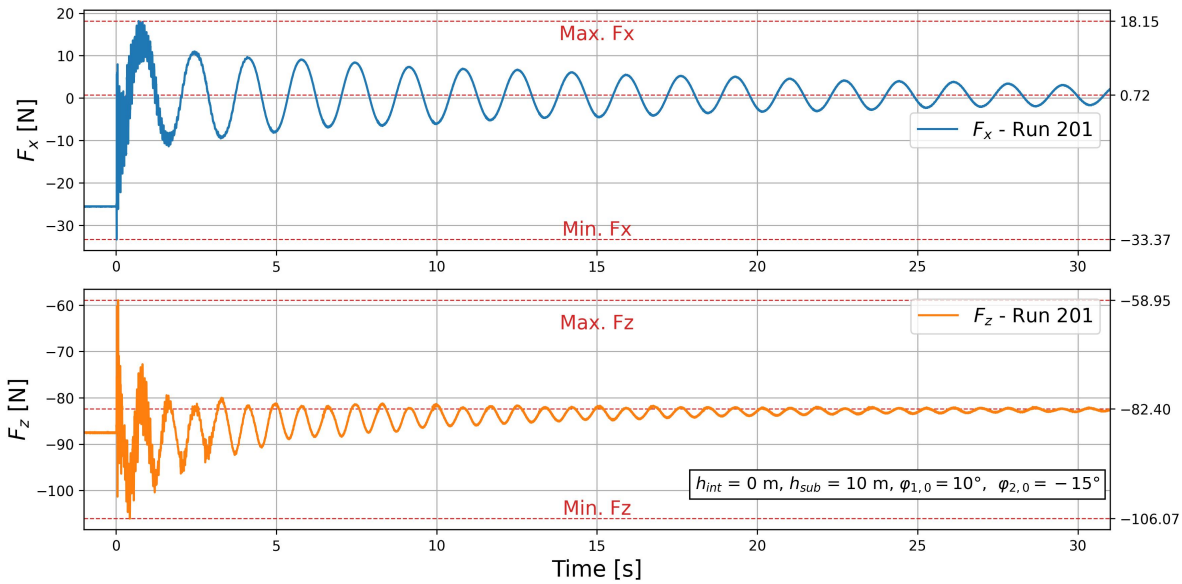

Figure 6.22: Forces in x- and z-direction for $h(0,10)$

The forces in the cranetip can be divided into two components: a static component and a dynamic component. The static component represents the weight of the system when it is at rest. From the information provided in Figure 6.22, it can be observed that the horizontal force F_x is nearly zero, while the vertical force F_z is measured to be 82.4 N. If the dynamic part is examined, the oscillations in the measured forces, the minimal F_x and the maximum F_z are not representative because these are the forces measured just after the system is set in motion. This means that unwanted side effects during release can influence this magnitude of the force. The maximum F_x and minimal F_Z in the figure is therefore used as reference.

Figures 6.23 and 6.24 provide a visual representation of the relationship between the oscillations in the pitch angle and variations in the magnitudes of the forces. It should be noted that the peaks immediately after the release are disregarded due to their unrealistic representation, attributed to the high initial angles and accelerations. In both figures, the highest considered peak is denoted by the red dot ●, while the blue dot ●

represents the subsequent peak. Considering the absence of initial angles, positions, and a release during full-scale operations, the subsequent peaks represented by the blue dots are considered representative of the expected forces.

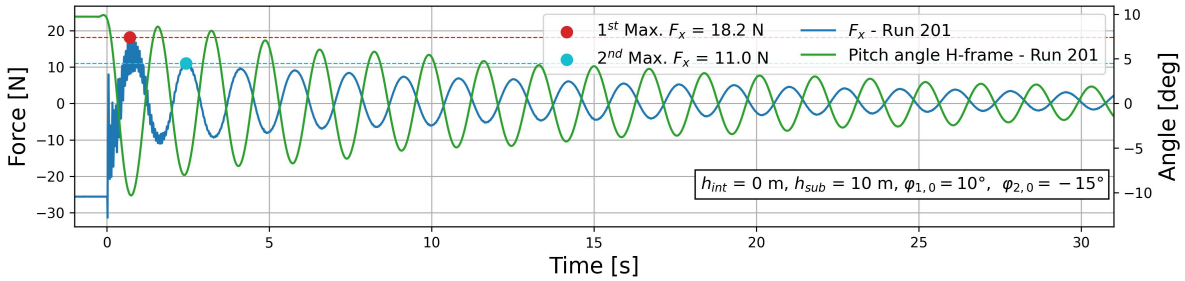

Figure 6.23: Two maximum forces in x-direction including the pitch angle for $h(0,10)$

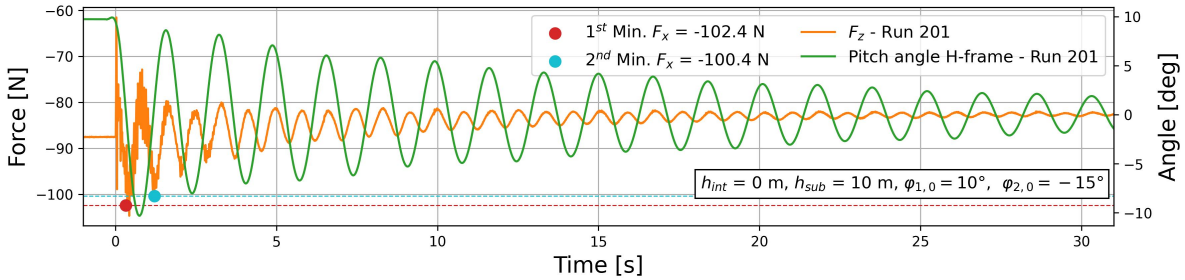

Figure 6.24: Two minimal forces in z-direction including the pitch angle for $h(0,10)$

Furthermore, the translation of the forces in x- and z-direction in the cranetip to full-scale values is accomplished using the scale factor $\lambda = 56.5$. The expected maximum F_x and F_z in the cranetip at full scale for each configuration is presented in table 6.5. It is important to consider that the magnitudes of these values include the weight of the H-frame, which significantly contributes to the overall force. The weight of the H-frame is scaled to 512t on a full scale, whereas in reality, it is roughly Xt. In the current analysis, it is necessary to apply a correction to the measured forces in order to account for the contribution of the H-frame. This correction involves subtracting the weight of the H-frame from the measured forces and then scaling it to full-scale values. Additionally, to obtain the full-scale forces at the cranetip, the full-scale weight of the crane cables should be added to the scaled forces. By following this procedure, the analysis will provide accurate full-scale forces in the cranetip, taking into consideration the effects of the H-frame and crane cables. The model forces need to be scaled to full scale using the scale factor $\lambda = 56.5$. As indicated in table 5.2, the scaling of forces is carried out according to the following relation:

$$F_{\text{real}} = F_{\text{model}} \cdot \lambda^3 \tag{6.10}$$

Table 6.5: Maximum forces in the cranetip corresponding to the 2nd peak ● for large initial angles

ϕ_1 = 10°, ϕ_2 = -15°	**Model scale**			**Full scale***			**Full scale***		
Configuration	F_x	F_z	**Unit**	F_x	F_z	**Unit**	F_x	F_z	**Unit**
$h(0,0)$	24,6	165,4	N	4437	25082	kN	452	2557	t
$h(0,10)$	11,0	100,4	N	1984	13358	kN	202	1362	t
$h(10,10)$	17,8	159,2	N	3210	23963	kN	327	2443	t
$h(10,20)$	12,1	99,6	N	2182	13214	kN	222	1347	t
$h(20,20)$	19,0	167,6	N	3427	25478	kN	349	2597	t
$h(20,30)$	10,2	100,0	N	1840	13286	kN	188	1354	t
$h(30,30)$	15,6	172,0	N	2814	26272	kN	287	2678	t

* Excl. weight of the H-frame. Incl. weight of the full scale cable (≈ Xt)

It is worth noting that these maximum forces are observed for relatively large initial angles. The initial angles of 10° and -15° may result in overly conservative maximum forces. In order to provide a comprehensive analysis, these tests are also conducted with smaller initial angles to facilitate a comparison of responses. The

maximum forces in both x- and z-direction are determined for model scale and for full scale and presented in table 6.6.

Table 6.6: Maximum forces in the cranetip corresponding to the 2nd peak ● for small initial angles

ϕ_1 = 5°, ϕ_2 = -5°	**Model scale**			**Full scale***			**Full scale***		
Configuration	F_x	F_z	**Unit**	F_x	F_z	**Unit**	F_x	F_z	**Unit**
$h(0,0)^{**}$	-	-		-	-		-	-	
$h(0,10)$	4,6	84,9	N	830	10562	kN	85	1077	t
$h(10,10)$	10,3	124,9	N	1858	17777	kN	189	1812	t
$h(10,20)$	6,0	80,9	N	1082	9841	kN	110	1003	t
$h(20,20)$	8,7	125,0	N	1569	17795	kN	160	1814	t
$h(20,30)$	5,2	78,9	N	938	9480	kN	96	966	t
$h(30,30)$	8,7	124,3	N	1569	17669	kN	160	1801	t

* Excl. weight of the H-frame. Incl. weight of the full scale cable (≈ Xt) ** Data not available

As shown in table 6.6, it is clear that in the absence of induced buoyancy, the maximum absolute forces are highest. From the table, it can be observed that the side-lead force is significantly smaller when the system experiences buoyancy. This observation is convenient as it should increase the workability of such operations. The values corresponding to the red peaks as depicted in figure 6.23 and 6.24 for every configuration, are stated in tables E.1 and E.2.

The maximum vertical force observed in the case of buoyancy, is significantly smaller than without buoyancy. This indicates that the presence of buoyancy effectively reduces the vertical load suspended from the cranetip. Table 6.7 presents an overview of the forces measured in the cranetip as a percentage of the maximum allowed loads according to the crane manual.

Table 6.7: Forces experienced in the cranetip as percentage of maximum allowed forces

Max. allowed loads	**Crane Radius**	**Load**	
Max. Side lead load	-	X	t
Max. Vertical load	X m	X	t
	X m	X	t

Measured loads in model tests				% of max. side-lead load	
Side-lead load	Without Buoyancy	160 - 190	t	X - X	
	With Buoyancy	85 - 110	t	X - Y	
				% of max. vertical load at R = Xm	at R = Xm
Vertical load	Without Buoyancy	1800 - 1810	t	X - Y	X - Y
	With Buoyancy	960 - 1080	t	X - Y	X - Y

From table 6.7, it is evident that the presence of buoyancy in the system significantly reduces the side-lead load. The load in horizontal direction, under the influence of buoyancy, is approximately X% to Y% of the maximum allowed side-load in the cranetip. When considering the vertical load limits of the crane, it is important to analyze the case where the crane operates at a radius of Xm. Here, the maximum allowed load is significantly less than at an operating radius of Xm, indicating the governing scenario. In this case, when the system experiences buoyancy, the maximum vertical load is reduced to approximately X% to Y% of the maximum allowed vertical load in the cranetip.

This reduction in both the horizontal and vertical direction highlights the effectiveness of buoyancy in mitigating the forces exerted on the cranetip, ensuring that they remain within safe limits.

Displacements

To track the trajectory of the decaying MP, the displacements in the y- and z-directions can be plotted against the x-displacement. Figure E.39 visualizes the paths of both the H-frame and the MP. It is noteworthy that the MP itself exhibits a relatively large deviation compared to the H-frame. In other words, there is a significant difference in the y-displacement between the top and the bottom of the MP. This observation suggests the occurrence of vortex-induced motions when the MP is submerged, potentially contributing to the observed deviations. The significant displacements in the y-direction of the MP were previously observed during the exploratory tests described in Chapter 4. Furthermore, it is observed that in the absence of induced buoyancy, the displacements in the y-direction are considerably larger compared to when the system experiences buoyancy. This observation suggests that the presence of buoyancy in the system significantly reduces motions in y-direction.

Yaw and Roll angles

In addition to the pitch angle, the roll and yaw angles were also monitored during the model experiments. While the pitch angle is of primary importance for this research, examining the roll and yaw angles can provide insights into any unintended side-effects of the decay tests. For the purpose of this analysis, the configuration $h(10,10)$ is considered, as the eigenfrequency of the system in roll and yaw was specifically tested in this configuration.

Figure 6.25 presents the test results of the previously mentioned angles when the system does not experiences a buoyancy force. While the pitch angle has already been discussed, the response observed in roll and yaw angles can be examined. The roll angle, denoted by θ, reaching approximately $\pm 1.0°$ may not be considered substantial. However, the yaw angle ψ, reaching angles of approximately $+5°$, is relatively significant. Both angles require further investigation.

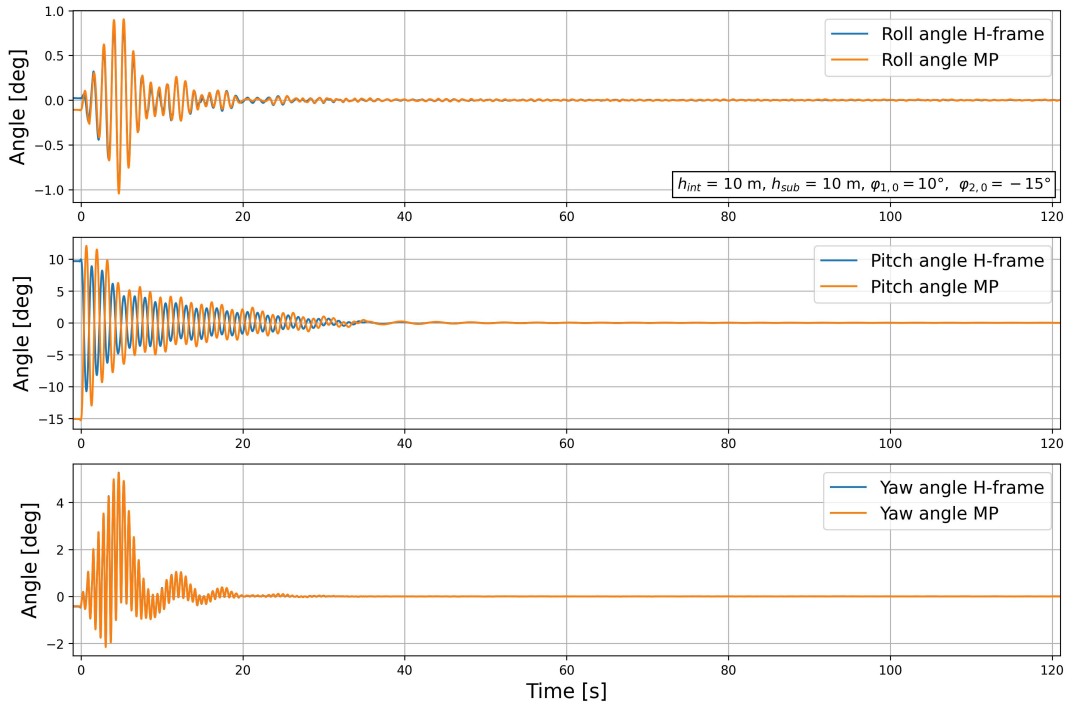

Figure 6.25: Displacements in x- and z-direction for $h(10,10)$ (Run 207)

Roll

The roll angle demonstrates a distinct oscillatory pattern with potentially one single frequency. It exhibits an initial growth within the first five seconds, followed by a subsequent decay. This observation suggests two possible explanations: the presence of vortex-induced motions or the activation of the system's eigenmode in the roll degree of freedom during the decay test. To test the latter case, the system was given a roll angle $\theta \approx -0.2°$, shown in figure 6.26.

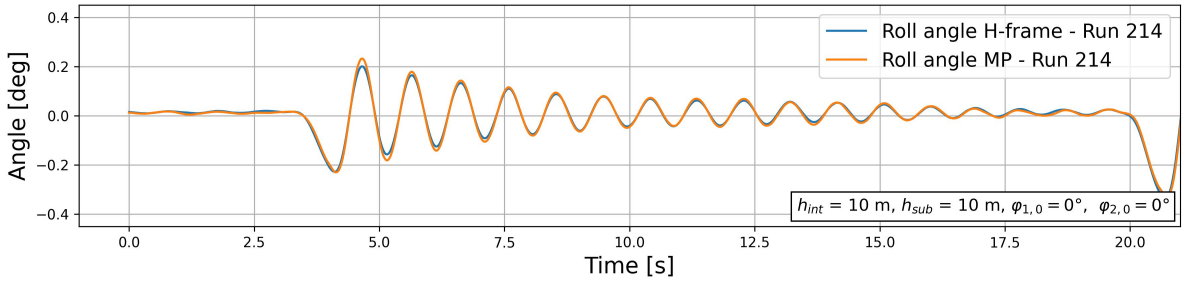

Figure 6.26: Roll angle when given a certain initial angle $\theta = 0.2°$ for $h(10,10)$ (Run 207)

The damped signal has a natural damped period $T_d \approx 0.95s$. In order to compare this result with the test run, the frequency $f_\theta = \frac{1}{T_n}$ is needed. For this particular roll signal, the frequency is estimated as $f_\theta \approx 1.06$ Hz. Figure 6.27 displays the FFT of the signal.

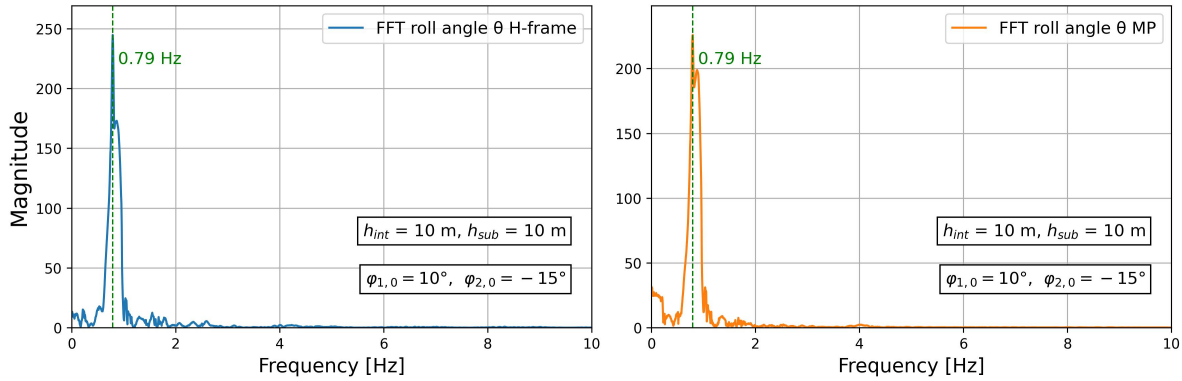

Figure 6.27: FFT for roll motion for $h(10,10)$, extreme angles (Run 207)

Since the system is relatively rigid in roll motion, the roll angles of both the H-frame and the MP align perfectly with each other. As a result, the FFTs of both signals show a similar pattern, with a prominent peak at the same frequency of 0.79 Hz. A frequency of 1.06 being close to 0.79 does not provide certainty that the observed oscillations in roll direction are due to resonance of the eigenfrequency of the H-frame.

Yaw

The observed signal of the yaw angle in figure 6.25 suggests that the system experiences oscillations with potentially two or more frequencies around its z-axis. In a similar manner to the decay test for the roll motion, the decay test was also performed to investigate the behavior of the eigenmode in the yaw motion. Figure 6.28 illustrates the response of the system during this eigenmode decay test.

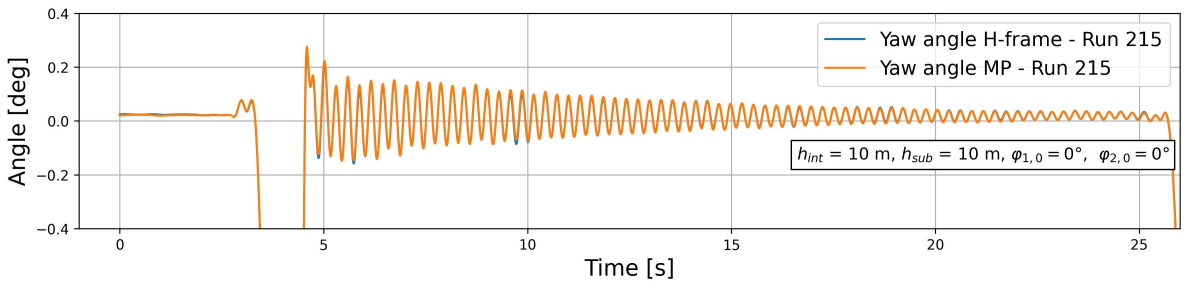

Figure 6.28: Yaw angle when given a certain initial angle $\psi = -4°$ for $h(10,10)$

The damped signal has a natural damped period $T_d \approx 0.28s$. To make a comparison between the decay test and the eigenmode decay test for yaw motion, the frequency $f_\psi = \frac{1}{T_n} = 3.52$ Hz is determined. The FFT of the yaw motion of the test run in figure 6.29 depicts two prominent peaks and two less prominent peaks. The peak corresponding to 3.10 Hz, is significantly close to the eigenfrequency in yaw direction of the system.

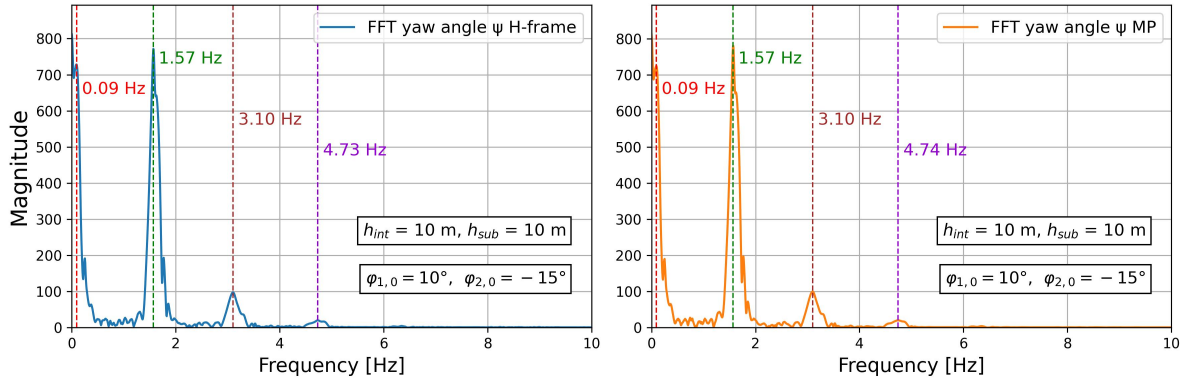

Figure 6.29: FFT for yaw motion for $h(10,10)$, extreme angles (Run 207)

The peak at 1.57 Hz can be interpreted as a possible 2nd harmonic of the roll frequency. In this case, the frequency of the roll oscillation is 0.79 Hz and multiplying it by 2 yields 1.58 Hz. The proximity of the observed peak at 1.57 Hz to the 2nd harmonic of the roll frequency suggests a potential relationship between the two frequencies.

The less prominent peak at 4.74 Hz cannot be explained by looking at the roll or pitch oscillations. A phenomenon that is assumed to be present in the oscillatory system is sloshing. As discussed in section 2.4, the sloshing frequency of an internal water column depends on the ratio of the diameter of the cylinder and the height of the internal water column. The predicted natural frequencies on full-scale are stated in tables 2.3 and 2.4 for the first and second mode, respectively. For convenience, the values for the configuration of $h(10,10)$ are revisited and presented in table 6.8. The scale factors for frequencies and periods are $\lambda^{-0.5}$ and $\lambda^{0.5}$ respectively, as stated in table 5.2.

Table 6.8: Predicted sloshing frequencies ω_{11} and ω_{12} on full scale and model scale with λ = 56.5, h_{int} = 10m

λ = 56.5	Full scale	Model scale		Full scale	Model scale	Unit
D_{MP}	9.5	0.168	D_{MP}	9.5	0.168	[m]
h_{int}	10	0.177	h_{int}	10	0.177	[m]
ω_{11}	1.949	14.650	ω_{12}	3.318	24.940	[rad s^{-1}]
T_{11}	3.224	0.429	T_{12}	1.894	0.252	[s]
f_{11}	0.310	2.330	f_{12}	0.528	3.969	[s^{-1}]

As shown in the table above, the first mode of the natural sloshing frequency on model scale would be f_{11} = 2.33 Hz. Interestingly, this specific frequency is not directly visible in the FFT analysis of the yaw signal, as depicted in figure 6.29. However, the second harmonic, which is twice the fundamental frequency, corresponds to a natural frequency of f_{11-2} = 4.66 Hz. This value closely aligns with the observed frequency peak in the FFT analysis of the yaw angle. The close alignment between the sloshing frequency and the frequency observed in the FFT analysis suggests a potential relationship between these two phenomena. To further verify the analysis of sloshing frequency, a series of decay tests were conducted where the initial angles were much smaller, with ϕ_1 = 5° and ϕ_2 = -5°. The FFT of the yaw motion is plotted in figure 6.30.

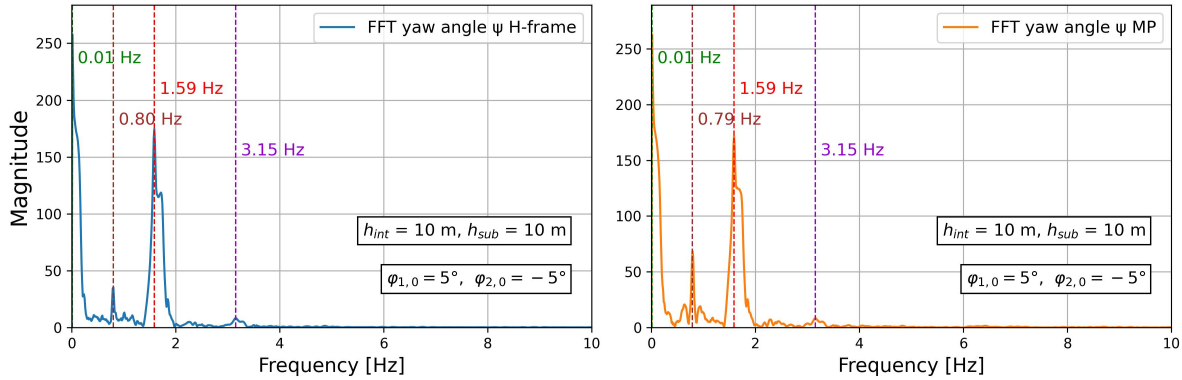

Figure 6.30: FFT for yaw motion for $h(10,10)$, small angles (Run 272)

The relatively small initial angles of the double pendulum lead to lower velocities of the system, suggesting that sloshing may have less influence compared to high-velocity situations. The absence of the peak at approximately $f_\psi \approx 4.74$ Hz confirms this hypothesis and that this frequency thus is likely related to the sloshing frequency. However, the approximation of the sloshing frequency is valid for cylinders with large diameters. Scaling the frequencies determined in the full-scale scenario to a smaller model-scale cylinder, may lead to inaccurate results. The validity of this scaling method should be noted, considering the potential uncertainties associated with the scaling process.

The excessive oscillatory motion in the yaw direction, as shown in figure 6.25, is consistently observed in every other experiment conducted with the double pendulum out-line system. An explanation for this observed yaw motion is potentially related to the x- and y-displacements. Figure 6.31 illustrates the x- and y-displacements of the top of the MP, while the green line represents the measured yaw angle of MP. The x-displacement is scaled with a factor 5 to analyze the phase difference of the signals.

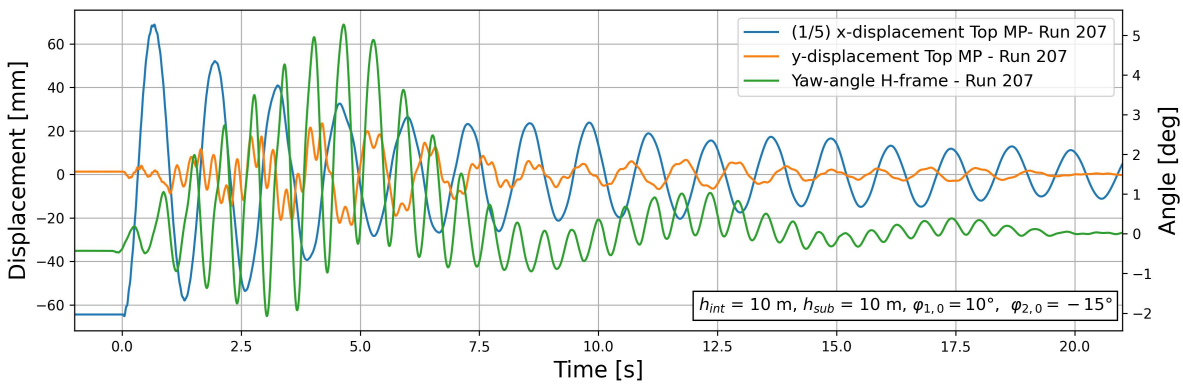

Figure 6.31: x-, y-displacement and yaw angle of top MP vs. time for $h(10,10)$ (Run 207)

In an ideal 2D system, the y-displacement should be zero but as can be seen from figure 6.31, it oscillates for a certain amount of time and reaches values of 20mm. The y-displacement likely generates a moment around the x-axis and combined with an oscillating x-displacement, it generates yaw oscillations of the MP. The largest yaw angles correspond to large positive x-displacements and large negative y-displacements or vise-versa. This is clearly visible in figure 6.32.

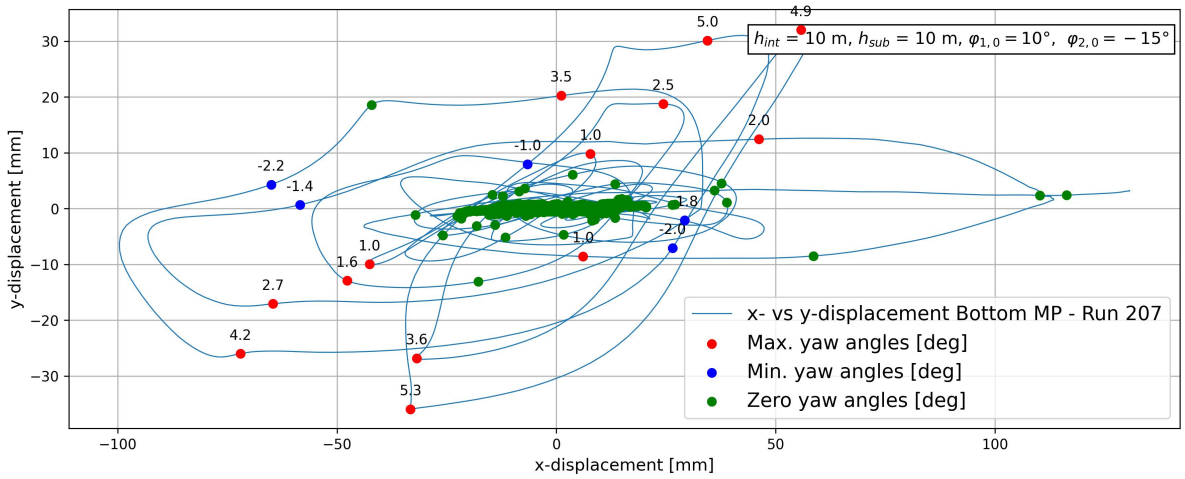

Figure 6.32: x- vs. y-displacement including yaw angle of bottom MP for $h(10,10)$, extreme angles (Run 207)

The figures for all configurations can be found in Appendix E.3.3. The large observed yaw angles are potentially caused by a notable offset of the top of the MP in both the x- and y-directions. To validate the hypothesis that high yaw angles are a consequence of the high x-y offset, the x-y displacement plot of the double pendulum system with small initial angles is examined in Appendix E.3.3. It can be concluded with smaller initial angles, the yaw oscillations of the MP become significantly smaller. Additionally, the observed y-displacements are not attributed to any misalignment in the setup.

6.4.2. Vortex induced motions

To investigate the presence of vortices, the frequency content of the y-displacement is analyzed. The shedding frequency of vortices is influenced by various factors, including the Strouhal number, maximum current velocity and cylinder diameter. The FFTs of the y-displacement of each configuration are presented in Appendix E.3.4. Given the relatively consistent Reynolds number across different configurations, a Strouhal number of 0.2 is assumed, as can be found in figure 2.7. The maximum velocity of the MP relative to the water is determined and is used to calculate the vortex shedding frequency for each configuration (see eq. 2.7). The results are presented in table 6.9.

Table 6.9: Max. velocity of object w.r.t. fluid, Reynolds nr. and vortex shedding frequency for each configuration

Configuration	**Max. Velocity MP** u_m [m s^{-1}]	**Reynolds number** Re [-] ($\cdot 10^4$)	**Vortex shedding frequency** f_v [Hz] (model-scale)
$h(0,10)$	0.356	5.98	0.424
$h(10,10)$	0.404	6.78	0.481
$h(10,20)$	0.226	3.79	0.268
$h(20,20)$	0.312	5.24	0.371
$h(20,30)$	0.321	5.40	0.382
$h(30,30)$	0.376	6.32	0.448

The analysis leads to the conclusion that the calculated vortex frequencies cannot be directly correlated with the observed frequency content of the model experiments. However, further data analysis is required to definitively determine the presence or absence of vortex-induced motions.

6.5. Reliability

As said, the ensure the reliability of the results, three or at least two iterations per test run have been performed. Figures E.63 and E.64 present the results related to the various iterations within a specific test run. It can be concluded that each iteration of every specific test shows a high degree of similarity and alignment. When iterations align, it indicates that the experiments yield consistent and reproducible outcomes. The alignment between the runs suggests that the consistency of the test runs is of good quality, indicating that the results can be considered reliable.

6.5.1. Uncertainties

It is assumed that the experimental setup is rigid and provides a stable foundation for the experiments. However, the stiffness characteristics of the experimental set-up can introduce resonant frequencies that may affect the system's dynamics. The supporting structure can have natural frequencies that coincide with the frequencies of the system's motion. When these resonant frequencies align, it can lead to unwanted vibrations and oscillations, potentially amplifying the response of the system.

It is essential to ensure proper alignment of the double pendulum to maintain the intended motion and minimize any undesirable effects on the system's behavior. However, misalignment in the x-z plane can have unintended side effects on the system. This misalignment can cause deviations from the desired motion and introduce additional forces and moments that may impact the system's response.

The force transducers are calibrated prior to the experimental phase, which is essential for ensuring accurate and reliable measurements. Calibration involves comparing the output of the transducers against known reference forces or weights, allowing for adjustments or corrections to be made in order to obtain accurate measurements. It is expected that because of accurate calibration, the error is minimal.

Variations free water surface can affect the buoyancy forces and drag forces acting on the system. Regular monitoring and adjustment of the water level and thus maintaining an equal submergence across different experimental runs, help ensure consistent testing conditions and reliable data comparisons. While there may be a minor margin of error in determining and maintaining a constant water level, its impact on the overall results is considered negligible.

6.6. Conclusions

As observed the exploratory tests, the MP started to drift away from its equilibrium and initiates instability in the system. This was observed for a certain level of submergence and thus a waterlevel difference between the in- and outside of the MP. This waterlevel difference was estimated to be roughly X meters on full scale for this specific MP. This means that buoyancy force needs to be roughly X-Y% of the gravitational forces to initiate this instability. These values should serve as the maximum values for the buoyancy force.

The determination of whether the side-lead angles will be exceeded is challenging due to the high initial angles given to the system. However, the limiting factor is the measured vertical and horizontal forces at the cranetip, which are scaled to a full-cale scenario. The inclusion of buoyancy in the system results in a significant reduction in the side-lead load, reaching approximately X%-Y% of the maximum allowable load in the horizontal direction, which is nearly half of the load observed without the presence of buoyancy. Additionally, the vertical forces are reduced to approximately X%-Y% of the maximum vertical loads. The presence of buoyancy effectively reduces both the vertical and horizontal forces experienced in the cranetip. Furthermore, the presence of buoyancy leads to a significant lower natural frequency of the system.

The examination of the test results identified that the decaying motion of the pitch angle resulted in significant oscillations in roll and yaw-direction. The frequency analysis gave insight in the frequency content of the yaw signal, where four frequency peaks were identified. One peak related given initial angle and one related to the second harmonic of the roll signal and one of the pitch signal. The smallest peak frequency suggests the presence of the second harmonic frequency of the sloshing mode but this phenomenon needs to be further analyzed.

These excessive yaw angles are consistently observed throughout each test run. Upon examining the displacement of the MP in the x- and y- direction, it was found that the greatest yaw angles coincided with the largest x-y offsets. This suggests that the combination of a significant y offset and motion in the x-direction generates a moment that leads to the formation of the yaw angle. While the x-displacement is a result of the decaying motion, the offset in the y-direction is attributed to a potentially different phenomenon, such as vortex-induced motions. However, this is a suggestion that requires further investigation.

The damping coefficients can be estimated using a linear approach, although it is uncertain whether this method is suitable for signals with non-linear interactions. In this research, it is primarily used as an approximation for the damping present in the system.

7

Numerical model

Numerical modeling is a valuable tool for investigating complex engineering systems. By using mathematical algorithms and computer simulations, numerical models provide a detailed understanding of a system's response under various conditions, enabling for optimization and predictions regarding the system's behavior. This chapter elaborates on the method used for the model made with Python and focuses on the implementation of damping and the definition of inertia. Finally, the results will be discussed in Chapter 6 and compared to the experimental results from Chapter 5.

7.1. Method

Lagrange's method is previously introduced as a verification of the principle of virtual work in Chapter 3, section 3.6. In order to create a numerical model to describe the system, Lagrange's method is revisited, followed by verifying the derived equations of motion using Newton's second law of motion. If Newton's method yields the same equations of motion, Lagrange's equations of motion will serve as the basis for the numerical model. It is important to note that the system being considered for this verification has been simplified to only include two particles, namely m_1 and m_2 with corresponding lengths l_1 and l_2. This simplification has been made to ensure that the derivations remain clear and easy to comprehend, while still preserving its principle. Figure 7.1 shows the simplification and the definitions of the parameters used.

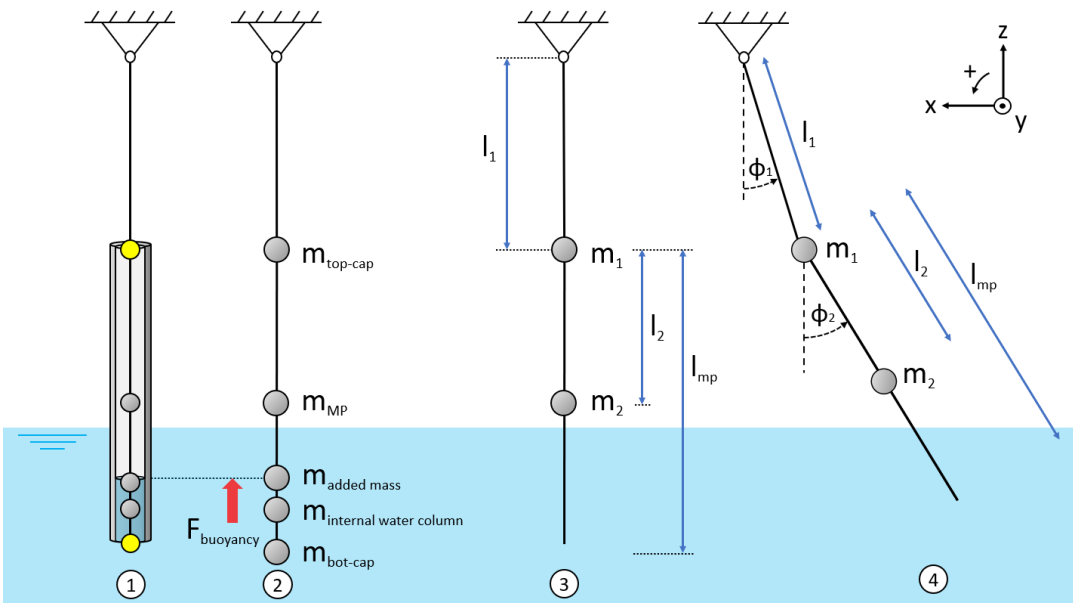

Figure 7.1: 1: The system converted to a simplification 2: The system represented as point masses 3,4: The system including two particles m_1 and m_2 and angles ϕ_1 and ϕ_2

Lagrange's method

Equations 7.1 and 7.2 are the equations of motion derived with Lagrange's method for only particles m_1 and m_2 with lengths l_1 and l_2. The full derivation can be found in Appendix A.4.

$$\mathrm{EoM}_1 = l_1^2(m_1+m_2)\ddot{\phi}_1 + l_1(m_2 l_2)\ddot{\phi}_2\cos(\phi_1-\phi_2) + l_1(m_2 l_2)\dot{\phi}_2^2\sin(\phi_1-\phi_2) + l_1\left(m_1+m_2\right)g\sin(\phi_1) = 0 \tag{7.1}$$

$$\mathrm{EoM}_2 = m_2 l_2^2\ddot{\phi}_2 + l_1(m_2 l_2)\ddot{\phi}_1\cos(\phi_1-\phi_2) - l_1(m_2 l_2)\dot{\phi}_1^2\sin(\phi_1-\phi_2) + (m_2 l_2)g\sin(\phi_2) = 0 \tag{7.2}$$

Newton's method

Newton's Second Law of Motion, as formulated by Sir Isaac Newton, states that the acceleration of an object is directly proportional to the net force acting on it and inversely proportional to its mass. Mathematically, this can be expressed as done in equation 7.3, where F represents the net force applied to the object, m represents the mass of the object and a represents the resulting acceleration of the object. A clarification on the principle of this principle can be found in section 3.3.2.

$$F = ma = m\ddot{\mathbf{r}} \tag{7.3}$$

The use of Newton's second law of motion results in the equations of motion 7.4 and 7.5 and can be easily compared to the ones derived with Lagrangian:

$$\mathrm{EoM}_1 = (m_1+m_2)l_1^2\ddot{\phi}_1 + l_1(m_2 l_2)\ddot{\phi}_2\cos\left(\phi_2-\phi_1\right) - l_1(m_2 l_2)\dot{\phi}_2^2\sin\left(\phi_2-\phi_1\right) + l_1(m_1+m_2)g\sin\phi_1 = 0 \tag{7.4}$$

$$\mathrm{EoM}_2 = m_2 l_2^2\ddot{\phi}_2 + l_1(m_2 l_2)\ddot{\phi}_1\cos\left(\phi_2-\phi_1\right) + l_1(m_2 l_2)\dot{\phi}_1^2\sin\left(\phi_2-\phi_1\right) + m_2 l_2 g\sin\phi_2 = 0 \tag{7.5}$$

These equations of motion are derived for only particles m_1 and m_2 with lengths l_1 and l_2. The full derivation of these equations can be found in section B.3.

Conclusion

By verifying the equations of motion obtained from Lagrange's method with Newton's second law of motion, any errors or inconsistencies in the derived equations can be identified and corrected. This verification process is crucial in ensuring that the numerical model accurately represents the system being analyzed.

The equations of motion 7.1 and 7.2 derived with Lagrange's method are stated below.

$$\boxed{\begin{aligned} &l_1^2(m_1+m_2)\ddot{\phi}_1 + l_1(m_2 l_2)\ddot{\phi}_2\cos(\phi_1-\phi_2) + l_1(m_2 l_2)\dot{\phi}_2^2\sin(\phi_1-\phi_2) + l_1\left(m_1+m_2\right)g\sin(\phi_1) = 0 \\ &m_2 l_2^2\ddot{\phi}_2 + l_1(m_2 l_2)\ddot{\phi}_1\cos(\phi_1-\phi_2) - l_1(m_2 l_2)\dot{\phi}_1^2\sin(\phi_1-\phi_2) + (m_2 l_2)g\sin(\phi_2) = 0 \end{aligned}}$$

Applying the trigonometric rules stated below to equations 7.4 and 7.5 yields identical equations of motion for Newton's method compared to the equations obtained through Lagrange's method.

$$\sin(\phi_2-\phi_1) = -\sin(\phi_1-\phi_2), \qquad \cos(\phi_2-\phi_1) = \cos(\phi_1-\phi_2)$$

$$\boxed{\begin{aligned} &(m_1+m_2)l_1^2\ddot{\phi}_1 + l_1(m_2 l_2)\ddot{\phi}_2\cos\left(\phi_2-\phi_1\right) - l_1(m_2 l_2)\dot{\phi}_2^2\sin\left(\phi_2-\phi_1\right) + l_1(m_1+m_2)g\sin\phi_1 = 0 \\ &m_2 l_2^2\ddot{\phi}_2 + l_1(m_2 l_2)\ddot{\phi}_1\cos\left(\phi_2-\phi_1\right) + l_1(m_2 l_2)\dot{\phi}_1^2\sin\left(\phi_2-\phi_1\right) + m_2 l_2 g\sin\phi_2 = 0 \end{aligned}}$$

It can be concluded that Lagrange's method is a valid method to derive the equations of motion of this system. The derivations done in Appendix A.4.1 and A.4.2 show that additional components in the system can be easily added to the set of equations. This method will therefore be used for the numerical model as it is the most convenient one to describe a system with two degrees of freedom, such as the double pendulum, including inertia.

7.2. System characterization

As said, the Lagrangian is used as a basis for the numerical model. Figure 7.2 provides a visualization of the system, including all the components already considered in the analytical model, discussed in Chapter 3.

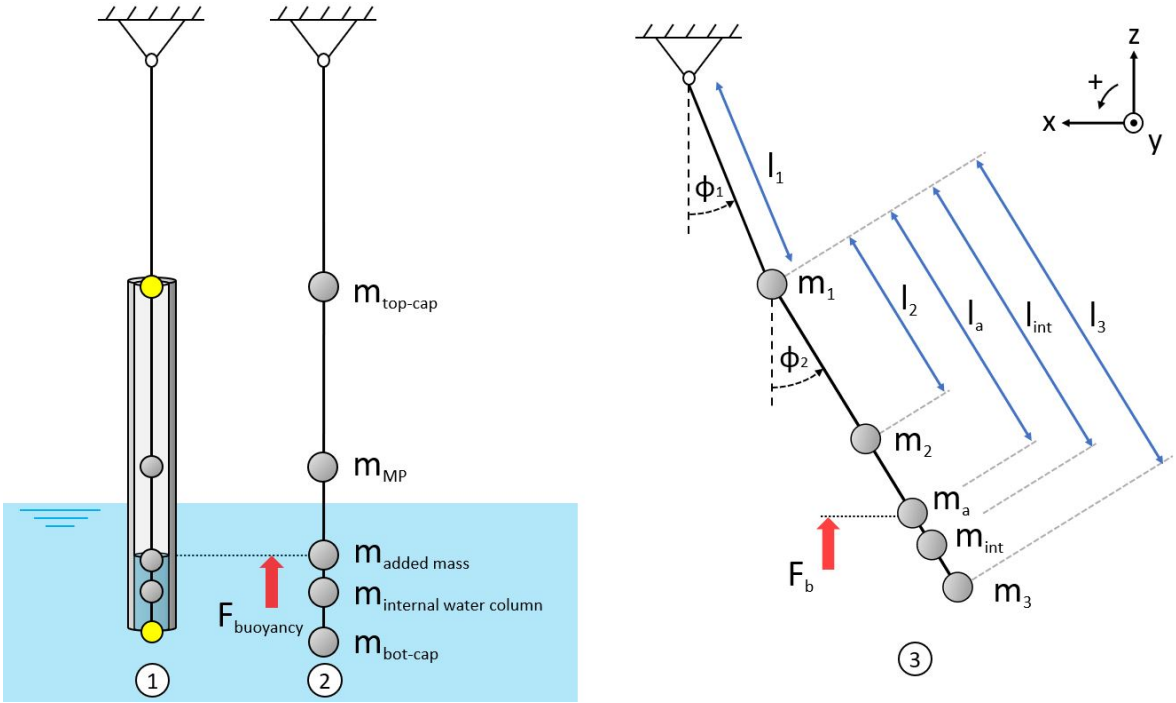

Figure 7.2: 1: The system converted to a simplification 2: The system represented as point masses 3: The system including all components with degrees of freedom, ϕ_1 and ϕ_2

Equations 7.6 and 7.7 form the basis for the equations of motion of the system.

$$\mathrm{EoM}_1 = J_{\phi_1}\ddot{\phi}_1 + J_x\,\ddot{\phi}_2\cos(\phi_1-\phi_2) + J_x\,\dot{\phi}_2^2\sin(\phi_1-\phi_2) + \mu_1\sin(\phi_1) = 0 \tag{7.6}$$

$$\mathrm{EoM}_2 = J_{\phi_2}\ddot{\phi}_2 + J_x\,\ddot{\phi}_1\cos(\phi_1-\phi_2) - J_x\,\dot{\phi}_1^2\sin(\phi_1-\phi_2) + \mu_2\sin(\phi_2) = 0 \tag{7.7}$$

To include all components in the equations of motion (eq. 7.6 and eq. 7.7), it is found that only the values for parameters $J_{\phi_1}, J_{\phi_2}, J_x$, μ_1 and μ_2 do change. This substitution of parameters is explained in Appendix A.4.2 and is convenient for expanding the numerical model. The aforementioned parameters are then defined as follows:

$$\begin{aligned}
J_{\phi_1} &= l_1^2\left(m_1+m_2+m_3+m_{\mathrm{int}}+m_a\right) & J_{\phi_2} &= m_2 l_2^2 + m_3 l_3^2 + m_{\mathrm{int}} l_{\mathrm{int}}^2 + m_a l_a^2 + J_2 + J_{\mathrm{int}} + J_a \\
J_x &= l_1\left(m_2 l_2 + m_3 l_3 + m_{\mathrm{int}} l_{\mathrm{int}} + m_a l_a\right) \\
\mu_1 &= l_1\left(\left(m_1+m_2+m_3+m_{\mathrm{int}}\right)g - F_b\right) & \mu_2 &= \left(m_2 l_2 + m_3 l_3 + m_{\mathrm{int}} l_{\mathrm{int}}\right)g - F_b l_a
\end{aligned}$$

In order to achieve a better understanding of the significance of these parameters, the system of differential equations can be represented as $M\ddot{\vec{\Phi}} + K\vec{\Phi} = \vec{0}$. This equation describes the free undamped oscillations with a certain frequency as stated in equation A.19:

$$M\ddot{\vec{\Phi}} + K\vec{\Phi} = \vec{0} \qquad \text{with} \qquad \Phi = \begin{bmatrix}\phi_1\\ \phi_2\end{bmatrix} \qquad \text{so} \qquad \begin{bmatrix} J_{\phi_1} & J_x \\ J_x & J_{\phi_2}\end{bmatrix}\begin{bmatrix}\ddot{\phi}_1\\ \ddot{\phi}_2\end{bmatrix} + \begin{bmatrix}\mu_1 & 0\\ 0 & \mu_2\end{bmatrix}\begin{bmatrix}\phi_1\\ \phi_2\end{bmatrix} = \begin{bmatrix}0\\0\end{bmatrix}$$

$$\begin{cases}
M = \begin{bmatrix} J_{\phi_1} & J_x \\ J_x & J_{\phi_2}\end{bmatrix} = \begin{bmatrix} l_1^2\left(m_1+m_2+m_3+m_{\mathrm{int}}+m_a\right) & l_1\left(m_2 l_2 + m_3 l_3 + m_{\mathrm{int}} l_{\mathrm{int}} + m_a l_a\right) \\ l_1\left(m_2 l_2 + m_3 l_3 + m_{\mathrm{int}} l_{\mathrm{int}} + m_a l_a\right) & m_2 l_2^2 + m_3 l_3^2 + m_{\mathrm{int}} l_{\mathrm{int}}^2 + m_a l_a^2 + J_2 + J_{\mathrm{int}} + J_a \end{bmatrix} \\
K = \begin{bmatrix}\mu_1 & 0\\ 0 & \mu_2\end{bmatrix} = \begin{bmatrix} l_1\left(\left(m_1+m_2+m_3+m_{\mathrm{int}}\right)g - F_b\right) & 0 \\ 0 & \left(m_2 l_2 + m_3 l_3 + m_{\mathrm{int}} l_{\mathrm{int}}\right)g - F_b l_a \end{bmatrix} \\
\vec{\Phi} = \begin{bmatrix}\phi_1\\ \phi_2\end{bmatrix} = \begin{bmatrix}\phi_{1i}\\ \phi_{2i}\end{bmatrix}\sin(\omega t)
\end{cases} \tag{7.8}$$

This set of equations of 7.8 still does not contain any damping terms, which are quite significant in reality. Section 7.4 elaborates on the damping present in the system and how to implement it into the equations of motion. First, the inertia components in the system are identified, as they are required to determine the damping coefficients.

7.3. Inertia

Throughout the research, it is assumed that the crane cable with length l_1, has no weight contribution. However, when constructing a scaled model, the cable (represented as the H-frame) does have a mass, denoted by m_{Hframe}. The inertia of the H-frame of the scaled model is taken w.r.t. the rotation point in the cranetip, as visualized in figure 7.3. Note that the length of the H-frame extends beyond the second rotation point. As a result, the actual length l_{Hframe} is slightly longer than the length of the cable, which leads to a larger contribution of inertia in the system. The inertia components used in the equations of motion are stated in equations 7.9 - 7.12.

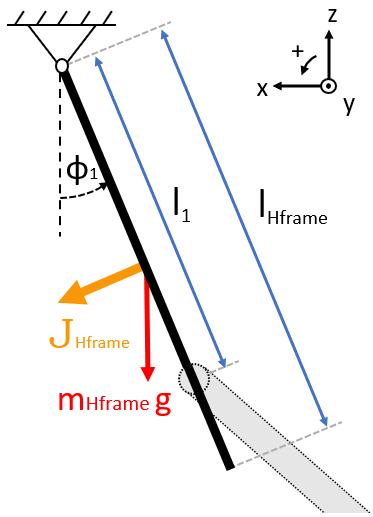

Figure 7.3: Simplification of the contribution of the inertia of the H-frame

$$J_{\text{Hframe}} = \frac{1}{12} m_{\text{Hframe}} l_{\text{Hframe}}^2 \tag{7.9}$$

$$J_2 = \frac{1}{12} m_2 l_{\text{mp}}^2 \tag{7.10}$$

$$J_{\text{int}} = \frac{1}{12} m_{\text{int}} h_{\text{int}}^2 \tag{7.11}$$

$$J_a = \frac{1}{12} m_a h_{\text{sub}}^2 \tag{7.12}$$

The inertia of the system is validated by fitting the numerical model with the data acquired from the model-scaled experiments. The total inertia in the system, is divided into two parts: the inertia of the H-frame corresponding to the first DoF and the sum of all the inertia components corresponding to the second degree of freedom. To create an insight of the contribution of inertia to the system, a visual representation is provided in Appendix G.2. It is important to note that the inertia terms presented in this visualization are not directly used in the numerical model. Instead, they serve as a tool to gain insights into the contribution of inertia to the system.

The addition of inertia of the H-frame results in a change of the constant parameters J_{ϕ_1}, J_{ϕ_2}, J_x, μ_2 and μ_2. The following set of equations is then used in the numerical model, as derived in section A.5.

$$J_{\phi_1} = l_1^2 \left(\frac{1}{4} m_{\text{Hframe}} + m_1 + m_2 + m_3 + m_{\text{int}} + m_a \right) + J_{\text{Hframe}} \qquad J_{\phi_2} = m_2 l_2^2 + m_3 l_3^2 + m_{\text{int}} l_{\text{int}}^2 + m_a l_a^2 + J_2 + J_{\text{int}} + J_a$$

$$J_x = l_1 \left(m_2 l_2 + m_3 l_3 + m_{\text{int}} l_{\text{int}} + m_a l_a \right)$$

$$\mu_1 = l_1 \left(\left(\frac{1}{2} m_{\text{Hframe}} + m_1 + m_2 + m_3 + m_{\text{int}} \right) g - F_b \right) \qquad \mu_2 = \left(m_2 l_2 + m_3 l_3 + m_{\text{int}} l_{\text{int}} \right) g - F_b l_a$$

where the red components are added to the equation as a result of the extra mass and corresponding inertia of the H-frame/cable. A detailed derivation of the modified equations of motion can be found in Appendix A.5. Note that while the weight of the cable changes over time on the full-scale system, as the MP is lifted. On model scale, the weight of the H-frame is considered to be constant.

7.4. Damping

Damping in a system refers to the dissipation of energy from the system, which leads to a decrease in the amplitude of oscillations or vibrations over time. Damping can be caused by a variety of factors, such as friction or viscosity, depending on the nature of the system. The damping coefficient is a key parameter that characterizes the damping behavior of a system and quantifies the rate at which energy is dissipated. In offshore operations, the following damping terms are considered:

- Air resistance
- Viscous drag due to surrounding water
- Linear damping components

The effect of air resistance is assumed to be negligible compared to the viscous drag acting on the MP. It will therefore not be taken into account in the formulations for the numerical model.

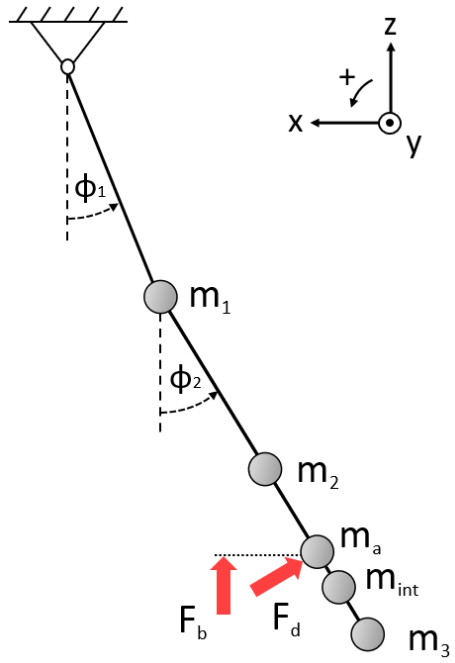

Figure 7.4: System including drag force F_d

Viscous drag arises from the interaction between a moving object and its surrounding fluid or medium. It can be modeled using a linear relationship between the velocity of the object and the opposing force of the fluid. In order to accurately describe the behavior of a system that is subject to viscous drag, it is essential to account for this damping effect in the system's equations of motion. Neglecting the effects of damping terms can lead to unrealistic predictions of the system's behavior.

To account for the viscous and linear damping in a system that is described using Lagrange's method, the Rayleigh dissipation function can be introduced. This function describes the amount of energy that dissipates in a system because of internal friction or other dissipative processes, such as energy loss due to viscous drag. By including this term in the Lagrangian, the equations of motion can be derived that take into account the loss of energy and accurately describe the behavior of the system.

Mathematically, the Rayleigh dissipation function D can include both linear and quadratic terms, as well as higher-order terms, depending on the system properties. The quadratic form of this function is often used in physical systems where energy dissipation is proportional to the velocity squared, such as in systems with viscous damping. The general dissipation function is defined as follows:

$$D = \frac{1}{n+1} \sum_j c_j v_j^{n+1} \tag{7.13}$$

and results in the following Lagrangian formulation:

$$\frac{\mathrm{d}}{\mathrm{d}t}\left(\frac{\partial L}{\partial \dot{q}_i}\right) - \frac{\partial L}{\partial q_i} + \frac{\partial D}{\partial \dot{q}_i} = Q_i \qquad \text{for} \qquad q_i = \phi_1, \phi_2 \tag{7.14}$$

7.4.1. Viscous damping

The dissipation or the energy loss in the system partly consists of the drag force acting on the monopile. The drag force in this case is defined in equation 7.15 and contains a quadratic velocity term. This means that the drag force is proportional to the square of the velocity: v^2.

$$F_d = \frac{1}{2} C_D \rho_{\text{fluid}} A_p v^2 = \frac{1}{2} C_D \rho_{\text{fluid}} A_p v^2 \tag{7.15}$$

where C_D is the drag coefficient, $\rho_f luid$ is the density of the fluid, A_p is equal to the projected area of the MP subjected to viscous drag and v is the velocity at which the point of application of the drag force moves. This point is defined as l_d and is the distance from the p.o.a. to the CoG of the MP. Every parameter can then be

assumed constant except for the velocity term. The velocity dependence in the dissipation function should be quadratic, so $n = 2$ in equation 7.13. With $n = 2$ and $c = \frac{1}{2}\rho_w C_D A_p$ and only one dissipation j to account for in this case, the dissipation function becomes:

$$D = \frac{1}{n+1}\sum_j c_j v_j^{n+1} = \frac{1}{2+1} c v^{2+1} = \frac{1}{3}\left(\frac{1}{2}C_D \rho_w A_p\right) v^3 = \frac{1}{6}\rho_w C_D A_p v^3 \tag{7.16}$$

with $v = l_d \dot{\phi}_2$ gives the following expression for the dissipation function D as a result of the viscous drag.

$$\frac{\partial D}{\partial \dot{q}_i} = \frac{\partial D}{\partial \dot{\phi}_1} = 0 \quad \text{and} \quad \frac{\partial D}{\partial \dot{q}_i} = \frac{\partial D}{\partial \dot{\phi}_2} = \frac{\partial}{\partial \dot{\phi}_2}\left(\frac{1}{6}\rho_w C_D A_p \left(l_d \dot{\phi}_2\right)^3\right) = \frac{1}{2}\rho_w C_D A_p \left(l_d \dot{\phi}_2\right)^2 l_d \tag{7.17}$$

Using the expression for the drag force in equation 7.15, the following expression for dissipation is retrieved:

$$\frac{\partial D}{\partial \dot{\phi}_2} = \frac{1}{2}\rho_w C_D A_p l_d \left|l_d \dot{\phi}_2\right| l_d \dot{\phi}_2 = c \left|l_d \dot{\phi}_2\right| l_d \dot{\phi}_2 \tag{7.18}$$

where $c = \frac{1}{2}\rho_w C_D A_p$ and the other parameters do not change. If the definition for the dissipation is taken into consideration and put into the extended Lagrange equation stated in equation 7.14. Equations of motion 7.6 and 7.7 will be extended with the these viscous damping terms. The equations of motion then become:

$$\text{EoM}_1 = J_{\phi_1}\ddot{\phi}_1 + J_x \ddot{\phi}_2 \cos(\phi_1 - \phi_2) + J_x \dot{\phi}_2^2 \sin(\phi_1 - \phi_2) + \mu_1 \sin(\phi_1) = 0 \tag{7.19}$$

$$\text{EoM}_2 = J_{\phi_2}\ddot{\phi}_2 + J_x \ddot{\phi}_1 \cos(\phi_1 - \phi_2) - J_x \dot{\phi}_1^2 \sin(\phi_1 - \phi_2) + \mu_2 \sin(\phi_2) + c\, l_d \left|l_d \dot{\phi}_2\right| l_d \dot{\phi}_2 = 0 \tag{7.20}$$

The system of equations then becomes:

$$\begin{bmatrix} J_{\phi_1} & J_x \\ J_x & J_{\phi_2} \end{bmatrix} \begin{bmatrix} \ddot{\phi}_1 \\ \ddot{\phi}_2 \end{bmatrix} + \underbrace{\begin{bmatrix} 0 & 0 \\ 0 & c\, l_d^2 \left|l_d \dot{\phi}_2\right| \end{bmatrix}}_{\text{Viscous damping matrix}} \begin{bmatrix} \dot{\phi}_1 \\ \dot{\phi}_2 \end{bmatrix} + \begin{bmatrix} \mu_1 & 0 \\ 0 & \mu_2 \end{bmatrix} \begin{bmatrix} \phi_1 \\ \phi_2 \end{bmatrix} = \begin{bmatrix} 0 \\ 0 \end{bmatrix} \tag{7.21}$$

7.4.2. Linear damping

Linear damping is a fundamental aspect of physical systems characterized by the presence of a damping force directly proportional to the system's velocity. It serves as a mathematical model to describe the dissipation of energy in systems where the damping force varies linearly with the velocity.

In the study of nonlinear systems, spring-damper systems have been used as a basis to investigate the chaotic motion of a double pendulum. Numerous researchers have explored the stability of elastic systems under external forces. Ziegler [33] was the first to discover the destabilizing influence of damping on these non-conservative linear elastic systems. Thomsen [25] and Jint et al. [17] both conducted an analysis on the dynamics of an elastically restrained inverted double pendulum subjected to external non-conservative loading and linear damping. The focus is primarily on the system's local behavior, specifically small amplitude motions around a central equilibrium point. In a related work, Yu et al. [31] explored a similar system but replaced the torsional springs used in Thomsen's study, with linear springs. The objective was to investigate the occurrence of chaos and stability in this system configuration.

Mathematically, linear damping can be represented by the following relation:

$$F = -b \cdot \dot{x}$$

In this equation, F denotes the damping force, b represents the damping coefficient, and $\dot{x}$ signifies the velocity of the system. The negative sign indicates that the damping force acts in the opposite direction relative to the motion. The presence of linear damping in a system leads to several effects. It mainly causes a reduction in the amplitude of oscillations, progressively dissipating energy over time. Furthermore, linear damping influences the system's natural frequency, resulting in alterations to its dynamic response and stability characteristics.

As stated in equation 6.1, the damping coefficient b is linear to the velocity $\dot{\phi}$. In the general dissipation function D of equation 7.13, it means that $n = 1$. The damping c is set to b_1, b_2 and are coupled through the angles ϕ_1 and ϕ_2, as shown in figure 7.5. With dissipation in two degrees of freedom ($j = 1,2$) in pitch direction, the dissipation function with $v_1 = \dot{\phi}_1$ and $v_2 = \dot{\phi}_2 - \dot{\phi}_1$ becomes:

$$D = \frac{1}{n+1}\sum_j c_j v_j^{n+1} = \frac{1}{2}b_1 v_1^2 + \frac{1}{2}b_2 v_2^2 = \frac{1}{2}b_1\dot{\phi}_1^2 + \frac{1}{2}b_2\left(\dot{\phi}_2 - \dot{\phi}_1\right)^2 \tag{7.22}$$

Using the Lagrange formulation for the dissipation function D as a result of the linear damping is in correspondence to what Jint et. al [17] and Thomson [25] found in their studies. The following expression for the dissipation function is stated below.

$$\frac{\partial D}{\partial \dot{q}_i} = \frac{\partial D}{\partial \dot{\phi}_1} = (b_1 + b_2)\dot{\phi}_1 - b_2\dot{\phi}_2 \quad \text{and} \quad \frac{\partial D}{\partial \dot{\phi}_2} = b_2\dot{\phi}_2 - b_2\dot{\phi}_1 \tag{7.23}$$

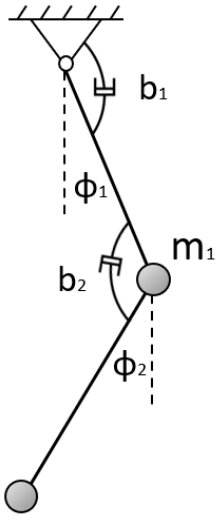

Figure 7.5: Damping in the degrees of freedom ϕ_1 and ϕ_2

As mentioned earlier, a system of differential equations can be represented as $M\ddot{\vec{\Phi}} + K\vec{\Phi} = \vec{0}$ without damping. If damping is considered, a damping matrix C is added to the set of equations and results in the following relation:

$$M\ddot{\vec{\Phi}} + C\dot{\vec{\Phi}} + K\vec{\Phi} = \vec{0} \tag{7.24}$$

The system of equations then becomes:

$$\begin{bmatrix} J_{\phi_1} & J_x \\ J_x & J_{\phi_2} \end{bmatrix}\begin{bmatrix} \ddot{\phi}_1 \\ \ddot{\phi}_2 \end{bmatrix} + \underbrace{\begin{bmatrix} b_1 + b_2 & -b_2 \\ -b_2 & b_2 \end{bmatrix}}_{\text{Linear damping matrix}}\begin{bmatrix} \dot{\phi}_1 \\ \dot{\phi}_2 \end{bmatrix} + \begin{bmatrix} \mu_1 & 0 \\ 0 & \mu_2 \end{bmatrix}\begin{bmatrix} \phi_1 \\ \phi_2 \end{bmatrix} = \begin{bmatrix} 0 \\ 0 \end{bmatrix} \tag{7.25}$$

The linear damping phenomenon is accounted for in the system by including the damping coefficients b_1 and b_2 in the system of equations. The dissipation effect can be implemented using equation 7.14. Consequently, the equations of motion, derived in 7.19 and 7.20, are further extended to account for the influence of linear damping.

$$\text{EoM}_1 = J_{\phi_1}\ddot{\phi}_1 + J_x\ddot{\phi}_2\cos(\phi_1 - \phi_2) + J_x\dot{\phi}_2^2\sin(\phi_1 - \phi_2) + \mu_1\sin(\phi_1) + (b_1 + b_2)\dot{\phi}_1 - b_2\dot{\phi}_2 = 0 \tag{7.26}$$

$$\begin{aligned}\text{EoM}_2 = {} & J_{\phi_2}\ddot{\phi}_2 + J_x\ddot{\phi}_1\cos(\phi_1 - \phi_2) - J_x\dot{\phi}_1^2\sin(\phi_1 - \phi_2) + \mu_2\sin(\phi_2) + c\,l_d\left|l_d\dot{\phi}_2\right|l_d\dot{\phi}_2 \\ & + b_2\dot{\phi}_2 - b_2\dot{\phi}_1 = 0\end{aligned} \tag{7.27}$$

Equations 7.26 and 7.27 represent the equations of motion used in the numerical model, accounting for both the linear damping term and the damping resulting from viscous drag. The total system of equations now becomes:

$$\begin{bmatrix} J_{\phi_1} & J_x \\ J_x & J_{\phi_2} \end{bmatrix}\begin{bmatrix} \ddot{\phi}_1 \\ \ddot{\phi}_2 \end{bmatrix} + \underbrace{\begin{bmatrix} b_1 + b_2 & -b_2 \\ -b_2 & b_2 + c\,l_d^2\left|l_d\dot{\phi}_2\right| \end{bmatrix}}_{\text{Total damping matrix}}\begin{bmatrix} \dot{\phi}_1 \\ \dot{\phi}_2 \end{bmatrix} + \begin{bmatrix} \mu_1 & 0 \\ 0 & \mu_2 \end{bmatrix}\begin{bmatrix} \phi_1 \\ \phi_2 \end{bmatrix} = \begin{bmatrix} 0 \\ 0 \end{bmatrix} \tag{7.28}$$

From this point forward, the damping coefficients b_1 and b_2 will be referred to as b_{Hframe} and b_{mp}, respectively.

7.4.3. Damping coefficients

Equation 7.29 and 7.30 are used to determine the damping coefficients. The calculated damping coefficients b_{Hframe} and b_{mp} for the double pendulum system can be found in Appendix G.4.

$$b_{\text{Hframe}} = 2\nu_{\text{Hframe}}(m + a) \quad : 2\nu\left(I_{\text{cable}}\right)_{\text{Model-scale}} \qquad [\text{kg m}^{-2}\,\text{s}^{-1}] \tag{7.29}$$

$$b_{\text{mp}} = 2\nu_{\text{mp}}(m + a) \quad : 2\nu\left(I_{\text{mp}} + I_{\text{int}} + I_a\right)_{\text{Model-scale}} \qquad [\text{kg m}^{-2}\,\text{s}^{-1}] \tag{7.30}$$

7.5. Model

The numerical model is implemented using the Python programming language. The model's structure and workflow are visualized in a flowchart, depicted in figure 7.6. The flowchart provides an overview of the steps involved in the numerical model, showing the sequence of operations and its data flow. The numerical model generates a series of plots and animations that provide valuable insights into the behavior of the system. These plots include the pitch angle, frequencies, and displacements for various scenarios. The animation is able to animate the MP as a double pendulum system, providing a visual representation of its dynamic behavior over time.

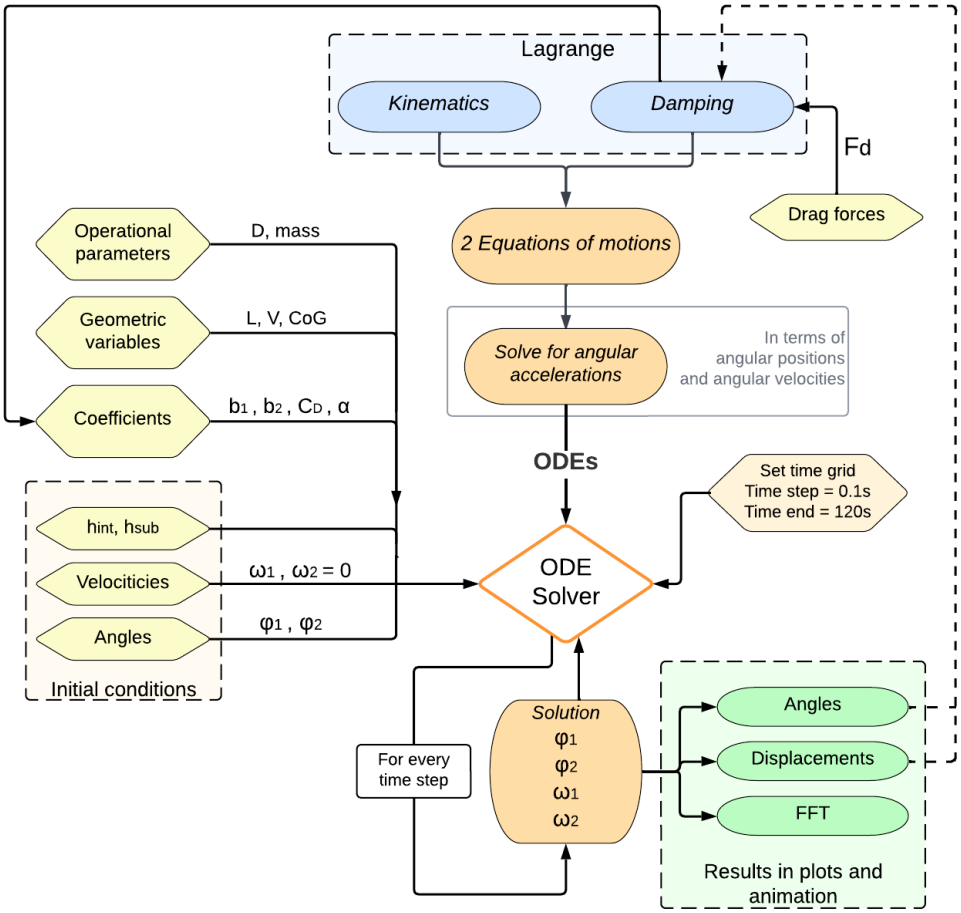

Figure 7.6: Flowchart of the numerical model written in Python

The solution to the equations of motion 7.26 and 7.27 is obtained by converting the equations into a first-order differential equations. These ODEs can be solved numerically using the 'odeint' solver from the 'scipy' package. The solver requires several inputs to compute the numerical solution. These inputs include the set of differential equations that describe the system, initial conditions for the variables and a time array that defines the desired time range for the solution. Once the inputs are provided, the solver applies the Runge-Kutta LSODA algorithm to numerically integrate the differential equations and compute the solution over the specified time range.

By applying the ODE solver, the values of the angles ϕ_1 and ϕ_2 can be computed and analyzed over the specified time span. This approach provides insights into the system's behavior in the time domain, allowing for a comprehensive understanding of how the angles change and evolve over time.

7.5.1. Scaled model characteristics

To validate and refine a numerical model, the obtained scaled model test data can be used to calibrate the model's parameters. This involves adjusting the numerical model's parameters to match the observed behavior and response of the scaled model during the experiments. This approach is meant to validate the numerical model's accuracy and reliability. If the calibrated numerical model can accurately predict the behavior of the scaled model, it provides confidence in using the model to simulate the behavior of the full-scale system under different conditions and scenarios.

Drag coefficient

The drag coefficient for the specific model in the experiments can be derived using the definition of the Reynolds number. The definition for the Reynolds number is stated in equation 2.3 and includes the maximum horizontal particle velocity of the current, u_m. The velocity of the MP w.r.t. to the fluid is found to be the highest for the lowest submergence with the presence of an internal water column. Figure 7.7 represents the x-displacement for the configuration $h(10,10)$.

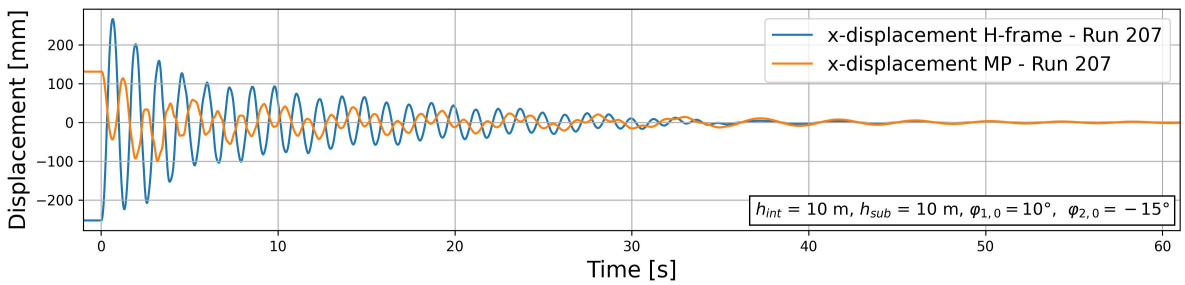

Figure 7.7: Model test run - x-displacement vs. time for $h(10,10)$ (Run 207)

The maximum horizontal velocity can be calculated as the steepest slope of the x-displacement of the bottom of the MP (orange) over time. The maximum horizontal velocity is estimated as approximately $u_m \approx 0.40\,\mathrm{m\,s^{-1}}$. The kinematic viscosity of fresh water at 20°C is taken from table 2.1 and is equal to $\nu_f = 1.00 \cdot 10^{-6}$. With D = 0.168m, this results in the following Reynolds number:

$$Re = \frac{u_m \cdot D}{\nu_f} = 6.72 \cdot 10^4 \qquad [\,-\,] \qquad (7.31)$$

With the given Reynolds number, the flow regime can be derived from figure 2.5 and is considered subcritical. In this regime, the approximate value for the drag coefficient for a smooth cylinder $C_D \approx 1.2$. The Reynolds number for each configuration can be found in table 6.9.

Damping

The damping coefficients obtained in this study serve as an approximation of the damping behavior of the system. To better match the numerical damping to the observed damping in the experiments, the damping coefficients can be fitted. The red cross terms in the damping matrix (equation 7.32) indicate the coefficients that were varied during the fitting process. Through experimentation, it was found that multiplying these coefficients by a factor of 0.1 yielded the best results in terms of achieving a closer match to the observed damping characteristics of the signals. This adjustment allows for a more accurate representation of the system's damping behavior in the numerical model.

$$\begin{bmatrix} b_1 + b_2 & -b_2 \\ -b_2 & b_2 + c\,l_d^2 \left| l_d \dot{\phi}_2 \right| \end{bmatrix} = \begin{bmatrix} b_{\mathrm{Hframe}} + b_{\mathrm{mp}} & -b_{\mathrm{mp}} \\ -b_{\mathrm{mp}} & b_{\mathrm{mp}} + c\,l_d^2 \left| l_d \dot{\phi}_2 \right| \end{bmatrix} \qquad (7.32)$$

8

Numerical results

This chapter presents the results obtained from the numerical model. The results from the numerical simulations provide insights into the system's response, including the oscillation frequencies, periods and other relevant characteristics.

8.1. Numerical model - Scaled

To validate the numerical model, the experimental data obtained from the model tests needs to be used for fitting the model. This process involves trying to fit the model parameters, such as inertia, drag, and damping coefficients, in order to achieve a good fit between the model predictions and the measured data. The results of the numerical simulations compared to the model test data for each configuration can be found in Appendix G.3.1.

8.1.1. Excluding hydrodynamic effects

By examining the results in dry conditions, a baseline is established for comparison when introducing submergence and hydrodynamic influences. This enables a direct assessment of the effects of submerging the MP on the system's response. Furthermore, it serves as a basis for verifying the kinematics and describing the system analytically using the Lagrangian formulation. Figures 8.1 illustrates a comparison between the pitch angles ϕ_1 and ϕ_2 obtained from the experimental test run in dry conditions and the numerical model with the same initial conditions. The pitch angle ϕ_1 corresponds to the side lead angle at the crane tip, which represents the angle of the cable (H-frame). The angle ϕ_2 represents the angle that the MP makes with respect to the vertical.

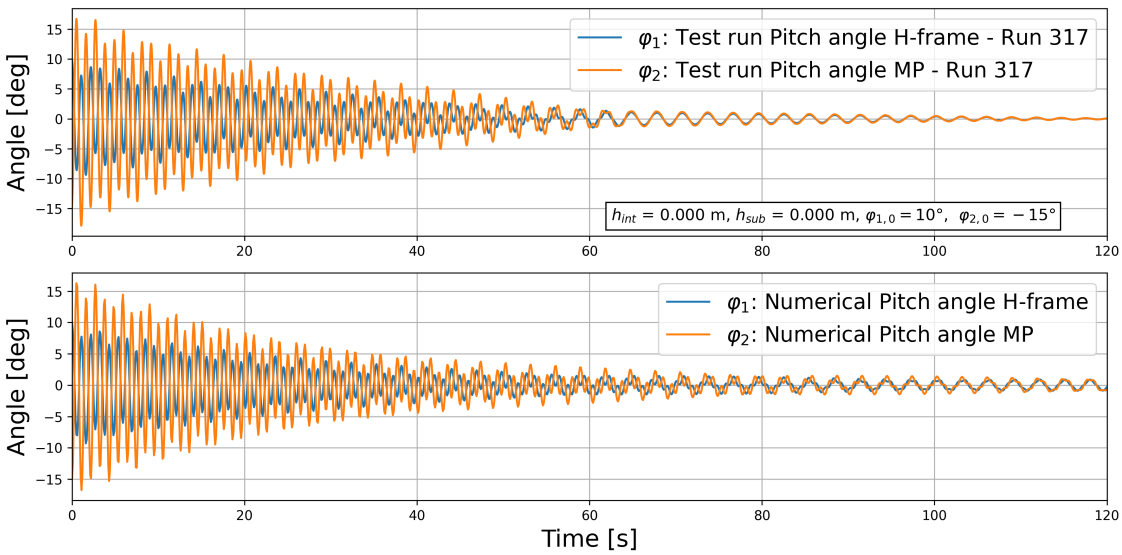

Figure 8.1: Test run pitch angles (Run 317) and Numerical pitch angles on model scale for $h(0,0)$

Figure 8.1 demonstrates a good resemblance between the numerical model and the experimental data, indicating a reasonably accurate representation of the system's response. However, it is convenient to examine the response of the cable and the MP separately. Figure 8.2 displays the responses of both pitch angles, ϕ_1 and ϕ_2, over a time period of 60 seconds. The figure clearly shows the agreement between the numerical approximation and the actual response observed in the experiments.

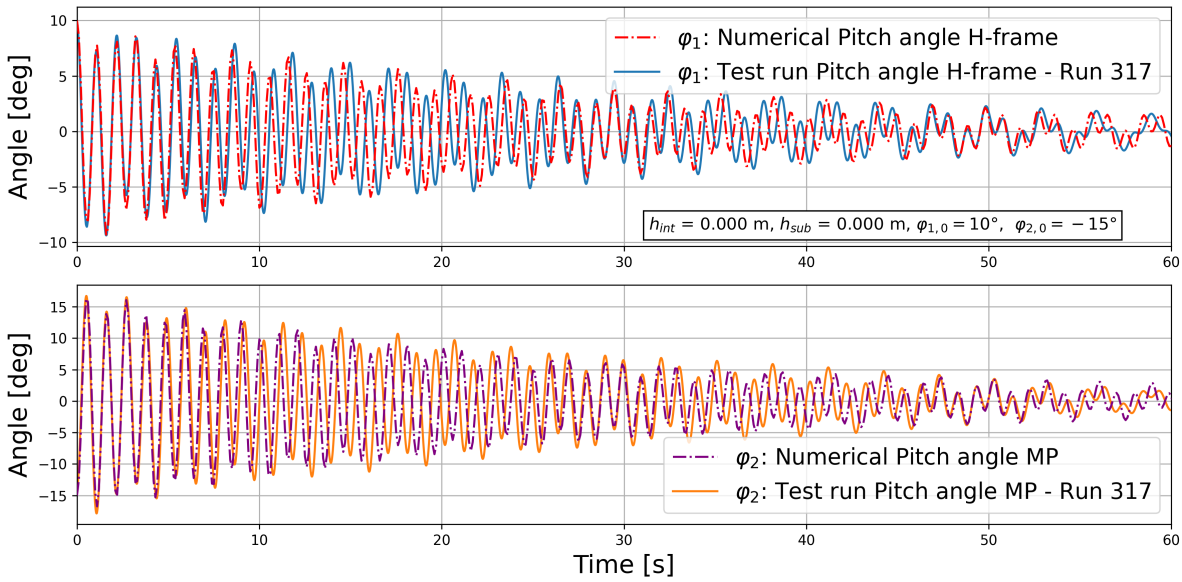

Figure 8.2: Test run (Run 317) vs. Numerical pitch angles for $h(0,0)$ on model scale, for large initial angles

In order to quantify the observed signals, a frequency analysis conducted. Figure 8.3 shows the Fourier transform of the pitch signal from the experiment. Similarly, figure 8.4 displays the Fourier transform of the numerical pitch angle approximation in dry conditions. Both frequency spectra indicate the presence of different frequency components in the signal.

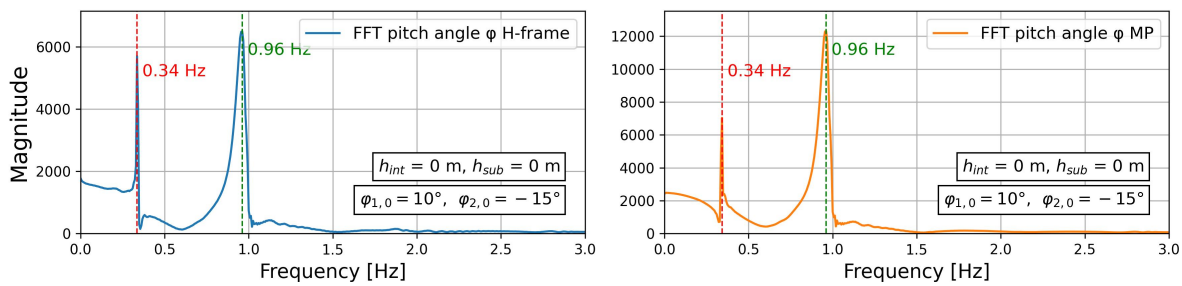

Figure 8.3: Test run (Run 317) - FFT for pitch motion for $h(0,0)$, for large initial angles

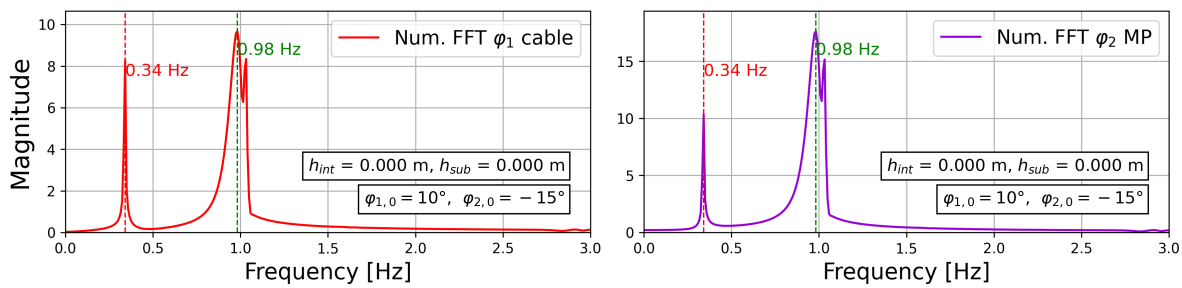

Figure 8.4: Numerical model - FFT for pitch motion for $h(0,0)$, for large initial angles

The presence of two prominent peaks with the same frequency in both frequency analyses suggests that the signal characteristics have been accurately captured and modeled. This observation provides evidence that the numerical approach models the dominant frequencies present in the system's response, quite ac-

curately. The absence of hinge friction in the numerical model results in the signal not damping out as observed in the test results, as discussed in Appendix G.3.1.

8.1.2. Including hydrodynamic effects

This section presents the results of the partial submergence of the MP, taking into account the hydrodynamic effects. It was observed that when these effects were included, the approximation of the natural frequency remained consistent when considering large or small initial angles. However, it was found that small initial angles resulted in a more precise approximation of the natural frequency. Figure 8.5 depicts the results of the experimental test run for the configuration $h(10,20)$, considering small initial angles.

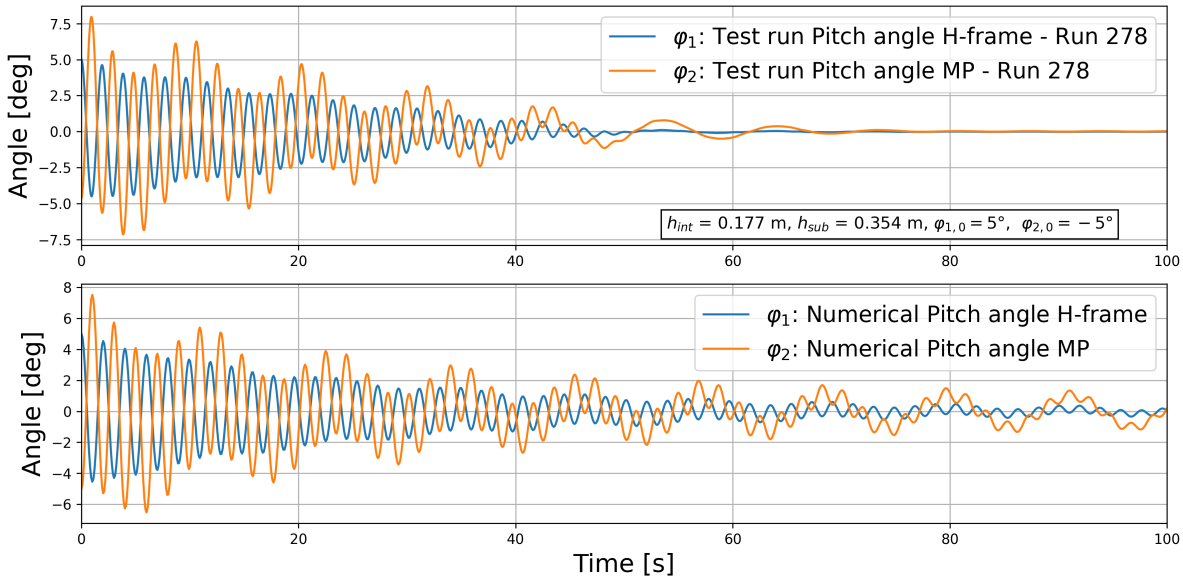

Figure 8.5: Test run pitch angles (Run 278) and Numerical pitch angles for $h(10,20)$, for small initial angles

It is evident that the damping behavior of the numerical approximation of the pitch angles is less accurate considering small initial angles. This indicates that the inclusion of the damping may not be sufficiently accurate.

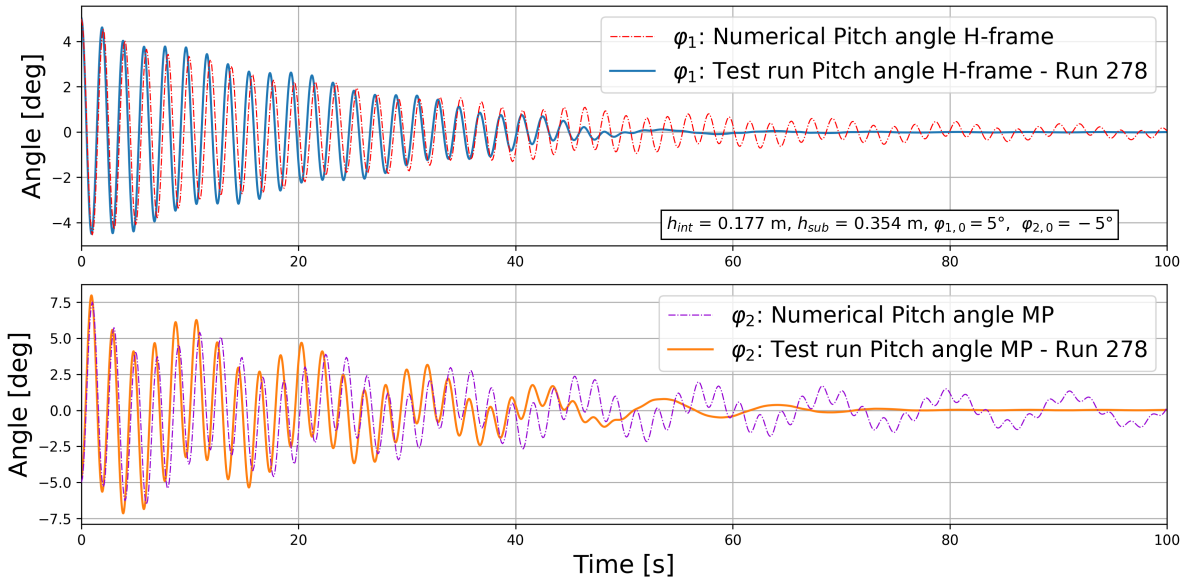

Figure 8.6: Test run (Run 278) vs. Numerical pitch angles for $h(10,20)$ on model scale, for small initial angles

A frequency analysis was conducted to analyze the frequency content of the pitch signal from the experiment and the corresponding numerical approximation for the configuration $h(10,20)$. Figure 8.7 shows the Fourier transform of the pitch signal obtained from the experiment, while figure 8.8 presents the numerical

approximation. These figures allow for a comparison of the frequency content between the experimental data and the approximation of the numerical model.

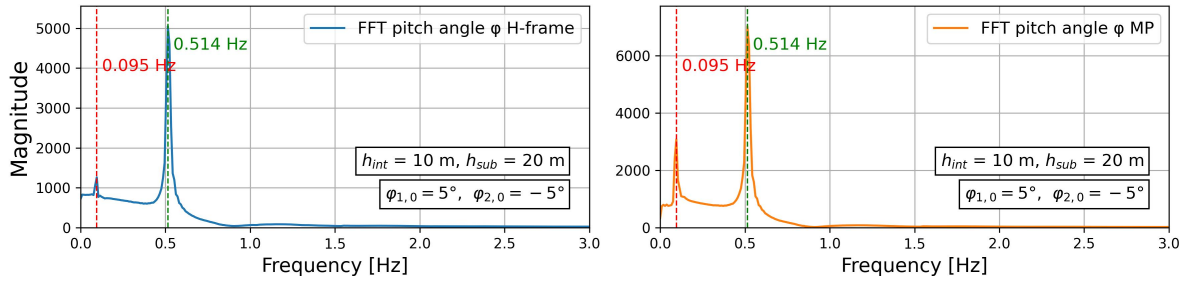

Figure 8.7: Test run (Run 278) - FFT for pitch motion for $h(10,20)$, for small initial angles

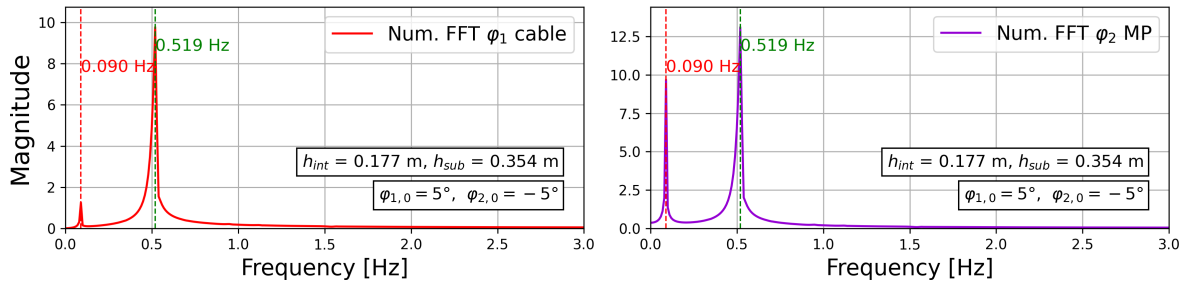

Figure 8.8: Numerical model - FFT for pitch motion for $h(10,20)$, for small initial angles

From the comparison of frequencies between the numerical model and the experimental results, it can be concluded that the numerical model accurately captures the natural frequency of the system, especially for smaller initial angles. The numerical approximations with both the small and large initial angles can be found in Appendix G.3.1. It should be mentioned that the damping defined for these approximations, potentially leads to a decrease of the natural period over time. This range of frequencies present in the numerical approximation should be accounted for.

Furthermore, it is observed that the frequency range considering small initial angles is narrower, indicating a higher level of precision in capturing the system's natural frequency. This phenomenon can be attributed to the mathematical approximation used in the numerical model. The use of the small angle theorem results in smaller errors considering smaller angles. As a result, the accuracy but specifically the precision of the numerical model improves as the initial angles decrease. Additionally, lower initial angles correspond to lower velocities, leading to a reduced drag contribution to the damping effect. This contributes to a narrower frequency range in the pitch response of the system.

8.2. Numerical model - Full scale

With the validation of the numerical model using the experimental data, it is now possible to simulate the numerical model with full-scale parameters. This means that the model can be used to simulate the behavior of the system at a larger scale, considering the actual dimensions and properties of the full-scale scenario, as stated in table 3.1.

Inertia

To define the inertia in the system correctly, the inertia of the cable at full scale needs to be redefined. While in the model scale, the H-frame had a substantial weight and significantly contributed to the mass and inertia of the system, the cable at full scale has less impact on the overall inertia. The cable has a mass of 28t and is distributed over length l_1. Therefore, the equation for the inertia of the cable can be expressed as follows:

$$J_{\text{cable}} = \frac{1}{12} m_{\text{cable}} l_1^2 \tag{8.1}$$

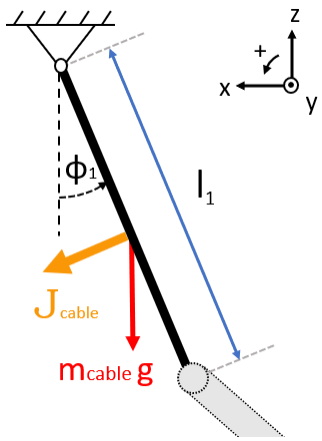

Figure 8.9: Simplification of the mass and inertia contribution of the cable

Damping

The linear damping coefficients for the full scale scenario are approximated using the following equations, as derived in section 7.4:

$$b_{\text{cable}} = 2\nu_{\text{cable}}(m+a) \quad : 2\nu\left(I_{\text{cable}}\right)_{\text{Full-scale}} \qquad [\text{kg m}^{-2}\,\text{s}^{-1}] \quad (8.2)$$

$$b_{\text{mp}} = 2\nu_{\text{mp}}(m+a) \quad : 2\nu\left(I_{\text{mp}} + I_{\text{int}} + I_a\right)_{\text{Full-scale}} \qquad [\text{kg m}^{-2}\,\text{s}^{-1}] \quad (8.3)$$

where ν represents the value for the decay rate obtained through the experiments. By defining the inertia of the full-scale scenario, the damping coefficients b_{cable} and b_{mp} can be calculated and can be found in Appendix G.4.

8.2.1. Excluding hydrodynamic effects

First, the full-scale scenario without hydrodynamic effects is examined in Figure 8.10. The results are obtained by incorporating the full-scale dimensions of the MP into the numerical model. The accuracy of the numerical approximation on the model scale with small initial angles provides high confidence in the outcome of the full scale scenario. The frequency content is illustrated by the use of an FFT in figure 8.11, highlighting two prominent peaks of both modes. This observation aligns with the pitch signal depicted in figure 8.10.

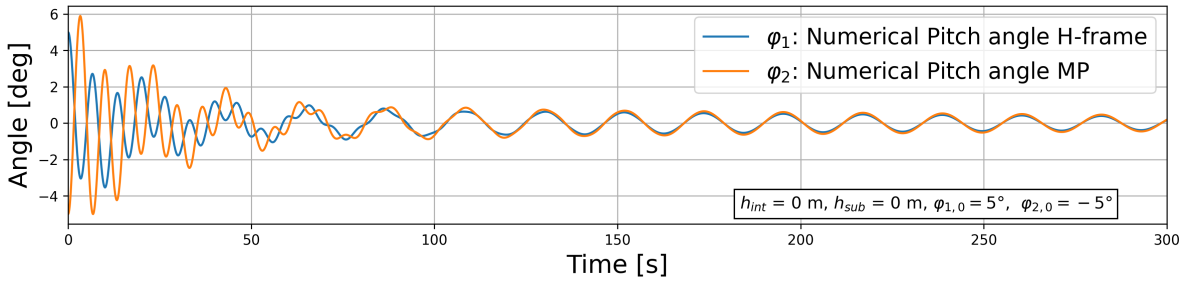

Figure 8.10: Numerical pitch angle for $h(0,0)$ on full scale, for small initial angles

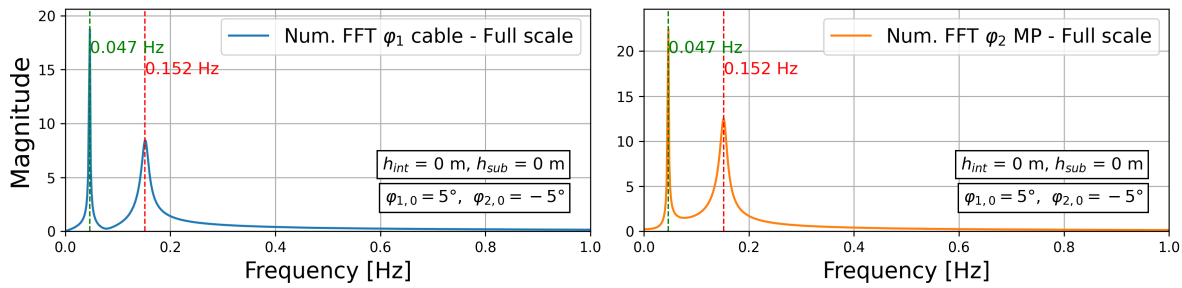

Figure 8.11: Numerical model - FFT for pitch motion for $h(0,0)$ on full scale, for small initial angles

8.2.2. Including hydrodynamic effects

When taking into account the hydrodynamic effects on a full-scale scenario, the period of oscillation is much higher. This is in correspondence to the observations of the model test results. One notable difference is that the pitch signal of the cable (blue) does not show large oscillations in the low frequency mode, unlike the response of the MP (orange). When observing figure 8.10, both angles eventually align with each other and both oscillate in the low-frequency mode.

The frequency analysis in figure 8.13 shows a decrease in the natural frequency of the system when hydrodynamics are considered. Additionally, a more prominent peak of the low-frequency mode is observed for the MP compared to the FFT of the cable's pitch angle.

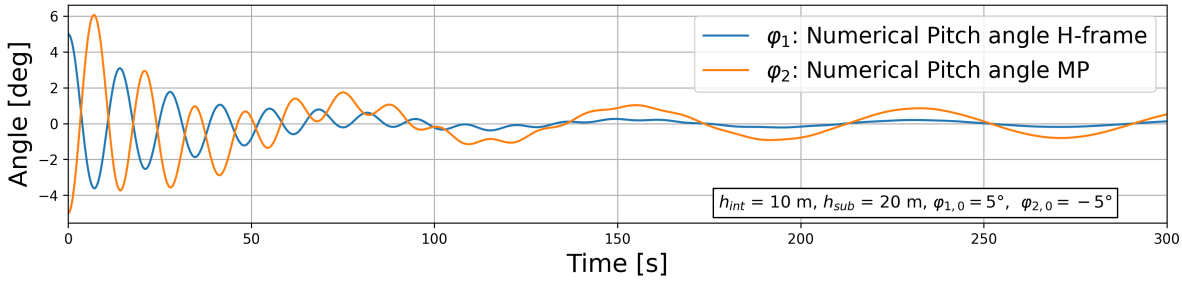

Figure 8.12: Numerical pitch angle for $h(10,20)$ on full scale, for small initial angles

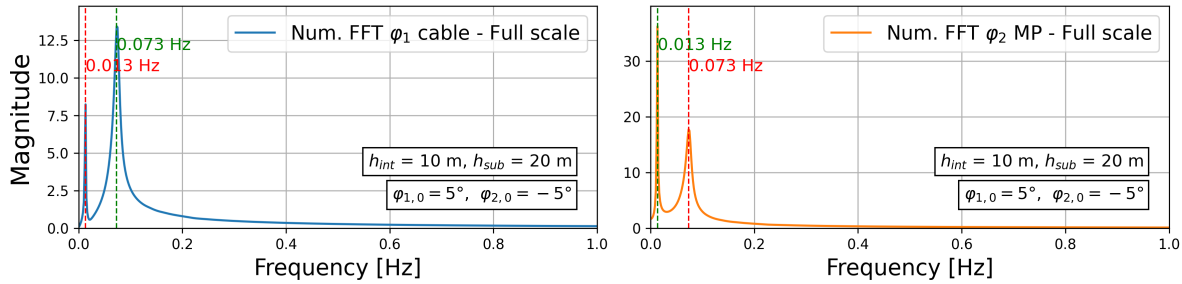

Figure 8.13: Numerical model - FFT for pitch motion for $h(10,20)$ on full scale, for small initial angles

8.3. Conclusion

To provide remarks on the outcome of the numerical simulations, a comprehensive comparison needs to be made with all three approaches used throughout this research:

1. Analytical model results
2. Model test results
3. Numerical model results for *large* initial angles
4. Numerical model results for *small* initial angles

Natural frequency assessment

To assess the accuracy of the numerical model capturing the dynamics of the full scale scenario, validation can be performed by comparing the results with those obtained from the analytical model, discussed in Chapter 3 and the observed frequencies during the model test, presented in Chapter 6. Tables 8.1 and 8.2 provide the comparison of the frequencies obtained trough all three methods, for the low- and high frequency mode respectively. These tables serve to evaluate the consistency between the analytical model, the numerical model and the model test results.

It can be observed that the approximation of the analytical and numerical model closely align with the scaled natural frequencies of the model experiments. Furthermore, the numerical approximation considering small angles shows the consistency and accuracy in determining the natural frequencies of the system.

Table 8.1: Comparison frequencies of Analytical model vs. Model test result vs. Numerical model - **Mode 1**

Unit [Hz]	**Analytical model**	**Model tests results**		**Numerical model** *Large initial angles*		*Small initial angles*	
Configuration	f_{real}	f_{model}	f_{real}*	f_{model}	f_{real}	f_{model}	f_{real}
$h(0,0)$	0.046	0.335	0.045	0.341	0.045	0.340	0.047
$h(0,10)$	0.015	0.150	0.020	0.133	0.015	0.140	0.015
$h(10,10)$	0.027	0.219	0.029	0.208	0.027	0.210	0.027
$h(10,20)$	0.013	0.103	0.014	0.090	0.013	0.090	0.013
$h(20,20)$	0.021	0.165	0.022	0.158	0.022	0.160	0.022
$h(20,30)$	0.012	0.090	0.012	0.083	0.012	0.080	0.012
$h(30,30)$	0.018	0.135	0.018	0.133	0.018	0.130	0.018

* Model test frequency scaled using eq. 6.9 and scalefactor $\lambda = 56.5$

Table 8.2: Comparison frequencies of Analytical model vs. Model test result vs. Numerical model - **Mode 2**

Unit [Hz]	**Analytical model**	**Model tests results**		**Numerical model** *Large initial angles*		*Small initial angles*	
Configuration	f_{real}	f_{model}	f_{real}*	f_{model}	f_{real}	f_{model}	f_{real}
$h(0,0)$	0.153	0.961	0.128	0.983	0.150	1.039	0.152
$h(0,10)$	0.077	0.594	0.079	0.591	0.075	0.599	0.077
$h(10,10)$	0.124	0.781	0.104	0.808	0.120	0.829	0.122
$h(10,20)$	0.075	0.516	0.069	0.490	0.072	0.519	0.073
$h(20,20)$	0.118	0.742	0.099	0.691	0.112	0.779	0.117
$h(20,30)$	0.074	0.477	0.063	0.441	0.070	0.500	0.072
$h(30,30)$	0.112	0.716	0.095	0.658	0.102	0.719	0.110

* Model test frequency scaled using eq. 6.9 and scalefactor $\lambda = 56.5$

Model scale

It can be concluded that the numerical model has been successfully validated using the scaled model dimensions. The natural frequencies obtained from the model experiments closely match the observed frequencies. A comparison between the frequencies obtained from the model experiments and the numerical approximations for the model scale is presented in figure 8.14. The frequency range for each of the three approaches is determined and presented in tables G.1 and G.2. These absolute frequency ranges are visualized in the figures below and demonstrate the accuracy and precision of the results.

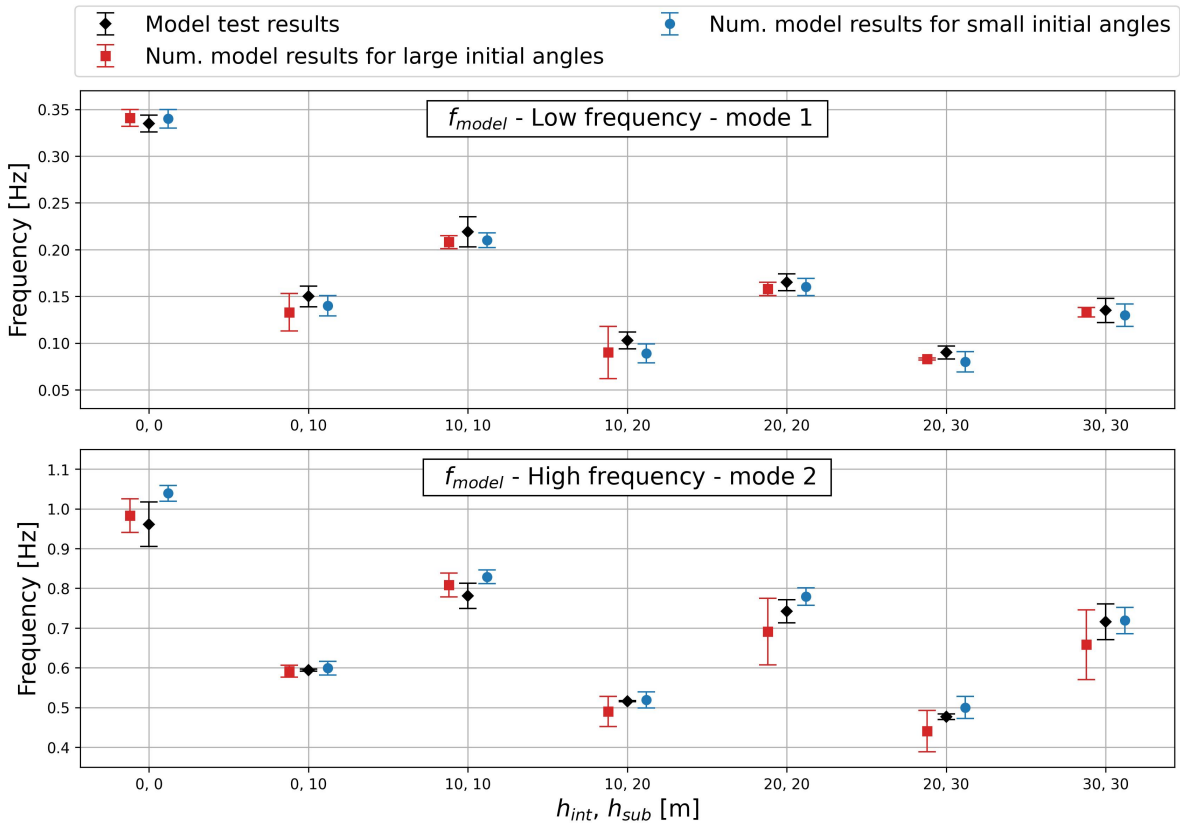

Figure 8.14: Comparison of **model scale** frequencies of the Model tests vs. Numerical model

From figure 8.14, it can be observed that both numerical models exhibit a similar level of accuracy in capturing the natural frequencies of the system. However, the numerical model considering small initial angles appears to have slightly higher precision, as indicated by the narrower frequency range and sharper peak in the FFTs in Appendix G. This suggests that the numerical model with small initial angles provides a more precise estimation of the system's frequency response.

Full scale

As found, the numerical model considering small initial angles provides more confidence in simulating the dynamics and determining the natural frequencies of full-scale scenarios. Figure 8.15 visualizes the frequency comparison made between the three approaches. The frequencies corresponding to the low-frequency mode exhibit a close alignment, indicating a consistent trend across the different configurations. The approximations for the second, high-frequency mode demonstrate a lower level of accuracy compared to the low-frequency mode. However, the overall alignment between the three approaches provides confidence in the accuracy of the numerical model used to predict both modes of the system.

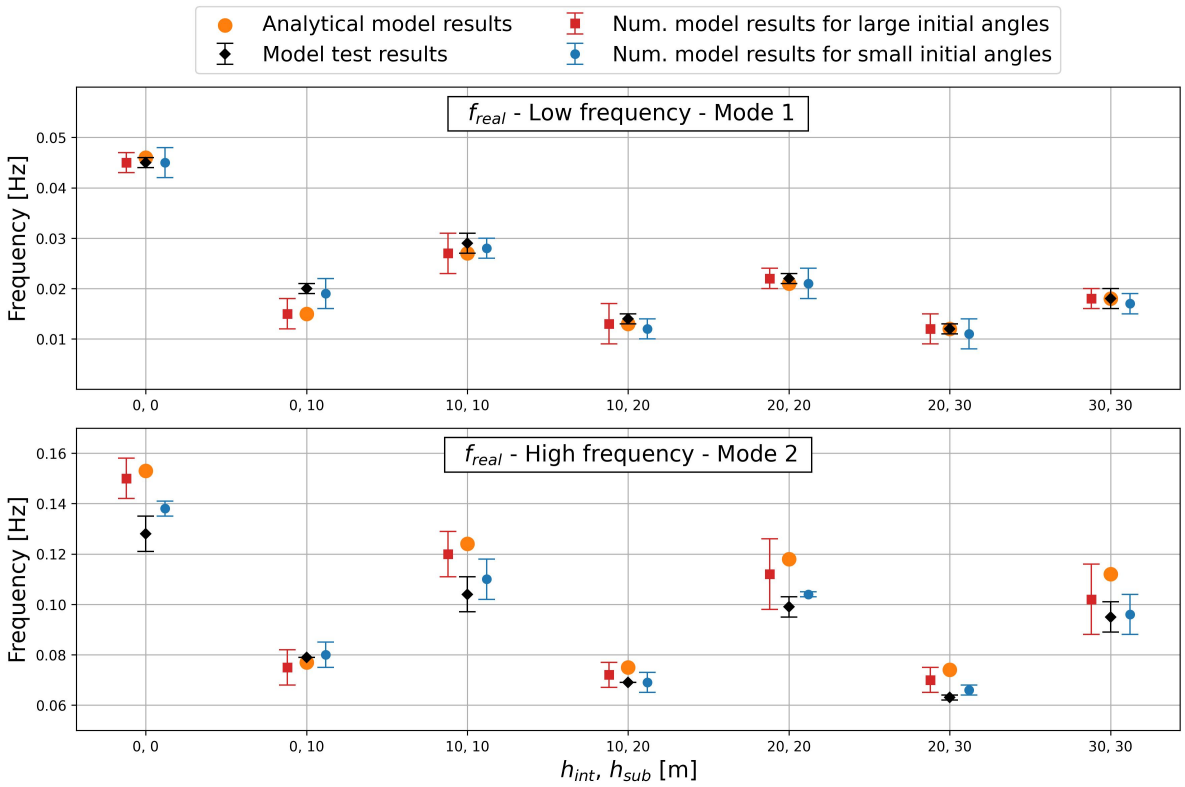

Figure 8.15: Comparison of **full scale** frequencies of the Analytical model vs. Model tests vs. Numerical model

Furthermore, the approach considering small initial angles exhibits higher precision and accuracy for the numerical approximations of the natural frequencies for each configuration. Note that high the natural frequencies obtained through the analytical approach, which does not incorporate damping, significantly deviates from the model test results. This difference highlights the importance of accurately modeling the damping present in the system. The damping in the numerical model is also not fully accurate since it does not account for the friction present hinges. Additionally, the drag contribution in the system of equations could also be slightly inaccurate and could lead to deviations in the model's predictions. However, the model does approximate the overall damping behavior reasonably well.

As observed in the model experiments and in the numerical approximations for the scaled model, the buoyancy exerted on the system has a significant influence on its natural frequency. An increase of the buoyancy leads to a longer natural period, which subsequently decreases the natural frequencies that govern the system's behavior.

The close agreement observed between the natural frequencies predicted by the analytical model, numerical model and the observed frequencies provides strong evidence that the numerical model accurately captures the system's key dynamic characteristics, especially in the high-frequency range. The consistency and accuracy of the numerical model make it a valuable tool for analyzing and predicting the dynamic response of the system.

9 Conclusions

Several final remarks can be made to conclude this research and reflect upon the objectives outlined in Chapter 1. The primary objective of this research is to investigate the natural frequencies of a semi-floating monopile, gain insights into the important parameters and quantify the workable limits. The research question that defined the scope and direction of this study was:

What is the behavior of a semi-floating monopile during the most critical stage of upending, using the concept of trapped air?

To address the main research question, several sub-questions have been formulated. The following questions include the key elements that lead this research and will be discussed individually.

1. Which equations of motion represent the simplified system and how do the various components influence the system's natural frequency?

The equations of motion for such a complex system cannot be obtained directly. Therefore, the primary focus in addressing the first research question was on analyzing multiple simplified versions of the real situation. Based on the analytical assessment of the natural frequencies, the following conclusions are drawn:

- The double pendulum model including inertia was found to be the best representation of reality. The calculated natural frequencies align closely with expected values in offshore conditions. The inertia terms turned out to have significant influence on the dynamics of the system.
- The added mass and its inertia doe not influence the natural frequency significantly. However, the other inertia terms have a substantial impact on reducing the natural frequency, which aligns with the expectations.
- The critical zone (T = 6-8s) was only reached for no internal water column and within the first couple meters of submergence. As the monopile was further lowered to the seabed, the natural periods increased to 10-20 seconds, thereby increasing the workability of the concept.
- It was found beneficial to fill the monopile and increase the internal water column while in the 10-15 meters of submergence. This filling process results in an increase of the natural period, providing a practical solution to avoid entering the critical zone.

Based on the analytical approach, model experiments can be used to validate the calculated frequencies and serve as a foundation for the development of a numerical model.

2. How will the scaled monopile behave during different decay tests and can the limiting factors be determined?

The second research question was initially addressed through simple exploratory tests,leading to the following key observations:

- Under an applied current, excessive motions of the MP were observed in the sway direction, suggesting the presence of vortex-induced motions.
- It was observed that, when hydrodynamic effects were introduced into the system, the CoG immediately shifted towards the waterline, or just below the waterline. These observations were primarily qualitative in nature, quantitative assessments can be made during the model tests.
- The MP deviating from its equilibrium during lowering indicates a maximum submergence threshold due to an excessive buoyancy force. The main conclusion is that the water level difference should not become too large. By maintaining and controlling this water level difference between the inside and outside of the MP, a smooth lowering of the MP can be achieved.

Following the exploratory tests, model experiments provide a valuable dataset and a more comprehensive understanding of the behavior of the MP. The following remarks can be made:

- The inclusion of buoyancy leads to a significant lower natural frequency of the system.
- The maximum allowable buoyancy force should be approximately X%-Y% of the gravitational forces to avoid the MP from deviating from its vertical position. This corresponds to a maximum water level difference of approximately X meters for the MP considered in this research.
- It is challenging whether the side-lead angles will be exceeded, because decay tests were conducted without subjecting the system to an external input frequency. However, the measured loads in the cranetip serve as a limiting factor. The presence of buoyancy in the system reduces the horizontal load to X%-Y% of the maximum allowed side-lead of Xt. This is almost half of the horizontal loads experienced without buoyancy. The vertical loads in the crane tip are reduced to X%-Y% of the maximum allowed vertical loads at an operating radius of Xm. The presence of buoyancy effectively reduces the loads experienced in the cranetip and therefore increases the workability of the concept.
- Large yaw angles coincide with large x-y offsets of the MP, suggesting a relationship between the two.

The third question can be addressed by the comparison and validation of the numerical simulations with the data obtained from the model experiments.

3. Can numerical simulations accurately reproduce the behavior of the scaled monopile observed in the experiments and predict its behavior in full-scale scenario's?

The numerical model is developed based on the defined kinematics derived from the analytical approach. It can be concluded that the numerical model successfully captures the system's dynamics. The close correspondence between the numerical approximation and the experimental response, validates the accuracy and reliability of the numerical model in simulating the natural frequencies of the scaled MP in different circumstances.

However, it should be noted that the modeled damping behavior in each configuration does not accurately match the desired behavior. Several factors could contribute to this discrepancy, including the linear approach used to determine the decay of the signals, the absence of hinge friction in the numerical model or the process of fitting the damping coefficients. Further improvements in these areas may help achieve a more accurate representation of the damping behavior in future models.

Following the successful validation of the numerical model that accurately reproduces the dynamics observed in the model experiments, it can be used to simulate the dynamics of a full-scale MP. The contribution of the cable's inertia to the system behavior is significantly smaller, which leads to a more accurate representation of reality compared to the model experiments. The frequencies observed in the model-scale experiments, scaled to full-scale, closely match those calculated using both the analytical and numerical models. This consistency provides confidence in the accuracy of the numerical model and its ability to capture the natural frequencies of the system.

In conclusion, the close agreement between the frequencies predicted by the analytical model, the numerical model, and the observed frequencies during the model experiments indicates that the numerical model accurately captures the system's dynamic behavior, especially for small initial angles. This alignment reinforces the reliability of the analytical model and the numerical model, providing a solid foundation for analyzing similar systems.

10 Recommendations

This chapter presents recommendations for future research, divided into two parts. First, recommendations regarding the modeling experiments are presented, followed by suggestions for potential improvements in the numerical approximations.

The model experiments are conducted in two dimensions provide valuable insights, but adopting a three dimensional approach in the analysis and modeling would offer a more accurate representation of the system's dynamics. Without the MP being constrained in its movements in six degrees of freedom, factors such as yaw angles, sloshing and vortex-induced motions can be more accurately captured. These phenomena require closer examination and attention.

Exploring alternative approaches to simulate trapped air in experimental tests could enhance the validity of the findings. The experimental test setup, which featured a closed bottom, may not fully capture the behavior of the system in real-world scenarios where the monopile has an open bottom and closed top. Conducting experiments with an open bottom configuration could lead to different observations. The model experiments yielded a comprehensive dataset consisting of over 100 qualitative tests but further extensive data analysis is required to find additional patterns and relationships within the collected data.

Future research should prioritize dynamic tests of the upending procedure or at different stages of inclination. Additionally, it would be beneficial to incorporate waves as input to capture the system's response and validate the natural frequencies obtained in this study. By integrating wave conditions into the numerical model, a more comprehensive understanding of the monopile's response to varying wave conditions can be achieved, strengthening the foundation for executing full-scale operations.

Further refinement of the numerical model is necessary to address certain approximations and assumptions made in the current formulation. These include considering point masses, assuming the internal water column as a rigid water body and excluding hinge friction from the numerical simulations. One important aspect that needs to be accounted for is the effect of sloshing in the internal water column, which is currently not included in the model. To improve the representation of sloshing, an additional pendulum model can be integrated within the MP simulate the motion of the water column. This will potentially provide a more accurate representation of the system's behavior. Furthermore, the drag coefficient is determined trough the literature, model experiments to obtain these coefficients could provide better approximations.

In this research, the linear damping coefficient was used as an approximation to model the damped behavior of the pitch signal. However, it is important to investigate whether linear damping coefficients are applicable and sufficient to capture the damping characteristics of signals with non-linear interactions.

It is important to note that while the close agreement between the models and observed frequencies is encouraging, it is still necessary to conduct thorough validation and verification studies. This may involve comparing the numerical predictions with additional experimental data or comparing against other analytical or numerical approaches. These validation efforts help further confirm the accuracy and reliability of the numerical model.

A

Kinematics and derivations

This chapter presents the work done on the kinematics of the simplified systems. For each of the following pendulum models, the small-angle approximation is used to simplify the kinematics of the system. This method is applicable because small rotations are assumed and the approximations below are to be valid. This method is stated in chapter 3 and for these particular systems, equation 3.12 can be written as follows:

$$\begin{aligned} \sin(\phi_1), \quad \sin(\phi_2) &\approx \phi_1, \quad \phi_2 \\ \cos(\phi_1), \quad \cos(\phi_2) &\approx 1 \end{aligned}$$

Because the angles ϕ_1 and ϕ_2 present in the handled systems are assumed to be small, equation A.1 from chapter 3 can be rewritten as:

$$\begin{aligned} \phi_1^2, \quad \phi_2^2 &\approx 0 \\ \dot{\phi}_1^2, \quad \dot{\phi}_2^2 &\approx 0 \\ \phi_1\dot{\phi}_1, \quad \phi_2\dot{\phi}_2 &\approx 0 \\ \phi_1\ddot{\phi}_1, \quad \phi_2\ddot{\phi}_2 &\approx 0 \end{aligned} \tag{A.1}$$

A.1. Single pendulum - Vertical

The first system is only considering the motion of the monopile with point masses m_2 and m_{int} representing the mass of the MP and internal water column respectively. The buoyancy force is taken into consideration in every iteration of making the system more complex. In contrast to a floating installation vessel, a jack-up is hardly subjected to environmental conditions that cause motions of the vessel. Because of these negligible vessel motions, the jack-up vessel can be assumed to be fixed and the crane tip can be represented as a fixed support.

In this first case, the situation is simplified by a simple pendulum model where the MP is assumed to stay upright, a sketch can be found in figure A.1. In this first iteration, only the masses of the MP (m_2) and the internal water column (m_{int}) are considered. This simplifies the situation to a single pendulum with only two masses to account for. The system can be solved easily using the principle of virtual work because it only has one degree of freedom, the rotation of angle ϕ_1. When assuming small angle rotations, the small angle approximation is applicable. This single pendulum system serves as a basis because it contains only one degree of freedom and its kinematics provide a foundation for more complex analyses later on.

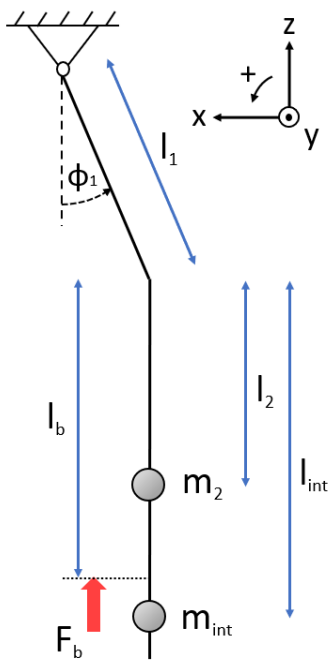

Figure A.1: Single pendulum - Vertical (for m_2 and m_{int})

Kinematics

The kinematics of a single vertical pendulum with mass m_2, m_{int} and buoyancy force F_b can be obtained in a simple manner. The kinematics for both masses and F_b are the same in this case and are presented below.

For m_2, m_{int} and F_b with l_1:

$$x = -l_1 \sin(\phi_1)$$
$$z = -l_1 \cos(\phi_1)$$

$$\dot{x} = -\dot{\phi}_1 l_1 \cos(\phi_1)$$
$$\dot{z} = \dot{\phi}_1 l_1 \sin(\phi_1)$$

$$\ddot{x} = -\ddot{\phi}_1 l_1 \cos(\phi_1) + \dot{\phi}_1^2 l_1 \sin(\phi_1)$$
$$\ddot{z} = \ddot{\phi}_1 l_1 \sin(\phi_1) + \dot{\phi}_1^2 l_1 \cos(\phi_1)$$

$$\delta x = -l_1 \cos(\phi_1)\delta\phi_1$$
$$\delta z = l_1 \sin(\phi_1)\delta\phi_1$$

Small angle approximation:

$$x = -l_1\phi_1$$
$$z = -l_1$$

$$\dot{x} = -\dot{\phi}_1 l_1$$
$$\dot{z} = \dot{\phi}_1 l_1 \phi_1 = 0$$

$$\ddot{x} = -\ddot{\phi}_1 l_1$$
$$\ddot{z} = \ddot{\phi}_1 l_1 \phi_1 = 0$$

$$\delta x = -l_1 \delta\phi_1$$
$$\delta z = l_1 \phi_1 \delta\phi_1$$

Principle of virtual work

The principle of virtual work is used to solve the relatively simple single pendulum model. To work with the kinematics, the displacement, velocity, acceleration and virtual displacement of the point masses and forces have to be determined. The kinematics and the principal of virtual work for this system can are presented below.

$$\begin{aligned}\delta T &= \delta x m_2 \ddot{x} + \delta z m_2 \ddot{z} + \delta x m_{\text{int}} \ddot{x} + \delta z m_{\text{int}} \ddot{z} \\ &= l_1^2 (m_2 + m_{\text{int}}) \delta\phi_1 \ddot{\phi}_1\end{aligned}$$

$$\begin{aligned}\delta V &= \delta z m_2 g + \delta z m_{\text{int}} g - \delta z F_b \\ &= l_1 \left((m_2 + m_{\text{int}})g - F_b\right) \delta\phi_1 \phi_1\end{aligned}$$

$$\begin{aligned}E &= \delta T + \delta V = 0 \\ &= l_1^2 (m_2 + m_{\text{int}}) \delta\phi_1 \ddot{\phi}_1 + l_1 \left((m_2 + m_{\text{int}})g - F_b\right) \delta\phi_1 \phi_1 = 0 \qquad \text{with } \delta\phi_1 = 1 \\ &= l_1^2 (m_2 + m_{\text{int}}) \ddot{\phi}_1 + l_1 \left((m_2 + m_{\text{int}})g - F_b\right) \phi_1 = 0 = 0\end{aligned}$$

$$M = l_1^2 (m_2 + m_{\text{int}}) \qquad K = l_1 \left((m_2 + m_{\text{int}})g - F_b\right)$$

The derived equation of the natural frequency without considering the related damping, is formulated as follows:

$$f_n = \frac{1}{2\pi}\sqrt{\frac{K}{M}} \quad = \frac{1}{2\pi}\sqrt{\frac{l_1\left((m_2 + m_{\text{int}})g - F_b\right)}{l_1^2 (m_2 + m_{\text{int}})}} \quad = \frac{1}{2\pi}\sqrt{\frac{(m_2 + m_{\text{int}})g - F_b}{l_1 (m_2 + m_{\text{int}})}} \quad [\text{s}^{-1}] \tag{A.2}$$

The principle of virtual work resulted in the equation of the natural frequency for this particular system. The units of K and M in this principle of virtual work can differ from the expected stiffness [N m^{-1}] and mass [kg] respectively. This is because these values in equation A.2 represent a virtual stiffness and a virtual mass. But if the numerator is considered, the restoring force is defined as the gravitational forces opposed by the upward buoyancy force. This makes sense considering the fact that there is no other mass or force present in this system.

The result is in accordance with the unit of the natural frequency [Hz]:

$$f_n = \frac{1}{2\pi}\sqrt{\frac{K}{M}} \quad = \frac{1}{2\pi}\sqrt{\frac{m \cdot (kg \cdot ms^{-2})}{m^2 \cdot kg}} \quad = \frac{1}{2\pi}\sqrt{\frac{kg \cdot m \cdot s^{-2}}{m \cdot kg}} \quad = \sqrt{s^{-2}} \quad = s^{-1} \quad = \text{Hz}$$

Results

This single pendulum model where the MP is assumed to stay vertical is the simplest model that can be created. As said earlier, this system can be solved easily because it only has one degree of freedom (ϕ_1) and consists of two masses and a buoyancy force. The results of the first natural frequency assessment are shown in figure A.2. From the results can be seen that the natural frequency of the system decreases over an increasing submerged length of the MP. This can also be concluded from the derivation shown in equation A.2. If the submerged length increases, the buoyancy force increases because F_b and h_{sub} are positively related. As can be seen in equation A.2, the buoyancy force is subtracted in the numerator and thus an increase in F_b results in a decrease of the natural frequency ω. It can therefore be concluded that the buoyancy force and the natural frequency are negatively related. It should be noted that a decrease in natural frequency is equivalent to an increase in the natural period of the system. This means that the natural period of the system is positively related to the buoyancy force, i.e. more buoyancy relates to a larger natural period.

Looking at the cases where h_{int} = 0 m and h_{int} = 10 m, it is interesting to see that the equation for the natural frequency is going to zero for a certain submerged length of the MP and the equation seems not valid anymore. This is the moment where the buoyant force is becoming too large and the numerator in equation A.2 becomes negative. A negative square root gives an imaginary result and cannot be depicted in the natural frequency graph. This can be related to the 'searching phenomenon' shown in figure 4.6 in section 4.2 where the submerged length of the MP is becoming larger while the internal water level does not change. In that case, the MP experiences a buoyant force larger than than the weight of the MP minus the lifting force. If this resultant force is positive upwards, the bottom of the MP will lift towards the sea surface and is of course an undesired situation. It is important to note that the length of the cable, denoted as l_1, is directly related to the submergence of the system. As the submerged length increases, the cable length also increases.

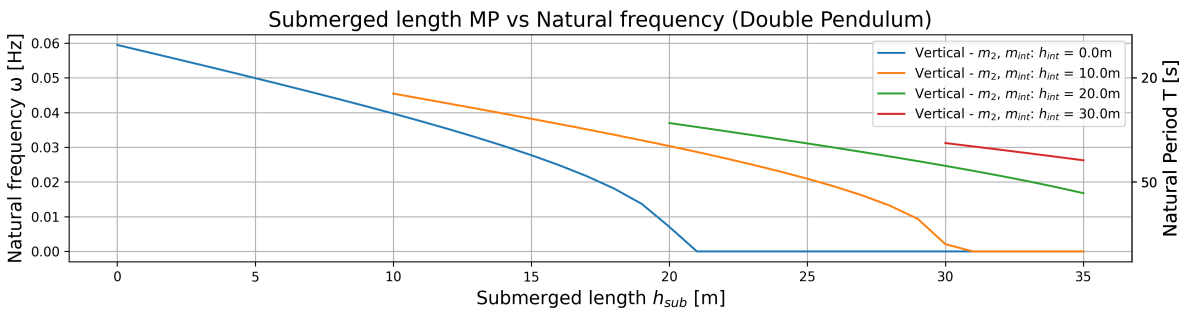

Figure A.2: Natural frequency vs submerged length for different h_{int}, considering m_2 and m_{int}

The natural frequency of this system is very low and therefore the natural period is rather high. An increase in the number of mass components will result in a different natural frequency behavior of the system. If the masses m_1, m_3 and the added mass component m_a are included, the equation becomes:

$$f_n = \frac{1}{2\pi}\sqrt{\frac{(m_1 + m_2 + m_3 + m_{\text{int}})g - F_b}{l_1(m_1 + m_2 + m_3 + m_{\text{int}} + m_a)}} \qquad [\text{s}^{-1}] \quad \text{(A.3)}$$

From equation A.3 can be seen that the components shown in red are added in a relatively easy way. The mass components are added to the numerator and denominator whereas the added mass component is only added to the latter. This is because the added mass component is only present in the kinetic energy T and therefore only ends up in the denominator M of the natural frequency equation. The natural frequency is expected to decrease faster over an increasing submerged length because the denominator increases significantly more than the nominator.

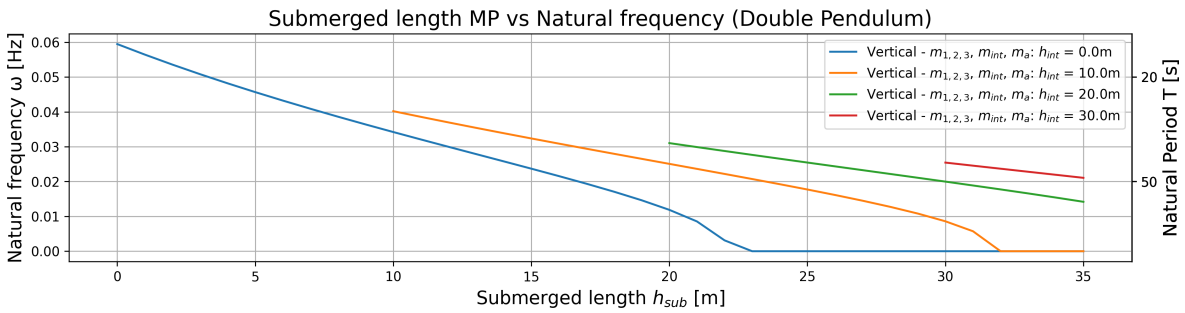

Figure A.3: Natural frequency vs submerged length for different h_{int}, considering $m_{1,2,3}$, m_{int} and m_a

The natural frequency behavior of the system including all components is shown in the figure above. As expected, the frequency declines faster over an increasing submerged length of the MP and is mainly because of the added mass component in equation A.3. The first approximation of the natural frequency of this single pendulum system is a good start, but it is not representing reality. An improvement of this system is a single pendulum where the MP is inline with the crane wire, taking into account the rotation of the MP.

A.2. Single pendulum - Inline

The next system is another single pendulum system in which the rotation of the MP is considered. In the system where the MP was assumed to stay vertical, the momentum of the mass of the MP and the water column were not taken into account. To improve the previous system and include the momentum that the MP experiences during the motion, a single pendulum system is investigated where the MP is in line with the crane wire. By doing so, the lengths at which m_2, m_{int} and F_b apply to, are extended with l_2, l_{int} and l_b respectively. This simplified system is depicted in figure A.4.

This second system can be solved easily and only consists of one degree of freedom, the rotation of angle ϕ_1. This system will give a good insight of the influence of the momentum of the MP. Again, this system is representing reality in adequately but it is an improvement of the first pendulum system.

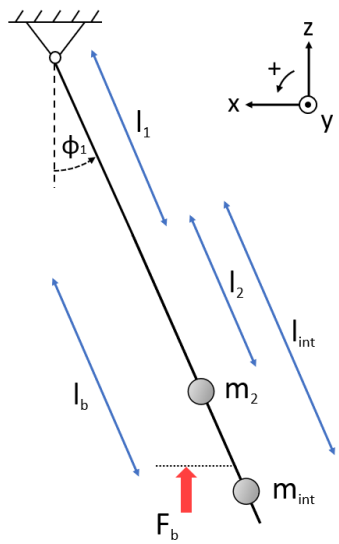

Figure A.4: Single pendulum - Inline (for m_2 and m_{int})

Kinematics

The kinematics of a single inline pendulum with masses m_2 and m_{int} can also be obtained quite simple and both are presented below.

For m_2 and m_{int} with $l_i = l_2, l_{\text{int}}$:

$$x_i = -(l_1 + l_i)\sin(\phi_1)$$
$$z_i = -(l_1 + l_i)\cos(\phi_1)$$

$$\dot{x}_i = -\dot{\phi}_1(l_1 + l_i)\cos(\phi_1)$$
$$\dot{z}_i = \dot{\phi}_1(l_1 + l_i)\sin(\phi_1)$$

$$\ddot{x}_i = -\ddot{\phi}_1(l_1 + l_i)\cos(\phi_1) + \dot{\phi}_1^2(l_1 + l_i)\sin(\phi_1)$$
$$\ddot{z}_i = \ddot{\phi}_1(l_1 + l_i)\sin(\phi_1) + \dot{\phi}_1^2(l_1 + l_i)\cos(\phi_1)$$

$$\delta x_i = -(l_1 + l_i)\cos(\phi_1)\delta\phi_1$$
$$\delta z_i = (l_1 + l_i)\sin(\phi_1)\delta\phi_1$$

Small angle approximation:

$$x_i = -(l_1 + l_i)\phi_1$$
$$z_i = -(l_1 + l_i)$$

$$\dot{x}_i = -(l_1 + l_i)\dot{\phi}_1$$
$$\dot{z}_i = (l_1 + l_i)\phi_1\dot{\phi}_1 = 0$$

$$\ddot{x}_i = -(l_1 + l_i)\ddot{\phi}_1$$
$$\ddot{z}_i = (l_1 + l_i)\phi_1\ddot{\phi}_1 = 0$$

$$\delta x_i = -(l_1 + l_i)\delta\phi_1$$
$$\delta z_i = (l_1 + l_i)\phi_1\delta\phi_1$$

For F_b with l_b:

$$z_b = -(l_1 + l_b)\cos(\phi_1)$$

$$\dot{z}_b = \dot{\phi}_1(l_1 + l_b)\sin(\phi_1)$$

$$\ddot{z}_b = \ddot{\phi}_1(l_1 + l_b)\sin(\phi_1) + \dot{\phi}_1^2(l_1 + l_b)\cos(\phi_1)$$

$$\delta z_b = (l_1 + l_b)\sin(\phi_1)\delta\phi_1$$

Small angle approximation:

$$z_b = -(l_1 + l_b)$$

$$\dot{z}_b = (l_1 + l_b)\phi_1\dot{\phi}_1 = 0$$

$$\ddot{z}_b = (l_1 + l_b)\phi_1\ddot{\phi}_1 = 0$$

$$\delta z_b = (l_1 + l_b)\phi_1\delta\phi_1$$

Principle of virtual work

The kinematics for this system differ from the single pendulum - Vertical. Here, the extended lengths l_2, l_{int} and l_b cause the kinematics to be a bit more complicated than the ones from the previous system. The application of virtual work with its corresponding kinematics can be found in appendix A.2. Using the general equation to find the natural frequency of the system, the following expression is found for an inline pendulum:

$$\begin{aligned}
\delta T &= \delta x_2 m_2 \ddot{x}_2 + \delta z_2 m_2 \ddot{z}_2 + \delta x_{\text{int}} m_{\text{int}} \ddot{x}_{\text{int}} + \delta z_{\text{int}} m_{\text{int}} \ddot{z}_{\text{int}} \\
&= \left(m_2(l_1 + l_2)^2 + m_{\text{int}}(l_1 + l_{\text{int}})^2\right)\delta\phi_1\ddot{\phi}_1 \\
&= \left(l_1^2(m_2 + m_{\text{int}}) + l_1(2m_2 l_2 + 2m_{\text{int}} l_{\text{int}}) + m_2 l_2^2 + m_{\text{int}} l_{\text{int}}^2\right)\delta\phi_1\ddot{\phi}_1
\end{aligned}$$

$$\begin{aligned}
\delta V &= \delta z_2 m_2 g + \delta z_{\text{int}} m_{\text{int}} g - \delta z_b F_b \\
&= m_2 g(l_1 + l_2)\delta\phi_1\phi_1 + m_{\text{int}} g(l_1 + l_{\text{int}})\delta\phi_1\phi_1 - F_b(l_1 + l_b)\delta\phi_1\phi_1 \\
&= \left(l_1(m_2 g + m_{\text{int}} g - F_b) + m_2 g l_2 + m_{\text{int}} g l_{\text{int}} - F_b l_b\right)\delta\phi_1\phi_1
\end{aligned}$$

$$\begin{aligned}
E &= \delta T + \delta V = 0 \\
&= \left(l_1^2(m_2 + m_{\text{int}}) + l_1(2m_2 l_2 + 2m_{\text{int}} l_{\text{int}}) + m_2 l_2^2 + m_{\text{int}} l_{\text{int}}^2\right)\delta\phi_1\ddot{\phi}_1 \\
&\qquad + \left(l_1(m_2 g + m_{\text{int}} g - F_b) + m_2 g l_2 + m_{\text{int}} g l_{\text{int}} - F_b l_b\right)\delta\phi_1\phi_1 = 0 \qquad \text{with } \delta\phi_1 = 1 \\
&= \left(l_1^2(m_2 + m_{\text{int}}) + l_1(2m_2 l_2 + 2m_{\text{int}} l_{\text{int}}) + m_2 l_2^2 + m_{\text{int}} l_{\text{int}}^2\right)\ddot{\phi}_1 \\
&\qquad + \left(l_1(m_2 g + m_{\text{int}} g - F_b) + m_2 g l_2 + m_{\text{int}} g l_{\text{int}} - F_b l_b\right)\phi_1 = 0
\end{aligned}$$

$$\begin{aligned}
M &= l_1^2(m_2 + m_{\text{int}}) + l_1(2m_2 l_2 + 2m_{\text{int}} l_{\text{int}}) + m_2 l_2^2 + m_{\text{int}} l_{\text{int}}^2 \\
K &= l_1(m_2 g + m_{\text{int}} g - F_b) + m_2 g l_2 + m_{\text{int}} g l_{\text{int}} - F_b l_b
\end{aligned}$$

$$f_n = \frac{1}{2\pi}\sqrt{\frac{K}{M}} \qquad = \frac{1}{2\pi}\sqrt{\frac{l_1\left((m_2 + m_{\text{int}})g - F_b\right) + (m_2 l_2 + m_{\text{int}} l_{\text{int}})g - F_b l_b}{l_1^2(m_2 + m_{\text{int}}) + 2l_1(m_2 l_2 + m_{\text{int}} l_{\text{int}}) + m_2 l_2^2 + m_{\text{int}} l_{\text{int}}^2}} \tag{A.4}$$

Results

The results from this single pendulum system can be seen in figure A.5. The behavior is roughly the same as the one in figure A.2 but there are some noteworthy differences. Because of the aforementioned increase in length, the movement of m_2 and m_{int} is extended. This decreases the natural frequency slightly and can be seen clearly in figure A.8 later in this section. Furthermore, the natural frequency goes to zero more rapidly than it did in the vertical pendulum system. These phenomena are caused by the additional length for the m_2, m_{int} and F_b in the K and M term. The length terms in M are quadratic and will therefore increase more than the K term. Since M is in the denominator of the equation, the frequency will decrease faster. At last, it should be noted that the blue line starts with a notable higher frequency. This is because in the case of $h_{\text{int}} = h_{\text{sub}} = 0$, the ratio $\frac{K}{M}$ becomes slightly larger than when h_{int} is not equal to zero and thus results in a higher frequency.

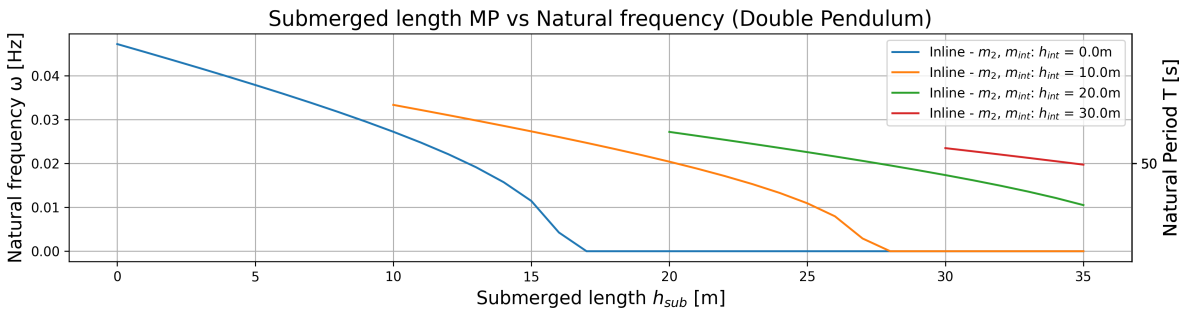

Figure A.5: Natural frequency vs submerged length for different h_{int}, considering m_2 and m_{int}

Figure A.5 shows the natural frequency behavior of the system considering only two components. An increase in the number of mass components will result in a slightly different behavior of the system. If the masses m_1, m_3 and the added mass component m_a are included, the equation becomes:

$$f_n = \frac{1}{2\pi}\sqrt{\frac{l_1\left((m_1+m_2+m_3+m_{\text{int}})g - F_b\right) + (m_2 l_2 + m_3 l_3 + m_{\text{int}} l_{\text{int}})g - F_b l_b}{l_1^2(m_1+m_2+m_3+m_{\text{int}}+m_a) + 2l_1(m_2 l_2 + m_3 l_3 + m_{\text{int}} l_{\text{int}} + m_a l_a) + m_2 l_2^2 + m_3 l_3^2 + m_{\text{int}} l_{\text{int}}^2 + m_a l_a^2}} \tag{A.5}$$

Again, the components shown in red in equation A.5 can be added added relatively easy. It happens to be that the additional mass components end up in the equation the same way as they did in equation A.3 for the vertical pendulum. As explained earlier, the mass components are added to the numerator and denominator whereas the added mass component is only added to the latter. It is convenient to see this trend of adding components to the equation in a simple matter, because it makes it more straightforward to add other components to the equation if necessary such as additional damping or mass terms. Furthermore, it is surprising to see that the added mass components only appear in the denominator and not as a damping term in the numerator. It would make sense that the surrounding water (e.q. the added mass) acts as a damping factor in the system but apparently this is not the case.

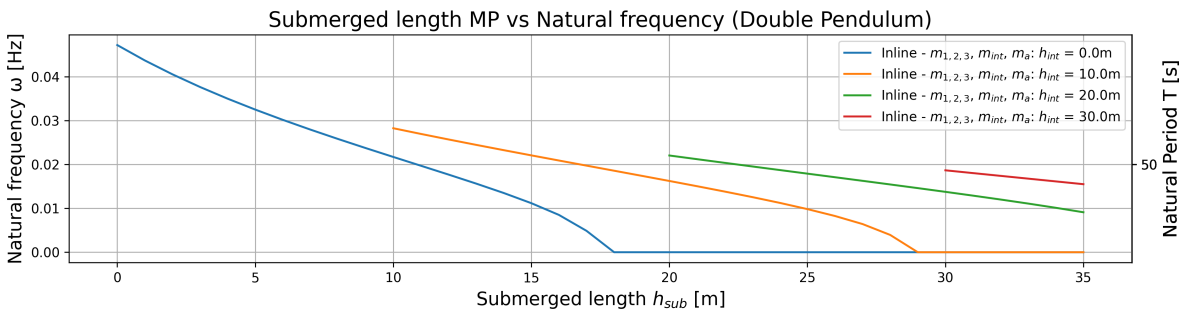

Figure A.6: Natural frequency vs submerged length for different h_{int}, considering $m_{1,2,3}$, m_{int} and m_a

Comparison

To check the influence of the different components of the inline single pendulum, a comparison between the three cases has been made and is shown in figure A.7. The most interesting thing to see is that the influence of the masses of the top and bottom cap on the behavior of the natural frequency is small in this case. The influence of the added mass however, is significant and should always be taken into consideration.

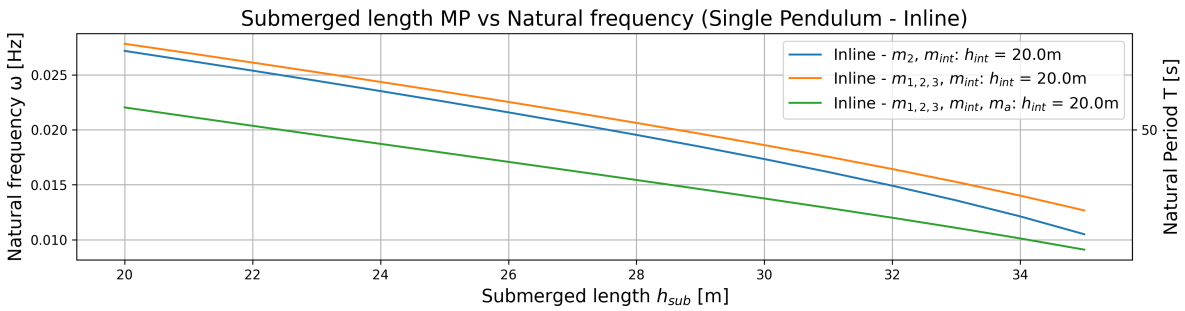

Figure A.7: Comparison of the natural frequency behavior with h_{int} = 20 m

In order to examine the influence of the momentum of the mass components, the behavior of the vertical and inline single pendulum are plotted against each other in figure A.8. Only the third case is considered in this comparison because it shows the difference when all components are included.

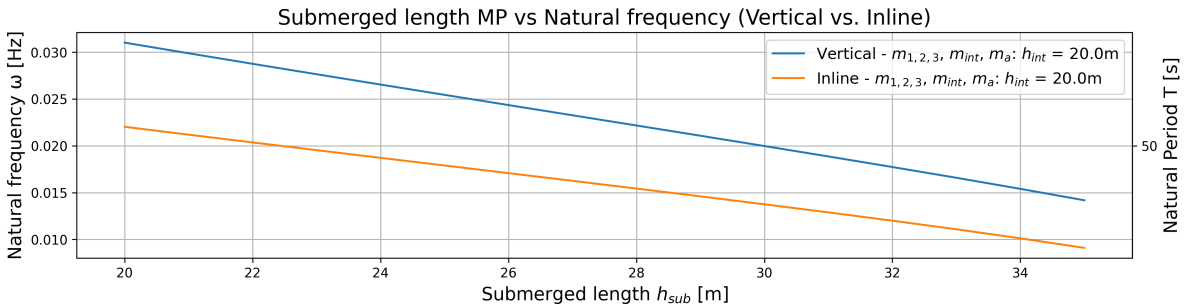

Figure A.8: Comparison of the natural frequency behavior of the Single Pendulum (Vertical vs Inline) with h_{int} = 20 m

It can be seen that the natural frequency decreases when taking into account the rotation of the monopile but their behavior is almost identical. This second iteration of a simplified system is already a better approximation of reality but this system does not represent the real situation either. Therefore, it is convenient to introduce a second degree of freedom to create a double pendulum system.

A.3. Double pendulum

The system discussed in this section is a double pendulum system, introducing a second degree of freedom. It is worth noting that, similar to the single pendulum inline case discussed in Section A.2, there is minimal difference between the first and second cases when adding the mass components m_1 and m_3. It is found that this is indeed the case for the double pendulum system. Therefore, for convenience and simplicity, it is more preferable to only consider the second and third cases as described in Section 3.2. This means that the masses of the top- and bottom-cap are included. Figure A.9 provides a schematic representation of the system, with the additional mass components depicted in yellow. The second degree of freedom that is introduced is the inclination angle the MP makes w.r.t. the vertical. This angle is referred to as the angle ϕ_2 and is clarified in the figure on the right.

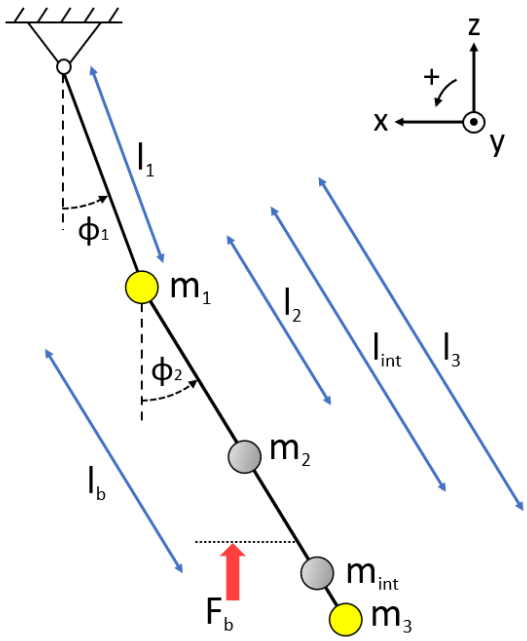

Figure A.9: Double pendulum (for $m_{1,2,3}$ and m_{int})

The introduction of a second degree of freedom, represented by the angles ϕ_1 and ϕ_2, adds complexity to the system compared to the single pendulum. These angles are independent of each other and are treated

as separate degrees of freedom. As a result, the natural frequency analysis of the system yields two distinct mode shapes: one where the masses m_1 and $m_{2,3}$ & m_{int} are in phase and another where these masses are out of phase. The details and implications of these mode shapes will be discussed further in this analysis.

Due to the presence of two unrestricted degrees of freedom, this system provides a closer approximation to the real-world scenario where the MP is not constrained in its movements except for the restriction imposed by the crane wire. As a result, this model is expected to be a better approximation compared to the single pendulum system.

Kinematics

For m_2 and m_{int} with $l_i = l_2, l_{\text{int}}$:

$$x_i = -l_1 \sin(\phi_1) - l_i \sin(\phi_2)$$
$$z_i = -l_1 \cos(\phi_1) - l_i \cos(\phi_2)$$

$$\dot{x}_i = -\dot{\phi}_1 l_1 \cos(\phi_1) - \dot{\phi}_2 l_i \cos(\phi_2)$$
$$\dot{z}_i = \dot{\phi}_1 l_1 \sin(\phi_1) + \dot{\phi}_2 l_i \sin(\phi_2)$$

$$\ddot{x}_i = -\ddot{\phi}_1 l_1 \cos(\phi_1) + \dot{\phi}_1^2 l_1 \sin(\phi_1) - \ddot{\phi}_2 l_i \cos(\phi_2) + \dot{\phi}_2^2 l_i \sin(\phi_2)$$
$$\ddot{z}_i = \ddot{\phi}_1 l_1 \sin(\phi_1) + \dot{\phi}_1^2 l_1 \cos(\phi_1) + \ddot{\phi}_2 l_i \sin(\phi_2) + \dot{\phi}_2^2 l_i \cos(\phi_2)$$

$$\delta x_i = -l_1 \cos(\phi_1)\delta\phi_1 - l_i \cos(\phi_2)\delta\phi_2$$
$$\delta z_i = l_1 \sin(\phi_1)\delta\phi_1 + l_i \sin(\phi_2)\delta\phi_2$$

Small angle approximation:

$$x_i = -l_1\phi_1 - l_i\phi_2$$
$$z_i = -l_1 - l_i$$

$$\dot{x}_i = -l_1\dot{\phi}_1 - l_i\dot{\phi}_2$$
$$\dot{z}_i = l_1\phi_1\dot{\phi}_1 + l_i\phi_2\dot{\phi}_2 = 0$$

$$\ddot{x}_i = -l_1\ddot{\phi}_1 - l_i\ddot{\phi}_2$$
$$\ddot{z}_i = l_1\phi_1\ddot{\phi}_1 + l_i\phi_2\ddot{\phi}_2 = 0$$

$$\delta x_i = -l_1\delta\phi_1 - l_i\delta\phi_2$$
$$\delta z_i = l_1\phi_1\delta\phi_1 + l_i\phi_2\delta\phi_2$$

For F_b with l_b:

$$z_b = -l_1 \cos(\phi_1) - l_b \cos(\phi_2)$$

$$\dot{z}_b = \dot{\phi}_1 l_1 \sin(\phi_1) + \dot{\phi}_2 l_b \sin(\phi_2)$$

$$\ddot{z}_b = \ddot{\phi}_1 l_1 \sin(\phi_1) + \dot{\phi}_1^2 l_1 \cos(\phi_1) + \ddot{\phi}_2 l_b \sin(\phi_2) + \dot{\phi}_2^2 l_b \cos(\phi_2)$$

$$\delta z_b = l_1 \sin(\phi_1)\delta\phi_1 + l_b \sin(\phi_2)\delta\phi_2$$

Small angle approximation:

$$z_b = -(l_1 + l_b)$$

$$\dot{z}_b = l_1\phi_1\dot{\phi}_1 + l_b\phi_2\dot{\phi}_2 = 0$$

$$\ddot{z}_b = l_1\phi_1\ddot{\phi}_1 + l_b\phi_2\ddot{\phi}_2 = 0$$

$$\delta z_b = l_1\phi_1\delta\phi_1 + l_b\phi_2\delta\phi_2$$

Principle of virtual work

The kinematics of this system become more complex but with the use of the small angle approximation they can be rewritten to a matrix form that can be solved. The small approximation method is applicable in this case because small rotations of ϕ_1 and ϕ_2 are assumed. It is important to mention that the derivations are done for m_2 and m_{int} to keep the derivations relatively short and simple. The results of this derivation are formulated in equation A.7.

$$
\begin{aligned}
\delta T &= \delta x_2 m_2 \ddot{x}_2 + \delta z_2 m_2 \ddot{z}_2 + \delta x_{\text{int}} m_{\text{int}} \ddot{x}_{\text{int}} + \delta z_{\text{int}} m_{\text{int}} \ddot{z}_{\text{int}} \\
&= m_2(-l_1\delta\phi_1 - l_2\delta\phi_2)(-l_1\ddot{\phi}_1 - l_2\ddot{\phi}_2) + m_{\text{int}}(-l_1\delta\phi_1 - l_{\text{int}}\delta\phi_2)(-l_1\ddot{\phi}_1 - l_{\text{int}}\ddot{\phi}_2) \\
&= \left(l_1^2(m_2 + m_{\text{int}})\ddot{\phi}_1 + l_1(l_2 m_2 + l_{\text{int}} m_{\text{int}})\ddot{\phi}_2\right)\delta\phi_1 + \left(l_1(l_2 m_2 + l_{\text{int}} m_{\text{int}})\ddot{\phi}_1 + (l_2^2 m_2 + l_{\text{int}}^2 m_{\text{int}})\ddot{\phi}_2\right)\delta\phi_2
\end{aligned}
$$

$$
\begin{aligned}
\delta V &= \delta z_2 m_2 g + \delta z_{\text{int}} m_{\text{int}} g - \delta z_b F_b \\
&= l_1\left((m_2 + m_{\text{int}})g - F_b\right)\delta\phi_1\phi_1 + \left((l_2 m_2 l_{\text{int}} m_{\text{int}})g - F_b l_b\right)\delta\phi_2\phi_2
\end{aligned}
$$

$$
\begin{aligned}
E &= \delta T + \delta V = 0 \\
&= \left(l_1^2(m_2 + m_{\text{int}})\ddot{\phi}_1 + l_1(l_2 m_2 + l_{\text{int}} m_{\text{int}})\ddot{\phi}_2\right)\delta\phi_1 + \left(l_1(l_2 m_2 + l_{\text{int}} m_{\text{int}})\ddot{\phi}_1 + (l_2^2 m_2 + l_{\text{int}}^2 m_{\text{int}})\ddot{\phi}_2\right)\delta\phi_2 \\
&\quad + l_1\left((m_2 + m_{\text{int}})g - F_b\right)\delta\phi_1\phi_1 + \left((l_2 m_2 l_{\text{int}} m_{\text{int}})g - F_b l_b\right)\delta\phi_2\phi_2 = 0
\end{aligned}
$$

$$
\begin{aligned}
&\delta\phi_1 = 1, \qquad \delta\phi_2 = 0 \\
&\quad = l_1^2(m_2 + m_{\text{int}})\ddot{\phi}_1 + l_1(l_2 m_2 + l_{\text{int}} m_{\text{int}})\ddot{\phi}_2 + l_1(m_2 g + m_{\text{int}} g - F_b)\phi_1 = 0
\end{aligned}
$$

$$
\begin{aligned}
&\delta\phi_1 = 0, \qquad \delta\phi_2 = 1 \\
&\quad = l_1(l_2 m_2 + l_{\text{int}} m_{\text{int}})\ddot{\phi}_1 + (l_2^2 m_2 + l_{\text{int}}^2 m_{\text{int}})\ddot{\phi}_2 + (l_2 m_2 g + l_{\text{int}} m_{\text{int}} g - F_b l_b)\phi_2 = 0
\end{aligned}
$$

This system of differential equations can be represented as $M\ddot{\vec{\phi}} + K\vec{\Phi} = \vec{0}$. This equation describes the free undamped oscillations with a certain frequency. Because this a double pendulum, the solution will contain two characteristic frequencies, referred to as the normal modes. They represent the real part of the complex-values function.

$$
\text{Convert to matrix:} \qquad M\begin{bmatrix}\ddot{\phi}_1\\ \ddot{\phi}_2\end{bmatrix} + K\begin{bmatrix}\phi_1\\ \phi_2\end{bmatrix} = \begin{bmatrix}0\\0\end{bmatrix} \qquad \text{results in:} \tag{A.6}
$$

$$
\begin{bmatrix} l_1^2(m_2 + m_{\text{int}}) & l_1(l_2 m_2 + l_{\text{int}} m_{\text{int}}) \\ l_1(l_2 m_2 + l_{\text{int}} m_{\text{int}}) & l_2^2 m_2 + l_{\text{int}}^2 m_{\text{int}} \end{bmatrix}\begin{bmatrix}\ddot{\phi}_1\\ \ddot{\phi}_2\end{bmatrix} + \begin{bmatrix} l_1(m_2 g + m_{\text{int}} g - F_b) & 0 \\ 0 & l_2 m_2 g + l_{\text{int}} m_{\text{int}} g - F_b l_b \end{bmatrix}\begin{bmatrix}\phi_1\\ \phi_2\end{bmatrix} = \begin{bmatrix}0\\0\end{bmatrix}
$$

$$
M\ddot{\vec{\Phi}} + K\vec{\Phi} = \vec{0} \quad \begin{cases} M = \begin{bmatrix} l_1^2(m_2 + m_{\text{int}}) & l_1(m_2 l_2 + m_{\text{int}} l_{\text{int}}) \\ l_1(m_2 l_2 + m_{\text{int}} l_{\text{int}}) & m_2 l_2^2 + m_{\text{int}} l_{\text{int}}^2 \end{bmatrix} \\[2ex] K = \begin{bmatrix} l_1(m_2 g + m_{\text{int}} g - F_b) & 0 \\ 0 & (m_2 l_2 + m_{\text{int}} l_{\text{int}})g - F_b l_b \end{bmatrix} \\[2ex] \vec{\Phi} = \begin{bmatrix}\phi_1\\ \phi_2\end{bmatrix} = \begin{bmatrix}\phi_{1i}\\ \phi_{2i}\end{bmatrix}\sin(\omega t) \end{cases} \tag{A.7}
$$

This set of equations is validated and improved trough the Lagrangian method in section A.4.2. The natural frequency of this system is found by assuming the general solution will be a sine function. This assumption reduces the set of equations to an eigenvalue problem that can be solved.

$$
\vec{\Phi} = \begin{bmatrix}\phi_1\\ \phi_2\end{bmatrix} = \begin{bmatrix}\phi_{1i}\\ \phi_{2i}\end{bmatrix}\sin(\omega t) \qquad \rightarrow \qquad \ddot{\vec{\Phi}} = -\omega^2\begin{bmatrix}\phi_{1i}\\ \phi_{2i}\end{bmatrix}\sin(\omega t)
$$

$$
M\ddot{\vec{\Phi}} + K\vec{\Phi} = 0 \qquad \rightarrow \qquad -\omega^2 M\vec{\Phi} + K\vec{\Phi} = 0 \qquad \rightarrow \qquad K\vec{\Phi} = \omega^2 M\vec{\Phi}
$$

Mathematically, the equation above is an eigenvalue problem where ω^2 is the eigenvalue. For a system with 2 degrees of freedom, 2 natural frequencies can be expected. Because ω^2 is used as an eigenvalue in the

matrix above, 4 roots are found for ω from the characteristic equation of the matrix. Due to the square, the roots come in pairs of positive and negative numbers of the same magnitude. The positive roots are selected as the natural frequencies.

The components m_1 and m_3 are included in this double pendulum system and leads to the following set of equations where the additional terms are shown in red.

$$M\ddot{\vec{\Phi}} + K\vec{\Phi} = \vec{0} \quad \begin{cases} M = \begin{bmatrix} l_1^2(m_1 + m_2 + m_3 + m_{\text{int}}) & l_1(m_2 l_2 + m_3 l_3 + m_{\text{int}} l_{\text{int}}) \\ l_1(m_2 l_2 + m_3 l_3 + m_{\text{int}} l_{\text{int}}) & m_2 l_2^2 + m_3 l_3^2 + m_{\text{int}} l_{\text{int}}^2 \end{bmatrix} \\ K = \begin{bmatrix} l_1\left(m_2 g + m_3 g + m_{\text{int}} g - F_b\right) & 0 \\ 0 & (m_2 l_2 + m_3 l_3 + m_{\text{int}} l_{\text{int}})g - F_b l_b \end{bmatrix} \\ \vec{\Phi} = \begin{bmatrix} \phi_{1i} \\ \phi_{2i} \end{bmatrix} \sin(\omega t) \end{cases} \tag{A.8}$$

Results

The results of the eigenvalue problem are shown in figure A.10a and b. As said, only the second and third case stated in section 3.2 are examined. It is interesting to see that the behavior of the in-phase mode in the low-frequency range is quite similar to the results from the single pendulum. The frequency behavior of the second mode is in a much higher frequency range. This range translates to a natural period that can be seen on the right side of the graph. These natural periods of the second mode converge more to the periods that Van Oord commonly experiences during their offshore installations. This critical period range is commonly between 6-8 seconds. This shift to lower natural periods is interesting to see and will be elaborated on in section 3.6.

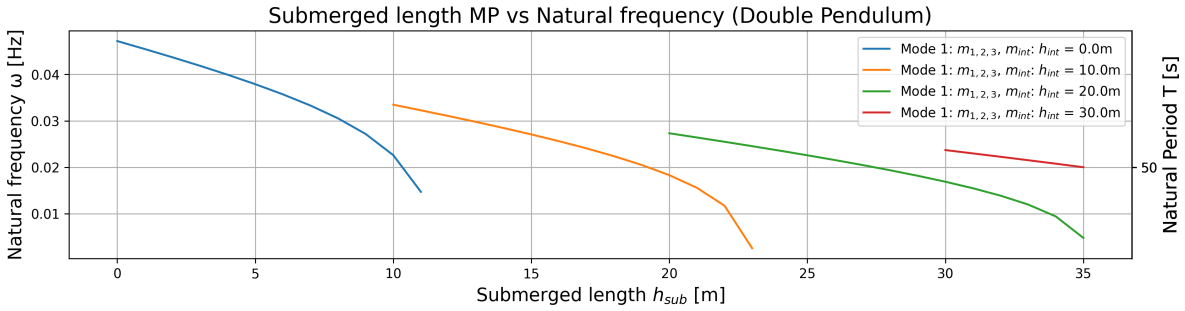

(a) In-phase mode

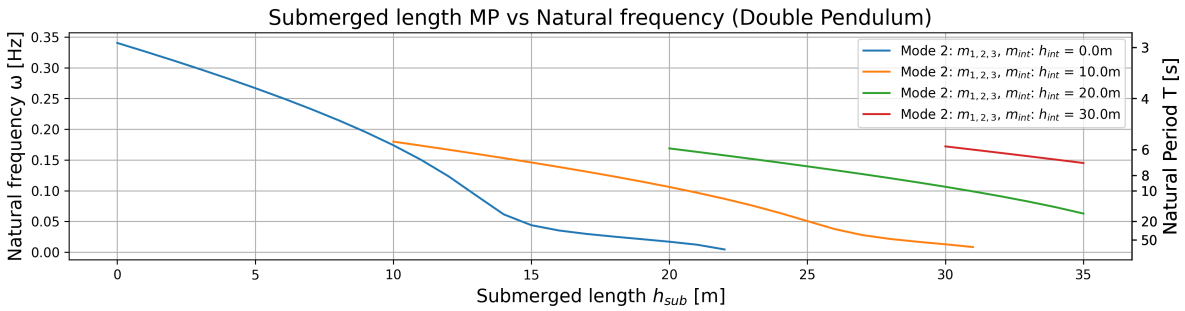

(b) Out-phase mode

Figure A.10: Natural frequency vs submerged length for different h_{int}, considering m_2 and m_{int}

By going to the iteration steps again and including the added mass term, the following set of equations is obtained where the added mass terms are shown in red.

$$M\ddot{\vec{\Phi}} + K\vec{\Phi} = \vec{0} \quad \begin{cases} M = \begin{bmatrix} l_1^2(m_1+m_2+m_3+m_{\text{int}}+m_a) & l_1(m_2l_2+m_3l_3+m_{\text{int}}l_{\text{int}}+m_al_a) \\ l_1(m_2l_2+m_3l_3+m_{\text{int}}l_{\text{int}}+m_al_a) & m_2l_2^2+m_3l_3^2+m_{\text{int}}l_{\text{int}}^2+m_al_a^2 \end{bmatrix} \\ K = \begin{bmatrix} l_1\left(m_2g+m_3g+m_{\text{int}}g-F_b\right) & 0 \\ 0 & (m_2l_2+m_3l_3+m_{\text{int}}l_{\text{int}})g-F_bl_b \end{bmatrix} \\ \vec{\Phi} = \begin{bmatrix} \phi_{1i} \\ \phi_{2i} \end{bmatrix} \sin(\omega t) \end{cases} \tag{A.9}$$

The results of including the added mass terms are shown in figure A.11. It can be seen that the added mass component influences the natural frequency behavior but a significant shift of the natural frequency is not observed. Especially when the MP is lowered through the first meters, the added mass flattens the curve. This means that higher natural periods are reached more rapidly. After a submerged length of approximately 15 meters, the behavior for each internal water level is roughly the same as the one without including the added mass.

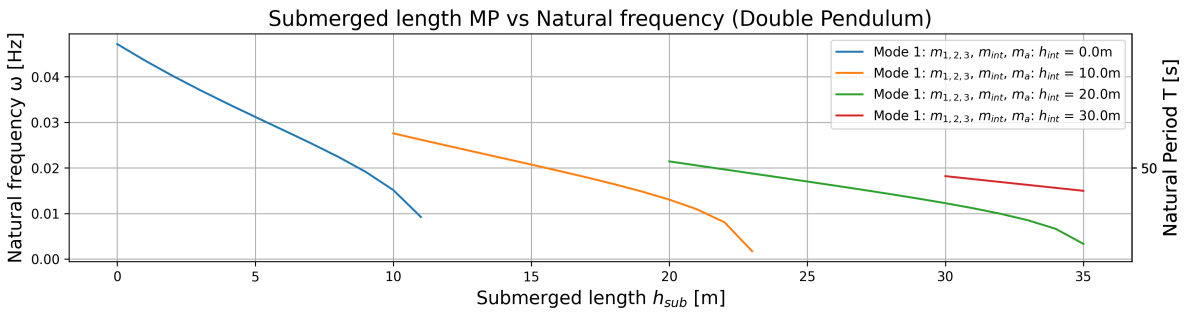

(a) In-phase mode

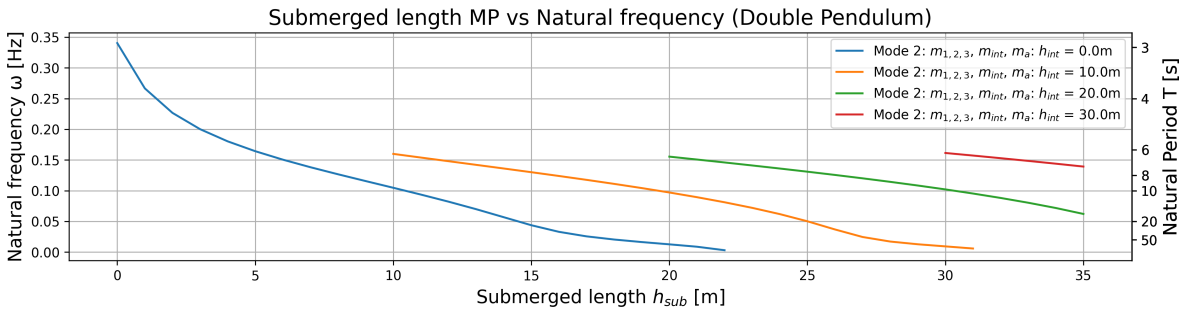

(b) Out-phase mode

Figure A.11: Natural frequency vs submerged length for different h_{int}, considering $m_{1,2,3}$, m_{int} and m_a

Another interesting phenomena is when these two modes coexist. This would result in very inconvenient motions of the MP. By plotting both modes in the same graph and looking for a potential overlap between the two modes, it was concluded that these two modes will not occur simultaneously.

A.4. Double pendulum - Inertia

In order to find the equations of motion of the double pendulum system including the inertia of the mass components, the Lagrangian method is used. This method is used later in this section to validate the system of equations that resulted from derivations of the double pendulum in section 3.5. This is done using the small angle approximation method.

A.4.1. Lagrangian method

The Lagrangian for a double pendulum system is given by $L = T - V$, where T and V are the kinetic and potential energy respectively. For this method, the Euler-Lagrange equation is used:

$$\frac{\mathrm{d}}{\mathrm{d}t}\left(\frac{\partial L}{\partial \dot{q}_i}\right) - \frac{\partial L}{\partial q_i} = Q_i \qquad \text{for} \qquad q_i = \phi_1, \phi_2 \tag{A.10}$$

By differentiating the quantities x_i and z_i w.r.t. time, the velocities $\dot{x}_i$ and $\dot{z}_i$ of the masses m_i can be formulated.

For m_2 and m_{int} with $l_i = l_2$, l_{int}:

$$\begin{aligned} x_i &= -l_1 \sin(\phi_1) - l_i \sin(\phi_2) \\ z_i &= -l_1 \cos(\phi_1) - l_i \cos(\phi_2) \end{aligned}$$

$$\begin{aligned} \dot{x}_i &= -\dot{\phi}_1 l_1 \cos(\phi_1) - \dot{\phi}_2 l_i \cos(\phi_2) \\ \dot{z}_i &= \dot{\phi}_1 l_1 \sin(\phi_1) + \dot{\phi}_2 l_i \sin(\phi_2) \end{aligned}$$

$$\begin{aligned} \dot{x}_i{}^2 &= \dot{\phi}_1^2 l_1^2 \cos^2(\phi_1) + 2 l_1 l_i \dot{\phi}_1 \dot{\phi}_2 \cos(\phi_1)\cos(\phi_2) + \dot{\phi}_2^2 l_i^2 \cos^2(\phi_2) \\ \dot{z}_i{}^2 &= \dot{\phi}_1^2 l_1^2 \sin^2(\phi_1) + 2 l_1 l_i \dot{\phi}_1 \dot{\phi}_2 \sin(\phi_1)\sin(\phi_2) + \dot{\phi}_2^2 l_i^2 \sin^2(\phi_2) \end{aligned}$$

$$\dot{x}_i{}^2 + \dot{z}_i{}^2 = l_1^2 \dot{\phi}_1^2 \left(\sin^2(\phi_1) + \cos^2(\phi_1)\right) + 2 l_1 l_i \dot{\phi}_1 \dot{\phi}_2 \left(\sin(\phi_1)\sin(\phi_2) + \cos(\phi_1)\cos(\phi_2)\right) + l_i^2 \dot{\phi}_2^2 \left(\cos^2(\phi_2) + \sin^2(\phi_2)\right)$$

Using the following trigonometry rules:

$$\sin^2\phi_{1,2} + \cos^2\phi_{1,2} = 1, \qquad \sin\phi_1 \sin\phi_2 + \cos\phi_1 \cos\phi_2 = \cos(\phi_1 - \phi_2) \qquad \text{with} \qquad \phi_{1,2} = \phi_1, \phi_2$$

gives:

$$\begin{aligned} \dot{x}_i{}^2 + \dot{z}_i{}^2 &= l_1^2 \dot{\phi}_1^2 \left(\sin^2(\phi_1) + \cos^2(\phi_1)\right) + 2 l_1 l_i \dot{\phi}_1 \dot{\phi}_2 \left(\sin(\phi_1)\sin(\phi_2) + \cos(\phi_1)\cos(\phi_2)\right) + l_i^2 \dot{\phi}_2^2 \left(\cos^2(\phi_2) + \sin^2(\phi_2)\right) \\ &= l_1^2 \dot{\phi}_1^2 + 2 l_1 l_i \dot{\phi}_1 \dot{\phi}_2 \cos(\phi_1 - \phi_2) + l_i^2 \dot{\phi}_2^2 \end{aligned} \tag{A.11}$$

Replacing l_i with l_2 and l_{int} results in:

$$\dot{x}_2{}^2 + \dot{z}_2{}^2 = l_1^2 \dot{\phi}_1^2 + 2 l_1 l_2 \dot{\phi}_1 \dot{\phi}_2 \cos(\phi_1 - \phi_2) + l_2^2 \dot{\phi}_2^2 \tag{A.12}$$

$$\dot{x}_{\text{int}}^2 + \dot{z}_{\text{int}}^2 = l_1^2 \dot{\phi}_1^2 + 2 l_1 l_{\text{int}} \dot{\phi}_1 \dot{\phi}_2 \cos(\phi_1 - \phi_2) + l_{\text{int}}^2 \dot{\phi}_2^2 \tag{A.13}$$

Using the Lagrangian method, the kinetic energy T and potential energy V can be formulated and the Lagrangian L can be determined. Here, the rotatory inertia of the monopile J_2 and the rotatory inertia of the internal water column J_{int} are accounted for.

$$\begin{aligned} T &= \overbrace{\underbrace{\frac{1}{2} m_2 \left(\dot{x}_2{}^2 + \dot{z}_2{}^2\right)}_{\text{Monopile}} + \underbrace{\frac{1}{2} m_{\text{int}} \left(\dot{x}_{\text{int}}^2 + \dot{z}_{\text{int}}^2\right)}_{\text{Water column}}}^{\text{Translational Kinetic Energy}} + \overbrace{\underbrace{\frac{1}{2} J_2 \dot{\phi}_2^2}_{\text{Monopile}} + \underbrace{\frac{1}{2} J_{\text{int}} \dot{\phi}_2^2}_{\text{Water column}} + \underbrace{\frac{1}{2} J_a \dot{\phi}_2^2}_{\text{Added mass}}}^{\text{Rotatory Kinetic Energy}} \\ &= \frac{1}{2} m_2 \left[l_1^2 \dot{\phi}_1^2 + 2 l_1 l_2 \dot{\phi}_1 \dot{\phi}_2 \cos(\phi_1 - \phi_2) + l_2^2 \dot{\phi}_2^2\right] + \frac{1}{2} m_{\text{int}} \left[l_1^2 \dot{\phi}_1^2 + 2 l_1 l_{\text{int}} \dot{\phi}_1 \dot{\phi}_2 \cos(\phi_1 - \phi_2) + l_{\text{int}}^2 \dot{\phi}_2^2\right] \\ &\quad + \frac{1}{2} J_2 \dot{\phi}_2^2 + \frac{1}{2} J_{\text{int}} \dot{\phi}_2^2 + \frac{1}{2} J_a \dot{\phi}_2^2 \\ &= \frac{1}{2}\left[m_2 l_1^2 + m_{\text{int}} l_1^2\right] \cdot \dot{\phi}_1^2 + \frac{1}{2}\left[m_2 l_2^2 + m_{\text{int}} l_{\text{int}}^2 + J_2 + J_{\text{int}}\right] \cdot \dot{\phi}_2^2 + l_1 \left[m_2 l_2 + m_{\text{int}} l_{\text{int}}\right] \dot{\phi}_1 \dot{\phi}_2 \cos(\phi_1 - \phi_2) \\ &= \frac{1}{2} J_{\phi_1} \dot{\phi}_1^2 + \frac{1}{2} J_{\phi_2} \dot{\phi}_2^2 + J_x \dot{\phi}_1 \dot{\phi}_2 \cos(\phi_1 - \phi_2) \end{aligned}$$

with: $\quad J_{\phi_1} = l_1^2 (m_2 + m_{\text{int}}) \qquad J_{\phi_2} = m_2 l_2^2 + m_{\text{int}} l_{\text{int}}^2 + J_2 + J_{\text{int}} + J_a \qquad J_x = l_1 (m_2 l_2 + m_{\text{int}} l_{\text{int}})$

$$J_2 = \frac{1}{12} m_2 l_{\text{mp}}^2 \qquad J_{\text{int}} = \frac{1}{12} m_{\text{int}} h_{\text{int}}^2 \qquad J_a = \frac{1}{12} m_a h_{\text{sub}}^2$$

$$
\begin{aligned}
V &= \overbrace{\underbrace{m_2 g z_2}_{\text{Monopile}} + \underbrace{m_{\text{int}} g z_{\text{int}}}_{\text{Water column}} - \underbrace{F_b z_b}_{\text{Buoyancy}}}^{\text{Potential Energy}} \\
&= m_2 g\left(-l_1\cos(\phi_1) - l_2\cos(\phi_2)\right) + m_{\text{int}} g\left(-l_1\cos(\phi_1) - l_{\text{int}}\cos(\phi_2)\right) - F_b\left(-l_1\cos(\phi_1) - l_b\cos(\phi_2)\right) \\
&= -l_1\left(m_2 g + m_{\text{int}} g - F_b\right)\cos(\phi_1) - \left(m_2 g l_2 + m_{\text{int}} g l_{\text{int}} - F_b l_b\right)\cos(\phi_2)
\end{aligned}
$$

$$
= -\mu_1\cos\phi_1 - \mu_2\cos\phi_2 \qquad \text{with:} \qquad \mu_1 = l_1\left(m_2 g + m_{\text{int}} g - F_b\right) \qquad \mu_2 = (m_2 l_2 + m_{\text{int}} l_{\text{int}})g - F_b l_b
$$

The Lagrangian for a double pendulum system can be found with the following equation:

$$
L = T - V = \frac{1}{2}J_{\phi_1}\dot{\phi}_1^2 + \frac{1}{2}J_{\phi_2}\dot{\phi}_2^2 + J_x\dot{\phi}_1\dot{\phi}_2\cos(\phi_1 - \phi_2) + \mu_1\cos\phi_1 + \mu_2\cos\phi_2 \tag{A.14}
$$

Keeping in mind that $J_{\phi_1}, J_{\phi_2}, J_x, J_2$ and J_{int} are not dependent on time and can therefore be seen as constants when using the Euler-Lagrange equations, the Lagrangian L is substituted in equation A.10. $Q_i = 0$ because there is no external force acting on the system yet. Equation A.10 is then solved for $q_i = \phi_1$ and ϕ_2, the red terms cancel each other out and the result is formulated below:

$$
\begin{aligned}
L_{\phi_1} &= J_{\phi_1}\ddot{\phi}_1 + J_x\ddot{\phi}_2\cos(\phi_1 - \phi_2) - J_x\dot{\phi}_2\sin(\phi_1 - \phi_2)(\dot{\phi}_1 - \dot{\phi}_2) - \left[-J_x\dot{\phi}_1\dot{\phi}_2\sin(\phi_1 - \phi_2) - \mu_1\sin(\phi_1)\right] = 0 \\
&= J_{\phi_1}\ddot{\phi}_1 + J_x\ddot{\phi}_2\cos(\phi_1 - \phi_2) - J_x\dot{\phi}_1\dot{\phi}_2\sin(\phi_1 - \phi_2) + J_x\dot{\phi}_2^2\sin(\phi_1 - \phi_2) + J_x\dot{\phi}_1\dot{\phi}_2\sin(\phi_1 - \phi_2) + \mu_1\sin(\phi_1) = 0 \\
&= J_{\phi_1}\ddot{\phi}_1 + J_x\ddot{\phi}_2\cos(\phi_1 - \phi_2) + J_x\dot{\phi}_2^2\sin(\phi_1 - \phi_2) + \mu_1\sin(\phi_1) = 0
\end{aligned}
$$

$$
\begin{aligned}
L_{\phi_2} &= J_{\phi_2}\ddot{\phi}_2 + J_x\ddot{\phi}_1\cos(\phi_1 - \phi_2) - J_x\dot{\phi}_1\sin(\phi_1 - \phi_2)(\dot{\phi}_1 - \dot{\phi}_2) - \left[J_x\dot{\phi}_1\dot{\phi}_2\sin(\phi_1 - \phi_2) - \mu_2\sin(\phi_2)\right] = 0 \\
&= J_{\phi_2}\ddot{\phi}_2 + J_x\ddot{\phi}_1\cos(\phi_1 - \phi_2) - J_x\dot{\phi}_1^2\sin(\phi_1 - \phi_2) + J_x\dot{\phi}_1\dot{\phi}_2\sin(\phi_1 - \phi_2) - J_x\dot{\phi}_1\dot{\phi}_2\sin(\phi_1 - \phi_2) + \mu_2\sin(\phi_2) = 0 \\
&= J_{\phi_2}\ddot{\phi}_2 + J_x\ddot{\phi}_1\cos(\phi_1 - \phi_2) - J_x\dot{\phi}_1^2\sin(\phi_1 - \phi_2) + \mu_2\sin(\phi_2) = 0
\end{aligned}
$$

Rewriting L_{ϕ_1} and L_{ϕ_2} respectively for $\ddot{\phi}_1$ and $\ddot{\phi}_2$ gives:

$$
\ddot{\phi}_1 + \frac{J_x}{J_{\phi_1}}\cos(\phi_1 - \phi_2)\ddot{\phi}_2 = -\frac{J_x}{J_{\phi_1}}\sin(\phi_1 - \phi_2)\dot{\phi}_2^2 - \frac{\mu_1}{J_{\phi_1}}\sin(\phi_2) \qquad \rightarrow \qquad \ddot{\phi}_1 + a_1\ddot{\phi}_2 = f_1 \tag{A.15}
$$

$$
\ddot{\phi}_2 + \frac{J_x}{J_{\phi_2}}\cos(\phi_1 - \phi_2)\ddot{\phi}_1 = \frac{J_x}{J_{\phi_2}}\sin(\phi_1 - \phi_2)\dot{\phi}_1^2 - \frac{\mu_2}{J_{\phi_2}}\sin(\phi_2) \qquad \rightarrow \qquad \ddot{\phi}_2 + a_2\ddot{\phi}_1 = f_2 \tag{A.16}
$$

Equations A.15 and A.16 can be combined into a single equation in the form of a matrix:

$$
A\begin{bmatrix}\ddot{\phi}_1\\ \ddot{\phi}_2\end{bmatrix} = \begin{bmatrix}1 & a_1\\ a_2 & 1\end{bmatrix}\begin{bmatrix}\ddot{\phi}_1\\ \ddot{\phi}_2\end{bmatrix} = \begin{bmatrix}f_1\\ f_2\end{bmatrix} \qquad \text{with the inverse of matrix A:} \qquad A^{-1} = \frac{1}{1 - a_1 a_2}\begin{bmatrix}1 & -a_1\\ -a_2 & 1\end{bmatrix}
$$

$$
\text{so:} \qquad \begin{bmatrix}\ddot{\phi}_1\\ \ddot{\phi}_2\end{bmatrix} = \phi^{-1}\begin{bmatrix}f_1\\ f_2\end{bmatrix} = \frac{1}{1 - a_1 a_2}\begin{bmatrix}f_1 - a_1 f_2\\ -a_2 f_1 + f_2\end{bmatrix}
$$

These aforementioned formulations result in the following equations of motion for this specific double pendulum system accounting for m_2 and m_{int}:

$$
\ddot{\phi}_1 = \frac{f_1 - a_1 f_2}{1 - a_1 a_2} \qquad \text{and} \qquad \ddot{\phi}_2 = \frac{-a_2 f_1 - f_2}{1 - a_1 a_2} \qquad \text{with:} \tag{A.17}
$$

$$
\begin{aligned}
f_1 &= -\frac{J_x}{J_{\phi_1}}\sin(\phi_1 - \phi_2)\dot{\phi}_2^2 - \frac{\mu_1}{J_{\phi_1}}\sin(\phi_2) & f_2 &= \frac{J_x}{J_{\phi_2}}\sin(\phi_1 - \phi_2)\dot{\phi}_1^2 - \frac{\mu_2}{J_{\phi_2}}\sin(\phi_2) \\
a_1 &= \frac{J_x}{J_{\phi_1}}\cos(\phi_1 - \phi_2) & a_2 &= \frac{J_x}{J_{\phi_2}}\cos(\phi_1 - \phi_2) \\
\mu_1 &= l_1\left(m_2 g + m_{\text{int}} g - F_b\right) & \mu_2 &= (m_2 l_2 + m_{\text{int}} l_{\text{int}})g - F_b l_b
\end{aligned}
$$

$$J_{\phi_1} = l_1^2(m_2 + m_{\text{int}}) \qquad J_{\phi_2} = m_2 l_2^2 + m_{\text{int}} l_{\text{int}}^2 + J_2 + J_{\text{int}} + J_a \qquad J_x = l_1(m_2 l_2 + m_{\text{int}} l_{\text{int}})$$
$$J_2 = \frac{1}{12} m_2 l_{\text{mp}}^2 \qquad J_{\text{int}} = \frac{1}{12} m_{\text{int}} h_{\text{int}}^2 \qquad J_a = \frac{1}{12} m_a h_{\text{sub}}^2$$

As can be seen from equation A.17 the following statements hold: $\ddot{\phi}_1 = f(\phi_1, \phi_2, \dot{\phi}_2)$ and $\ddot{\phi}_2 = f(\phi_1, \phi_2, \dot{\phi}_1)$. This set of equations is therefore a coupled second order differential set of equations and can be solved with python by rewriting these equations to first order differential equations.

The equations of motion of the double pendulum can be rewritten as a system of coupled first order differential equations by letting the following two equations hold:

$$\omega_1 = \dot{\phi}_1 \qquad \text{and} \qquad \omega_2 = \dot{\phi}_2$$

$$\text{then} \qquad \frac{\mathrm{d}}{\mathrm{d}t}\begin{bmatrix}\phi_1\\ \phi_2\\ \dot{\phi}_1\\ \dot{\phi}_2\end{bmatrix} = \begin{bmatrix}\dot{\phi}_1\\ \dot{\phi}_2\\ \ddot{\phi}_1\\ \ddot{\phi}_2\end{bmatrix} = \begin{bmatrix}\omega_1\\ \omega_2\\ g_1(\phi_1, \phi_2, \omega_1, \omega_2)\\ g_2(\phi_1, \phi_2, \omega_1, \omega_2)\end{bmatrix} \qquad \text{with:} \qquad g_1 = \frac{f_1 - a_1 f_2}{1 - a_1 a_2} \qquad \text{and} \qquad g_2 = \frac{-a_2 f_1 - f_2}{1 - a_1 a_2}$$

This can then be solved numerically by using the 'ODEint' function from the 'scipy' package that uses the Runge Kutta LSODA method to solve these first order differential equations.

A.4.2. Verification using small approximation method

By assuming the angles ϕ_1 and ϕ_2 to be small, the oscillations of the the double pendulum can be described by a linear system of equations. By applying this method, the formulations for the natural frequency of the double pendulum found in A.3 can be validated. Again, the Lagrangian in equation A.14 is used:

$$L = \frac{1}{2} J_{\phi_1} \dot{\phi}_1^2 + \frac{1}{2} J_{\phi_2} \dot{\phi}_2^2 + J_x \dot{\phi}_1 \dot{\phi}_2 \cos(\phi_1 - \phi_2) + \mu_1 \cos\phi_1 + \mu_2 \cos\phi_2$$

Writing this Lagrangian in a simpler form using the following trigonometry rules and using the small angle approximation:

$$\cos\phi_{1,2} \approx 1 - \frac{\phi_{1,2}^2}{2} \qquad \text{and} \qquad \cos(\phi_1 - \phi_2) \approx 1 - \frac{(\phi_1 - \phi_2)^2}{2} \approx 1 \qquad \text{with} \qquad \phi_{1,2} = \phi_1, \phi_2$$

Substituting these assumptions in the original Lagrangian, the following equation is obtained:

$$L = \frac{1}{2} J_{\phi_1} \dot{\phi}_1^2 + \frac{1}{2} J_{\phi_2} \dot{\phi}_2^2 + J_x \dot{\phi}_1 \dot{\phi}_2 + \mu_1 - \mu_1 \frac{\phi_1^2}{2} + \mu_2 - \mu_2 \frac{\phi_2^2}{2}$$

Again, equation A.10 is solved for ϕ_1 and ϕ_2. Here, the small angle approximation of equation A.1 is used and the result is the following set of equations:

$$L_{\phi_1} = J_{\phi_1} \ddot{\phi}_1 + J_x \ddot{\phi}_2 + \mu_1 \phi_1 = 0$$
$$L_{\phi_2} = J_{\phi_2} \ddot{\phi}_2 + J_x \ddot{\phi}_1 + \mu_2 \phi_2 = 0$$

With the substitution of the parameters of equation A.17 this set can be written in the following matrix form:

$$M\ddot{\vec{\phi}} + K\vec{\Phi} = \vec{0} \qquad \text{with} \qquad \phi = \begin{bmatrix}\phi_1\\ \phi_2\end{bmatrix} \qquad \text{so} \qquad \begin{bmatrix}J_{\phi_1} & J_x\\ J_x & J_{\phi_2}\end{bmatrix}\begin{bmatrix}\ddot{\phi}_1\\ \ddot{\phi}_2\end{bmatrix} + \begin{bmatrix}\mu_1 & 0\\ 0 & \mu_2\end{bmatrix}\begin{bmatrix}\phi_1\\ \phi_2\end{bmatrix} = \begin{bmatrix}0\\ 0\end{bmatrix}$$

$$M\ddot{\vec{\Phi}} + K\vec{\Phi} = \vec{0} \quad \begin{cases} M = \begin{bmatrix}J_{\phi_1} & J_x\\ J_x & J_{\phi_2}\end{bmatrix} = \begin{bmatrix} l_1^2(m_2 + m_{\text{int}}) & l_1(m_2 l_2 + m_{\text{int}} l_{\text{int}}) \\ l_1(m_2 l_2 + m_{\text{int}} l_{\text{int}}) & m_2 l_2^2 + m_{\text{int}} l_{\text{int}}^2 + J_2 + J_{\text{int}} + J_a \end{bmatrix} \\ K = \begin{bmatrix}\mu_1 & 0\\ 0 & \mu_2\end{bmatrix} = \begin{bmatrix} l_1(m_2 g + m_{\text{int}} g - F_b) & 0 \\ 0 & (m_2 l_2 + m_{\text{int}} l_{\text{int}}) g - F_b l_b \end{bmatrix} \\ \vec{\Phi} = \begin{bmatrix}\phi_1\\ \phi_2\end{bmatrix} = \begin{bmatrix}\phi_{1i}\\ \phi_{2i}\end{bmatrix} \sin(\omega t) \end{cases} \tag{A.18}$$

Equation A.18 is almost identical as equation A.7 derived with the small angle approximation method except for the fact that equation A.18 accounts for inertia of the monopile J_2, the internal water column J_{int} and for the added mass J_a. This method therefore verifies and improves the derivations done in section A.3 regarding the double pendulum system.

Another interesting thing to mention is that in the case of considering more components, they all end up in the constant parameters J_x, J_{ϕ_1}, J_{ϕ_2}, μ_1 and μ_2. This is very convenient because these components can simply be added without going through all iteration steps again. If the two masses m_1, m_3 and the added mass m_a are added to the previous set of equations, the result is as follows:

$$M\ddot{\vec{\Phi}} + K\vec{\Phi} = \vec{0} \quad \begin{cases} M = \begin{bmatrix} l_1^2(m_1 + m_2 + m_3 + m_{\text{int}} + m_a) & l_1(m_2 l_2 + m_3 l_3 + m_{\text{int}} l_{\text{int}} + m_a l_a) \\ l_1(m_2 l_2 + m_3 l_3 + m_{\text{int}} l_{\text{int}} + m_a l_a) & m_2 l_2^2 + m_3 l_3^2 + m_{\text{int}} l_{\text{int}}^2 + m_a l_a^2 + J_2 + J_{\text{int}} + J_a \end{bmatrix} \\ K = \begin{bmatrix} l_1\left((m_1 + m_2 + m_3 + m_{\text{int}})g - F_b\right) & 0 \\ 0 & (m_2 l_2 + m_3 l_3 + m_{\text{int}} l_{\text{int}})g - F_b l_b \end{bmatrix} \\ \vec{\Phi} = \begin{bmatrix} \phi_{1i} \\ \phi_{2i} \end{bmatrix} \sin(\omega t) \end{cases} \tag{A.19}$$

A.4.3. Equations of motion

As mentioned, extra components eventually end up in the constant parameters J_x, J_{ϕ_1}, J_{ϕ_2}, μ_1 and μ_2. That means that these additional components end up in the equations of motion of equation A.17 and results in the following set of equations of motions:

$$\ddot{\phi}_1 = \frac{f_1 - a_1 f_2}{1 - a_1 a_2} \quad \text{and} \quad \ddot{\phi}_2 = \frac{-a_2 f_1 - f_2}{1 - a_1 a_2} \quad \text{with:} \tag{A.20}$$

$$f_1 = -\frac{J_x}{J_{\phi_1}} \sin(\phi_1 - \phi_2)\dot{\phi}_2^2 - \frac{\mu_1}{J_{\phi_1}} \sin(\phi_2) \qquad f_2 = \frac{J_x}{J_{\phi_2}} \sin(\phi_1 - \phi_2)\dot{\phi}_1^2 - \frac{\mu_1}{J_{\phi_2}} \sin(\phi_2)$$

$$a_1 = \frac{J_x}{J_{\phi_1}} \cos(\phi_1 - \phi_2) \qquad a_2 = \frac{J_x}{J_{\phi_2}} \cos(\phi_1 - \phi_2)$$

$$J_{\phi_1} = l_1^2(m_1 + m_2 + m_3 + m_{\text{int}} + m_a) \qquad J_{\phi_2} = m_2 l_2^2 + m_3 l_3^2 + m_{\text{int}} l_{\text{int}}^2 + m_a l_a^2 + J_2 + J_{\text{int}} + J_a$$

$$J_x = l_1(m_2 l_2 + m_3 l_3 + m_{\text{int}} l_{\text{int}} + m_a l_a)$$

$$\mu_1 = l_1\left((m_1 + m_2 + m_3 + m_{\text{int}})g - F_b\right) \qquad \mu_2 = (m_2 l_2 + m_3 l_3 + m_{\text{int}} l_{\text{int}})g - F_b l_b$$

$$J_2 = \frac{1}{12} m_2 l_{\text{mp}}^2 \qquad J_{\text{int}} = \frac{1}{12} m_{\text{int}} h_{\text{int}}^2 \qquad J_a = \frac{1}{12} m_a h_{\text{sub}}^2$$

A.5. Compound double pendulum

To take into account the mass and inertia of the cable in the numerical model, the kinematics have to be derived. For simplicity, only the masses of the cable, m_c and the MP, m_2, are considered. The kinematics of the mass component m_c are defined as:

For m_c with $\frac{l_1}{2}$:

$$x_c = -\frac{l_1}{2}\sin(\phi_1)$$
$$z_c = -\frac{l_1}{2}\cos(\phi_1)$$

$$\dot{x}_c = -\dot{\phi}_1\frac{l_1}{2}\cos(\phi_1)$$
$$\dot{z}_c = \dot{\phi}_1\frac{l_1}{2}\sin(\phi_1)$$
$$\dot{x_c}^2 + \dot{z_c}^2 = \frac{1}{4}l_1^2\dot{\phi}_1^2\left(\sin^2(\phi_1) + \cos^2(\phi_1)\right)$$

Small angle approximation:

$$x_c = -\frac{l_1}{2}\phi_1$$
$$z_c = -\frac{l_1}{2}$$

$$\dot{x}_c = -\dot{\phi}_1\frac{l_1}{2}$$
$$\dot{z}_c = \dot{\phi}_1\frac{l_1}{2}\phi_1 = 0$$
$$\dot{x_c}^2 + \dot{z_c}^2 = \frac{1}{4}l_1^2\dot{\phi}_1^2$$

Revisiting equation A.12:

$$\dot{x_2}^2 + \dot{z_2}^2 = l_1^2\dot{\phi}_1^2 + 2l_1l_2\dot{\phi}_1\dot{\phi}_2\cos(\phi_1 - \phi_2) + l_2^2\dot{\phi}_2^2$$

Results in the kinetic energy T and potential energy V that includes the weight and inertia of the cable, m_c and J_c respectively.

$$T = \overbrace{\underbrace{\frac{1}{2}m_c\left(\dot{x_c}^2 + \dot{z_c}^2\right)}_{\text{Cable}} + \underbrace{\frac{1}{2}m_2\left(\dot{x}_2^2 + \dot{z}_2^2\right)}_{\text{Monopile}}}^{\text{Translational Kinetic Energy}} + \overbrace{\underbrace{\frac{1}{2}J_c\dot{\phi}_1^2}_{\text{Cable}} + \underbrace{\frac{1}{2}J_2\dot{\phi}_2^2}_{\text{Monopile}}}^{\text{Rotatory Kinetic Energy}}$$
$$= +\frac{1}{2}m_c\left[\frac{1}{4}l_1^2\dot{\phi}_1^2\right] + \frac{1}{2}m_2\left[l_1^2\dot{\phi}_1^2 + 2l_1l_2\dot{\phi}_1\dot{\phi}_2\cos(\phi_1 - \phi_2) + l_2^2\dot{\phi}_2^2\right] + \frac{1}{2}J_c\dot{\phi}_1^2 + \frac{1}{2}J_2\dot{\phi}_2^2$$
$$= \frac{1}{2}\left[\frac{1}{4}m_cl_1^2 + m_2l_1^2 + J_c\right]\cdot\dot{\phi}_1^2 + \frac{1}{2}\left[m_2l_2^2 + J_2\right]\cdot\dot{\phi}_2^2 + l_1\left[m_2l_2\right]\dot{\phi}_1\dot{\phi}_2\cos(\phi_1 - \phi_2)$$
$$= \frac{1}{2}J_{\phi_1}\dot{\phi}_1^2 + \frac{1}{2}J_{\phi_2}\dot{\phi}_2^2 + J_x\dot{\phi}_1\dot{\phi}_2\cos(\phi_1 - \phi_2)$$

with: $J_{\phi_1} = l_1^2\left(\frac{1}{4}m_c + m_2\right) + J_c$ $\quad J_{\phi_2} = m_2l_2^2 + J_2$ $\quad J_x = l_1(m_2l_2)$

$$J_c = \frac{m_c}{12}l_1^2 \qquad J_2 = \frac{m_2}{12}l_{mp}^2$$

Considering that $l_2 = \frac{l_{mp}}{2}$, J_{ϕ_1} and J_{ϕ_2} can be rewritten as:

$$J_{\phi_1} = \frac{1}{3}m_cl_1^2 + m_2l_1^2 \qquad J_{\phi_2} = \frac{1}{4}m_2l_{mp}^2 + \frac{1}{12}m_2l_{mp}^2 = \frac{1}{3}m_2l_{mp}^2$$

It can be seen that J_{ϕ_1} equals the moment of inertia of a rod about its end- or pivot point ($\frac{1}{3}ml^2$). Additionally, there is an extra term $m_2l_1^2$ that can be regarded as a concentrated mass located at the end of the rod. Similarly, J_{ϕ_2} also corresponds to the moment of inertia of a rod around its end- or pivot point. Based on these observations, it can be concluded that the moment of inertia for both 'rods' were appropriately chosen for this method. For convenience of writing, the notation of l_2 will still be used.

$$V = \overbrace{\underbrace{m_cgz_c}_{\text{Cable}} + \underbrace{m_2gz_2}_{\text{Monopile}}}^{\text{Potential Energy}}$$
$$= m_cg\left(-\frac{l_1}{2}\cos(\phi_1)\right) + m_2g\left(-l_1\cos(\phi_1) - l_2\cos(\phi_2)\right)$$
$$= -l_1\left(\frac{1}{2}m_c + m_2\right)\cos(\phi_1) - \left(m_2gl_2\right)\cos(\phi_2)$$

$$= -\mu_1\cos\phi_1 - \mu_2\cos\phi_2 \qquad \text{with:} \qquad \mu_1 = l_1\left(\frac{1}{2}m_c + m_2\right)g \qquad \mu_2 = (m_2l_2)g$$

Again, the Lagrangian in equation A.14 is used to derive the following equations of motion:

$$L_{\phi_1} = J_{\phi_1}\ddot{\phi}_1 + J_x\,\ddot{\phi}_2\cos(\phi_1-\phi_2) + J_x\,\dot{\phi}_2^2\sin(\phi_1-\phi_2) + \mu_1\sin(\phi_1) = 0 \tag{A.21}$$

$$L_{\phi_2} = J_{\phi_2}\ddot{\phi}_2 + J_x\,\ddot{\phi}_1\cos(\phi_1-\phi_2) - J_x\,\dot{\phi}_1^2\sin(\phi_1-\phi_2) + \mu_2\sin(\phi_2) = 0 \tag{A.22}$$

The other components can be included in the same way as the mass m_2 is included. That means only the constant parameters $J_{\phi_1}, J_{\phi_2}, J_x$, μ_2 and μ_2 do change and results in the following:

$$J_{\phi_1} = l_1^2\left(\frac{1}{4}m_c + m_1 + m_2 + m_3 + m_{\text{int}} + m_a\right) + J_c \qquad J_{\phi_2} = m_2 l_2^2 + m_3 l_3^2 + m_{\text{int}} l_{\text{int}}^2 + m_a l_a^2 + J_2 + J_{\text{int}} + J_a$$

$$J_x = l_1\left(m_2 l_2 + m_3 l_3 + m_{\text{int}} l_{\text{int}} + m_a l_a\right)$$

$$\mu_1 = l_1\left(\left(\frac{1}{2}m_c + m_1 + m_2 + m_3 + m_{\text{int}}\right)g - F_b\right) \qquad \mu_2 = \left(m_2 l_2 + m_3 l_3 + m_{\text{int}} l_{\text{int}}\right)g - F_b l_a$$

Where the red components are added to the equation as a result of the extra mass and corresponding inertia of the cable. According to the cable specifications provided by Van Oord [22], the weight of the cable is 11.6 kg m^{-1}. In the 1600t crane configuration, the crane is equipped with two crane blocks, each consisting of six falls that are reeved twice, as shown in figure A.12. This means that the wire weight below the crane tip should be multiplied by 24.

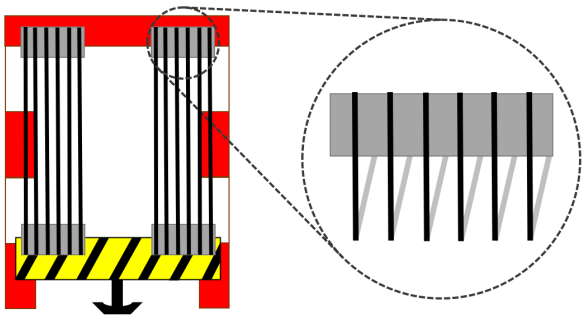

Figure A.12: Closer look to the crane wire that is reeved twice

The H-frame used in the model experiments had a measured mass of 2.84 kg. However, when considering the scale factor of $\lambda = 56.5$ and scaling the mass by a factor of 3, the estimated weight of the full-scale cable would be approximately 512 t. The weight and inertia of the H-frame should be considered during the validation of the numerical mode. When modelling the full scale scenario, the influence of the mass and inertia of the cable is accounted for but almost negligible compared to the weight of the MP.

Table A.1: Desired and actual weight of the cable on full- and model scale

Parameter	Desired	Actual	Unit	Difference (n times)
Max. length l_c	100	100	m	0
Max. length $l_{\text{H-frame}}$	1.77	1.77	m	0
Weight cable per meter full scale	X	289.4	kg m^{-1}/t m^{-1}	X
Weight cable per meter model scale	X	1.60	g/kg	X
Total weight cable on full scale	X	512.2	t	X
Total weight cable on model scale	X	2.84	kg	X

B

Newton's second law of motion

Newton's second law of motion asserts that an object's acceleration is directly proportional to the net force acting on it and inversely proportional to its mass. This concept can be expressed mathematically in equation B.1, where F represents the net force applied to the object, m represents the object's mass, and a represents the resulting acceleration.

$$F = ma = m\ddot{\mathbf{r}} \tag{B.1}$$

The simplification of the system is shown in figure B.1 and includes multiple components. For the derivation using Newton's second law, the system is simplified and consists of two masses m_1 and m_2 with corresponding lengths l_1 and l_2. The coordinate system is chosen with the origin at the suspension point, the x-axis as a horizontal axis and the z-axis is pointing downwards so gravity components are positively defined in these derivations.

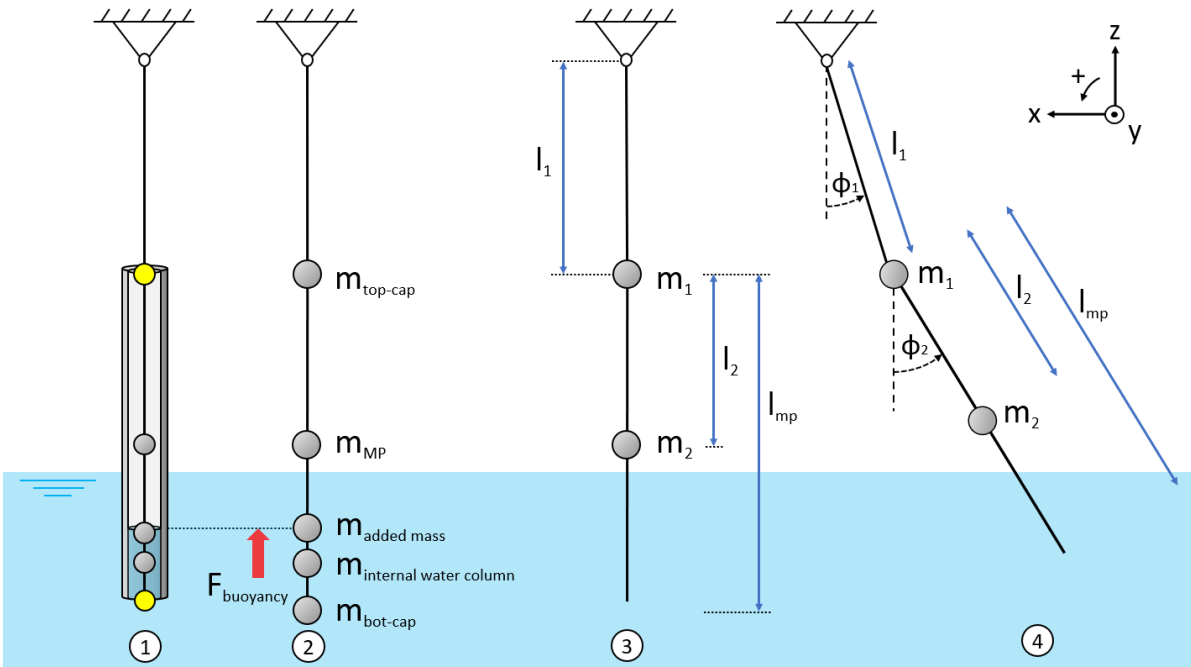

Figure B.1: 1: The system converted to a simplification 2: The system represented as point masses 3,4: The system including two particles m_1 and m_2 and angles ϕ_1 and ϕ_2

B.1. Constraints

A single pendulum has one particle with a corresponding position vector $\mathbf{r} = (x, y, z)$. Here, only two constraints are present because of the examination in the 2D plane with oscillations in the (x,z) plane. The particle m_1 is restrained by the suspension point and mathematically that means:

$$z = 0 \qquad \text{and} \qquad |\mathbf{r}| = l \tag{B.2}$$

The double pendulum however, has two particles with corresponding position vectors $\mathbf{r}_1$ and $\mathbf{r}_2$, defined by (x_i, y_i, z_i). The constraints for the double pendulum can be defined by:

$$\begin{aligned} z_1 &= 0 & \left|\mathbf{r}_1\right| &= l_1 \\ z_2 &= 0 & \left|\mathbf{r}_2 - \mathbf{r}_1\right| &= l_2 \end{aligned} \tag{B.3}$$

These constraints for the single pendulum can be defined by the generalized coordinate $\mathbf{r}$ and is defined as the angular position of the angle ϕ. Because the system is analyzed in the 2D-plane, only the coordinates x and z are considerd.

$$\mathbf{r} = l(x, z) = l(\sin\phi, \cos\phi) \tag{B.4}$$

For the two particles of the double pendulum, the generalized coordinates $\mathbf{r}_1$ and $\mathbf{r}_2$ for ϕ_1 and ϕ_2 respectively can be expressed as:

$$\mathbf{r}_1 = l_1\left(\sin\phi_1, \cos\phi_1\right) \tag{B.5}$$

$$\mathbf{r}_2 = \mathbf{r}_1 + l_2\left(\sin\phi_2, \cos\phi_2\right) \tag{B.6}$$

The velocity and acceleration vectors for the single pendulum can be expressed in terms of the generalized coordinate $\mathbf{r}$:

$$\mathbf{r} = l(\sin\phi, \cos\phi) \tag{B.7}$$

$$\dot{\mathbf{r}} = \mathbf{v} = l\dot{\phi}(\cos\phi, -\sin\phi) \tag{B.8}$$

$$\ddot{\mathbf{r}} = \mathbf{a} = l\ddot{\phi}(\cos\phi, -\sin\phi) - l\dot{\phi}^2(\sin\phi, \cos\phi) \quad = l\ddot{\phi}\hat{\mathbf{v}} - l\dot{\phi}^2\hat{\mathbf{r}} \tag{B.9}$$

The velocity vector $\mathbf{v}$ is perpendicular to the position vector $\mathbf{r}$ and $\mathbf{r} = l =$ constant. The derivation of equation B.7 can also be done for the first particle m_1 of the double pendulum:

$$\mathbf{r}_1 = l_1\left(\sin\phi_1, \cos\phi_1\right) \tag{B.10}$$

$$\dot{\mathbf{r}}_1 = \mathbf{v}_1 = l_1\dot{\phi}_1\left(\cos\phi_1, -\sin\phi_1\right) \tag{B.11}$$

$$\begin{aligned} \ddot{\mathbf{r}}_1 = \mathbf{a}_1 &= l_1\ddot{\phi}_1\left(\cos\phi_1, -\sin\phi_1\right) - l_1\dot{\phi}_1^2\left(\sin\phi_1, \cos\phi_1\right) \\ &= l_1\ddot{\phi}_1\hat{\mathbf{v}}_1 - l_1\dot{\phi}_1^2\hat{\mathbf{r}}_1 \end{aligned} \tag{B.12}$$

And for the second particle m_2:

$$\mathbf{r}_2 = \mathbf{r}_1 + l_2\left(\sin\phi_2, \cos\phi_2\right) \tag{B.13}$$

$$\dot{\mathbf{r}}_2 = \mathbf{v}_2 = \mathbf{v}_1 + l_2\dot{\phi}_2\left(\cos\phi_2, -\sin\phi_2\right) \tag{B.14}$$

$$\ddot{\mathbf{r}}_2 = \mathbf{a}_2 = \mathbf{a}_1 + l_2\ddot{\phi}_2\left(\cos\phi_2, -\sin\phi_2\right) - l_2\dot{\phi}_2^2\left(\sin\phi_2, \cos\phi_2\right) \tag{B.15}$$

B.2. Single Pendulum

To analyze the simple pendulum, a free body diagram (FBD) must me defined and is depicted in figure B.2. It includes the gravitational force $m_1 g$ and the tension T.

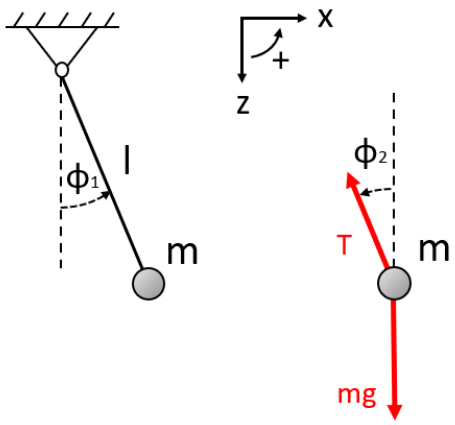

Figure B.2: A single pendulum (left) with its free body diagram (right)

Forces

For the single pendulum, the forces on the particle m_2 are the gravity $m_1 g$ and the tension T. Gravity is defined as positive downwards along the z-axis, $\mathbf{g} = g(0,1)$ The tension is pointing towards the suspension point along the direction of $-\mathbf{r}$ so that the forces F becomes:

$$\mathbf{F} = T\frac{-\mathbf{r}}{|\mathbf{r}|} + m\mathbf{g} = -\frac{T}{l}\mathbf{r} + m\mathbf{g} \tag{B.16}$$

Equations of motion

Newton's second law is defined in equation B.1 and for the single pendulum, equation B.16 can be used to define the force F acting on the particle m_1:

$$\begin{aligned} F = m\ddot{\mathbf{r}} &= -\frac{T}{l}\mathbf{r} + m\mathbf{g} \\ ml\left(\ddot{\phi}(\cos\phi, -\sin\phi) - \dot{\phi}^2(\sin\phi, \cos\phi)\right) &= -T(\sin\phi, \cos\phi) + mg(0,1). \end{aligned} \tag{B.17}$$

$$ml\left(\ddot{\phi}\cos\phi - \dot{\phi}^2\sin\phi\right) = -T\sin\phi \tag{B.18}$$

$$-ml\left(\ddot{\phi}\sin\phi + \dot{\phi}^2\cos\phi\right) = -T\cos\phi + mg \tag{B.19}$$

Multiplying equation B.18 with $\cos\phi$ and equation B.19 with $-\sin\phi$ gives equation B.20 and B.21 respectively:

$$ml\ddot{\phi}\cos^2 - ml\dot{\phi}^2\sin\phi\cos\phi = -T\sin\phi\cos\phi \tag{B.20}$$

$$ml\ddot{\phi}\sin^2\phi + ml\dot{\phi}^2\sin\phi\cos\phi = T\sin\phi\cos\phi - mg\sin\phi \tag{B.21}$$

Adding equation B.21 to B.20 gives the following formulation:

$$ml\ddot{\phi}\left(\cos^2\phi + \sin^2\phi\right) - ml\dot{\phi}^2\sin\phi\cos\phi + ml\dot{\phi}^2\sin\phi\cos\phi = -T\sin\phi\cos\phi + T\sin\phi\cos\phi - mg\sin\phi \tag{B.22}$$

The red and orange terms in equation B.22 cancel out and use of the trigonometry rule, $\cos^2\phi + \sin^2\phi = 1$, results in the following equation of motion for a single pendulum:

$$ml\ddot{\phi} = -mg\sin\phi \tag{B.23}$$

B.3. Double Pendulum

To analyze the system shown in figure B.1, a FBD must me defined and is depicted in figure B.3. It includes the gravitational forces $m_1 g$, $m_2 g$ and both the tension components T_1 and T_2.

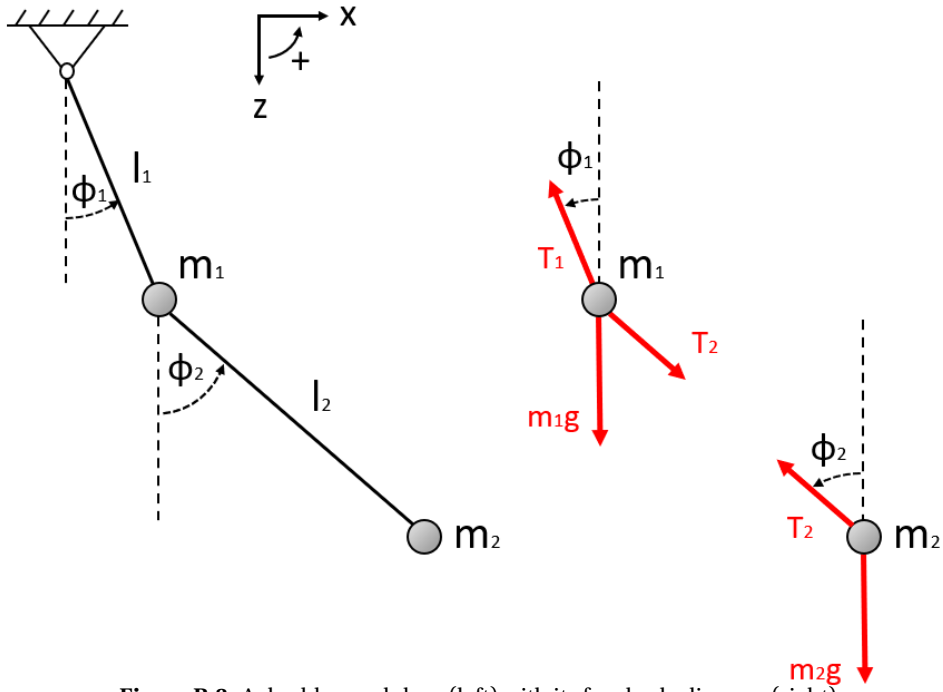

Figure B.3: A double pendulum (left) with its free body diagram (right)

Forces

For the double pendulum, the forces on the particle m_1 are the gravitational force $m_1 g$ and both tension components T_1 and T_2. Tension T_1 is along the direction $-\mathbf{r}_1$ and T_2 is directed along $(\mathbf{r}_2 - \mathbf{r}_1)$. The force F_1 can be written as:

$$\mathbf{F}_1 = T_1 \frac{-\mathbf{r}_1}{|\mathbf{r}_1|} + T_2 \frac{\mathbf{r}_2 - \mathbf{r}_1}{|\mathbf{r}_2 - \mathbf{r}_1|} + m_1 \mathbf{g} = -\frac{T_1}{l_1}\mathbf{r}_1 + \frac{T_2}{l_2}(\mathbf{r}_2 - \mathbf{r}_1) + m_1 \mathbf{g} \tag{B.24}$$

The forces on the second particle m_2 are the gravitational force $m_2 g$ and the tension T_2 acting along the direction $-(\mathbf{r}_2 - \mathbf{r}_1)$.

$$\mathbf{F}_2 = T_2 \frac{-(\mathbf{r_2} - \mathbf{r_1})}{|\mathbf{r_2} - \mathbf{r_1}|} + m_2 \mathbf{g} = -\frac{T_2}{l_2}(\mathbf{r_2} - \mathbf{r_1}) + m_2 \mathbf{g} \tag{B.25}$$

Equations of motion

For a double pendulum, Newton's second law of motion for each particle is defined as $\mathbf{F}_i = m_i \ddot{\mathbf{r}}_i$: and results in the following equations:

$$m_1 \ddot{\mathbf{r}}_1 = -\frac{T_1}{l_1}\mathbf{r}_1 + \frac{T_2}{l_2}(\mathbf{r}_2 - \mathbf{r}_1) + m_1 \mathbf{g} \tag{B.26}$$

$$m_2 \ddot{\mathbf{r}}_2 = -\frac{T_2}{l_2}(\mathbf{r_2} - \mathbf{r}_1) + m_2 \mathbf{g} \tag{B.27}$$

With gravity defined as positive downwards along the z-axis, $\mathbf{g} = g(0,1)$. Equations B.26 and B.27 have two non-zero components in the x-z-plane and contain four unknowns: ϕ_1, ϕ_2, T_1 and T_2. This results in four equations with four unknowns and is a system that can be solved. If the formulations in equations B.26 and B.27 can be split into the following set of differential equations:

$$m_1 l_1 (\ddot{\phi}_1 \cos\phi_1 - \dot{\phi}_1^2 \sin\phi_1) = -T_1 \sin\phi_1 + T_2 \sin\phi_2 \tag{B.28}$$

$$-m_1 l_1 (\ddot{\phi}_1 \sin\phi_1 + \dot{\phi}_1^2 \cos\phi_1) = -T_1 \cos\phi_1 + T_2 \cos\phi_2 + m_1 g \tag{B.29}$$

$$m_2\left(l_1\ddot{\phi}_1\cos\phi_1 - l_1\dot{\phi}_1^2\sin\phi_1 + l_2\ddot{\phi}_2\cos\phi_1 - l_2\dot{\phi}_2^2\sin\phi_2\right) = -T_2\sin\phi_2 \tag{B.30}$$

$$-m_2\left(l_1\ddot{\phi}_1\sin\phi_1 + l_1\dot{\phi}_1^2\cos\phi_1 + l_2\ddot{\phi}_2\sin\phi_2 + l_2\dot{\phi}_2^2\cos\phi_2\right) = -T_2\cos\phi_2 + m_2 g \tag{B.31}$$

These four differential equations for these four unknowns can be simplified by the same method used for equations B.18 and B.19 and by using the following trigonometric rules:

$$\boxed{\cos^2\phi + \sin^2\phi = 1 \qquad \text{and} \qquad \sin\phi_2\cos\phi_1 - \cos\phi_2\sin\phi_1 = \sin(\phi_2 - \phi_1)}$$

Applying these formulations to equations B.28 - B.31 result in the following equations of motion:

$$l_1\ddot{\phi}_1 = \left(\frac{T_2}{m_1}\right)\sin\left(\phi_2 - \phi_1\right) - g\sin\phi_1 \tag{B.32}$$

$$l_1\dot{\phi}_1^2 = \left(\frac{T_1}{m_1}\right) - \left(\frac{T_2}{m_1}\right)\cos\left(\phi_2 - \phi_1\right) - g\cos\phi_1 \tag{B.33}$$

$$m_2\left(l_1\ddot{\phi}_1\cos\left(\phi_2 - \phi_1\right) + l_1\dot{\phi}_1^2\sin\left(\phi_2 - \phi_1\right) + l_2\ddot{\phi}_2\right) = -m_2 g\sin\phi_2 \tag{B.34}$$

$$m_2\left(-l_1\ddot{\phi}_1\sin\left(\phi_2 - \phi_1\right) + l_1\dot{\phi}_1^2\cos\left(\phi_2 - \phi_1\right) + l_2\dot{\phi}_2^2\right) = T_2 - m_2 g\cos\phi_2 \tag{B.35}$$

Equations B.32 and B.33 can then be substituted in equations B.34 and B.35. Using trigonometric rules, these formulations can be simplified further and rewritten as follows:

$$\begin{aligned} m_2 l_2\ddot{\phi}_2 =& - m_2 g\sin\phi_2 - \left(\left(\frac{T_2}{m_1}\right)\sin\left(\phi_2 - \phi_1\right) - g\sin\phi_1\right) m_2\cos\left(\phi_2 - \phi_1\right) \\ & - \left(\left(\frac{T_1}{m_1}\right) - \left(\frac{T_2}{m_1}\right)\cos\left(\phi_2 - \phi_1\right) - g\cos\phi_1\right) m_2\sin\left(\phi_2 - \phi_1\right) \\ =& - m_2\left(\frac{T_1}{m_1}\right)\sin\left(\phi_2 - \phi_1\right) \end{aligned} \tag{B.36}$$

$$\begin{aligned} m_2 l_2\dot{\phi}_2^2 =& T_2 - m_2 g\cos\phi_2 + \left(\left(\frac{T_2}{m_1}\right)\sin\left(\phi_2 - \phi_1\right) - g\sin\phi_1\right) m_2\sin\left(\phi_2 - \phi_1\right) \\ & - \left(\left(\frac{T_1}{m_1}\right) - \left(\frac{T_2}{m_1}\right)\cos\left(\phi_2 - \phi_1\right) - g\cos\phi_1\right) m_2\cos\left(\phi_2 - \phi_1\right) \\ =& T_2 + m_2\left(\frac{T_2}{m_1}\right) - m_2\left(\frac{T_1}{m_1}\right)\cos\left(\phi_2 - \phi_1\right) \end{aligned} \tag{B.37}$$

The derivations above lead to the following set of equations of motion:

$$l_1\ddot{\phi}_1 = \left(\frac{T_2}{m_1}\right)\sin\left(\phi_2 - \phi_1\right) - g\sin\phi_1 \tag{B.38}$$

$$l_1\dot{\phi}_1^2 = \left(\frac{T_1}{m_1}\right) - \left(\frac{T_2}{m_1}\right)\cos\left(\phi_2 - \phi_1\right) - g\cos\phi_1 \tag{B.39}$$

$$m_2 l_2\ddot{\phi}_2 = -m_2\left(\frac{T_1}{m_1}\right)\sin\left(\phi_2 - \phi_1\right) \tag{B.40}$$

$$m_2 l_2\dot{\phi}_2^2 = T_2 + m_2\left(\frac{T_2}{m_1}\right) - m_2\left(\frac{T_1}{m_1}\right)\cos\left(\phi_2 - \phi_1\right) \tag{B.41}$$

The formulations for T_1 and T_2 can be derived from equations B.38 and B.40 and results in the following formulations:

$$T_1 = -\frac{m_1 m_2 l_2\ddot{\phi}_2}{m_2\sin\left(\phi_2 - \phi_1\right)} = -\frac{m_1 l_2\ddot{\phi}_2}{\sin\left(\phi_2 - \phi_1\right)} \tag{B.42}$$

$$T_2 = \frac{m_1 l_1\ddot{\phi}_1 + m_1 g\sin\phi_1}{\sin\left(\phi_2 - \phi_1\right)} \tag{B.43}$$

Using these expressions and substitute them in equations B.39 and B.41 results in the following two equations of motion:

$$l_1\dot{\phi}_1^2 = -\frac{l_2\ddot{\phi}_2}{\sin(\phi_2-\phi_1)} - \frac{l_1\ddot{\phi}_1 + g\sin\phi_1}{\sin(\phi_2-\phi_1)}\cos(\phi_2-\phi_1) - g\cos\phi_1 \tag{B.44}$$

$$m_2 l_2\dot{\phi}_2^2 = \frac{m_1 l_1\ddot{\phi}_1 + m_1 g\sin\phi_1}{\sin(\phi_2-\phi_1)} + m_2\left(\frac{l_1\ddot{\phi}_1 + g\sin\phi_1}{\sin(\phi_2-\phi_1)}\right) + m_2\left(+\frac{l_2\ddot{\phi}_2}{\sin(\phi_2-\phi_1)}\right)\cos(\phi_2-\phi_1) \tag{B.45}$$

Rewriting equation B.44 by multiplying with $-\sin(\phi_2-\phi_1)$:

$$-l_1\dot{\phi}_1^2\sin(\phi_2-\phi_1) = l_2\ddot{\phi}_2 + l_1\ddot{\phi}_1\cos(\phi_2-\phi_1) + (g\sin\phi_1\cos(\phi_2-\phi_1) + g\cos\phi_1\sin(\phi_2-\phi_1))^*$$

$$l_2\ddot{\phi}_2 = -l_1\ddot{\phi}_1\cos(\phi_2-\phi_1) - l_1\dot{\phi}_1^2\sin(\phi_2-\phi_1) - g\sin\phi_2^* \tag{B.46}$$

Multiplying equation B.46 with $m_2 l_2$ gives the following relation:

$$m_2 l_2^2\ddot{\phi}_2 = -l_1(m_2 l_2)\ddot{\phi}_1\cos(\phi_2-\phi_1) - l_1(m_2 l_2)\dot{\phi}_1^2\sin(\phi_2-\phi_1) - m_2 l_2 g\sin\phi_2 \tag{B.47}$$

Equation B.47 coincides with the formulation for the equation of motion B.53 found with Lagrange's method method. Rewriting equation B.45 by multiplying with $\sin(\phi_2-\phi_1)$:

$$m_2 l_2\dot{\phi}_2^2\sin(\phi_2-\phi_1) = m_1 l_1\ddot{\phi}_1 + m_1 g\sin\phi_1 + m_2 l_1\ddot{\phi}_1 + m_2 g\sin\phi_1 + m_2 l_2\ddot{\phi}_2\cos(\phi_2-\phi_1)$$

$$(m_1+m_2)l_1\ddot{\phi}_1 = -m_2 l_2\ddot{\phi}_2\cos(\phi_2-\phi_1) + m_2 l_2\dot{\phi}_2^2\sin(\phi_2-\phi_1) - (m_1+m_2)g\sin\phi_1 \tag{B.48}$$

Multiplying equation B.48 with l_1 gives the following relation:

$$(m_1+m_2)l_1^2\ddot{\phi}_1 = -l_1(m_2 l_2)\ddot{\phi}_2\cos(\phi_2-\phi_1) + l_1(m_2 l_2)\dot{\phi}_2^2\sin(\phi_2-\phi_1) - l_1(m_1+m_2)g\sin\phi_1 \tag{B.49}$$

Equation B.49 coincides with the formulation for the equation of motion B.52 found with Lagrange's method method.

Equations found with Newton's method

$$(m_1+m_2)l_1^2\ddot{\phi}_1 = -l_1(m_2 l_2)\ddot{\phi}_2\cos(\phi_2-\phi_1) + l_1(m_2 l_2)\dot{\phi}_2^2\sin(\phi_2-\phi_1) - l_1(m_1+m_2)g\sin\phi_1 \tag{B.50}$$

$$m_2 l_2^2\ddot{\phi}_2 = -l_1(m_2 l_2)\ddot{\phi}_1\cos(\phi_2-\phi_1) - l_1(m_2 l_2)\dot{\phi}_1^2\sin(\phi_2-\phi_1) - m_2 l_2 g\sin\phi_2 \tag{B.51}$$

Equations found with Lagrange's method

$$(m_1+m_2)\,l_1^2\ddot{\phi}_1 = -m_2 l_1 l_2\ddot{\phi}_2\cos(\phi_2-\phi_1) + m_2 l_1 l_2\dot{\phi}_2^2\sin(\phi_2-\phi_1) - l_1(m_1+m_2)\,g\sin\phi_1 \tag{B.52}$$

$$m_2 l_2^2\ddot{\phi}_2 = -m_2 l_1 l_2\ddot{\phi}_1\cos(\phi_2-\phi_1) - m_2 l_1 l_2\dot{\phi}_1^2\sin(\phi_2-\phi_1) - m_2 g\, l_2\sin\phi_2 \tag{B.53}$$

---

* Using the following trigonometric rules:

$$\boxed{\begin{aligned}\sin(\phi_2-\phi_1) &= \sin\phi_2\cos\phi_1 - \cos\phi_2\sin\phi_1\\ \cos(\phi_2-\phi_1) &= \cos\phi_2\cos\phi_1 + \sin\phi_2\sin\phi_1\\ \cos^2\phi + \sin^2\phi &= 1\end{aligned}}$$

The expression; $g\sin\phi_1\cos(\phi_2-\phi_1) + g\cos\phi_1\sin(\phi_2-\phi_1)$ can be rewritten as:

$$\begin{aligned}
&= g\sin\phi_1(\cos\phi_2\cos\phi_1 + \sin\phi_2\sin\phi_1) + g\cos\phi_1(\sin\phi_2\cos\phi_1 - \cos\phi_2\sin\phi_1)\\
&= g\sin\phi_1\cos\phi_2\cos\phi_1 + g\sin\phi_1\sin\phi_2\sin\phi_1 + g\cos\phi_1\sin\phi_2\cos\phi_1 - g\cos\phi_1\cos\phi_2\sin\phi_1\\
&= g\sin\phi_1\sin\phi_2\sin\phi_1 + g\cos\phi_1\sin\phi_2\cos\phi_1\\
&= g\sin^2\phi_1\sin\phi_2 + g\cos^2\phi_1\sin\phi_2\\
&= g\left((\sin^2\phi_1 + \cos^2\phi_1)\sin\phi_2\right)\\
&= g\sin\phi_2
\end{aligned}$$

C

Exploratory test set-up

This Appendix provides detailed pictures regarding the exploratory tests presented in Chapter 4.

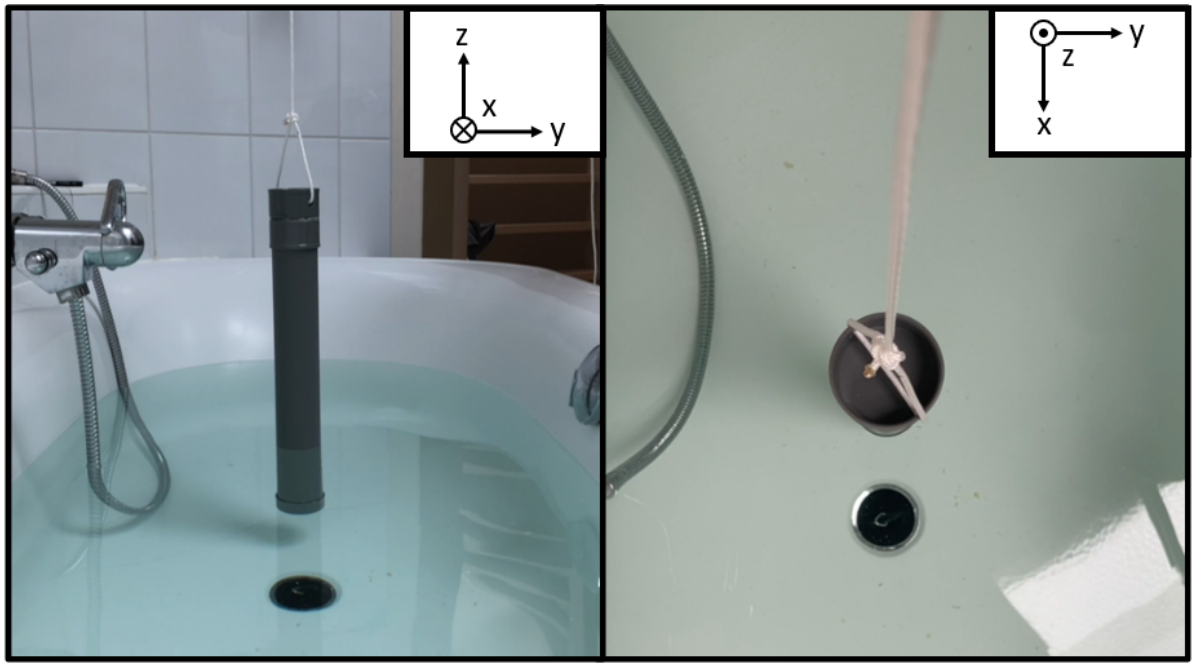

Figure C.1: Camera views of the exploratory experimental set-up

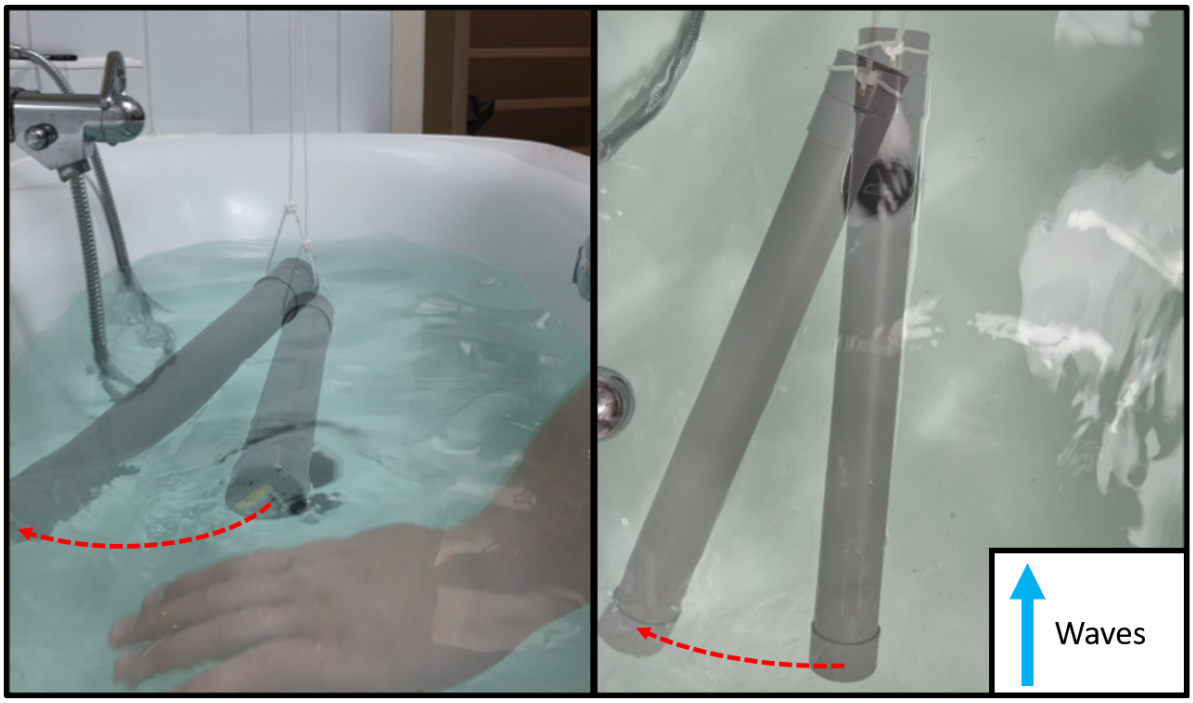

Figure C.2: Static offset in sway direction increases because of the manually generated wave forces acting on the MP

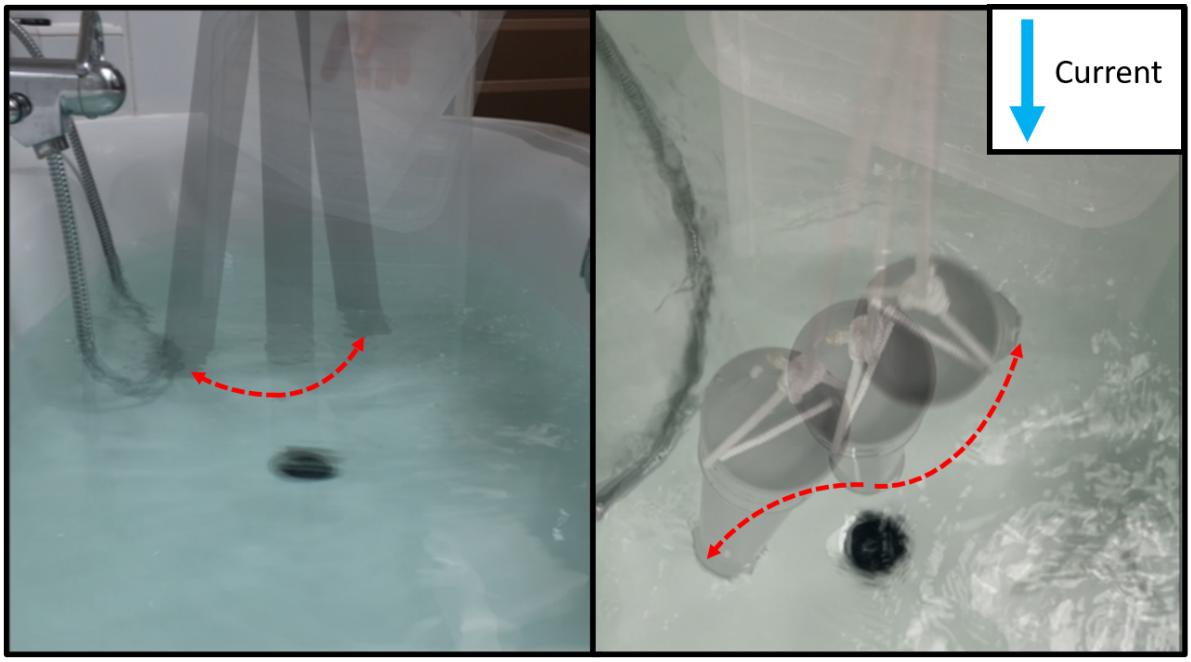

Figure C.3: Motions of the MP in surge and sway direction as a result of vortices around the MP caused by the applied current

Bibliography

[1] Sithik Aliyar et al. "Experimental investigation of offshore crane load during installation of a wind turbine jacket substructure in regular waves". In: *Ocean Engineering* 241 (Dec. 2021).

[2] H.F. Bauer. "Tables and graphs of zero of cross product Bessel functions". In: *MTP-AERO* (1963), pp. 63–50.

[3] United Nations Climate Change. *The Paris Agreement*. 2015. URL: https://unfccc.int/process-and-meetings/the-paris-agreement/the-paris-agreement (visited on 03/24/2022).

[4] T.M. Charlton. *Energy principles in theory of structures*. ISBN 0-19-714102-1. Oxford University Press, 1973.

[5] International Towing Tank Conference. "Fresh water and seawater properties". In: *ITTC - Recommended Procedures* (2011). Revision 2, 5 and 8.

[6] Global Wind Energy Council. "Global Offshore Wind Report 2021". In: *GWEC* (2021).

[7] M. Dam. *Monopile installation assessment*. Thesis, Delft University of Technology, 2018.

[8] O.M. Faltinsen and A.N. Timokha. *Sloshing*. Cambridge University Press, 2009.

[9] J. Gerritsen. *The hydrodynamics of a suspended cylinder in waves*. Thesis, Delft University of Technology, 2017, p. 40.

[10] H.Schlichting and K. Gersten. *Boundary-layer Theory*. 9th ed. ISBN 978-3-662-52917-1. Cambridge University Press, 2017.

[11] L.H. Holthuijsen. *Waves in oceanic and coastal waters*. Cambridge University Press, 2007.

[12] Prislin I., Steen A., and Halkjard J. "Upending of a Spar Offshore Platform: Prediction of Motions and Loading". In: *Proceedings of the International Offshore and Polar Engineering Conference, Stavanger, Norway* 1 (2001).

[13] R.A. Ibrahim. *Liquid Sloshing Dynamics: Theory and Applications*. Cambridge University press, 2005.

[14] Daniel J. Inman. *Engineering Vibrations*. 4th ed. ISBN-13:978-0-13-287169-3. Pearson Education, 2014.

[15] IRENA. "Renewable Power generation costs in 2020, International Renewable Energy Agency, Abu Dhabi". In: *IRENA* (2021). ISBN: 978-92-9260-348-9, p. 101.

[16] IRENA. "World Energy Transitions Outlook 2021, International Renewable Energy Agency, Abu Dhabi". In: *IRENA* (2021).

[17] J.D. Jint and Y. Matsuzaki. "Bifurcations in a two-degree-of-freedom elastic system with follower forces". In: *Journal of Sound and Vibration 126 (2)* (1988), pp. 265–277.

[18] J.M.J. Journée and W.W. Massie. *Offshore Hydromechanics*. 3rd ed. Delft University of Technology, 2015.

[19] G.H. Keulegan and L.H. Carpenter. "Forces on Cylinders and Plates in an Oscillating fluid". In: *Journal of Research of the National Bureau of Standards* 60.5 (1958).

[20] Liu L. et al. "Experimental study on wet tow and upending of a truss spar". In: *Proceedings of the ASME 2011 30th International Conference on Ocean, Offshore and Arctic Engineering OMAE2011* (2011).

[21] NASA. *NASA climate change, carbon dioxide*. 2022. URL: https://climate.nasa.gov/vital-signs/carbon-dioxide/ (visited on 03/24/2022).

[22] Van Oord. *Primary reeving diagram*. Tech. rep. Huisman Equipment B.V.

[23] P. Ruponen et al. "Air compression in a flooded tank of a damaged ship". In: *Ocean Engineering* 57 (2013), pp. 64–71.

[24] T. Sarpkaya. "In-line and Transverse Forces on Cylinders in Oscillatory Flow at High Reynolds Numbers". In: *Offshore Technology Conference* (1976). doi: 10.4043/2533-MS.

[25] J.J. Thomsen. “Chaotic dynamics of the partially follower-loaded elastic double pendulum”. In: *Journal of Sound and Vibration 188 (3)* (1995), pp. 385–405.

[26] A. Vellekoop. *Conceptual design of a Time-efficient Method for the Installation of Mono-piles exceeding Crane Capacity*. Thesis, Delft University of Technology, 2015.

[27] Det Norske Veritas. “Environmental conditions and environmental loads”. In: *Recommended practice DNV-RP-C205* (2010), p. 250.

[28] Det Norske Veritas. “Environmental conditions and environmental loads”. In: *Recommended practice DNV-RP-C205* (2010), pp. 86–99.

[29] P. Voges et al. “Craneless Upending of Large Offshore Monopiles Using a Specialised Floater”. In: *Coastal Engineering Proceedings* 1 (2019).

[30] P.R. Wellens. “Introduction to Ship and Offshore Hydromechanics”. In: *Lecture Notes* (2019), 5 and 8.

[31] P. Yu and Q. Bi. “Analysis of non-linear dynamics and bifurcations of a double pendulum”. In: *Journal of Sound and Vibration 217 (4)* (1998), pp. 691–736.

[32] X. L. Zhang et al. “Time domain simulation of damage flooding considering air compression characteristics”. In: *Water (Switzerland)* 11 (Apr. 2019).

[33] H. Ziegler. “Die stabilitatskriterien der elastomechanik”. In: *Ingenieur-Archiv 20* (1952), pp. 49–56.